



AFAL-TR-88-076

AD:

Interim Report
January 1984 to
January 1988

Solid Propellant Flame Spectroscopy

AD-A199 334

August 1988

Author:
J. Tim Edwards

Approved for Public Release

Distribution is unlimited. The AFAL Technical Services Office has reviewed this report, and it is releasable to the National Technical Information Service, where it will be available to the general public, including foreign nationals.

**Air Force
Astronautics
Laboratory**

Air Force Space Technology Center
Space Division, Air Force Systems Command
Edwards Air Force Base,
California 93523-5000

DTIC
ELECTE
SEP 1 6 1988
S H D

NOTICE

When U.S. Government drawings, specifications, or other data are used for any purpose other than a definitely related Government procurement operation, the fact that the Government may have formulated, furnished, or in any way supplied the said drawings, specifications, or other data, is not to be regarded by implication or otherwise, or in any way licensing the holder or any other person or corporation, or conveying any rights or permission to manufacture, use, or sell any patented invention that may be related thereto.

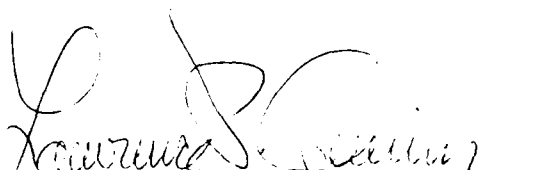
FOREWORD

This interim report summarizes the experimental results obtained during the combustion mechanisms project in the Combustion Research Laboratory at the Air Force Astronautics Laboratory (AFAL), Edwards Air Force Base, CA. The project covered a 6.5 year period from January 1981 to September 1987. AFAL project managers were David Mann, David P. Weaver, and Tim Edwards.

This report has been reviewed and is approved for release and distribution in accordance with the distribution statement on the cover and on the DD Form 1473.

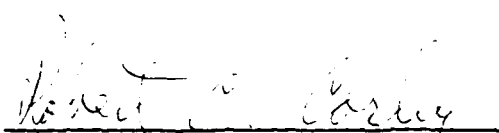


J. TIM EDWARDS
Project Manager



LAWRENCE P. QUINN
Chief, Aerothermochemistry Branch

FOR THE COMMANDER



ROBERT C. CORLEY
Deputy Chief, Astronautical Sciences
Division

REPORT DOCUMENTATION PAGE				Form Approved OMB No. 0704-0188	
1a. REPORT SECURITY CLASSIFICATION UNCLASSIFIED			1b. RESTRICTIVE MARKINGS		
2a. SECURITY CLASSIFICATION AUTHORITY			3. DISTRIBUTION/AVAILABILITY OF REPORT		
2b. DECLASSIFICATION/DOWNGRADING SCHEDULE			Approved for public release. Distribution is unlimited.		
4. PERFORMING ORGANIZATION REPORT NUMBER(S) AFAL-TR-88-076			5. MONITORING ORGANIZATION REPORT NUMBER(S)		
6a. NAME OF PERFORMING ORGANIZATION Air Force Astronautics Laboratory		6b. OFFICE SYMBOL (If applicable) LSCC	7a. NAME OF MONITORING ORGANIZATION		
6c. ADDRESS (City, State, and ZIP Code) AFAL/LSCC Edwards AFB, CA 93523-5000			7b. ADDRESS (City, State, and ZIP Code)		
8a. NAME OF FUNDING/SPONSORING ORGANIZATION		8b. OFFICE SYMBOL (If applicable)	9. PROCUREMENT INSTRUMENT IDENTIFICATION NUMBER		
8c. ADDRESS (City, State, and ZIP Code)			10. SOURCE OF FUNDING NUMBERS		
			PROGRAM ELEMENT NO 61102F	PROJECT NO 2308	TASK NO M1
				WORK UNIT ACCESSION NO E3	
11. TITLE (Include Security Classification) Solid Propellant Flame Spectroscopy (U)					
12. PERSONAL AUTHOR(S) Edwards, J. Tim					
13a. TYPE OF REPORT Interim		13b. TIME COVERED FROM 84/1 TO 88/1		14. DATE OF REPORT (Year, Month, Day)	
				15. PAGE COUNT	
16. SUPPLEMENTARY NOTATION					
17. COSATI CODES			18. SUBJECT TERMS (Continue on reverse if necessary and identify by block number)		
FIELD	GROUP	SUB-GROUP			
21	08		Laser-Induced Fluorescence, Combustion Spectroscopy, Solid Propellant Combustion, Combustion Diagnostics		
19. ABSTRACT (Continue on reverse if necessary and identify by block number)					
<p>This report summarizes the progress made in solid propellant flame chemistry studies during the Combustion Mechanisms project at the AFAL from 1/84 to 1/88. These chemistry studies involved the spectroscopic determination of species concentration and temperature profiles in solid propellant flames at pressures from atmospheric to 7 MPa (1000 psi). The propellants involved contained AP and HMX, as well as several other formulations. The molecules studied were OH, CN, NH, and NO, primarily, although other atomic and molecular species were seen in the propellant flames in emission. The primary diagnostic employed was laser-induced fluorescence (LIF), although the chemiluminescence (emission) from the propellant flames was also studied. These experiments are continuing.</p>					
20. DISTRIBUTION/AVAILABILITY OF ABSTRACT <input checked="" type="checkbox"/> UNCLASSIFIED/UNLIMITED <input type="checkbox"/> SAME AS RPT <input type="checkbox"/> DTIC USERS			21. ABSTRACT SECURITY CLASSIFICATION Unclassified/Unlimited distribution		
22a. NAME OF RESPONSIBLE INDIVIDUAL Tim Edwards			22b. TELEPHONE (Include Area Code) (805) 275-5656		22c. OFFICE SYMBOL LSCC

TABLE OF CONTENTS

1.0 Introduction	1
1.1. Homogeneous propellants	2
1.2. HMX composite propellants	6
1.3. AP composite propellants	9
1.4. Metalized composite propellants	13
2.0 Equipment and procedures	17
2.1. Combustor	17
2.2. Lasers	19
2.3. Detectors and electronics	20
3.0 Propellant data	27
3.1. Propellant formulations	27
3.2. Propellant burn rate data	28
3.3. Propellant theoretical predictions	34
3.4. Propellant control information	42
4.0 Emission spectroscopy of flames	43
4.1. CH ₄ /N ₂ O flame emission spectra	45
4.2. C ₃ H ₈ /air flame emission spectra	54
4.3. AP1 propellant emission studies	56
4.4. AP2 propellant emission studies	64
4.5. HMX1 propellant emission studies	69
4.6. Emission spectra from other propellants	75
4.7. Modeling of emission spectra-CN	76
4.8. Modeling of emission spectra-NH	87
5.0 Laser-induced fluorescence experiments	99
5.1. OH LIF experiments (Part 1)	99
5.2. CN LIF experiments	114
5.3. NH LIF experiments	134
5.4. OH LIF experiments (Part 2)	145
5.5. Raman scattering utilizing 308 nm light	155
6.0 Summary, conclusions, recommendations	165
7.0 References	167



Accession For	
NTIS GPA&I	<input checked="" type="checkbox"/>
DTIC TAB	<input type="checkbox"/>
Unannounced	<input type="checkbox"/>
Justification	
By	
Distribution/	
Availability Codes	
Dist	Avail and/or Special
A-1	

Appendix A. Listing of CN temperature fitting program	183
Appendix B. Listing of NH temperature fitting program	193
Appendix C. Listing of heat of explosion (Hex) program	213
Appendix D. Propellant ingredients	217
Appendix E. Flame emission summary	219

LIST OF FIGURES

Figure	Page
Figure 1. AP propellant flame structure changes as a function of pressure and particle size.	15
Figure 2. High pressure combustor.	18
Figure 3. Schematic of experimental apparatus.	22
Figure 4. Reticon sensitivity as measured by tungsten filament standard lamp.	23
Figure 5. Broadband emission spectrum of inner cone of CH ₄ /N ₂ O flame.	23
Figure 6. Photograph of laboratory equipment.	24
Figure 7. Photograph of laboratory equipment.	24
Figure 8. Photograph of laboratory equipment.	25
Figure 9. Photograph of burning propellant strand. AP1 propellant, 0.8 MPa.	25
Figure 10. HMX1 propellant burn rate as a function of pressure, English units.	29
Figure 11. HMX1 propellant burn rate as a function of pressure, SI units.	29
Figure 12. AP1 propellant burn rate as a function of pressure, English units.	30
Figure 13. AP1 propellant burn rate as a function of pressure, SI units.	30
Figure 14. AP2 propellant burn rate as a function of pressure, English units.	31
Figure 15. AP2 propellant burn rate as a function of pressure, SI units.	31
Figure 16. DB propellant burn rate as a function of pressure, English units.	32
Figure 17. DB propellant burn rate as a function of pressure, SI units.	32
Figure 18. HMX1 propellant burn rate as a function of pressure, plotted as log-log.	33
Figure 19. AP1 propellant burn rate as a function of pressure, plotted as log-log.	33
Figure 20. Theoretical predictions of CH ₄ /N ₂ O flame properties.	35

Figure 21. Theoretical predictions of $\text{CH}_4/\text{N}_2\text{O}$ flame properties.	35
Figure 22. Theoretical predictions of $\text{CH}_4/\text{N}_2\text{O}$ flame properties.	36
Figure 23. Theoretical predictions of DB (NG/PEG) propellant flame properties.	36
Figure 24. Theoretical predictions of AP/polybutadiene propellant flame properties.	37
Figure 25. Correlation between adiabatic flame temperature and heat of explosion calculations.	37
Figure 26. CN ($\text{B}^2\Sigma\text{-X}^2\Sigma$) emission spectrum.	46
Figure 27. CN ($\text{B}^2\Sigma\text{-X}^2\Sigma$) emission spectrum.	46
Figure 28. CN ($\text{B}^2\Sigma\text{-X}^2\Sigma$) emission spectrum.	47
Figure 29. CN ($\text{B}^2\Sigma\text{-X}^2\Sigma$) emission spectrum.	47
Figure 30. NH ($\text{A}^3\Pi\text{-X}^3\Sigma$) emission spectrum.	48
Figure 31. CH ($\text{A}^2\Delta\text{-X}^2\Pi$) emission spectrum.	48
Figure 32. C_2 ($\text{A}^3\Pi\text{-X}^3\Pi$) emission spectrum.	49
Figure 33. C_2 ($\text{A}^3\Pi\text{-X}^3\Pi$) emission spectrum.	49
Figure 34. OH ($\text{A}^2\Sigma\text{-X}^2\Pi$) emission spectrum.	50
Figure 35. OH ($\text{A}^2\Sigma\text{-X}^2\Pi$) emission spectrum.	50
Figure 36. Emission spectrum of CN ($\text{B}^2\Sigma\text{-X}^2\Sigma$) and CH ($\text{A}^2\Delta\text{-X}^2\Pi$).	51
Figure 37. Cr emission spectrum	51
Figure 38. Ni emission spectrum	52
Figure 39. Reference emission spectrum for Figure 37.	52
Figure 40. NO emission spectrum.	53
Figure 41. Same as Figure 40, corrected for Reticon wavelength response	53

Figure 42. CH ($B^2\Sigma-X^2\Pi$) emission spectrum.	54
Figure 43. CH ($A^2\Delta-X^2\Pi$) emission spectrum.	55
Figure 44. OH ($A^2\Sigma-X^2\Pi$) emission spectrum.	55
Figure 45. C_2 ($A^3\Pi-X^3\Pi$) emission spectrum.	56
Figure 46. CN ($B^2\Sigma-X^2\Sigma$) emission spectrum.	59
Figure 47. CN ($B^2\Sigma-X^2\Sigma$) emission spectrum.	59
Figure 48. CN ($B^2\Sigma-X^2\Sigma$) emission spectrum.	60
Figure 49. CaCl ($A^2\Pi-X^2\Sigma$) emission spectrum.	60
Figure 50. NH ($A^3\Pi-X^3\Sigma$) emission spectrum.	61
Figure 51. OH ($A^2\Sigma-X^2\Pi$) emission spectrum.	61
Figure 52. OH ($A^2\Sigma-X^2\Pi$) emission spectrum.	62
Figure 53. OH ($A^2\Sigma-X^2\Pi$) emission spectrum.	62
Figure 54. CH ($A^2\Delta-X^2\Pi$) emission spectrum.	63
Figure 55. Emission intensity as a function of distance above surface.	63
Figure 56. Emission intensity as a function of distance above surface.	64
Figure 57. Emission spectra.	65
Figure 58. Emission intensity as a function of distance.	66
Figure 59. CN emission intensity profiles for two AP propellants	66
Figure 60. Na emission spectra.	67
Figure 61. Na emission intensity as a function of distance.	67
Figure 62. Comparison of continuous emission from AP2 propellant and a tungsten calibration source.	68
Figure 63. Black body predictions.	68
Figure 64. Black body predictions.	69

Figure 65. OH ($A^2\Sigma-X^2\Pi$) emission.	71
Figure 66. OH ($A^2\Sigma-X^2\Pi$) emission.	71
Figure 67. NH ($A^3\Pi-X^3\Sigma$) emission.	72
Figure 68. CN ($B^2\Sigma-X^2\Sigma$) emission.	72
Figure 69. Fe emission.	73
Figure 70. Emission.	73
Figure 71. Emission.	74
Figure 72. Emission.	74
Figure 73. Relative emission intensity as a function of distance above surface.	75
Figure 74. Sample CN ($B^2\Sigma-X^2\Sigma$) emission spectra.	79
Figure 75. Model CN ($B^2\Sigma-X^2\Sigma$) emission spectrum.	80
Figure 76. Model CN ($B^2\Sigma-X^2\Sigma$) emission spectrum.	80
Figure 77. Model CN ($B^2\Sigma-X^2\Sigma$) emission spectrum.	81
Figure 78. Model CN ($B^2\Sigma-X^2\Sigma$) emission spectrum.	81
Figure 79. Model CN ($B^2\Sigma-X^2\Sigma$) emission spectrum.	82
Figure 80. Model CN ($B^2\Sigma-X^2\Sigma$) emission spectrum.	82
Figure 81. Model CN ($B^2\Sigma-X^2\Sigma$) emission spectrum.	83
Figure 82. Model CN ($B^2\Sigma-X^2\Sigma$) emission spectrum.	83
Figure 83. CN ($B^2\Sigma-X^2\Sigma$) emission spectrum in AP1 propellant flame.	84
Figure 84. CN emission spectra in AP1 propellant flame.	84
Figure 85. Comparison of model and experimental CN peak heights.	85
Figure 86. Comparison of model and experimental CN peak heights.	85
Figure 87. Comparison of model and experimental CN peak heights.	86

Figure 88. Comparison of model and experimental CN peak heights.	86
Figure 89. Comparison of model and experimental CN peak heights.	87
Figure 90. Comparison of theoretical (F1 R, F2 R, F3 R) NH 0,0 R branch lines with literature (Dixon) values.	89
Figure 91. Comparison of theoretical (F1 Q, F2 Q, F3 Q) NH 0,0 Q branch lines with literature (Dixon) values.	89
Figure 92. Comparison of theoretical (F1 P) NH 0,0 P branch lines with literature (Dixon) values.	90
Figure 93. Comparison of theoretical (F1 R, F2 R, F3 R) NH 1,1 R branch lines with literature (Funke) values.	90
Figure 94. Comparison of theoretical (F1 Q, F2 Q, F3 Q) NH 1,1 Q branch lines with literature (Funke) values.	91
Figure 96. Comparison of theoretical (F1 P) NH 1,1 P branch lines with literature (Funke) values.	91
Figure 96. Model NH ($A^3\Pi-X^3\Sigma$) emission spectrum	92
Figure 97. Model NH ($A^3\Pi-X^3\Sigma$) emission spectrum	92
Figure 98. Fitting of model bandhead ratio data.	93
Figure 99. Variation of NH T_v in AP1 propellant flame with distance above surface.	93
Figure 100. Model NH ($A^3\Pi-X^3\Sigma$) emission spectrum	94
Figure 101. Model NH ($A^3\Pi-X^3\Sigma$) emission spectrum	94
Figure 102. NH ($A^3\Pi-X^3\Sigma$) emission spectrum.	95
Figure 103. Model NH ($A^3\Pi-X^3\Sigma$) emission spectrum.	95
Figure 104. Model NH ($A^3\Pi-X^3\Sigma$) emission spectrum .	96
Figure 105. Model NH ($A^3\Pi-X^3\Sigma$) emission spectrum .	96
Figure 106. Model NH ($A^3\Pi-X^3\Sigma$) emission spectrum.	97

Figure 107. Model NH ($A^3\Pi-X^3\Sigma$) emission spectrum.	97
Figure 108. Model NH ($A^3\Pi-X^3\Sigma$) emission spectrum.	98
Figure 109. OH ($A^2\Sigma-X^2\Pi$) LIF, CH_4/O_2 flame, 306.38 nm excitation.	102
Figure 110. Same as Figure 109, 306.42 nm excitation.	102
Figure 111. Same as Figure 109, 306.51 nm excitation.	103
Figure 112. Same as Figure 109, 306.61 nm excitation.	103
Figure 113. Same as Figure 109, 306.65 nm excitation.	104
Figure 114. Same as Figure 109, 306.75 nm excitation.	104
Figure 115. Same as Figure 109, 306.81 nm excitation.	105
Figure 116. Same as Figure 109, 306.86 nm excitation.	105
Figure 117. Same as Figure 109, 306.9 nm excitation.	106
Figure 118. Same as Figure 109, 306.94 nm excitation.	106
Figure 119. Same as Figure 109, 306.99 nm excitation.	107
Figure 120. Same as Figure 109, 307.03 nm excitation.	107
Figure 121. Same as Figure 109, 307.03 nm excitation.	108
Figure 122. Same as Figure 109, 307.25 nm excitation.	108
Figure 123. Replication of Figure 109.	109
Figure 124. OH ($A^2\Sigma-X^2\Pi$) LIF, AP1 propellant flame.	109
Figure 125. OH ($A^2\Sigma-X^2\Pi$) LIF, AP1 propellant flame.	110
Figure 126. Same conditions as Figure 125.	110
Figure 127. OH ($A^2\Sigma-X^2\Pi$) LIF, AP1 propellant flame.	111
Figure 128. Laser transmittance through flame as a function of pressure.	111
Figure 129. OH LIF intensity as a function of laser power.	112

Figure 130. OH LIF intensity (scaled to 3.5 mJ/pulse attenuated laser energy in flame) as a function of pressure.	112
Figure 131. OH LIF and emission intensities as a function of distance above surface.	113
Figure 132. OH LIF intensity as a function of horizontal position in flame.	113
Figure 133. Dye laser output as a function of wavelength.	123
Figure 134. CN ($B^2\Sigma-X^2\Sigma$) LIF, CH_4/N_2O flame.	123
Figure 135. CN ($B^2\Sigma-X^2\Sigma$) LIF, CH_4/N_2O flame.	124
Figure 136. CN ($B^2\Sigma-X^2\Sigma$) LIF, CH_4/N_2O flame.	124
Figure 137. CN ($B^2\Sigma-X^2\Sigma$) LIF, AP1 propellant flame.	125
Figure 138. CN ($B^2\Sigma-X^2\Sigma$) emission, AP1 propellant flame.	125
Figure 139. Relationship between CN LIF intensity and (nominal) distance above the propellant surface.	126
Figure 140. Schematic of CN LIF experiments with PMT detector.	126
Figure 141. CN LIF, AP1 propellant.	127
Figure 142. Same conditions as Figure 140.	127
Figure 143. Influence of pressure on AP1 propellant flame quantities.	128
Figure 144. CN LIF, HMX1 propellant flame.	128
Figure 145. Same conditions as Figure 143	129
Figure 146. CN LIF, HMX1 propellant flame.	129
Figure 147. CN LIF, HMX1 propellant flame.	130
Figure 148. CN LIF, HMX2 propellant flame.	130
Figure 149. Comparison of CN LIF intensity profiles for propellants HMX1 and HMX2 at 1.8 MPa.	131
Figure 150. CN LIF, AN1 propellant flame.	131

Figure 151. Reaction zone thickness as a function of propellant burn rate.	132
Figure 152. Reaction zone thickness as a function of pressure.	132
Figure 153. Relationship between width of transition region (defined in Figure 139) and propellant burn rate.	133
Figure 154. Relationship between width of transition region (defined in Figure 139) and propellant burn rate.	133
Figure 155. CN LIF, CH ₄ /N ₂ O flame.	134
Figure 156. Comparison of dye output (PTP dye) and filter transmission (Ealing 35-9224 filter) curves.	136
Figure 157. NH (A ³ Π-X ³ Σ) LIF intensity as a function of excitation wavelength	137
Figure 158. NH (A ³ Π-X ³ Σ) LIF, 343 nm excitation.	137
Figure 159. NH LIF, 342.2 nm excitation.	138
Figure 160. NH LIF, 341.8 nm excitation.	138
Figure 161. NH LIF, 341.0 nm excitation.	139
Figure 162. NH LIF, 340 nm excitation.	139
Figure 163. NH LIF, 338.5 nm excitation.	140
Figure 164. NH (A ³ Π-X ³ Σ) LIF, AP1 propellant.	140
Figure 165. NH LIF, AP1 propellant.	141
Figure 166. Same conditions as Figure 165	141
Figure 167. NH (A ³ Π-X ³ Σ) LIF, Reticon detector.	142
Figure 168. NH LIF, Reticon detector, HMX1 propellant flame.	142
Figure 169. Same conditions as Figure 167	143
Figure 170. Same conditions as Figure 167 but laser blocked.	143
Figure 171. NH LIF, Reticon detector, AP1 propellant.	144

Figure 172. $\text{NH}(\text{A}^3\Pi\text{-X}^3\Sigma)$ LIF, 305 nm exc. (NH 1,0 band).	144
Figure 173. Excimer-pumped dye laser output with Rhodamine B (LC 6100) dye.	146
Figure 174. Estimated frequency-doubled excimer-pumped dye laser output with Rhodamine B dye.	147
Figure 175. $\text{OH}(\text{A}^2\Sigma\text{-X}^2\Pi)$ LIF, $\text{CH}_4/\text{N}_2\text{O}$ flame	147
Figure 176. $\text{OH}(\text{A}^2\Sigma\text{-X}^2\Pi)$ LIF, 308.0 nm excitation.	148
Figure 177. OH LIF, 310.0 nm excitation.	148
Figure 178. OH LIF, 306.4 nm excitation.	149
Figure 179. OH LIF, 306.4 nm excitation.	149
Figure 180. OH LIF, 306.4 nm excitation.	150
Figure 181. Saturation results for OH (A-X) LIF experiments,	150
Figure 182. Saturation results for OH (A-X) LIF experiments	151
Figure 183. Same conditions as Figure 178 but 3 ns gate width.	151
Figure 184. $\text{OH}(\text{A}^2\Sigma\text{-X}^2\Pi)$ LIF, AP1 propellant flame.	152
Figure 185. Comparison of OH LIF and CN LIF profiles in AP1 propellant flame.	152
Figure 186. OH LIF, DB1 propellant flame.	153
Figure 187. 313.8 nm channel of Figure 185 smoothed (3 pulse running average applied to collected data).	153
Figure 188. OH LIF, HMX1 propellant flame,	154
Figure 189. OH LIF excitation spectrum.	154
Figure 190. OH absorption spectrum.	155
Figure 191. $\text{OH}(\text{A}^2\Sigma\text{-X}^2\Pi)$ LIF from 308 nm excitation.	157
Figure 192. $\text{OH}(\text{A}^2\Sigma\text{-X}^2\Pi, 1,0 \text{ band})$ LIF from 308 nm excitation.	158

Figure 193. OH ($A^2\Sigma-X^2\Pi$, sR_{21} band) LIF from 308 nm excitation.	158
Figure 194. OH ($A^2\Sigma-X^2\Pi$, 0,1 band) LIF from 308 nm excitation.	159
Figure 195. NH ($A^3\Pi-X^3\Sigma$, 0,0 band sequence) LIF from 308 nm excitation.	159
Figure 196. CN ($B^2\Sigma-X^2\Sigma$, 0,0 band) LIF from 308 nm excitation.	160
Figure 197. C_2 ($A^2\Sigma-X^2\Pi$, 0,0 band) LIF from 308 nm excitation.	160
Figure 198. OH ($A^2\Sigma-X^2\Pi$, 0,0 band) LIF from 308 nm excitation.	161
Figure 199. OH ($A^2\Sigma-X^2\Pi$, 0,0 band) LIF from 308 nm excitation.	161
Figure 200. NH LIF and N_2 Raman from 308 nm excitation.	162
Figure 201. OH and NH LIF from 308 nm excitation.	162
Figure 202. Emission from AP1 propellant flame.	163
Figure 203. Emission from AP1 propellant flame.	163

LIST OF TABLES

Table	Page
Table 1. Summary of diagnostic measurements performed on propellants under combustion conditions.	14
Table 2. LIF excitation schemes.	19
Table 3. Propellant Formulations.	27
Table 4. Propellant Impurities.	27
Table 5. Assorted burn rate data.	28
Table 6. Theoretical propellant flame properties at 3.5 MPa.	34
Table 7. Hex calculations for propellants/ingredients.	39
Table 8. Heat of formation and density data for Hex and Tfl calculations.	39-40
Table 9. Comparison of calculated and literature Hex values.	40
Table 10. ISP results with suppressed product species.	41
Table 11. Species seen in emission in AP1 propellant flame.	58
Table 12. Species seen in emission in AP2 propellant flame.	65
Table 13. Species seen in emission in HMX1 propellant flame.	70
Table 14. Preliminary NH Tv results.	88
Table 15. Influence of propellant composition on OH LIF intensity.	101
Table 16. Previous NH LIF schemes.	136
Table 17. Equilibrium OH concentrations.	146
Table 18. Interferences with Raman measurements using 308 nm laser light.	157

1.0 INTRODUCTION

The purpose of this technical report is the documentation of experimental results obtained during the Combustion Mechanisms project in 1984-1987. These experiments were performed in the Combustion Research Laboratory of the Air Force Astronautics Laboratory. In general, the experiments involved the spectroscopic study of solid propellant flames at pressures from atmospheric to 7 MPa (1000 psig). Some of the results have been documented in journal publications and technical reports (Ref. 1-13), but much of the enclosed data has not been published and may be of interest to others. This technical report includes all the information in Ref. 2,4,6-9, as well as much unreported information. The rest of this introduction is intended to be a brief introduction to the subject to make the information in the rest of the report accessible to readers not familiar with the area. A good starting point for more detail is Ref. 14.

It is generally believed that future improvements in the understanding of solid propellant combustion must come from a clearer picture of the chemistry and physics occurring in high pressure solid propellant flames. Condensed phase reactions also need more study. The structure and reactions of solid propellant flames are not well understood under rocket motor conditions (pressures on the order of 7 MPa (1000 psia)), although enough is known that serviceable solid propellant combustion models have been created (Ref. 14). These models tend to emphasize the heat transfer aspects of combustion at the expense of the chemistry. This allows much useful information to be derived from the models, although many situations that are directly chemistry related, such as binder structure influences on burning behavior, are not well handled. To improve the understanding of solid propellant combustion, much more detailed information is needed on propellant flames, preferably under high pressure combustion conditions. It is important to understand the combustion chemistry since this is the type of information the propellant formulator or chemist can use to tailor and/or improve the performance of the propellant.

Laser-based combustion diagnostics (Ref. 15,16) have the potential to address many of the unknown aspects of propellant combustion, although the experimental difficulties are formidable. Propellant flames have large temperature gradients, very complex chemistry, and are often heterogeneous and time varying (Ref. 14). Under conditions where laser diagnostics are not feasible because of flame opacity or other considerations, emission (chemiluminescence) spectroscopy can yield useful information, although typically with poorer spatial and temporal resolution than laser-based diagnostics. This report describes the application of such diagnostic tools to the study of solid propellant flames at high pressures. Publications from this research have described modelling and experimental work. The modelling efforts were aimed at a better understanding of the influence of high pressure on such processes as quenching and self-absorption (Ref. 10-13). The experimental papers discussed studies of propellant flame structure by the analysis of flame chemiluminescence (Ref. 1-3,5). Several papers were mainly oriented to the experimental aspects of the application of OH and CN LIF to the study of high pressure solid propellant flames (Ref. 4,6-9). This report also includes a brief discussion of the application of laser-Raman scattering using the 308 nm beam from an excimer laser as a solid propellant flame diagnostic. The OH LIF work (Ref. 4,6) was performed to examine the influence of the high pressure, optically

thick propellant flame on laser diagnostics, while the CN LIF work (Ref. 4,7,8) is the initial work in planned studies of important radicals such as CN, CH, NH, and NO. Important work in this area is also that of Parr and Parr (Ref. 17), who have generated 2-D images of OH, CN, NH, NO, NO₂, and temperature in atmospheric pressure laser-driven solid propellant flames.

Radicals are only part of the chemistry picture in solid propellant flames. The distributions of temperature and stable species are also important and have been the subject of several research studies. Coherent anti-Stokes Raman spectroscopy has been used as a diagnostic in solid propellant combustion research as both a temperature and species probe (Ref. 18-21), although data on high pressure propellant flames is difficult to obtain. The temperature distribution in a number of solid propellants has been measured using very fine thermocouples (Ref. 22,23). This data gives some important information on the location and thickness of reaction zones. Several studies of the distribution of stable species in solid propellant flames have been made using sampling probes connected to mass spectrometers (Ref. 23). A summary of the species and temperature measurements made in solid propellant flames is given in Table 1. Other species are important and deserve study. For example, some important species that have not been studied in propellant flames and possible diagnostic probes for these species are H₂CN (IR absorption (Ref. 24)), C₂H₄ and C₂H₂ (Raman or CARS (Ref. 16,25)) and HCO (REMPI (Ref. 26)). These type of diagnostics may not be possible in propellant flames. Extensive research has been done on the thermal decomposition mechanisms of solid propellants and propellant ingredients (Ref. 27-29,202), although the application of these mechanisms to the much higher heating rates encountered in solid propellant combustion is difficult (Ref. 28,29). Several diagnostic approaches will have to be applied to high pressure propellant flames before the flame structure and chemistry will be well understood. A brief summary of the current understanding of the main solid propellant families is now appropriate as an introduction to the measurements discussed in the body of this report. Solid propellants are generally divided into two broad classes, homogeneous and heterogeneous, depending upon the physical structure of the solid phase. Homogeneous propellants are those propellants consisting only of a polymeric binder and a liquid plasticizer. A typical example would be a "double-base" propellant consisting of nitroglycerin and nitrocellulose. Heterogeneous propellants add a crystalline oxidizer to the polymer/plasticizer mixture before curing and thus the solid phase is heterogeneous. Common crystalline oxidizers are ammonium perchlorate (AP) and cyclotetramethylene tetranitramine (HMX). The combustion chemistry of homogeneous and heterogeneous propellants can be quite different, as described below. A compilation of the acronyms and structures of the propellant ingredients discussed in this report is listed in Appendix D. A convenient list of acronyms encountered in the propellant area has been published (Ref. 30).

HOMOGENEOUS PROPELLANTS

Homogeneous solid propellants based upon nitrate esters as the energetic ingredient were among the first solid propellants in widespread use. The first such propellants consisted of a mixture of nitrocellulose (NC) and nitroglycerin (NG), hence the name "double-base." More modern propellants utilize NG as an ingredient in an energetic binder, rather than as the basis for an entire propellant. Because of combustion differences between the various propellants, Cohen (Ref. 54,55) suggests it is desirable to sub-divide the generic "double-

base" propellant grouping into double-base (hereafter DB, consisting entirely of NG and NC), "cross-linked double base" (XLDB, e.g., NG/PEG or NG/PGA (Ref. 56)), and "nitroplastisol" (NP, e.g. TMETN/TEGDN/NC (Ref. 43)). The homogeneous nature of the solid propellant implies that the flame above the propellant surface should be one-dimensional, with temperature and composition varying only as a function of distance above the surface. These propellants have been the subject of much study, with the following picture generally agreed upon (Ref. 23,29,57,58). The burning propellant is divided up into several zones. The initial zone is the preheat zone where the propellant is heated up to some temperature where the propellant begins to decompose (the "foam zone"). The gaseous propellant decomposition products (generally thought to consist of aldehydes + NO₂) burn rapidly in the "fizz zone" until the NO₂ and aldehydes are consumed. At pressures below about 100 atm, an induction zone occurs (the "dark zone"), followed by a luminous flame where the NO from the fizz zone is finally consumed and the final product distribution is achieved. For example, mass spectrometer probe measurements (Ref. 23) have been made near the surface, but above the small fizz zone (25% NO, 2 % N₂, 42% CO, 15% CO₂, 14% H₂O, 0.6% H₂, 3% hydrocarbons) and in the luminous flame (0% NO, 15% N₂, 28% CO, 38% CO₂, 19% H₂O, 0.4% H₂). At higher pressures, the luminous flame zone and the fizz zone essentially merge and no dark zone is visible. When visible, the length of the dark zone is roughly proportional to P⁻¹ (Ref. 59). Except at higher pressures, the luminous flame zone is thought to have little influence on the propellant burn rate. However, the energy release in the NO→N₂ reaction is so large that if this energy release could be forced to occur close enough to the surface, the effect on the propellant burn rate would be large (Ref. 60). The propellant properties are usually correlated in terms of the propellant energy ("heat of explosion"). An important feature of these types of propellants is that the burning rate is modifiable over a large range by the addition of catalysts (typically lead salts), with the result that pressure regions can be found in the catalyzed propellants where the propellant burning rate is independent of pressure. This has important ballistic implications, and is one area of propellant combustion where an improved understanding of solid propellant combustion chemistry might yield valuable insight into this important yet poorly understood phenomena.

Homogeneous propellants are the simplest propellants to model and, as such, are a common basis for theoretical models that include complex phenomena such as transient behavior and two-phase flow (Ref. 61,62). The purpose of this discussion is not to review the various models, but to briefly discuss the current understanding of the propellant flame chemistry. For this reason, I will only discuss a few of the (simpler) homogeneous propellant models that have been used to correlate actual propellant behavior (Ref. 23,58,59,63-66). Note that HMX and AP as monopropellants could be defined as a homogeneous propellant, but discussion of HMX and AP is deferred until later in this section. In these models, a heat balance is performed at the propellant surface. The heat needed to raise the propellant from the bulk temperature to the surface temperature $\{c_s(T_s - T_0)\}$, where c_s is the propellant heat capacity, T_0 is the bulk propellant temperature and T_s is the surface temperature is equated to the heat released in condensed phase reactions $\{Q_s\}$ and the heat input from the flame $\{Q_g\}$. Q_s is generally modeled as being positive, but could be negative for endothermic condensed phase reactions. The condensed phase reactions of nitrate-ester propellants are net exothermic. The relative importance of Q_s and Q_g is a function of the propellant energy level and the pressure (Ref. 23). The simplest models are those of Kubota (Ref. 59) and Beckstead (Ref.

58), who assume Q_s is released at the surface and assume a simplified model for the gas phase, such as a single flame sheet or a uniform heat release in a specified reaction zone for the fizz zone. This heat balance approach is similar to the approach used in laminar flame theories (Ref. 67-69). Cohen (Ref. 63,64) integrates through the condensed phase rather than assuming a surface reaction. Cohen and Lo have also extended their modeling to other nitrate esters such as TMETN, TEGDN, and BTTN (Ref. 65). Lengelle (Ref. 23) assumes an in-depth condensed phase heat release and two overall global reactions (flame sheets), corresponding to the fizz zone flame and the luminous flame. Bizot (Ref. 66) modifies this approach by adding a third overall reaction between NO and carbon which improves the model performance at higher pressures (>100 atm) and allows for the effects of catalysts to be modeled. The influence of various catalysts on the combustion of various energetic ingredients has been studied in detail (Ref. 60,70), although the details of the catalysis of DB propellant combustion by lead compounds are still unclear (Ref. 23,29).

These models have several features in common. The fizz zone chemistry is modeled as aldehyde/ NO_2 reactions, generally lumped together into a single global reaction (Ref. 58,63). For example, nitroglycerin is modeled as decomposing (Ref. 64): $\text{C}_3\text{H}_5\text{N}_3\text{O}_9 \rightarrow 2 \text{CH}_2\text{O} + \text{HCO} + 3 \text{NO}_2$, with the CH_2O , HCO , and NO_2 reacting in the fizz zone. The fizz zone flame is modeled either as a high activation energy reaction (flame sheet) (Ref. 63,59) or a (lower activation energy) distributed reaction zone (Ref. 23,59). Use of a flame sheet approximation gives a flame height for a double-base propellant at 10 atm ($r=0.2$ cm/s) of approximately 50 μm (Ref. 63,59). The corresponding luminous flame height (or dark zone length/induction zone length) is on the order of 1 cm (Ref. 59). For the simplest models, the burning rate is found by solving the energy balance equation and the surface pyrolysis law $\{r \sim A_s \exp(-E_s/RT_s)\}$, where A and E are the Arrhenius parameters for the propellant pyrolysis} simultaneously. The heat input from the flame is calculated from the flame standoff distance and the flame heat release (Q_f) $\{Q_g = Q_f \exp(-\rho_s r c_g x_f / \lambda_g)\}$, where x_f is the flame standoff distance, c and λ are the gas phase heat capacity and thermal conductivity and the product of ρ_s and r is the mass burning rate of the propellant}. The flame standoff distance is calculated from the assumed flame (global) rate kinetics $\{x_f \sim (kP^\delta)^{-1} \sim (F^\delta A_g \exp(-E_g/RT_g))^{-1}\}$, where k is the rate constant, δ is the gas phase reaction order and A and E are the Arrhenius parameters, all for the assumed global reaction in the flame}. This simple model can be used to gain some physical insight into the propellant flame structure. For example, if a laser is used to add heat at the propellant surface (e.g., (Ref. 17)), the heat balance must shift to account for the added surface heat release. Assuming that the propellant surface temperature remains constant, the burn rate and flame standoff distance must change. Since the surface temperature is only a weak function of burn rate (Ref. 23), it seems likely that the main change in the event of laser heat addition would be an increase in the propellant burn rate and/or an increase in the propellant flame height. This is the reason for the large flame zones observed in laser pyrolysis work (Ref. 17). Another general observation is that the flame standoff or flame height is a strong function of the condensed phase heat release assumed for a given (known) burn rate. The heat release is generally calculated from microthermocouple traverses of the propellant condensed phase and flames (Ref. 44,59,71), although the accuracy of these profiles (actually the accuracy of the temperature gradient near the surface) at higher pressures has been questioned (Ref. 58). One difficulty that is common to all the models is that the maximum temperature (T_g) at the end of the fizz zone must be known. This temperature is not the

adiabatic (equilibrium) flame temperature, but is rather the temperature that accounts for the fact that most of the nitrogen is in the form of NO at the end of the fizz zone, rather than N₂. This temperature can be calculated on the assumption that NO is the main nitrogen-containing product, although this assumption still leads to imperfect results (Ref. 63,66). Non-equilibrium formation of solid carbon is also important in some propellants (Ref. 73).

Detailed chemical kinetic modeling has been performed for double-base propellants (Ref. 74,75). The decomposition mechanism of the solid ingredients must still be assumed (e.g., $C_3H_5N_3O_9 \rightarrow 2 CH_2O + HCO + 3 NO_2$, as above (Ref. 65)). The aldehydes are consumed by fast reactions with the H, O, and OH radicals in the fizz zone in this detailed analysis. The overall carbon mechanism is $CH_2O \rightarrow HCO \rightarrow CO \rightarrow CO_2$. The NO₂ is consumed by fast reactions with the same radicals to form NO and, eventually, N₂. The dark zone is generally perceived to be a chemical induction zone, where the radicals depleted in the fizz zone are built back up until the NO \rightarrow N₂ reaction can take place. Reactions in the luminous flame were an early target of kinetic modeling (Ref. 76), since mass spectrometric analyses of the dark zone and luminous flame were among the earliest successful diagnostic measurements in high pressure propellant flames (Ref. 23,29,57,77,78). However, the luminous flame has the least important influence on the propellant combustion since it occurs so far from the surface. As discussed above, double-base burn rate models ignore the luminous flame except at the highest pressures. However, from a chemistry standpoint, all gas-phase zones are of interest since part of the chemistry occurring in the fizz zone may be inferred from dark zone analyses. The major weaknesses of this type of detailed kinetic modeling are that the initial decomposition products must still be assumed and that the rate constants for many of the combustion reactions have not been studied under the temperature and pressure conditions encountered in propellant combustion.

The fizz zone is a difficult diagnostic target. Of the important radical species present, only OH (and perhaps NO) is a convenient subject for LIF in the difficult propellant flame environment. Probing a molecule such as HCO would be quite difficult. NO₂ LIF has been tentatively reported in propellant flames at atmospheric pressure (Ref. 17). Emission spectroscopic studies at the AFAL on a double base propellant (see Section 4.6) yielded no detectable emission from the common "interesting" radicals (OH, CH, CN, NH) at any point in the flame at pressures from 0.8-3.5 MPa. Weak Na emission (589 nm) was seen in the luminous flame zone. Other DB emission measurements have yielded similar results (Ref. 79-81), with only impurity spectra (such as Na and K) observed. However, an IR emission study observed (apparently) such reactive species as NO, NO₂, C₂H₂, and HCN (Ref. 79). Attempts at measuring CN concentrations with CN LIF (Section 5.2) were unsuccessful, which is not surprising since CN is not anticipated to play an important role in CH₂O/NO₂ flames. NH LIF experiments have not been performed, but again the likelihood of significant amounts of NH being found in the flame is small if the aldehyde/NO₂ theory is correct. OH and NO LIF experiments are planned in the DB propellant flames at AFAL (complementary to the successful OH LIF experiments in the AP1 and HMX1 propellant flames (Sections 5.1, 5.4) to see if the OH and NO profiles can be measured. One would expect (speculate?) that the OH profile would show two peaks, one in the fizz zone where the OH is actively involved in reactions with CH₂O and HCO, and one in the luminous flame where the OH is involved in the CO \rightarrow CO₂ and NO \rightarrow N₂ reactions. The NO profile should show a broad peak in the dark

zone. Much of this is still speculation since CH_2O is a very difficult fuel to handle and thus has not been commonly studied. However, a study of a $\text{CH}_2\text{O}/\text{NO}_2$ flame has been recently reported (Ref. 82). One of the key chemistry issues in double-base propellant combustion is the identity of the gas-phase species generated by the various solid propellant components. NG is proposed to form CH_2O , NO_2 , and HCO (Ref. 64,74), but what of other ingredients, especially the polymers such as PEG and PGA? The identification of the decomposition products of these polymers will be a key requirement of an accurate XLDB propellant chemical mechanism, since models that fit DB and NP propellants tend to fit XLDB propellants less well because of the unknown effects of the binder decomposition (Ref. 54,65). The pyrolysis of these binders will lead to various hydrocarbons and aldehydes (Ref. 17,83,84), as well as (probably) solid carbon. Solid carbon is known to be important in burn rate modification in catalyzed double-base propellants and may well be important in the kinetic mechanisms for double-base (Ref. 66), XLDB (Ref. 65), and nitramine flames. Certainly, the thermochemistry of these type of propellants is modified by the presence of solid carbon (Ref. 73). LIF experiments at AFAL in DB propellant flames at pressures from 0.8-3.5 MPa have found significant scattering from particulates, to the extent that the DB1 flame (where "flame" is defined here as the region above the surface, regardless of any visible emission) is essentially opaque at pressures much above 3.5 MPa where the dark zone is small. Interestingly, the opacity of the dark zone in the DB flame is a minimum at about 1.8 MPa, and increases as the pressure is lowered. If one assumes the gas opacity at these lower pressures is caused by soot or solid carbon, rather than the general increase in flame opacity seen with increases in pressure ((Ref. 1) and Section 5.1), then it is tempting to speculate that more carbon is being formed as the pressure is lowered, perhaps due to less complete combustion (?). Glowing particles can be seen in the dark zone in pictures of DB propellant flames taken by Kubota (Ref. 59), very obvious at 1 MPa and less obvious at 2 and 3 MPa. This carbon has important diagnostic implications and may, as stated, have important kinetic implications. For example, one would like to lower the pressure to extend the fizz zone and increase the diagnostic resolution close to the surface. However, if lowering the pressure causes large amounts of carbon to form, the chemistry may be changing significantly and thus the chemistry seen at low pressure may be difficult to relate to the high pressure combustion of the propellant.

HMX COMPOSITE PROPELLANTS

The combustion of nitramines and nitramine composite propellants has been the subject of a large number of research studies. A review (or even a detailed discussion) of the research in this area is beyond the scope of this report and the expertise of the author. However, a brief discussion of the combustion of nitramine propellants is appropriate as an introduction to the experimental results presented later. From this point, the discussion will focus on HMX, but many of the conclusions are appropriate to RDX also. The main differences in the combustion of RDX and HMX come about because of the differences in vapor pressure (Ref. 28). More detailed discussions of HMX thermal decomposition behavior are available (Ref. 28,29), although the application of this information to the higher temperatures and heating rates encountered in combustion is difficult (Ref. 28,29). The chemistry in HMX propellant flames under combustion conditions is not well understood (Ref. 28,29).

The combustion of HMX composite propellants is thought to be similar in many ways to that of double-base propellant flames, even though the propellants are heterogeneous (Ref. 22). HMX is much more stoichiometrically balanced than AP so that HMX composite propellants burn more like one-dimensional (premixed) double-base flames than the multi-dimensional AP composite propellant flames. For example, a dark zone has been reported for HMX propellants with non-energetic binders (Ref. 22). The chemistry of nitramines is thought to be more complex than the relatively simple aldehyde/ NO_2 chemistry seen in double-base flames. Although originally it was thought that the HMX decomposition could be modeled as a $\text{CH}_2\text{O}/\text{N}_2\text{O}$ flame (based on low temperature, low heating rate decomposition experiments), it now appears that HCN is an important, if not the principal, fuel species in the HMX flame under combustion conditions (Ref. 29,85,86). This leads to some interesting changes in the chemistry. HCN is an important intermediate in the combustion of fuel nitrogen, so the combustion chemistry of HCN has been studied, at least with O_2 as an oxidizer (Ref. 87). A model flame study of a $\text{C}_2\text{N}_2/\text{NO}_2$ flame is underway, with an extension to $\text{H}_2/\text{C}_2\text{N}_2/\text{NO}_2$ being planned (Ref. 88). The chemistry of this flame may be similar to that of a HCN/ NO_2 flame (not studied because of the hazards of HCN), although the C-C bond in C_2N_2 is stronger than the H-C bond in HCN. The combustion of HCN has been reported to occur through intermediate CN, NCO, and NH_x species to the final NO and N_2 products (Ref. 87,89,90). Although this mechanism was found in O_2 -oxidized flames, it should be relevant to NO_2 -oxidized flames since the initial NO_2 reaction is usually the breakdown of NO_2 into NO and O (or the abstraction of O by H to form OH + NO), with OH and O being more reactive oxidizers than NO. Thus, the active oxidizers should be O and OH radicals as in O_2 -oxidized flames.

The combustion of HMX and HMX composite propellants has been modeled by many investigators {e.g., (Ref. 54,55,91-99)}. Most of the models have used a two-step global kinetics model of the gas phase: $\text{HMX} \rightarrow \text{HCN}, \text{NO}_2, \text{CH}_2\text{O}, \text{N}_2\text{O} \rightarrow \text{CO}, \text{CO}_2, \text{H}_2, \text{H}_2\text{O}, \text{N}_2$. As with the nitrate-ester propellants, the final reactions are usually modeled as occurring too far from the surface to affect the burn rate at typical rocket motor pressures. This was seen in inert binder propellants where the length of the dark zone could be modified with a catalyst without affecting the propellant burn rate (Ref. 22). The differences between HMX monopropellant combustion and nitrate-ester combustion is that the condensed phase is probably endothermic, rather than exothermic (Ref. 54,55). The transition of HMX from solid to gas under combustion conditions is very complex (Ref. 28), but can be generalized as being a vaporization process, rather than a condensed phase decomposition (Ref. 54,55). This implies that the heat feedback from the vapor phase controls the combustion and that the heat release should occur closer to the surface than in a comparable nitrate-ester (double-base) propellant that has significant condensed phase heat release. A typical HMX composite propellant consists of HMX in an energetic binder (more precisely, an inert binder such as PGA with an energetic plasticizer such as NG or TMETN). Energetic polymers, such as NG, are rarely used. The HMX and energetic binder are usually modeled as non-interacting (Ref. 55), although not always (Ref. 97,98). If the binder and HMX are modeled as interacting, the diffusion flame between the two is modeled as "robbing" the HMX monopropellant flame of energy (Ref. 98). The addition of HMX to energetic binders reduces the net condensed phase heat release (and thus decreases the temperature sensitivity) and increases the gas phase control of the combustion (and thus increases the pressure exponent) (Ref. 55). In general, these

models imply that the gas phase reactions control the combustion of the HMX and that the majority of the rate-controlling heat release occurs very close to the surface.

Detailed kinetic modeling of HMX and RDX combustion (no binder) has been performed (Ref. 94,95,100). The limitations of this approach are similar to those discussed in the homogeneous propellant discussion, namely the limited knowledge of the initial propellant decomposition products and the lack of kinetic data taken under combustion conditions. The gas phase models are linked to the propellant surface through a boundary condition and the burn rate can then be predicted. The burn rate was found to be sensitive to many of the reactions, although the many uncertainties in the rate kinetics prevent firm conclusions so far. If the HMX decomposition was assumed to proceed through HCN and NO_2 , the important initial reactions were $\text{H} + \text{NO}_2 \rightarrow \text{NO} + \text{OH}$ (consumption of NO_2 and formation of the "kinetically sluggish" (Ref. 60) NO) and $\text{HCN} + \text{O} \rightarrow \text{NCO} + \text{OH}$ (fast consumption of HCN) (Ref. 94). CN is intimately involved in reactions involving HCN (Ref. 94), so measurements of CN (see below) could be used to track the combustion of HCN. Even more complex kinetic models have been constructed and used to model the ignition of nitramines (Ref. 95). Kinetic modeling of RDX combustion in the Soviet Union (Ref. 100) has also been performed and the results compared to mass spectrometric measurements of RDX flame species at 0.5 atm (Ref. 39,40,101,102). The lack of firm data on initial binder decomposition products is a large roadblock to further progress in modeling actual propellants (nitramine + binder).

HMX propellant combustion has been studied experimentally in several ways. HMX flames are rich in such radical intermediates as CN and NH, so emission and LIF are useful diagnostics. In fact, CN and NH have been seen in emission in HMX flames up to 7 MPa (Section 4.5), and CN LIF profiles have been obtained in both HMX propellants listed in Table 3.1.1 (Section 5.2). NO and NO_2 have been measured in atmospheric pressure HMX flames in ignition (Ref. 17), so the possibility of measuring these species in higher pressure flames exists and will be attempted at AFAL. Temperature profiles have been measured in HMX propellant flames with thermocouples (Ref. 22), with the results confirming the "two-stage" flame visually observed. CARS has been used to tentatively identify HCN in the propellant flames (Ref. 18,103). Mass spectrometric measurements of species have been made in the dark and luminous flame zones, as with double-base flames, with similar results. The interesting results of Parr and Parr (Ref. 17) showed that the CN and NH peak in concentration farther away from the surface than NO_2 , apparently indicating that these species are playing a role in the consumption of NO_2 . CN LIF experiments at AFAL in an inert-binder HMX propellant ("HMX2" in Table 3.1.1) showed a CN peak at the end of dark zone, with the CN in an energetic-binder HMX propellant ("HMX1" in Table 3.1.1) flame peaking near the surface (see Section 5.2). The energetic-binder HMX propellant shows no dark zone, so the source of the CN in the HMX1 flame is in doubt. CN at the upper end of the HMX2 dark zone can be explained by the reaction of the hydrocarbons and N_2O seen in the dark zone by Kubota (Ref. 22). CN would not be expected in the reaction of the classical dark zone reactants NO, CO, and H_2 (Ref. 46,104). Much work remains to be done on HMX propellant flames, with one useful goal being the selection of several "standard" propellants so that the data from various researchers could be combined and correlated. This is one reason that propellant HMX2 was selected for study (similar to Kubota's propellant HTPS (Ref. 22)), even though the stoichiometry of this propellant is more fuel rich than HMX propellants of current

propulsion interest. Propellant HMX1 is a more typical "energetic binder"/HMX propellant and would typically be modeled by assuming that the chemistry of the gas phase chemistry of the HMX and energetic binder are separate and then superimposing the heat transfer from both flames to calculate a burn rate (Ref. 55). This may not be accurate for propellant HMX1 since the heat of explosion of the binder is so low (by my calculations, the heats of explosion are 1352, 1183, 780, 1037, and 187 cal/gm for HMX, TMETN, propellants HMX2 and HMX1, and the HMX1 binder {63% TMETN, 37% PGA}, respectively). In this case, the binder may act more as a diluent to the HMX flame, rather than as a semi-independent flame.

Experimental data and modeling are close to being able to produce comparable data. This comparison is the only way to validate the predictions of the detailed kinetic modeling, as has been shown in hydrocarbon combustion situations (Ref. 105). One interesting comparison can be made between the 0.8 MPa predictions of Hatch of the CN distribution in an HMX flame (Ref. 94), and the experimental data obtained at AFAL in an 73% HMX propellant flame (Section 5.2). Hatch predicts that the CN distribution should "stand-off" the surface $\sim 100\text{ }\mu\text{m}$, with the CN distribution extending from 100 to 400 μm above the surface. In the propellant flame, the experimental data shows a more extended CN zone, with a thickness of about 500 μm . This extension of the reaction zone may be an aspect of the "cooling" of the propellant flame because of the presence of the less energetic binder, although this is only a preliminary explanation. Much more work is needed, both in extending the modeling to propellants (HMX + binders) and in obtaining better experimental data in flames of HMX and HMX propellants.

Other relevant experiments have been performed on HMX and HMX propellants under non-combustion conditions. Pyrolysis/decomposition experiments have been performed many times on HMX (Ref. 27-29,106), with the higher heating rate experiments demonstrating the presence of HCN and NO_2 in the products. Model compound experiments, such as those involving dimethyl nitramine (Ref. 86), have been used to bridge the gap between HMX decomposition studies and model flame studies.

AP COMPOSITE PROPELLANTS

In contrast to homogeneous and (perhaps) HMX propellants, AP-based propellants can not be modeled as one-dimensional flames. At pressures above approximately 0.5 MPa, the diffusion of gaseous reactants together becomes slower than the reaction kinetics and diffusion flames are formed between the AP decomposition products and the binder decomposition products (Ref. 2,107-112). This is illustrated in Fig. 1.1 (Ref. 113). Thus it is inappropriate to scale down the pressure to extend the flame zones as is commonly done in experimental studies of premixed flames because the chemistry in diffusion flames can be quite different from the chemistry in premixed flames (Ref. 46,114). Current AP propellant combustion models model the gas phase as consisting of diffusion flames above the various oxidizer/binder surfaces and use various types of averaging to obtain a burn rate for various oxidizer particle size distributions (Ref. 96,107,109,115). The AP monopropellant flame is modeled as a premixed flame. A "final flame" is also present where the slowest reactions ($\text{NO} \rightarrow \text{N}_2$ and $\text{CO} \rightarrow \text{CO}_2$) are completed. Thus, the gas phase above an AP-based solid propellant is very heterogeneous. At a given point above the surface, the gas phase is also time varying as oxidizer particles are exposed, burn, and are consumed (Ref. 110). In addition, the AP and

binder are thought to have different surface temperatures (Ref. 96). Detailed chemical kinetic modeling of two-dimensional flames is possible, although the computer time required is several orders of magnitude larger than that for one-dimensional flames. An interesting example, and one that has direct applications to the physical situation encountered in solid propellants, is a recent analysis of the chemical kinetics of a $\text{N}_2\text{H}_4/\text{NO}_2$ diffusion flame in a Burke-Schumann burner (Ref. 116). This type of Burke-Schumann burner is a burner consisting of concentric tubes through which oxidizer and fuel flow. This is similar to the situation one encounters in an AP propellant if one considers an AP particle surrounded by an annulus of fuel forming a "burner". This concept is frequently used in AP propellant modeling (Ref. 107). Convergence of the two-dimensional model required over 30 processor hours on an FPS processor, while typical one-dimensional flame situations converge in less than 30 minutes. This situation may improve as the two-dimensional models are improved. Thus, using a detailed kinetic model to predict the flame chemistry of an AP/binder diffusion flame as a function of time as the AP particle burns is pressing the limits of current combustion modeling, even if one neglects the time dependence of the structure and stoichiometry of the AP/binder "burner". Often, detailed modeling is too expensive and/or time-consuming to be applied to "practical" combustion situations, thus there is interest in applying mathematically appropriate subsets of these detailed mechanisms to more complicated situations (Ref. 117,118). Whether this will allow more than the 2 or 3 global reactions in current AP propellant combustion models remains to be seen. In any case, a better knowledge of the chemistry is needed to guide the necessary simplifications to avoid elimination of important parts of the chemistry. This is especially important for the binders, where small changes in chemistry, such as changes in the curative, can have large effects on the combustion of the propellant (see discussion below). Thus, it will probably not be good enough to assume the binder decomposes into monomer type fragments (such as butadiene, for which the combustion mechanism is known (Ref. 119)) without taking the (as yet unknown) detailed chemistry of the polymer breakup into account. The detailed kinetics of the AP monopropellant flame have been modeled (Ref. 120,204).

Obviously, then, this type of flame is a more difficult diagnostic subject than a propellant flame that is effectively one-dimensional. The difficulty of experimental measurements of flame details in these flames has long been recognized (Ref. 121,208,209). Although laser-diagnostic probes can resolve time varying processes with time scales on the order of tens of ns and distance scales on the order of tens of μm , it is very difficult to relate this information to the precise configuration of the propellant surface which created this flame. Perhaps the best way to resolve this difficulty is to create artificial situations with a known and controllable propellant flame structure, such as "sandwich" propellants (Ref. 111). Diagnostic probes of such a propellant flame could then be linked back to the surface. An alternative would be to collect species and/or temperature data at a fixed point in the flame, collecting data as a function of time and building histograms of flame properties such as species concentrations. The histograms would then have to be linked to possible surface configurations below the data collection point.

Model flame studies are another method of enhancing the understanding of propellant chemistry without having to deal with the difficulties of the actual propellant. At the pressures of interest to the rocket community (~ 7 MPa), the "primary diffusion flame" between the the AP and the binder is the controlling flame. The AP is oxidizer rich, generating more oxidizing

species (HClO_4 , Cl , Cl_2 , ClO , ClO_2 , OH , etc.) than fuel species (NH_3) (Ref. 122). For this reason, many studies have been carried out of model flames of fuels and either HClO_4 or ClO_2 (Ref. 123-135). In general, these studies found that ClO_x -oxidized flames are very fast, with hydrocarbons being oxidized much faster than NH_3 . Thus, it seems reasonable to expect that the active oxidizers in the AP propellant diffusion flame might be ClO_x species, although the structure of diffusion flames is much different from that of premixed flames (Ref. 46,104). In a hydrocarbon/oxygen diffusion flame, the fuel and the oxidizer do not encounter each other directly. The fuel is pyrolyzed in the absence of the oxidizer as it approaches the hot reaction zone of the flame, forming carbon-rich species and hydrogen. The fast-diffusing hydrogen is the only fuel component that encounters the original oxidizer. The carbon species are consumed by reactions with radicals such as OH . The pyrolysis of the fuel in the absence of the oxidizer is a key difference between diffusion and premixed flames. This general picture of diffusion flames (Ref. 104) has been confirmed by detailed species measurements in diffusion flames (Ref. 114). Thus, flames such as $\text{ClO}_2/\text{C}_2\text{H}_2$ (Ref. 132) and $\text{HClO}_4/\text{C}_2\text{H}_4$ (Ref. 129) may be appropriate models for AP propellant diffusion flames since C_2H_2 and C_2H_4 are produced in large quantities during the pyrolysis of binder-like polymers (Ref. 136,206,207). CH_4 is not a good analog of a propellant binder pyrolysis product since an H/C ratio of 4 is unrealistically high. The study of an appropriate diffusion flame (such as $\text{ClO}_2/\text{C}_2\text{H}_2$) would undoubtedly lead to useful new chemical information of propellant relevance. Similarly, AN propellants would have analogous flames, with the active oxidizer in the AN flame being HNO_3 (Ref. 137).

Many experimental studies have been made of AP propellant flames. A review of early work has been published (Ref. 121). Some advances have been made since that time because of improved equipment, but the AP propellant flame remains an difficult subject of study. A few interesting studies will be mentioned. Mass spectrometric measurements in AP (monopropellant) decomposition flames have been reported (Ref. 72) (preheated AP, subatmospheric pressure), leading to a detailed kinetic study of the monopropellant flame kinetics (Ref. 120). Laser-pyrolysis was used to induce combustion in another low pressure study of composite propellant flames (Ref. 42). In general, low pressure experiments have been sought because of the expansion of the flame zones, although the premixed nature of low pressure flames may have limited relevance to the diffusion flame controlled environment of the composite propellant flames. This remark doesn't apply to the monopropellant flame, of course. Higher pressure species-specific measurements of various types, such as emission spectroscopy (see below and Section 4.3), have generally been unsuccessful. Thermocouple measurements have been performed (Ref. 45,121), although the interpretation of the temperature profiles is difficult because of the heterogeneous nature of the propellant flame.

At AFAL, species profiles have been obtained in AP propellant flames in emission and LIF at pressures from 1 atm (N_2) to 1.8 MPa (250 psia) (see Section 4.3 and Section 5.2). Most of the common radicals, such as CN and NH rapidly disappeared as the pressure was raised above 1 atm. The exception was OH , which was visible at pressures up to 7 MPa. At 1 atm, the distribution of CN extended from the propellant surface to $\sim 500 \mu\text{m}$ (see Fig. 5.2.9). This is a larger reaction zone than would be expected from models of premixed flame sheets used in AP propellant combustion models. For example, from (Ref. 115), $x_f = m/kP^\delta$, where m =mass burning rate ($0.46 \text{ g/cm}^2\text{-s}$ for AP1 propellant at 1 atm), $k=30 \text{ g/cm}^2\text{-s-atm}^{1.5}$,

P =pressure (atm), $\delta=1.5$; thus $x_f \sim 150 \mu\text{m}$ at 1 atm ($x_f = x \cdot p_F$ in (Ref. 115)). However, since the "reaction zone" (defined by the presence of CN) of the premixed AP-fuel flame at 1 atm appears to be more of a distributed reaction zone, a flame sheet analysis should only be approximately correct anyway. Another complicating factor is that AP propellants have to be multi-modal (several particle sizes) since monomodal propellants have very fuel-rich stoichiometries (see Fig. 3.3.7, noting that the maximum monomodal AP loading assuming spheres is 67 vol% AP or ~ 76 wt% AP). For a multi-modal propellant at pressures near 1 atm, it is likely that the flames above small AP particles are premixed and the flames above the larger particles are diffusion flames. This complicates any flame analysis. At higher pressures, the influence of the premixed AP/fuel flames would be negligible, but the AP monopropellant (premixed) flame would start to become more important at pressures above about 100 atm. In the intermediate regime where the diffusion flames control the combustion, particle size and binder effects are large.

Some of the most thorough studies of the influence of particle size and binder type on AP propellant combustion behavior are those of Miller et al (Ref. 138,139). The stoichiometry (and therefore the shape and temperature) of the diffusion flames above the various particles are thought to be strongly particle size dependent (Ref. 96,140), so if a diagnostic probe could study a given point in an AP-composite propellant flame with a resolution sufficient to resolve particle-related processes (the histogram approach previously mentioned), large changes in flame chemistry should be seen. For example, small AP particles burn fuel rich and large particles burn fuel lean. Using the equations of Beckstead (Ref. 96), the burning stoichiometry of a given particle in an AP/HTPB propellant can be calculated. For example, the fuel/AP weight ratio ($\alpha_{f,i}/\alpha_{ox,i}$ in (Ref. 96)) ranges from 0.0074 for a $400 \mu\text{m}$ particle to 0.296 for a $10 \mu\text{m}$ particle in an 87% AP(44% $400 \mu\text{m}$, 43% $10 \mu\text{m}$ AP)/HTPB propellant. For comparison, the stoichiometric ratios are 0.11 (assuming CO_2 as the C-containing product) and 0.2 (assuming CO as the product). Again, this shows that the small particles burn fuel-rich and large particles burn fuel-lean. The equilibrium OH mole fractions and flame temperature above these particles would be 0.0002/1583 K ($400 \mu\text{m}$) and <0.000005 /1370 K ($10 \mu\text{m}$) at 18 atm (using the thermochemical equilibrium program discussed in Section 3.3). By comparison, the mole fraction OH/flame temperature in the stoichiometric (11% fuel) flame is 0.022/2955 K. The numbers used in this calculation are those listed in Table 3.3.3 for AP and polybutadiene. Different numbers for the fuel would change the answers slightly, but the trend would be the same. This was an extreme example, but the impact of the particle size on the flame stoichiometry is clear. A diagnostic probe such as OH LIF should be able to see chemistry differences on this scale (note that the equilibrium OH concentration may have little relevance to the actual OH concentration in the flame). A problem comes about in the random distribution of particles in the propellant. It is possible that a diagnostic probe in a wide-distribution (e.g., $400/10 \mu\text{m}$) propellant flame at a given point above the surface would be able to resolve stoichiometry differences even though statistically the probe volume would be at random points above any given large particle. The biggest problem would be the resolution required. The diffusion flames above the AP/fuel interface are typically modeled as being very small, on the order of 10's of μm or less (Ref. 140,141), so it is not known whether or not the stoichiometry differences will persist over a scale large enough to collect diagnostic data. Probably only laser-based diagnostics have any chance of obtaining any information on these scales.

Another interesting observation of Miller was the dramatic effect on propellant burn rate of the curative used in the binder (Ref. 138). The curative was only present in small amounts (~1 wt%), but changing from IPDI to DDI (see Appendix 6) caused burn rate changes by a factor of 2-3. The reasons for this change are not clear, but may be related to the larger size and thus lower vapor pressure or larger decomposition fragment size of the DDI-cured binders. In any case, it would be desirable to examine the influence of the curative change on the flame structure of the composite propellant flame. This will be difficult because of the small dimensions of the diffusion flames and the lack of "convenient" molecules in the diffusion flames. A convenient molecule is one that is readily accessible to a diagnostic probe (such as LIF or CARS) and one that is characteristic of (and limited to) the diffusion flame. OH is convenient but is found throughout the flame (Section 5.1, 5.4). CN and NH would be limited to the diffusion flame but are not present in the diffusion flame (Section 4.3 and 5.2). Perhaps the best candidate is a small hydrocarbon such as C_2H_2 or C_2H_4 , accessible by CARS. Whether or not detectable concentrations of these species are present in the diffusion flames and whether or not sufficient resolution can be obtained to resolve the flame structure remains to be seen. The measurements will be quite difficult.

METALIZED COMPOSITE PROPELLANTS

The addition of metals (principally aluminum) to solid propellants in the 10-20 wt% range is often desirable energetically. The addition of these metals creates several unique combustion problems (Ref. 142,143,189). Diagnostics in metalized propellant flames are quite difficult because of the high luminosity and low transparency of the flames at typical rocket motor pressures. However, the structure of metalized propellant flames at atmospheric pressure under ignition conditions has been successfully studied by Parr and Parr (Ref. 17). They found that the addition of metal extended the flame zone of an HMX propellant, where the flame zone is defined by the presence of CN and NH. A similar extension of the flame zone was seen in emission experiments in propellant "AP2" (see Table 3 and Section 4.4). At atmospheric pressure, the CN distribution was substantially extended compared to that seen in propellant "AP1". At higher pressures, the CN disappeared as the flame structure changed from premixed to diffusion, as seen in propellant AP1 (Sections 4.3, 5.2). In other experiments, it was found that the AP2 propellant flame was essentially opaque at pressures above 0.8 MPa, making laser diagnostics difficult if not impossible. It may be possible to use emission spectroscopy to study propellant flame structures at elevated pressures, but metalized propellants will remain a difficult diagnostic challenge. Kinetic data for proposed metal reactions in propellant flames exists (Ref. 144) so it is possible to construct tentative chemical mechanisms, but it appears that improving the understanding of the physics of metal combustion (such as agglomeration and particle break-up) is of more current interest to improve the combustion behavior of metalized propellants (Ref. 142,143).

In summary, then, for homogeneous propellant flames, enough is known about the propellant flame chemistry that detailed kinetic models have been constructed, using assumed initial decomposition products of the nitrate ester ingredients. The main limitation of this modeling approach is the lack of experimental data that unambiguously verify that these are the correct species, especially for the polymeric binders in XLDB propellants. These experimental

measurements are difficult because of the small dimensions of the fizz zone and the amount of soot/particulates in the flame. For HMX composite propellants, the situation is similar: one-dimensional detailed kinetic modeling is possible, limited by the lack of knowledge of the initial propellant decomposition products, especially for the binders. Experimental measurements of flame species and temperature may be easier for the HMX propellants because of the presence of radicals such as CN and NH, although the distance scales are still small, if not smaller than those in the double-base type flames. For AP propellants, the three-dimensional, time-dependent nature of the combustion process makes detailed modeling quite difficult. Even if this detailed modeling is possible, the computer time required appears to be too great to allow detailed kinetics to be incorporated into burn rate-type models for day-to-day use. However, detailed modeling would allow an informed decision to be made about the simplifications to the chemistry portion of the AP propellant combustion models that would retain the important features of the chemistry. Experimental measurements of flame species are complicated by the pressure dependence of the flame structure and the lack of diagnostically-accessible species in the high pressure diffusion flames. In metalized propellants, measurements are even more difficult because of the presence of the metal in the flame. However, the lack of knowledge about the physical processes of aluminum combustion, such as agglomeration, are probably more limiting to combustion modelers than the lack of detailed aluminum combustion kinetic mechanisms.

TABLE 1. Summary of diagnostic measurements performed on propellants *under combustion conditions*

Species/ temperature	Propellant of interest	Diagnostic method (Ref.)	Propellant comb. application reference
OH,CN,NH,NO	all	LIF (16)	4,17
OH,CN,CH,NH	all	emission	2,31-38
HCN	HMX	CARS (16)	18
CH ₂ O,NO ₂	all	LIF	17?
stable	all	mass spectrometry	39-42,23,22
T	all	thermocouples (43)	22,23,44,45
T	all	Na line reversal (46)	37
T	all	LIF (47,48)	17
T	all	CARS (16,49)	18-21,50
T	all	Raman (16,51)	4
HCN,NO ₂ ,etc.	all	IR absorption	27
n/a	all	high speed film	52
n/a	all	quenched surface	52
n/a	HMX	D-isotope effect	53

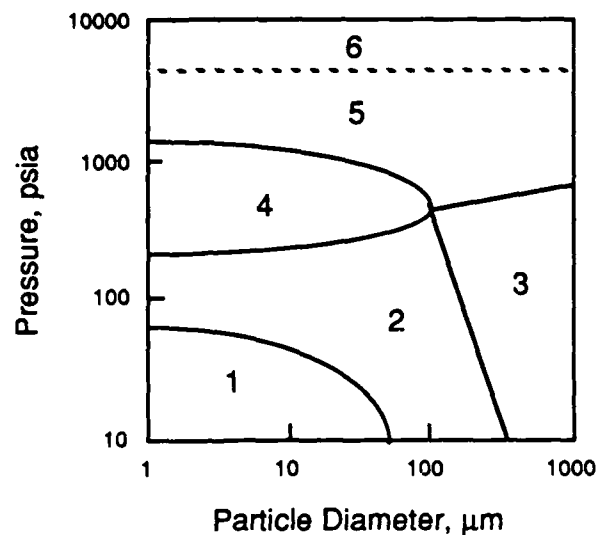


Figure 1. AP propellant flame structure changes as a function of pressure and particle size (Ref. 113). Region 1: premixed gas flame; Region 2: laminar diffusion flame; Region 3: turbulent diffusion flame; Region 4: transition (plateau) region; Region 5: AP monopropellant flame controlling; Region 6: thermal stress cracking controlling. Region boundaries strongly composition dependent.

2.0. EQUIPMENT AND PROCEDURES

2.1. COMBUSTOR

Several solid propellants were examined in this study, representing the major solid propellant families. The propellant composition and other details are listed in Section 3. The propellant flames were studied by burning propellant strands in a nitrogen-purged, high pressure combustor (Ref. 1). This combustor is illustrated in Fig. 2 and is a variant of the standard "window bomb" or "strand burner" in widespread use in solid propellant combustion studies. Optical access is provided by four 3.8 cm diameter, 2 cm thick sapphire windows distributed at 90 degree intervals around the combustor. The diagnostic laser beams (and presumably any LIF and Raman signals generated) were attenuated 20% in passing through one of the windows. For laser-diagnostic purposes, a means to keep the burning propellant surface at a constant level is often desirable. This is accomplished by a servo mechanism which elevates the surface of the solid propellant as it burns down, thus keeping the surface at a more-or-less constant level relative to the collection volume of the detection systems. The servo system employs a 200 mW HeNe laser passing across the propellant surface, with a feedback-control system elevating the propellant strand to keep the fraction of the beam blocked by the surface constant (Ref. 1). In general, the system works fairly well at pressures below 2 MPa (300 psia), but the increases in flame optical thickness and propellant burn rate that accompany increases in pressure cause the system to work poorly at pressures above approximately 2 MPa (300 psia), depending on the propellant. An alternative is to allow the propellant to burn down through the collection volume, in essence collecting sequential data at increasing distances above the propellant surface. All experiments were run under nitrogen. The propellant was burned in strands of about 3-4 cm in length and 6 mm in diameter, with the sides of the propellant coated with a thin layer of a fluorocarbon grease as an inhibitor. Depending on the pressure, these strands burned from 1 to 20 seconds. The short burn time of the strands did not permit spectral scanning; the detection systems were based on the need for rapid data collection. A premixed flame source constructed from 6 mm tubing could be placed in the combustor in place of the strand for tuning of the lasers and alignment of the detection systems. Although this flame is not suitable for flame studies (where a flat flame is desired), the structure of the flames of various gases is consistent with that seen in flat flames (Ref. 145,146). For example, a CH_4/NO_2 flame should show two "reaction zones", while a $\text{CH}_4/\text{N}_2\text{O}$ flame showed only one. For most of the reference LIF and emission spectra shown in this report, the $\text{CH}_4/\text{N}_2\text{O}$ flame was used. The "reaction zone" in a flat flame corresponds to the "inner cone" of the conical tubing flame used in this research. The flame was usually run with a $\text{N}_2\text{O}/\text{CH}_4$ (molar) ratio of approximately 2.

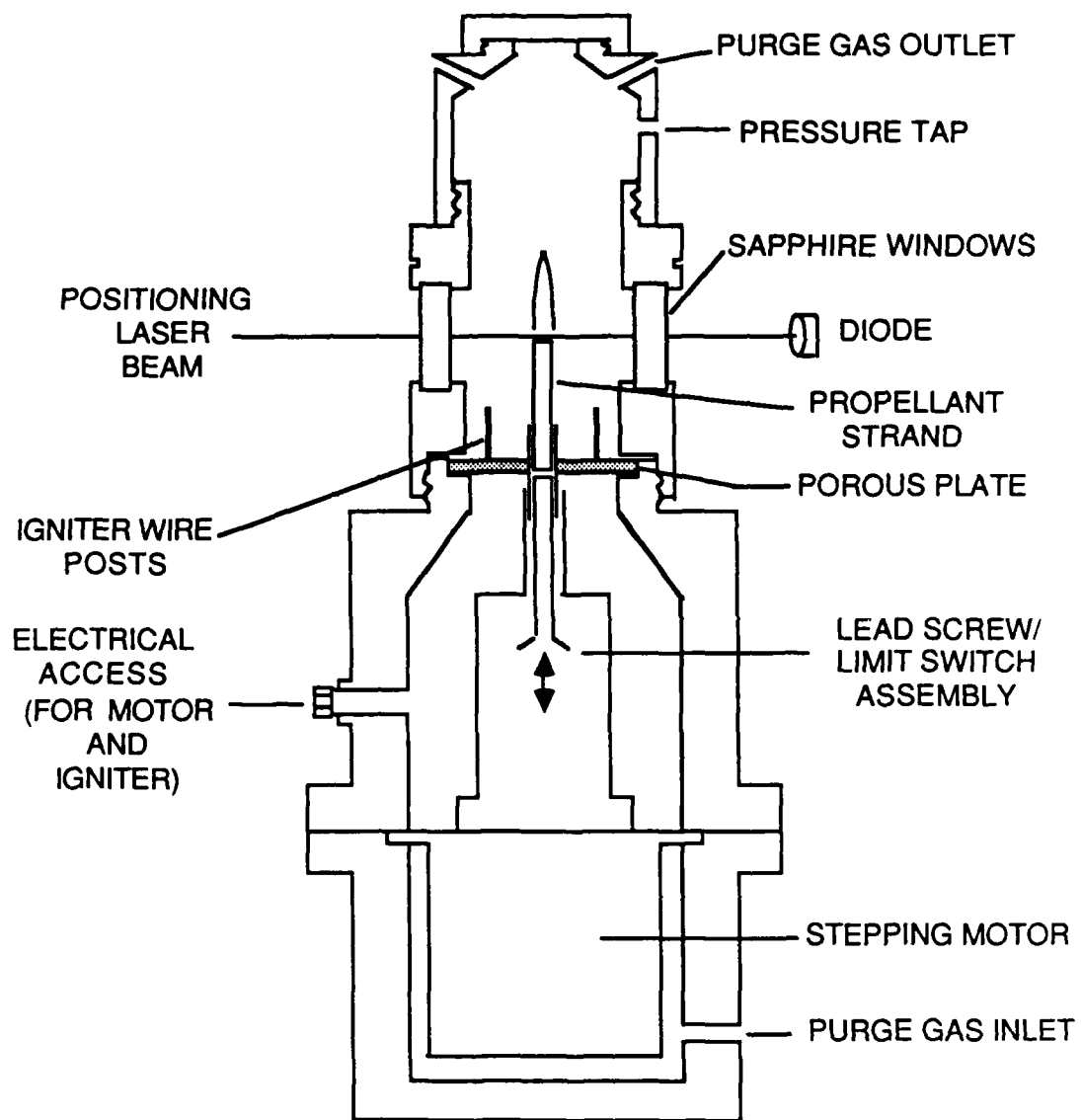


Figure 2. High pressure combustor.

2.2. LASERS

The laser used in the initial OH LIF experiments (Section 5.1) was a Quanta-Ray DCR Nd:YAG pulsed laser operated at 10 Hz. The 1.06 μm fundamental beam passed through a second harmonic crystal and the resulting 532 nm beam was used to pump a Quanta-Ray PDL-1 pulsed dye laser, with an output wavelength of approximately 610 nm (Exciton Sulforhodamine 640 dye). This beam was frequency doubled down into the UV in a Quanta-Ray WEX-1 wavelength extender, with a maximum output power of approximately 6 mJ/pulse in the UV and a nominal pulse width and divergence of 5 ns and 0.5 mrad, respectively. The laser was tuned from 306-309 nm to induce fluorescence in the OH molecule (0-0 vibrational band transitions in A-X electronic band transition).

The CN, NH, and later OH LIF experiments were performed by pumping a Lambda-Physik FL 2002 dye laser with 308 nm light from a Lambda-Physik EMG 201 MSC excimer laser. The excimer laser pulse energy was approximately 300 mJ/pulse at 308 nm, with a maximum repetition rate of 80 Hz, a pulse duration of 28 ns, and a vertical beam divergence of about 1 mrad. The dye laser was operated with various Lambdachrome dyes, with a nominal bandwidth of 0.003 nm and a nominal divergence of 0.5 mrad. The various LIF schemes used in these propellant investigations are summarized in Table 2. The Raman scattering experiments were performed with the 308 nm (actually 307.96 and 308.21 nm) excimer beam directly. All beams were focussed into the propellant flame with a 10 cm focal length fused silica lens. The resulting focal volume diameter was approximately 50 μm for the LIF experiments. The short focal length lens minimized damage to the sapphire windows. After passing through the combustor windows, the laser beam was split, with a small portion of the beam passing onto a photomultiplier tube for monitoring both pulse energy changes and the beam transmission through the combustor and propellant flame. The majority of the beam passed onto a Laser Precision Rj-7200 energy meter. CN LIF has been generated in a solid propellant flame with a CW Ar^+ laser (Ref. 149), but a pulsed laser was chosen for this work because of the larger peak powers obtainable and because the short time scale of the pulse allows effective rejection of background propellant flame emission which can be quite intense (Section 4).

Table 2. LIF excitation schemes

Species	Excitation wavelength, nm	Observation wavelength, nm	Section
OH	306.4 (OH 0,0)	310.6, 315.1 (OH 0,0)	5.1
CN	421.5 (CN 0,1)	388.3 (CN 0,0)	5.2
NH	341-342 (NH 0,0)	336.0 (NH 0,0)	5.3
NH	305 (NH 1,0)	336.0 (NH 0,0)	5.3
OH	306.4 (OH 0,0)	313.8 (OH 0,0)	5.4
OH, NH, CN, C_2	308 (excimer)	various	5.5

2.3. DETECTORS AND ELECTRONICS

The LIF and Raman signals were collected at 90 degrees from the laser beam, collimated, and focussed onto a spectrometer entrance slit with 1:1 magnification using two 10 cm focal length fused silica lenses. The image was rotated 90 degrees with a mirror assembly such that the vertical spectrometer entrance slits were projected horizontally onto the propellant flame. Two detection systems (Fig. 3) have been used to analyze the collected spectral signals. Each system has its strengths and weaknesses. One detection system used a photomultiplier tube coupled to a monochromator to collect narrowband information, while the other system employed a diode array detector coupled to a three-stage spectrometer to collect broadband spectral information. Both of these systems are illustrated in Fig. 3. The optical systems were aligned with a HeNe laser.

The photomultiplier tube (PMT) system employed a RCA C31034A tube attached to a Spex 1870 1/2 meter monochromator (1200 grooves/mm grating). The collected LIF or Raman signals were focussed onto the slit of the monochromator, with the vertical resolution of the system in the flame thus being the entrance slit width (typically 20-50 μm). The slit height, and thus the width of the collection volume along the path of the laser beam, was typically 2 mm. It was usually found necessary to add a narrowband (~ 10 nm bandwidth) filter to aid in the separation of the LIF or Raman signals and the scattered laser light in the propellant flames. The PMT signal was processed by a Stanford Research Systems SR250 gated integrator. An additional channel was used to collect simultaneous transmitted laser power readings, as illustrated in Fig. 3. The data collection was controlled by a Macintosh computer through a Stanford Research Systems SR245 computer interface. Post processing was accomplished on an Apple Macintosh computer. Propellant experiments were usually performed by setting the spectrometer on the desired wavelength and monitoring the LIF or Raman signal as a function of time as the propellant burned down through the collection volume, thus single-pulse data acquisition and high laser repetition rates were desirable to resolve the propellant flame structure as finely as possible. This system has several difficulties in operation in propellant flames. Heavily particulate laden flames cause Mie scattering (or laser-modulated particulate incandescence (Ref. 16) or rotational Raman (Ref. 150)) interference with the LIF or Raman signals even with a filter in the optical system. These interferences can usually be differentiated from the desired signal because the scattering signals are large- probably caused by (soot) particles passing through the collection volume and being struck by the laser- but short-lived (3-5 data points at 40-75 Hz). The LIF signal from a typical "reaction zone" species such as CN is typically 10-50 data points at pressures below 3.5 MPa, so the spurious signals are usually discernable. However, at higher pressures (>3.5 MPa), the signals are short-lived enough that the scattering "spikes" are similar (see results) to the desired LIF or Raman data. Obviously, the lack of a simultaneous measurement of a non-resonant wavelength as a background correction is a real limitation in this type of system, although separate experiments were performed with either the laser or spectrometer detuned from resonance to assess the contribution of the non-resonant scattering to the desired LIF signals. Additionally, the optical thickness of the propellant flames increases dramatically with pressure (higher soot density?), so higher pressure measurements are doubly difficult (see Section 5.1 and (Ref. 1)). However, for several propellants with relatively non-sooting flames, fairly unambiguous CN LIF signals could be obtained up to pressures of 3.5 MPa using the PMT

system. For very sooty propellants such as AN1, the desired signal was difficult to obtain under most circumstances (see Section 5.2).

For broadband experiments, detection was performed with an EG&G/PAR 1420 Reticon diode array (700 elements) attached to a Spex 1877 Triplemate spectrometer. The Reticon was controlled by an EG&G/PAR OMA II 1215/1218 detector controller and data acquisition system. An EG&G/PAR 1211 high voltage pulser was used to trigger the Reticon. The Triplemate is a triple spectrometer with an initial "filter" stage which allows effective discrimination between the desired LIF signal and the scattered laser light (see Section 5.1). Three turret-mounted gratings were available, with the highest resolution grating being a 2400 gr/mm grating with a dispersion of 0.0175 nm/pixel. The major disadvantage of this system is that the Reticon is not as sensitive as the photomultiplier tube, requiring multiple-pulse accumulations of data in most cases with the accompanying decrease in time resolution. The time resolution was adequate for OH LIF experiments in solid propellant flames, but inadequate for CN LIF experiments (see Sections 5.1 and 5.2). The Reticon was used extensively in studies of solid propellant flame chemiluminescence, where accurate background measurements were imperative due to the presence of a strong continuous background due to CO+O chemiluminescence or emitting particles (Section 4). The sensitivity of the Reticon is a fairly strong function of wavelength, as shown in Fig. 4. Note that this wavelength response makes it difficult to differentiate between CO+O and particle (assumed to resemble black-body) radiation. A composite spectrum that includes most of the species examined in this report is shown in Fig. 5.

Photographs of the experimental setup are shown in Fig. 6 and 7. The high pressure combustor (8 window version) is shown in Fig. 8. The calibration flame has been moved out of the combustor and is visible in the top of the figure. A picture of a burning strand of API propellant is shown in Fig. 9. Note that the propellant is translucent and the light from the flame makes the viewing of the surface difficult. Experiments with OH emission indicated that the center portion of the flame was unaffected by the purge gas at distances less than 15-20 mm from the surface.

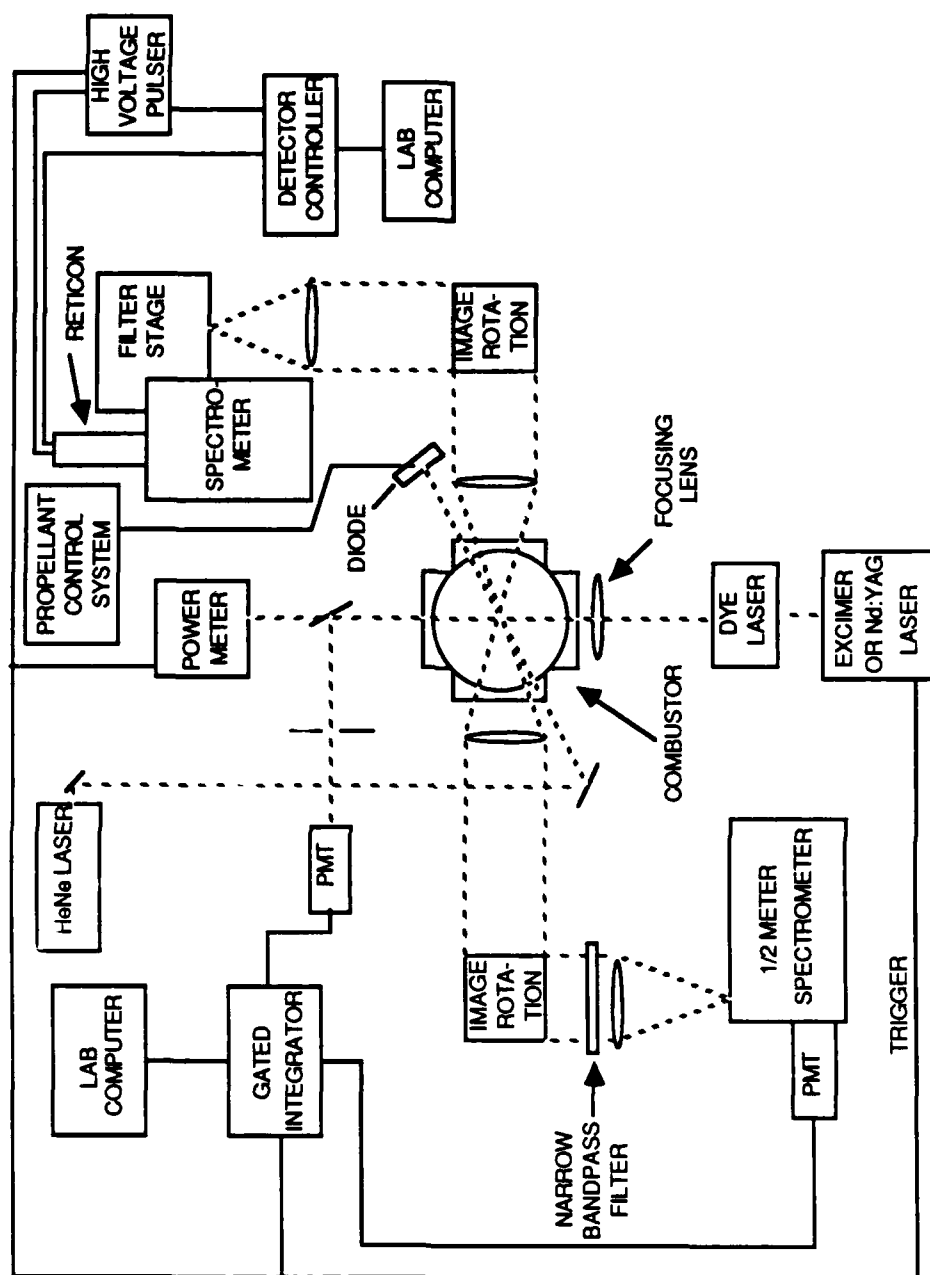


Figure 3. Schematic of experimental apparatus.

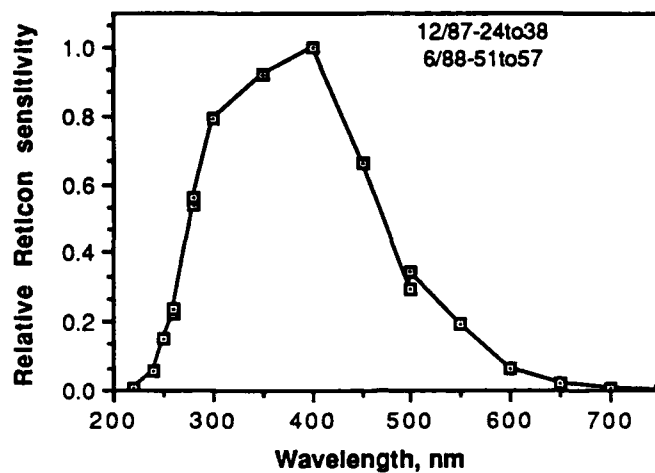


Figure 4. Reticon sensitivity as measured by tungsten filament standard lamp.

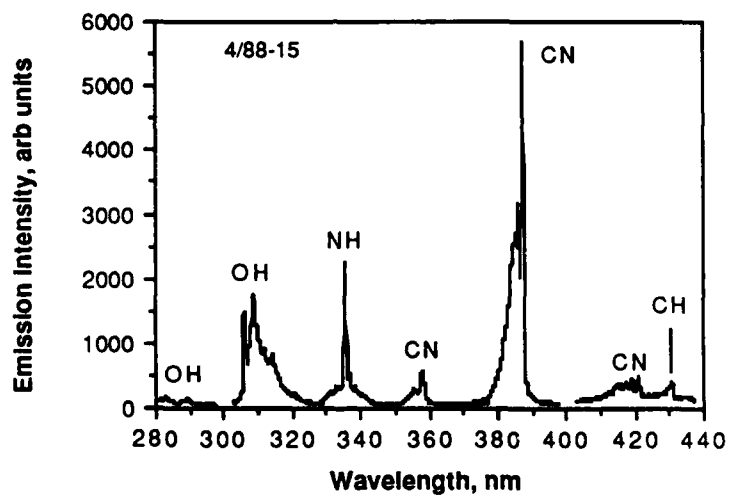


Figure 5. Broadband emission spectrum of inner cone of $\text{CH}_4/\text{N}_2\text{O}$ flame. 500/200 μm slits, 0.07 nm/pixel dispersion, 0.2 s exposure time.



Figure 6. Photograph of laboratory equipment.



Figure 7. Photograph of laboratory equipment.

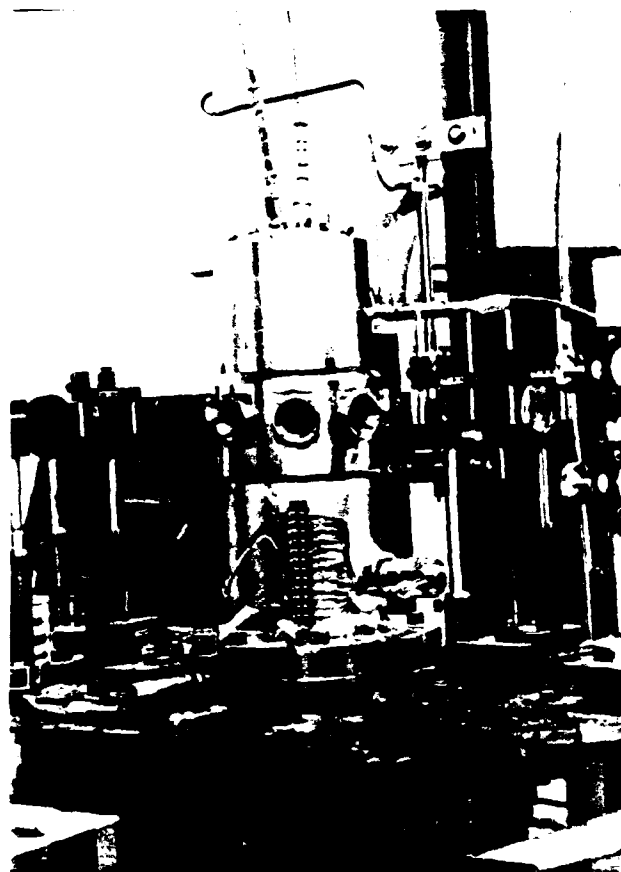


Figure 8. Photograph of laboratory equipment.



Figure 9. Photograph of burning propellant strand. AP1 propellant, 0.8 MPa.

3.0. PROPELLANT DATA

3.1. PROPELLANT FORMULATIONS

Most of the propellants used in this research were produced at the AFAL. The formulations are given in Table 3. The formulations have been left general to avoid any classification problems.

Table 3. Propellant Formulations.

	HMX1	HMX2	AP1	AP2	AN1	DB1	DB2
Ingredient, wt % (approx)							
HMX (200/20 μ m)	73	80	0	0	0	0	0
polyester binder	10	20	0	0	0	29	27
TMETN	17	0	0	0	12	0	0
NG	0	0	0	0	0	71	67
AP (400/20/2 μ m)	0	0	87	68	0	0	6
Polybutadiene binder	0	0	13	16	0	0	0
AN	0	0	0	0	16	0	0
GAP binder	0	0	0	0	16	0	0
Aluminum powder	0	0	0	16	0	0	0

HMX=cyclotetramethylene tetranitramine $C_4H_8N_8O_8$, TMETN=trimethylolethanetrinitrate $C_5H_9O_9N_3$, NG=nitroglycerin $C_3H_5N_3O_9$, AP=ammonium perchlorate NH_4ClO_4 , AN=ammonium nitrate NH_4NO_3 , GAP=glycidyl azide polymer. The "polyester" binder in the DB propellants is a polyethylene glycol-based polymer ("PEG"), while the HMX binder is based on polydiethylene glycol adipate ("PGA"). Empirical formulas for these binders are given in Table 8.

Table 4. Propellant Impurities.

	HMX1	AP1	AP2	AN1	DB1
Impurity, ppm					
Na	100	300	425	37	21
Fe	30	na	180	na	na
K	10	100	na	na	na
Ca	20	400	na	na	na
Cr	1	na	na	na	na

3.2. PROPELLANT BURN RATE DATA

Determination of propellant burn rate is not a major objective of this research; however, to convert temporal data (collected as the propellant burns down through the diagnostic collection volume) to spatial data, the propellant burn rate is needed. This data was collected in two ways. For the AP1 and HMX1 propellants in experiments where the surface position was controlled, the distance the propellant was elevated and the time elapsed were directly measured by the control system timer electronics. The time and distance measurements were delayed from ignition for a fraction of a second to avoid ignition transients. The total time the distance and time were measured was about 2.5 seconds. The timer electronics broke down irreparably partway through the project and subsequently the burn rate was calculated by measuring the time a known length of propellant required to burn completely with a stopwatch. This method is less accurate than the first method because any ignition and extinction transients were included in the burn rate measurement. Note that conditions where the control laser was unable to penetrate the propellant flame (AP2 flames above about 0.5 MPa and AP1 flames above about 1.5 MPa), the stopwatch method had to be used.

The accumulated data for propellants HMX1, AP1, AP2, DB1, and DB2 is presented in Fig. 5-17. The data is fairly consistent, except for the double-base propellants. Other burn rate data is presented in Table 5. It would be more rigorous to plot the data as log-log, so that the data could be fitted as $r=aP^n$ (see Fig. 18 and 19), but the data scatter is high so I don't want to encourage that this data be used to calculate any pressure exponents.

Table 5. Assorted burn rate data.

Propellant	Pressure, MPa	Burn rate data, mm/s
HMX2	3.5	1.5
	1.8	0.9
	0.8	will not burn
AN1	1.8	3.4
	0.8	1.7

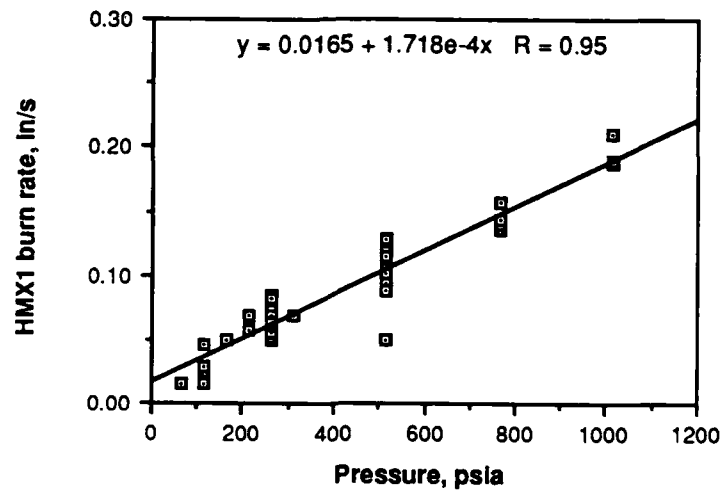


Figure 10. HMX1 propellant burn rate as a function of pressure, English units.

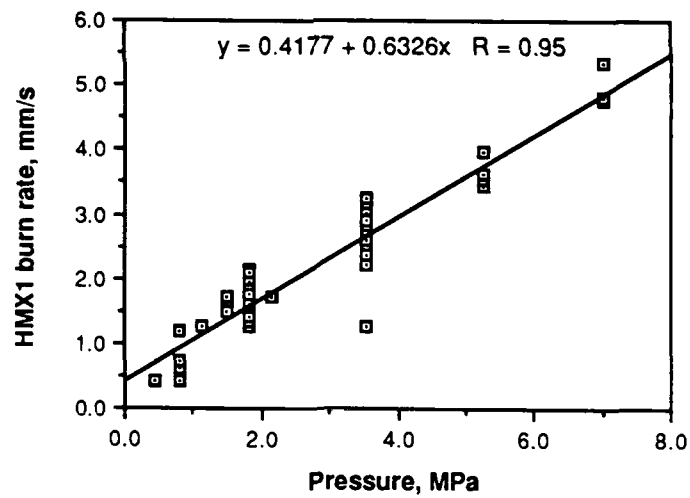


Figure 11. HMX1 propellant burn rate as a function of pressure, SI units.

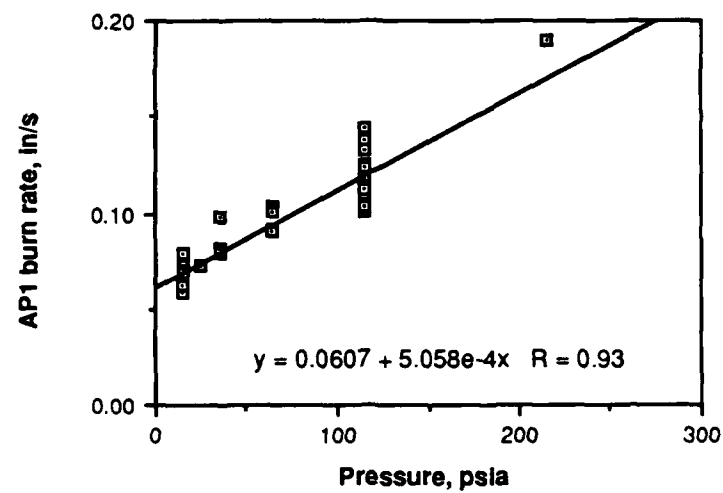


Figure 12. AP1 propellant burn rate as a function of pressure, English units.

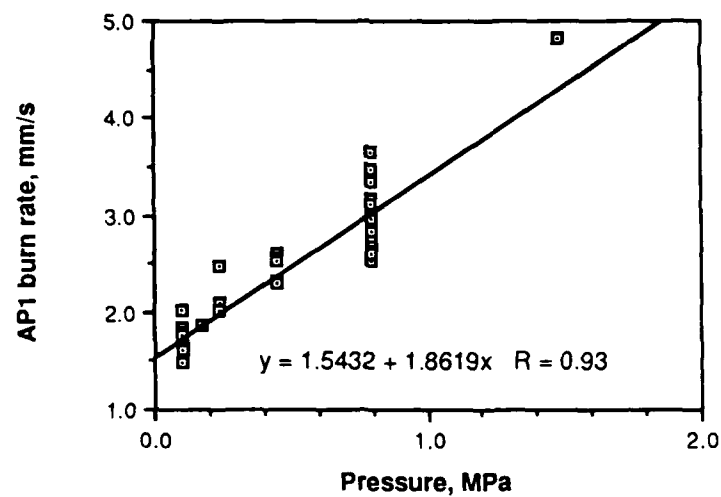


Figure 13. AP1 propellant burn rate as a function of pressure, SI units.

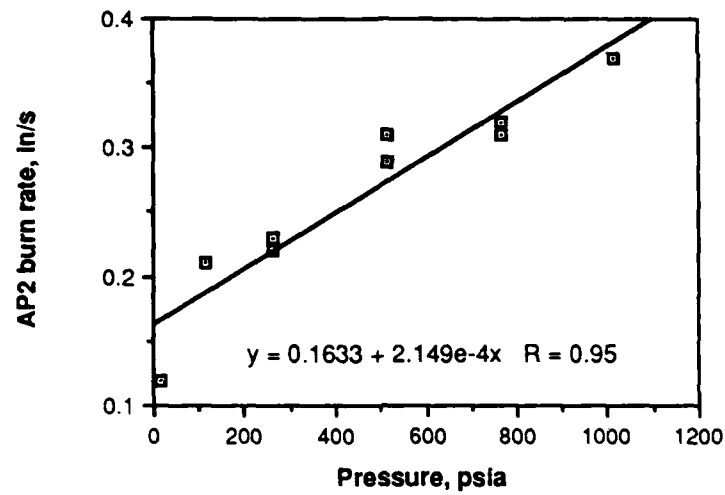


Figure 14. AP2 propellant burn rate as a function of pressure, English units.

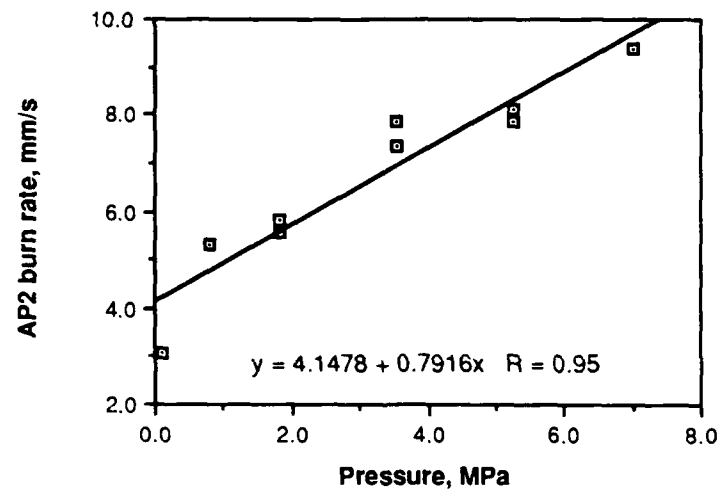


Figure 15. AP2 propellant burn rate as a function of pressure, SI units.

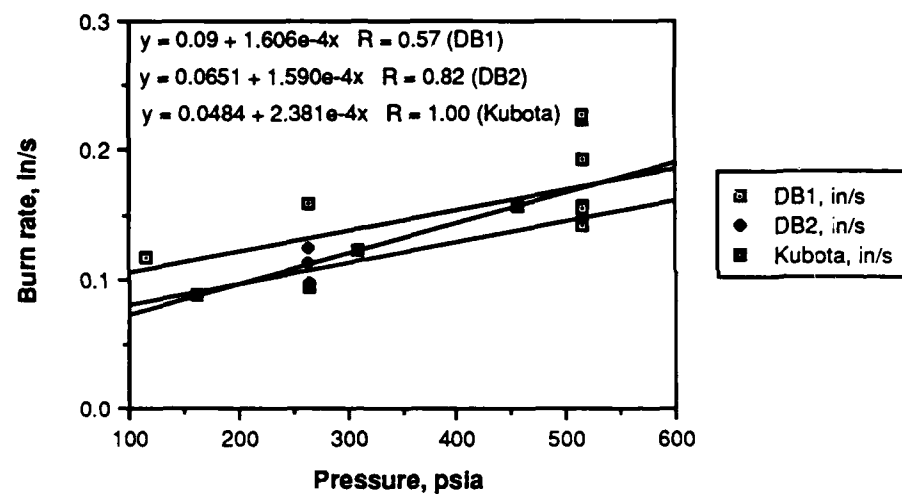


Figure 16. DB propellant burn rate as a function of pressure, English units. The "Kubota" propellant is the low Hex double-base propellant described in (Ref. 59).

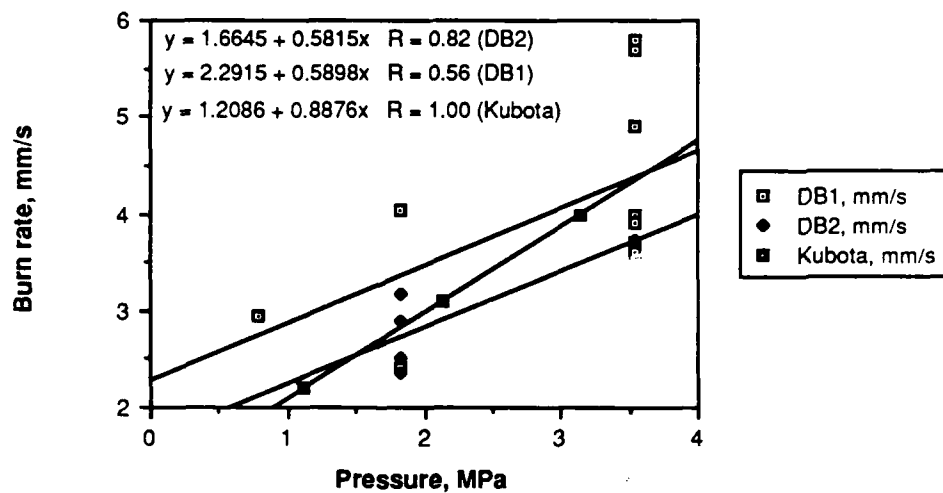


Figure 17. DB propellant burn rate as a function of pressure, SI units.

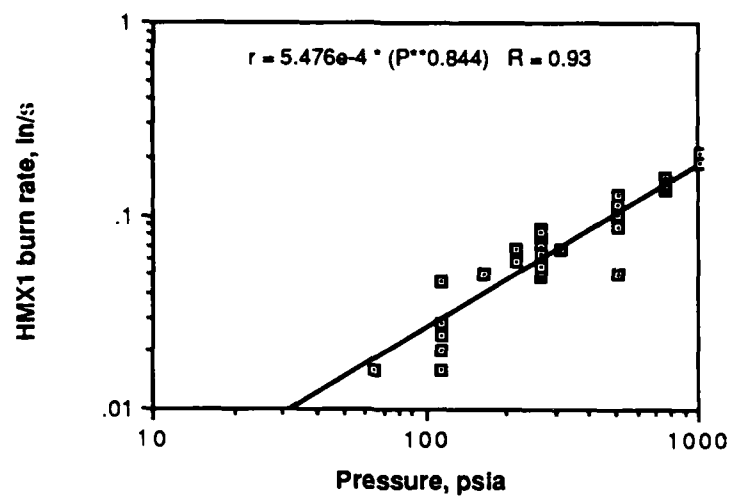


Figure 18. HMX1 propellant burn rate as a function of pressure, plotted as log-log.

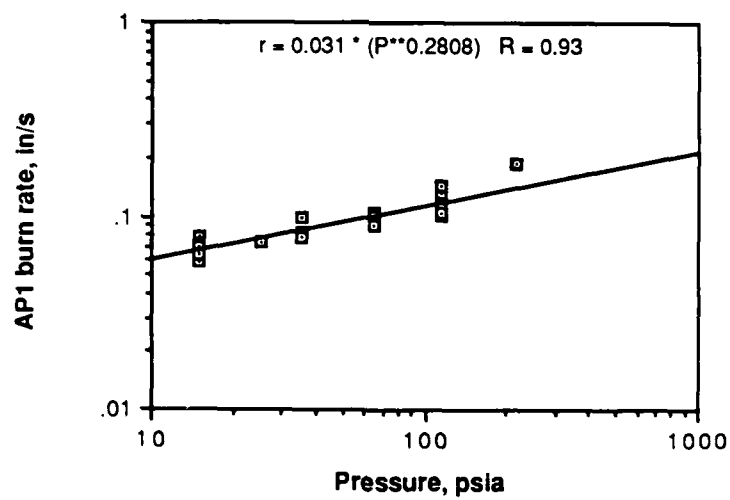


Figure 19. AP1 propellant burn rate as a function of pressure, plotted as log-log.

3.3. PROPELLANT THEORETICAL CALCULATIONS

Several theoretical calculations have been made for these propellants. The adiabatic flame temperature and equilibrium products at the equilibrium flame temperature have been calculated using the NASA thermochemical code and an in-house AFAL version called "ISP". These results are summarized in Table 6. The calculations require the elemental composition, heat of formation, and density of the various propellant ingredients (Table 8).

Table 6. Theoretical propellant flame properties at 3.5 MPa.

	HMX1	HMX2	AP1	AP2	AN1	DB1	DB2
Equil. species, mol %							
CO	34.5	38.2	11.1	24.0	16.0	41.0	38.7
CO ₂	4.7	2.5	11.6	1.6	6.5	6.2	6.9
Cl	0.0	0.0	1.3	1.2	0.0	0.0	0.0
HCl	0.0	0.0	17.7	12.7	0.0	0.0	1.1
NO	0.0	0.0	0.2	0.0	0.0	0.0	0.0
N ₂	24.0	22.1	9.5	8.2	25.5	10.6	10.8
H	0.3	0.02	0.6	3.6	0.03	0.03	0.07
H ₂	19.3	28.3	5.4	26.1	17.1	24.1	21.5
H ₂ O	17.1	8.9	40.8	13.5	34.8	18.2	21.0
O	0.0	0.0	0.1	0.1	0.0	0.0	0.0
OH	0.1	0.0	1.4	0.8	0.01	0.0	0.0
O ₂	0.0	0.0	0.3	0.0	0.0	0.0	0.0
Al ₂ O ₃	0.0	0.0	0.0	7.3	0.0	0.0	0.0
AlCl ₂ +AlCl	0.0	0.0	0.0	0.7	0.0	0.0	0.0
Other	0.0	0.0	0.0	0.2	0.1	0.0	0.0
Flame T (adiabatic), K	2620	2050	2970	3373	2140	2148	2283

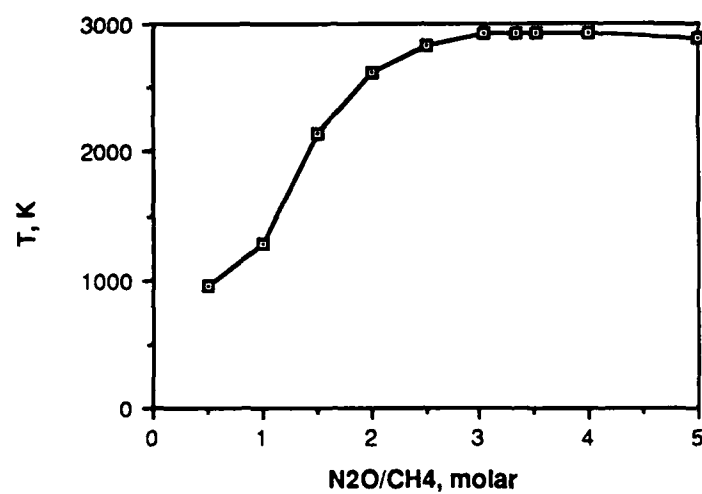


Figure 20. Theoretical predictions of CH₄/N₂O flame properties.

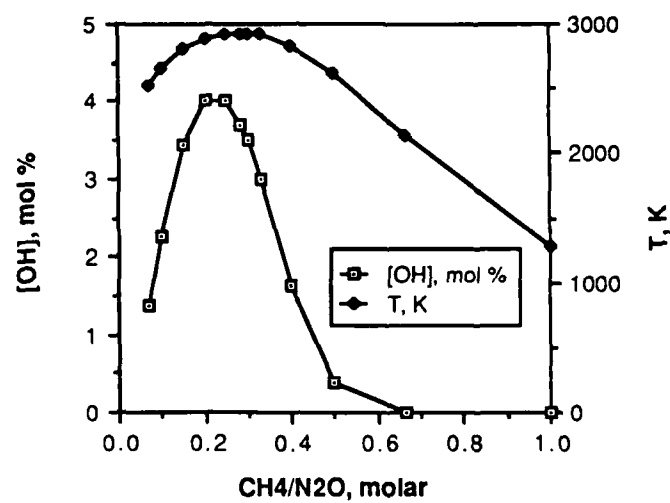


Figure 21. Theoretical predictions of CH₄/N₂O flame properties.

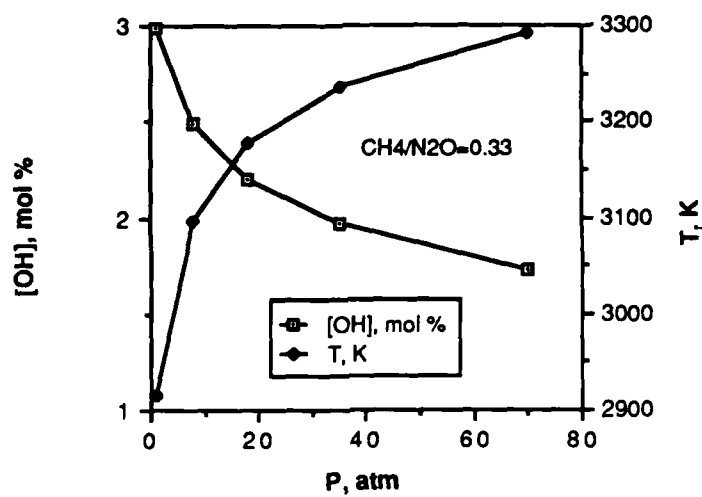


Figure 22. Theoretical predictions of CH₄/N₂O flame properties.

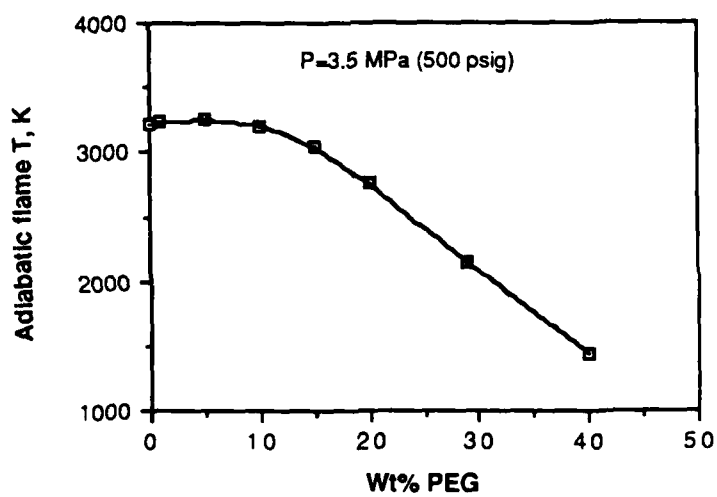


Figure 23. Theoretical predictions of DB (NG/PEG) propellant flame properties.

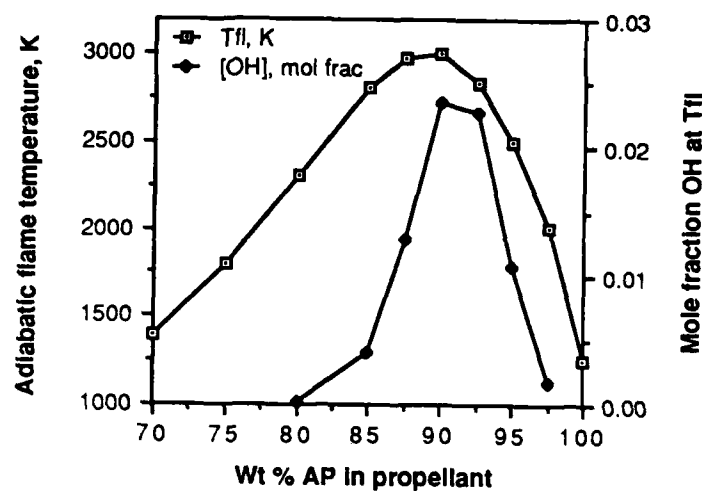


Figure 24. Theoretical predictions of AP/polybutadiene propellant flame properties. The fuel is defined as $C_4H_{6.006}O_{0.0345}$ (see Table 8).

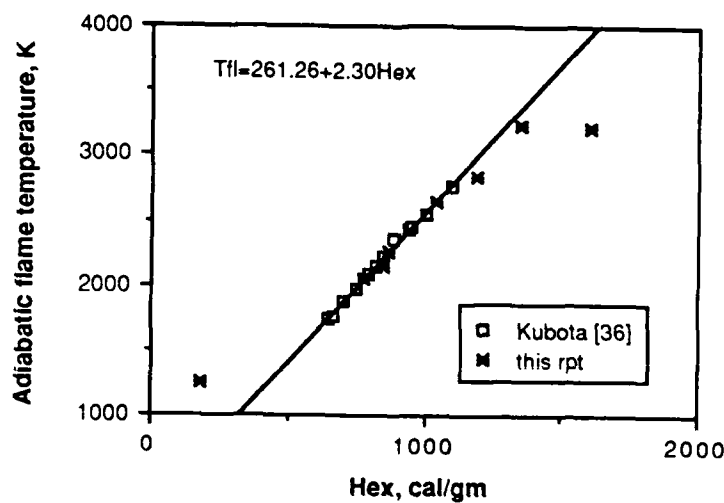
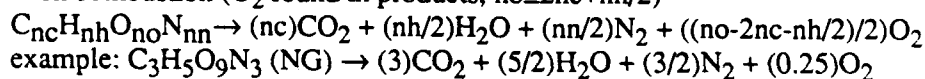


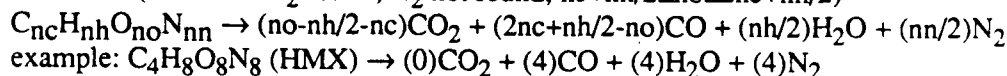
Figure 25. Correlation between adiabatic flame temperature and heat of explosion calculations.

The "heat of explosion", a commonly calculated quantity for double-base propellants, was also calculated for most of the propellants, with the results listed in Table 7. Hex is usually defined as the "energy" of combustion at 300 psia (ΔE), with the initial state being the unburned propellant at 25 C and the final state being the products at STP. ΔE differs from the "heat" of combustion by a (relatively small) term describing the work done in the creation of the gas ($=\Delta nRT$). At STP, the products usually only include stable molecules such as $H_2O(l)$, CO_2 , CO , N_2 , and H_2 . I calculated Hex as follows. First, a stoichiometry must be assumed, depending upon the relative ratio of the fuel components (C and H, where nc =stoichiometric factor for C, etc.) and the oxidizing components (O). Two assumptions are made: (1) all O is first distributed to CO , then to H_2O , then to CO_2 , and (2) all N is distributed only to N_2 . Note that assumption 2 is often violated where the kinetics dictate that the final N-containing product is NO , such as in low pressure flames (Ref. 82) and in the fizz zone of double-base propellants ((Ref. 23,29,210), and later in this section). These rules give reasonable results as discussed below.

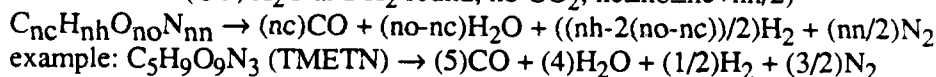
Oxygen rich combustion (O_2 found in products; $no \geq 2nc + nh/2$)



Intermediate case (CO and CO_2 found, H_2 not found; $nc + nh/2 \leq no \leq 2nc + nh/2$)



Fuel-rich combustion (CO , H_2O and H_2 found, no CO_2 ; $nc \leq no \leq nc + nh/2$)



Note that if $no < nc$, the solid carbon (or some other non-oxygenated form of carbon) must be formed as a product in addition to H_2 and N_2 . Once a stoichiometry is defined, then Hex is defined as the ΔE for the reaction, where $\Delta E = \Delta H_r + \Delta(PV)$, and $\Delta H_r = H_{prod} - H_{reac}$. $\Delta(PV) = (\Delta n)RT$ where $T = 298$ K and $\Delta n = n_{prod} - n_{reac}$, where $n_{reac} = 0$ (solid propellant). The heats of formation used in these calculations are listed in Table 8.

These results can be compared to literature values, as shown in Table 9. Note that "hot" (energetic) double-base propellants (Ref. 29,44) typically have Hex's of about 1100 cal/gm. DB1 and DB2 propellants are thus relatively "cool" and thus will probably have quite different flame characteristics (such as radical concentrations) from more energetic double-base propellants. Hotter propellants may also burn more cleanly (see Section 5.2), but this remains to be seen. Note also that Hex and T_{fl} are related. This relationship is shown in Fig. 25. NG (largest Hex) probably falls off the curve because O_2 is found in the products and thus some of the oxygen in the NG "flame" acts as a diluent.

Estimates of the flame temperature in the fizz zone can be made by suppressing the formation of various species, notably N_2 (Ref. 58,63). However, the suppression of N_2 leads to the formation of various improbable products, as shown in Table 10. The most reasonable answers need to allow for the formation of some type of (hydro)carbon species or C_xN_y

compounds will continue to be predicted. The calculations in Table 10 are performed for a propellant similar to DB1 (71% NG, 29% PEG).

Table 7. Hex calculations for propellants/ingredients.

Propellant/ingredient	Heat of explosion, cal/gm	Tfl, K (3.5 MPa)
NG	1608	3217
HMX	1352	3230
TMETN	1183	2825
HMX1	1037	2634
HMX2	780	2050
HMX1 binder + TMETN	187	1248
DB1	850	2148
DB2	872	2270

Table 8. Heat of formation and density data for Hex and Tfl calculations.

Species	Heat of formation (kcal/mol) (ref.); ρ (g/cc)
H ₂ , N ₂ , O ₂	0
CO ₂	-94.05 (Ref. 147)
CO	-26.42 (Ref. 147)
H ₂ O (l)	-68.32 (Ref. 147)
HCl	-22.06 (Ref. 147)
NG (C ₃ H ₅ O ₉ N ₃)	-90.75 (Ref. 148); 1.6
HMX (C ₄ H ₈ N ₈ O ₈)	+17.92 (Ref. 148); 1.9
TMETN (C ₅ H ₉ N ₃ O ₉)	-105.8 (Ref. 148); 1.5
DB binder (PEG) (C _{4.5} H _{9.1} O _{2.3})	-99.87 (Ref. 148);
HMX binder (PGA) (C _{4.58} H _{7.50} O _{2.34})	-118.3 (Ref. 148);
Nitrocellulose (NC), 12.2%N (C ₆ H _{7.78} N _{2.32} O _{9.645})	-172.146 (Ref. 148); 1.65
NC, 12.6%N (C ₆ H _{7.55} N _{2.45} O _{9.90})	-169.067 (Ref. 148); 1.65
NC, 13.15%N (C ₆ H _{7.365} N _{2.64} O _{10.29})	-164.789 (Ref. 148); 1.65
NC, 13.45%N (C ₆ H _{7.26} N _{2.74} O _{10.48})	-161.960 (Ref. 148); 1.65
NC, 14.1%N (C ₆ H ₇ N ₃ O ₁₁)	??
Diethyl Phthalate (DEP) (C ₁₂ H ₁₄ O ₄)	-180 (Ref. 148); 1.1
2-nitrodiphenylamine (2-NDPA) (C ₁₂ H ₁₀ N ₂ O ₂)	+17 (Ref. 148); 1.4
Triacetin (TA) (C ₉ H ₁₄ O ₆)	-317 (Ref. 148); 1.15
Ammonium perchlorate (AP) (NH ₄ ClO ₄)	-70.69 (Ref. 148); 1.95
Polybutadiene (C ₄ H _{6.006} O _{0.0345})	+0.152 (Ref. 148); 0.95

Table 8 (cont). Heat of formation and density data for Hex and T_{fl} calculations.

Species	Heat of formation (kcal/mol ^{ref.}); ρ (g/cc)
Ammonium nitrate (AN) (NH ₄ NO ₃)	-87.27 (Ref. 148); 1.7
Glycidyl azide polymer (GAP) (C ₃ H ₅ N ₃ O)	+34 (Ref. 148); 1.3
Isophorone diisocyanate (IPDI) (C ₁₂ H ₁₈ N ₂ O ₂)	-88.8 (Ref. 148); 1.06
Methane (CH ₄)	-17.69 (Ref. 147)
Nitrogen dioxide (NO ₂)	8.1 (Ref. 147)
Nitrous oxide (N ₂ O)	19.50 (Ref. 147)
Nitric oxide (NO)	21.60 (Ref. 147)

Table 9. Comparison of calculated and literature Hex values.

propellant/ingredient	Hex, this rpt	Hex, lit values	references
NG	1608	1510,1590,1770	45,148,23
NC (12.2%N)	892	895	148
NC (12.6%N)	949	942	148
NC (13.15%N)	1029	1027	148
NC (13.45%N)	1068	1063	148
NC (fully nitrated, 14.1%N)	na	968?	45
TMETN	1183	1236,1236	148,45
HMX	1352	1356	148
EC-5*	658	706	36
EC-1*	1066	1093	36
"propellant 2"*	1297	1449	80
AN	628	630	30

*EC-5=45.8%(wt) NC (12.2%N), 35% NG, 17% DEP, 2.2% 2-NDPA, EC-1=53.0% NC (12.2% N), 40.5% NG, 4.0% DEP, 2.5% 2-NDPA, "propellant 2"=43.5% NC (no %N specified), 20.0% NG, 36.3% HMX, 0.2% 2-NDPA.

Table 10. ISP results with suppressed product species.

Suppressed species	major unusual species	Tfl, K (P, atm)
none		2135 (70)
N ₂	NH ₃	2090 (70)
N ₂ , N ₂ O	NH ₃	2102 (70)
N ₂ , N ₂ O, N ₃		2142 (70)
NH ₃ , N ₂ , N ₃	HCN	1824 (35)
HCN, NH ₃ , N ₂ , N ₃	CHNO	1713 (35)
HCN, NH ₃ , N ₂ , N ₃ , CHNO	C ₂ N ₂	1636 (35)
above + C ₂ N ₂	H ₄ N ₂	1534 (35)
HCN, NH ₃ , N ₂ , N ₂ O, N ₃	CHNO	1850 (70)
above + CHNO + NH ₂ + H ₂ N ₂	C ₂ N ₂	1814 (70)
above + CN ₂ + C ₂ N ₂ + N ₂ H ₄	N ₂ H ₄ (l)	1663 (70)
above + C ₄ N ₂ + N ₂ H ₄ (l)	CH ₄ , CNN	1155 (70)
above + CH ₄ + CNN	C(s)	1150 (70)
above + C(s)	C ₂ H ₄	873 (70)
above + C ₂ H ₄	CN, CNO	709 (70)
above + NCO + CH ₃ OH + C ₂ N	CN	657 (70)
above + CN but incl. CH ₄		1128 (70)
above + CH ₄ but incl. C(s)		1151 (70)
same as above		1112(35)
same as above		1075(18)
same as above		1033(8)
same as above		962(2)

The major species in the last cases are (35 atm): CO (20%), CO₂ (10.5%), H₂(31%), H₂O (17%), NO (21.4%), C(s) (20.5%), and small amounts of HN (.006%) and HNO (0.02%). The prediction of large amounts of solid carbon may be fairly realistic-the DB flames seem relatively "sooty".

3.4. PROPELLANT CONTROL INFORMATION (Ref. 1)

The adequacy of the propellant surface position control system is dependent primarily on two aspects of the propellant combustion behavior: (1) the opacity or optical thickness of the propellant flame and (2) the propellant burn rate (Ref. 1). As the propellant flame becomes more opaque, the control system has more trouble distinguishing the flame from the solid propellant and, consequently, the degree of control over the surface position suffers. This problem is exacerbated by higher propellant burning rates since the feedback-control system has a harder time trying to correct for surface position over- and under-shoots. This section deals primarily with the optical thickness and "controllability" of the AP2, HMX2, AN1, and DB1 propellants. Information on AP1 and HMX1 propellants can be found in (Ref. 1).

The AP2 propellant flame was, not surprisingly, the most opaque propellant flame of the propellants listed in Table 3. The control system was only marginally effective at 0.8 MPa (100 psig), and the flame was totally opaque (no transmission of the 100 mW control laser) at 1.8 MPa (250 psig). The AN1 propellant flame was relatively "sooty," with a flame opacity that exceeded that of AP1 propellant at a given pressure. The HMX2 propellant flame was sootier than the HMX1 propellant flame at a given pressure, which is perhaps not surprising since the HMX2 flame is proportionally more oxygen-poor than the HMX1 flame (Table 6). The DB1 and DB2 propellant flames were also relatively sooty (on the order of HMX2), although the pressure behavior of the DB flames was rather different. The opacity of the DB propellant flames was a minimum at about 1.8 MPa (250 psig), and increased both as the pressure was increased and decreased. The increase in "soot" as the pressure is lowered may be a sign that the combustion is becoming more inefficient, with some of the large amount of flame NO not being reduced the N_2 and thus creating a lower flame temperature. This is speculation at this point.

4.0. EMISSION SPECTROSCOPY OF FLAMES

The use of combustion diagnostics in solid propellant flames is made more difficult by the complex nature of the flame. For example, the "flame" above an ammonium perchlorate (AP)-oxidized propellant is actually a combination of multiple flames: the oxidizer decomposition (monopropellant) flame, the primary (oxidizer/binder) flame, the energetic binder flame (if any), and the final flame (Ref. 14). The relative importance of these flames depends on the oxidizer particle size, nature of binder, and pressure. Low pressure (atmospheric and below) AP propellant flames tend to resemble a premixed flame, with little binder or particle size influence. As pressure increases, diffusion is retarded and reaction rates are enhanced, leading to diffusion flames between oxidizer and binder. These primary diffusion flames are strongly influenced by binder type and oxidizer particle size. At much higher pressures, the reaction rates have been accelerated so much relative to diffusion rates that the AP monopropellant flame begins to control the propellant burn rate (Ref. 113). In contrast, HMX propellants tend to have less interaction between HMX decomposition products and binder, primarily because HMX is not oxidizer rich. Experimental results support this observation. For example, the burn rate of HMX propellants is generally only weakly dependent on HMX particle size (Ref. 14,151). Addition of AP to HMX propellants was seen to change the flame structure dramatically by introducing oxidizer/binder diffusion flames, while the reverse was not true (Ref. 152). Thus, the flame chemistry in solid propellants is more complex than that usually seen in laboratory gas flames. Ideally, solid propellant flame diagnostics must be able to temporally and spatially resolve chemistry on the scale of oxidizer particle sizes and burn times, since the flame chemistry (at least for AP composite propellants) changes at a given point above the surface as oxidizer particles are uncovered and consumed. In the initial stages of a program to obtain the detailed chemical information needed for improved solid propellant combustion models, we have studied the structure of several different solid propellant flames using emission spectroscopy at pressures from atmospheric to 7 MPa (1000 psig).

Emission spectroscopy of solid propellants is not a new field of research. Emission spectra have been published for double-base propellants (Ref. 31,80,81) and several different AP-based composite propellants (Ref. 32-35,37). In general, few reactive radical species were seen in emission in double-base propellant combustion because continuous emission generally filled the spectral regions of interest, especially at pressures above atmospheric. Similar problems with continuous emission were encountered in AP-based composite propellants. "Clean" spectra could be obtained with atmospheric pressure propellant flames, showing C_2 , CH, OH, NH, CN, and NO (γ system), but continuous emission rapidly replaced or obscured the emission of these species at pressures above approximately 0.5 MPa (70 psig) (Ref. 32,34). The strength of the continuum was found to be a function of binder type and AP particle size. This continuum is generally attributed to the $CO + O$ recombination (Ref. 33), although the spectral distribution found in shock tube studies of the $CO + O$ reaction is somewhat different than that seen in these propellant experiments at similar temperatures (Ref. 153).

It must be emphasized that emission is not, in general, correlated with the overall concentration of the species. Emission is proportional to the concentration of the chemically

excited state of the species (Ref. 159), which is generally a small fraction of the overall species concentration. Thus, the species distribution shown by emission would generally be different than that shown by LIF, which measures the unexcited (ground) state distribution. Due to fast quenching times, the excited state population should be confined to the region of the flame where it was formed. Thus, emission spectroscopy can be used to locate reaction zones, although it must be kept in mind that the reactions forming the excited species may be minor channels in the overall chemistry of the species. Several previous attempts to characterize the structure of propellant flames used emission from highly reactive radicals such as CN as a characteristic of the "primary reaction zone." At atmospheric pressure, the spatial extent of the primary reaction zone was apparently quite variable, ranging from less than 500 μm to 2000 μm (Ref. 32,34,37). These reaction zones are much larger than the primary reaction zones used in current solid propellant combustion models, which range from approximately 1-100 μm (Ref. 91-93,107,112,204). It must be noted that a comparison of the "flame sheets" used in the combustion models and the columnar diffusion flames thought to be present in the propellant flame is inconsistent. Also, atmospheric pressure flames may have an appreciable premixed character, which disappears in the pressure range of interest, complicating the interpretation of the atmospheric pressure data.

In addition to flame structure, emission spectroscopy can also give some information about flame chemistry by a comparison of the propellant flame emission and the emission from known flames. The combustion chemistry of AP and HMX propellants has been the subject of many studies, although most chemical detail comes from experiments at conditions far different from those encountered during combustion in rocket motors. Ammonium perchlorate burning as a monopropellant is thought to dissociate into NH_3 and HClO_4 with the HClO_4 quickly decomposing into ClO , OH , and O_2 . The ammonia is subsequently oxidized by the very reactive ClO and OH radicals in a premixed flame (Ref. 122,123,131,154). At low pressure, a similar premixed flame would be formed with binder pyrolysis products as the fuel. At higher pressures, the AP/binder flame would become a diffusion flame. Premixed $\text{HClO}_4/\text{CH}_4$ flames have been studied at low pressures (Ref. 123,154), showing OH , CH , and C_2 emission and no ClO emission. Premixed NH_3/O_2 flames have also been examined, showing OH , NH , NH_2 , and $\text{NO} + \text{O}$ emission (Ref. 104). However, the chemistry (and thus the emission) from diffusion flames is quite different. In a hydrocarbon/oxygen diffusion flame, the initially unmixed fuel and oxidizer are separated by combustion products (Ref. 46). The fuel generally pyrolyzes significantly before it has diffused into the reaction zone, with C and H_2 from this pyrolysis reacting with the oxidizer in the reaction zone. This type of flame does not show the CH and C_2 emission from the reaction zone seen in premixed hydrocarbon/oxygen flames. Thus, the obscuration of the molecular emission discussed in the preceding paragraph may be due to the transition from a low pressure premixed propellant flame to a higher pressure diffusion-controlled flame. It is apparent that the relevance of premixed flame data to propellant flames controlled by diffusion is tenuous.

The HMX flame is thought to occur as a breakup of the cyclic nitramine molecule into smaller fragments such as CH_2O and HCN (fuels) and N_2O and NO_2 (oxidizers), with these species then forming a premixed flame above the propellant (Ref. 22,91-93,106). The emission from premixed flames with N_2O and NO_2 as oxidizers varies dramatically depending upon the fuel (Ref. 46,104,145,146). Flames with CH_2O as the fuel show OH , NH , and

NH₂ emission, but no C₂, CH, or CN emission. In contrast, hydrocarbon/NO₂ and N₂O flames show emission from OH, C₂, CH, CN, NH, and NH₂. The relative intensity of the emission is a strong function of the nature of the hydrocarbon and the mixture ratio. For example, rich flames and carbon-rich fuels generally show much stronger C₂ emission than lean flames of hydrogen rich fuels (e.g., CH₄). Thus, the flame emission can give some clues to the chemical processes occurring in flames.

4.1. CH₄/N₂O FLAME EMISSION SPECTRA

A flame was generally used in this research as a calibration flame for both emission and laser diagnostic measurements of propellant flames. The flame was used to tune the dye lasers to the appropriate lines and to align spectra on the Reticon detector. For this reason most of the experimental propellant spectra have their counterparts in the CH₄/N₂O flame. For some of the early OH LIF work, a CH₄/O₂ flame was used. A propane/air torch was also briefly studied. In Fig. 26 to 29, emission spectra from the CN (B²Σ-X²Σ) molecule are presented. The CN molecule will be described in the propellant flames in emission (Sections 4.3-4.5 and 4.7) and in laser-induced fluorescence (Section 5.2). The NH emission spectrum from the CH₄/N₂O flame is shown in Fig. 30. NH was studied in solid propellant flames in emission (Sections 4.3-4.5 and 4.8) and in LIF (Section 5.3). CH (A²Δ-X²Π) emission could be seen in the CH₄/N₂O flame (Fig. 31), but could only be seen in the AP1 propellant flame (Section 4.3). CH LIF experiments in the CH₄/N₂O flame were unsuccessful, perhaps due to a very low CH concentration (demonstrating again that emission intensity is not proportional to concentration). C₂ emission could be seen in the CH₄/N₂O flame (Fig. 32 and 33), but was not observed in any of the propellant flames. OH emission was observed in the CH₄/N₂O flame (Fig. 34 and 35), which is not surprising since OH is observed in essentially all flames that contain H and O (Ref. 104). OH emission was seen in the AP1 and HMX1 propellant flames (Sections 4.3 and 4.5), and the rotational temperature of this OH emission has been analyzed (Ref. 3). OH LIF was observed in many of the propellant flames, although low laser power created signal to noise problems in some experiments (Sections 5.1, 5.4, and 5.5). Occasionally, emission band sequences overlap to the extent that one sequence may be affecting the other. For example, Figure 36 shows that the peak heights of the CN 0,1 band sequence may be affected by the nearby CH emission, thus changing the vibrational and rotational temperatures that could be calculated from these spectra (see Section 4.7). The CN 0,0 band also interferes with CH emission (see Section 4.2). Emission from metals and other impurities is often observed in propellant flames (see Sections 4.3-4.5), so the identity of this emission was often confirmed by volatilizing the suspected impurity in the CH₄/N₂O flame and comparing spectra. For example, the emission spectra of Cr and Ni are shown in Figure 37 and 38. These metals are seen in the propellant flames (see Section 4.3 and 4.5), as are Fe and others, and often interfere with the analysis of propellant emission spectra. For example, an uncontaminated spectrum from the inner cone of a CH₄/N₂O flame is shown in Figure 39. Note that Ni emission could easily obscure the NH and OH (0,1 band sequence) emission. Fe emission often interferes with the analysis of the CN 0,0 band sequence (see Section 4.5). In the propellant flames, emission from many species is often observed and must be expected.

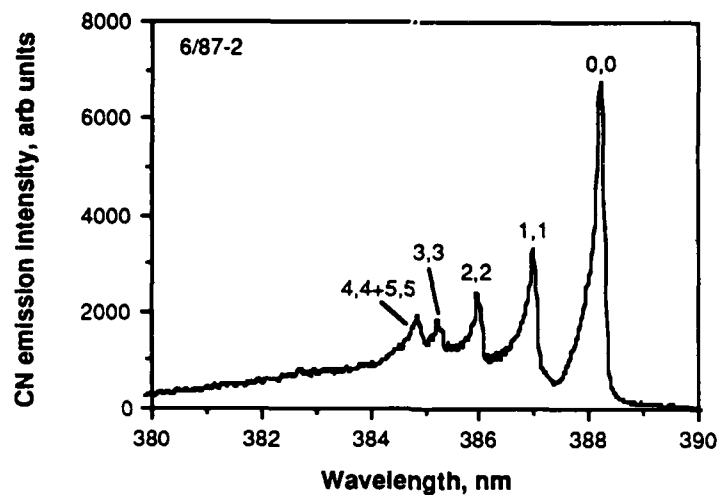


Figure 26. CN ($B^2\Sigma-X^2\Sigma$) emission spectrum. $\text{CH}_4/\text{N}_2\text{O}$ flame, Reticon detector, 700 pixels, 0.0175 nm/pixel dispersion, 500/200 μm slits, 0.13 s exp. time.

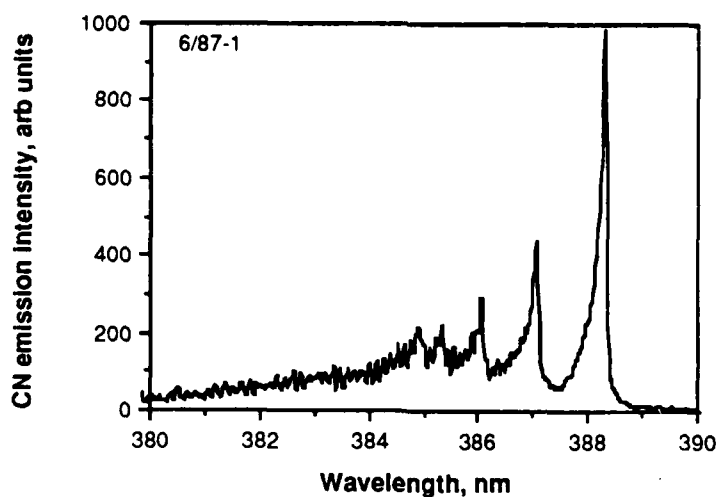


Figure 27. CN ($B^2\Sigma-X^2\Sigma$) emission spectrum. $\text{CH}_4/\text{N}_2\text{O}$ flame, Reticon detector, 700 pixels, 0.0175 nm/pixel dispersion, 100/100 μm slits, 0.13 s exp. time.

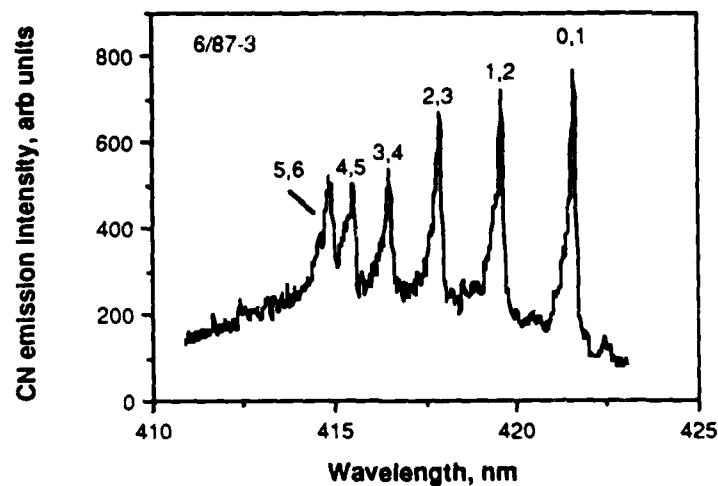


Figure 28. CN ($B^2\Sigma-X^2\Sigma$) emission spectrum. $\text{CH}_4/\text{N}_2\text{O}$ flame, Reticon detector, 700 pixels, 0.0175 nm/pixel dispersion, 500/200 μm slits, 0.13 s exp. time.

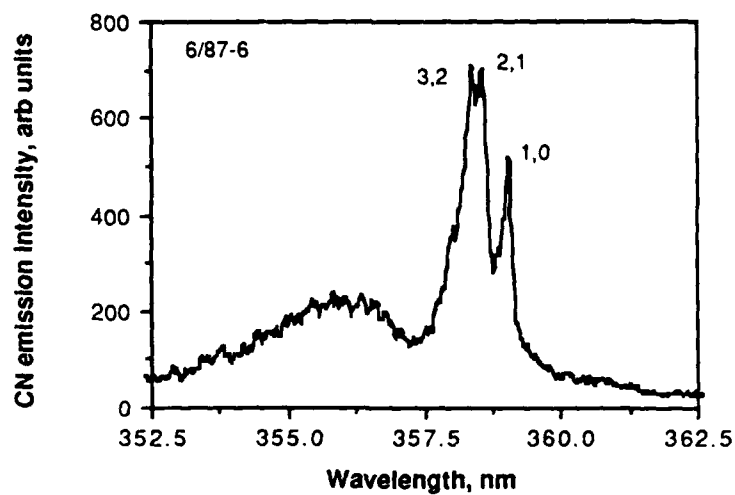


Figure 29. CN ($B^2\Sigma-X^2\Sigma$) emission spectrum. $\text{CH}_4/\text{N}_2\text{O}$ flame, Reticon detector, 700 pixels, 0.0175 nm/pixel dispersion, 500/200 μm slits, 0.13 s exp. time.

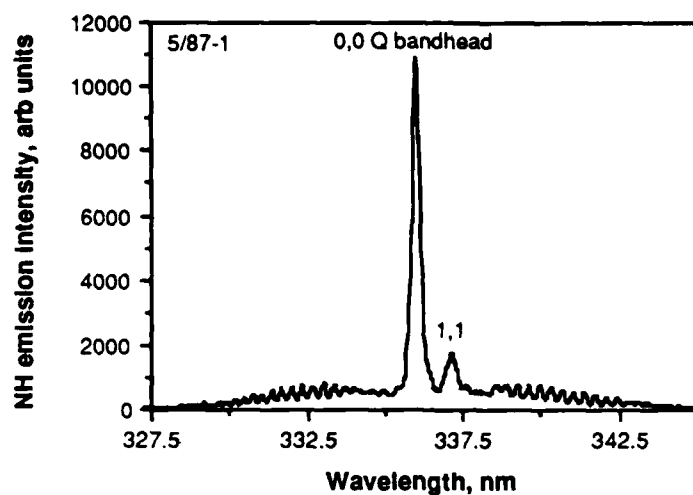


Figure 30. NH ($A^3\Pi-X^3\Sigma$) emission spectrum. $\text{CH}_4/\text{N}_2\text{O}$ flame, Reticon detector, 700 pixels, 0.035 nm/pixel dispersion, 100/100 μm slits, 0.59 s exp. time.

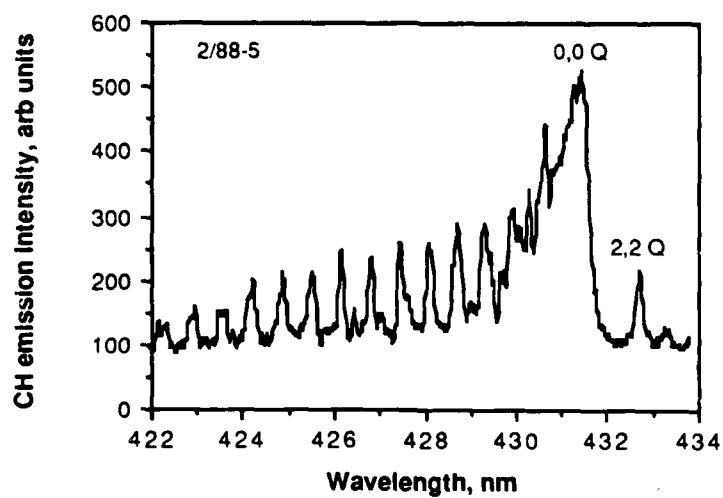


Figure 31. CH ($A^2\Delta-X^2\Pi$) emission spectrum. $\text{CH}_4/\text{N}_2\text{O}$ flame, Reticon detector, 700 pixels, 0.0175 nm/pixel dispersion, 500/200 μm slits, 0.5 s exp. time.

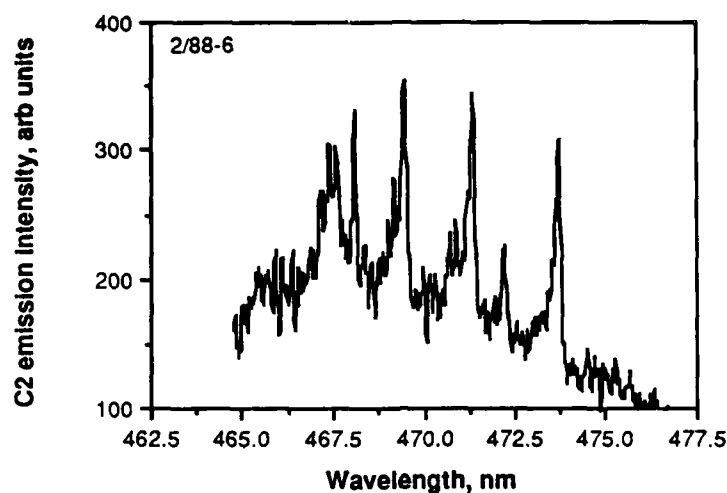


Figure 32. C_2 ($A^3\Pi-X^3\Pi$) emission spectrum. CH_4/N_2O flame, Reticon detector, 700 pixels. 0.0175 nm/pixel dispersion, 500/200 μm slits, 0.5 s exp. time, peaks identified in Figure 45.

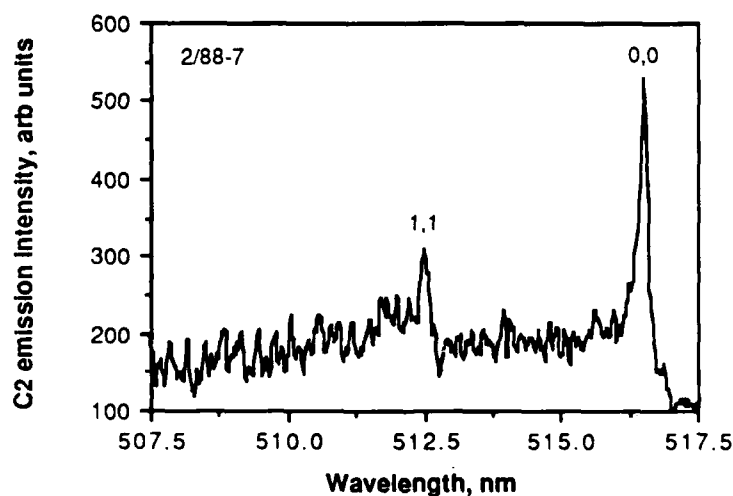


Figure 33. C_2 ($A^3\Pi-X^3\Pi$) emission spectrum. CH_4/N_2O flame, Reticon detector, 700 pixels. 0.0175 nm/pixel dispersion, 500/200 μm slits, 0.5 s exp. time.

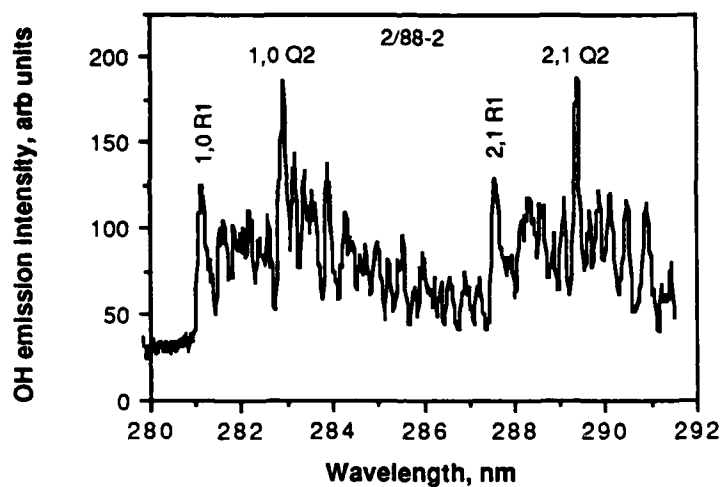


Figure 34. OH ($A^2\Sigma-X^2\Pi$) emission spectrum. $\text{CH}_4/\text{N}_2\text{O}$ flame, Reticon detector, 700 pixels, 0.0175 nm/pixel dispersion, 500/200 μm slits, 0.2 s exp. time.

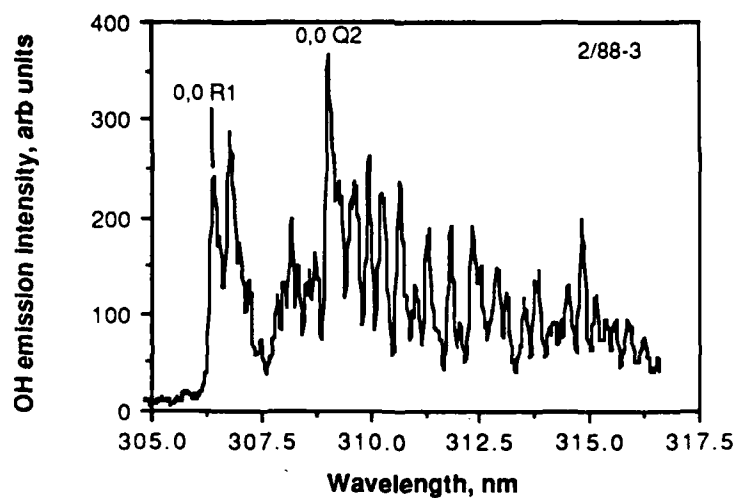


Figure 35. OH ($A^2\Sigma-X^2\Pi$) emission spectrum. $\text{CH}_4/\text{N}_2\text{O}$ flame, Reticon detector, 700 pixels, 0.0175 nm/pixel dispersion, 500/200 μm slits, 0.1 s exp. time.

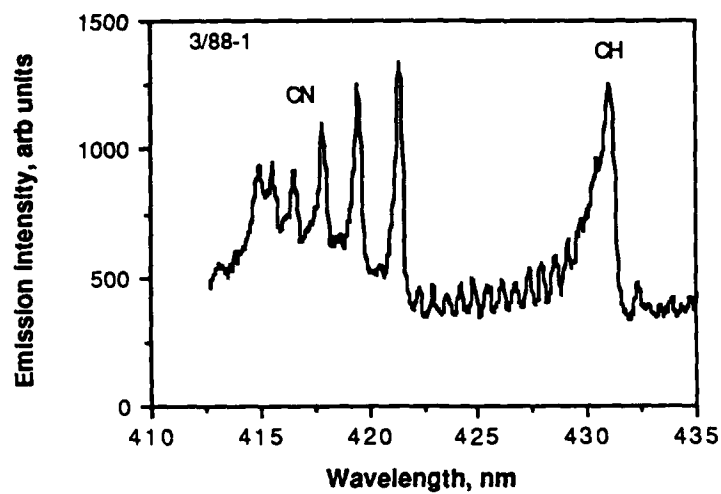


Figure 36. Emission spectrum of CN ($B^2\Sigma-X^2\Sigma$) and CH ($A^2\Delta-X^2\Pi$). Inner cone of CH_4/N_2O flame, Reticon detector, 700 pixels, 0.035 nm/pixel dispersion, 500/200 μm slits, 0.5 s exp. time.

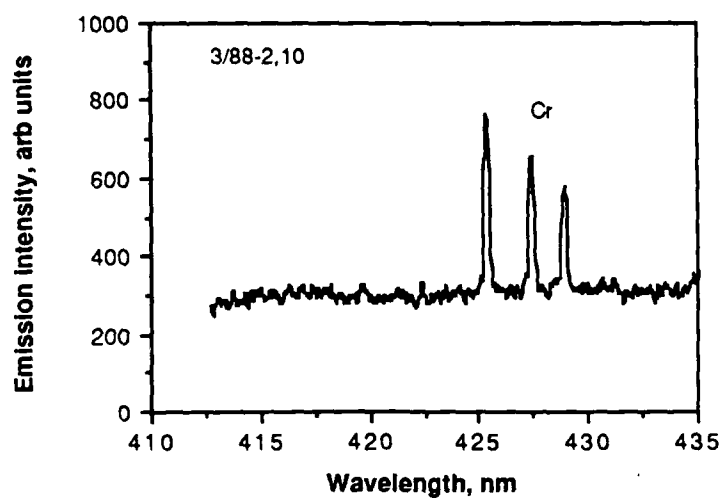


Figure 37. Cr emission spectrum (Nichrome wire vaporized into flame). Outer cone of CH_4/N_2O flame, Reticon detector, 700 pixels, 0.035 nm/pixel dispersion, 500/200 μm slits, 0.5 s exp. time.

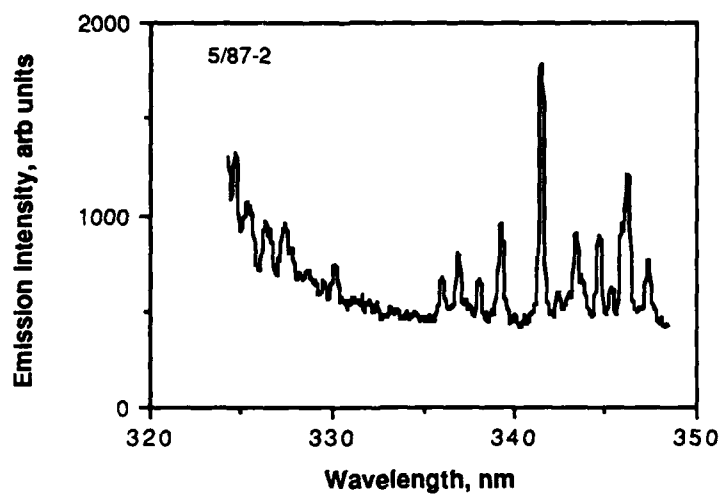


Figure 38. Ni emission spectrum (Nichrome wire vaporized into flame). $\text{CH}_4/\text{N}_2\text{O}$ flame, Reticon detector, 700 pixels, 0.035 nm/pixel dispersion, 500/200 μm slits, 0.59 s exp. time.

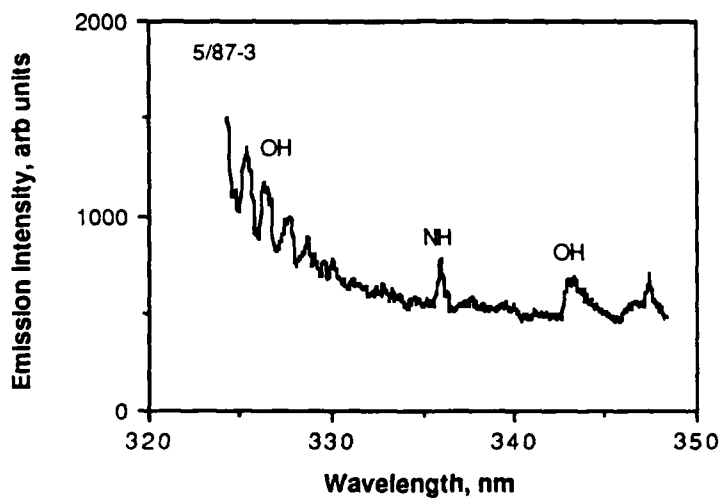


Figure 39. Reference emission spectrum for Figure 37. $\text{CH}_4/\text{N}_2\text{O}$ flame, Reticon detector, 700 pixels, 0.035 nm/pixel dispersion, 500/200 μm slits, 0.59 s exp. time.

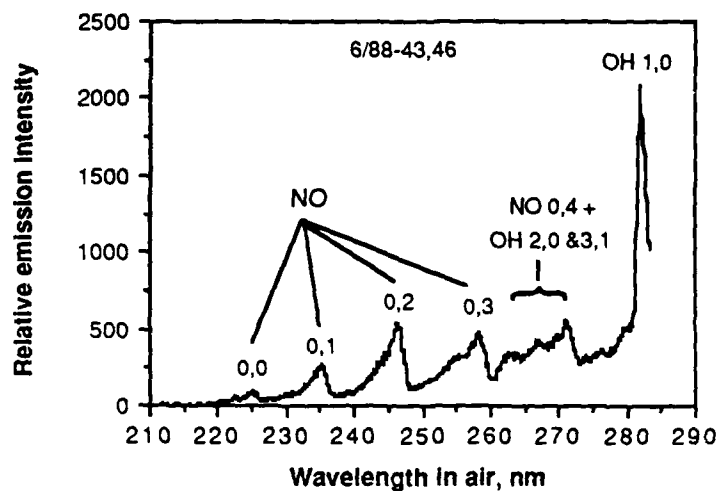


Figure 40. NO emission spectrum. $\text{CH}_4/\text{N}_2\text{O}/\text{NO}$ flame, 1 atm air, Reticon detector, 1000 data points (composite of 2 700 pixel spectra), 0.07 nm/pixel dispersion, 500/200 μm slits, 0.5 s exp. time.

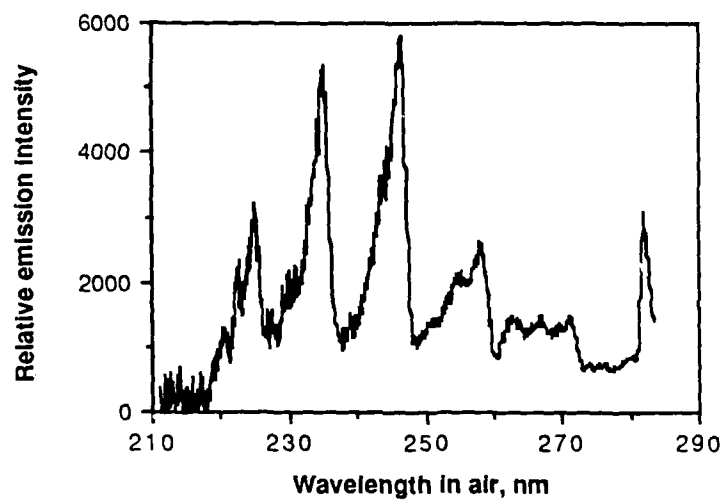


Figure 41. Same as Figure 40, corrected for Reticon wavelength response (Figure 4).

4.2. PROPANE/AIR FLAME EMISSION SPECTRA

Emission spectra were collected from a propane/air torch for several reasons. One, the torch offered a ready means of observing any differences from the standard $\text{CH}_4/\text{N}_2\text{O}$ flame. One of the most interesting observations was the CH B-X system (Fig. 42), which is mostly obscured by CN emission in the $\text{CH}_4/\text{N}_2\text{O}$ flame. The influence of the CN 0,1 system on the low wavelength end of the CH A-X system can also be assessed by comparing Fig 43 and Figure 28. C_2 emission spectra were stronger in the propane/air torch than in the $\text{CH}_4/\text{N}_2\text{O}$ flame, as can be seen by comparing Figure 45 with Figure 32. OH spectra were similar in appearance to the $\text{CH}_4/\text{N}_2\text{O}$ flame, as shown by Fig. 44 and 35.

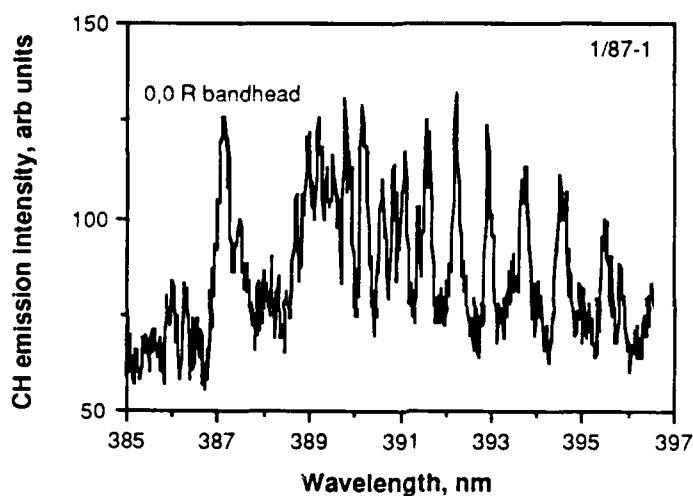


Figure 42. CH ($\text{B}^2\Sigma\text{-X}^2\Pi$) emission spectrum. $\text{C}_3\text{H}_8/\text{air}$ flame, Reticon detector, 700 pixels, 0.0175 nm/pixel dispersion, 500/200 μm slits, 1.17 s exp. time.

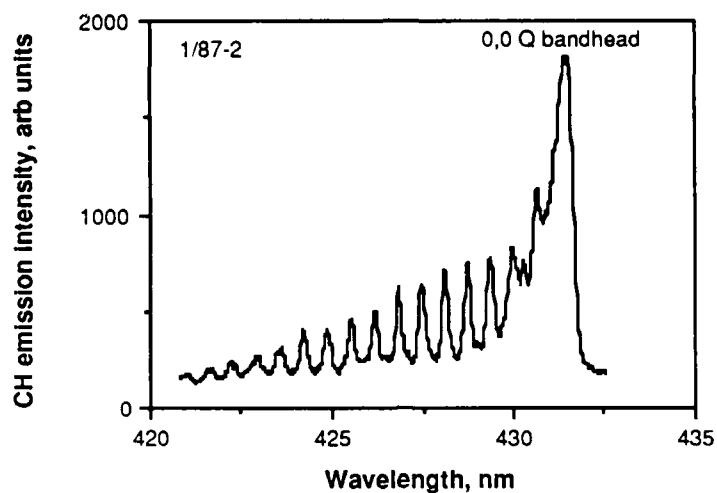


Figure 43. CH ($A^2\Delta$ - $X^2\Pi$) emission spectrum. C_3H_8 /air flame, Reticon detector, 700 pixels, 0.0175 nm/pixel dispersion, 500/200 μm slits, 1.17 s exp. time.

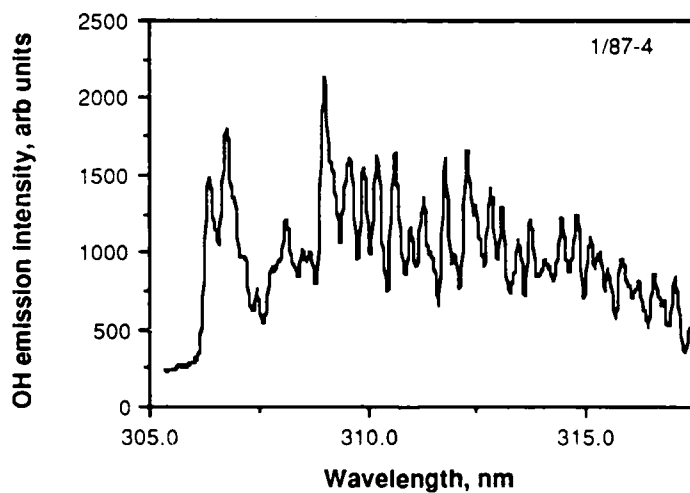


Figure 44. OH ($A^2\Sigma$ - $X^2\Pi$) emission spectrum. C_3H_8 /air flame, Reticon detector, 700 pixels, 0.0175 nm/pixel dispersion, 500/200 μm slits, 1.17 s exp. time.

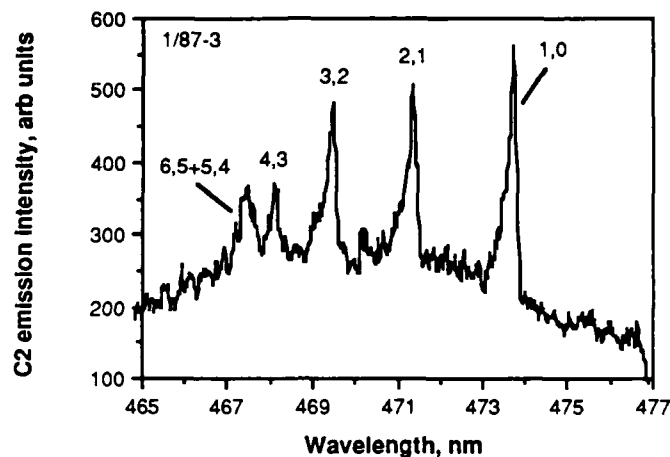


Figure 45. C_2 ($A^3\Pi-X^3\Pi$) emission spectrum. C_3H_8 /air flame, Reticon detector, 700 pixels, 0.0175 nm/pixel dispersion, 500/200 μm slits, 1.17 s exp. time.

4.3. AP1 PROPELLANT EMISSION STUDIES

A survey of the emission from both AP and HMX propellants in the wavelength range 280-700 nm was performed in this study. The important variables investigated were pressure and height of collection volume above surface. This height ("h") is defined as the height of the center of the 200-1000 μm thick collection volume above the surface. Thus, a height defined as $h=1000 \mu m$ with a resolution of 500 μm means that the chemiluminescent emission was collected from a region from approximately 750-1250 μm above the surface. The vertical resolution in these experiments is roughly the spectrometer entrance slit width (the first number in the figure caption), although this is a lower bound to the vertical thickness of the collection volume since the emission is being collected (integrated) over a horizontal slice of the flame.

The strength and character of the emission from the AP propellant varied strongly with pressure. At all pressures, the emission originated mainly from the trace impurities in the propellants (Na, K, Ca), combinations of the impurities with flame species (CaCl, CaOH), and OH emission. A continuum was also present in the wavelength range 330-550 nm, increasing rapidly in intensity as pressure increased. Only at the lowest pressures investigated could emission from CN, NH, and CH be detected. This emission was rapidly replaced by the continuum as the pressure increased above atmospheric, with the continuum totally replacing the molecular emission at pressures above 0.5 MPa. These results are similar to those discussed in the introduction, and are summarized in Table 11 and Figures 46 to 54. At 0.1 MPa (10 psig), the ratio of the highest peaks in the emission spectra of the important radicals was CN/OH/NH/CH=7/6/5/1. No C_2 emission was detected. Because of the photoelectric (as opposed to photographic) detection system and higher resolution spectrometer used in this

research, the spectra (notably OH, NH, and CH) are more highly resolved than those previously published (Ref. 31-35,37,80,81). However, individual rotational lines are not resolved (Ref. 1). For example, a series of OH emission spectra are shown in Figures 51 to 53. The emission in this region originates from the 0,0 and 1,1 vibrational bands of the OH A-X transition. This OH emission is an ubiquitous feature of flames containing hydrogen and oxygen (Ref. 104). Analysis of this spectrum is complicated by incomplete resolution of lines, possible self-absorption effects, pressure broadening of lines, and an apparent pressure-dependent background (Ref. 3,13); however, some general observations can be made. The structure of the OH emission spectrum (and consequently the rotational and vibrational populations) appears to be a function of pressure and height above the propellant surface. This is evident in Figure 2. Increasing the pressure and moving closer to the surface have a similar impact on a given OH spectrum, an apparent increase in the population of the $v'=1$ vibrational level. Another notable point is the large distances from the surface at which significant OH emission is still seen. A more detailed analysis, with the calculation of approximate rotational temperatures, has been performed (Ref. 3). Models of AP-based composite propellants generally predict final flame heights on the order of 100-500 μm (Ref. 107,112), implying that the conversion of reacting molecules to final products should be complete outside this flame zone. The fact that OH emission is seen at such large distances from the surface at these pressures indicates that significant reactions involving OH are occurring even at 10 mm (0.4 in) from the surface and that a flame sheet is a poor approximation to the extended final flame. Because of the high quenching rates at pressures above atmospheric (Ref. 10), this OH emission is not due to reactions occurring closer to the surface and radiating at a later time and larger distance away from the surface. As can be seen in Table 3.3.1, there is an appreciable equilibrium concentration of OH at the flame temperature, although this is ground state OH and not the excited state OH that causes the chemiluminescence. In any case, OH emission is usually found throughout a flame (Ref. 46,104), so the OH molecule is a poor indicator of primary reaction zones. Two-dimensional imaging of these propellant flames using a Vidicon two-dimensional detector tends to confirm the flame structure indicated by these results (Ref. 5). The UV emission from the flame (primarily OH and the continuum) tends to show a broad emission intensity distribution with the strong intensity region extending many mm above the propellant surface. The visible image of the flame is of similar size (Ref. 5). For this reason, another molecule, such as CN, NH, or CH, would be a better indicator of reaction zones. However, the emission from these molecules is obscured by the continuum at pressures much above 0.1 MPa. Apparently the monopropellant flame, which could show molecular emission (such as NH emission), does not create the right environment to yield much emission. Determining the structure of the AP propellant flame spectroscopically will require a diagnostic technique that will create a signal-to-noise ratio that is sufficiently large to overcome the background continuum at high pressures. Another consideration is that other types of spectroscopy will also allow observation of molecules that do not emit under the conditions in the propellant flame. Of course, it may be the case that the absence of emission from such molecules as CN and NH indicates that the diffusion flame is totally dominant and that these species do not exist in appreciable concentration in the AP propellant flame at pressures above about 0.1 MPa. This is discussed further in Section 5.2. Modeling of the CN emission is discussed in Section 4.7.

The distribution of emission from the species that do emit in the flame has been examined. In general, the emission from the impurities (Na, CaCl, etc.) and OH tends to

rapidly increase above the propellant surface, reaching a maximum at 2-3 mm above the surface and extending out past 10 mm. At low pressures, the CN, NH, and CH emission behaves quite differently, generally reaching a maximum and dropping back to low levels within 2-3 mm. Again, at higher pressures the emission of CN, NH, and CH is absent. This is illustrated in Figures 55 and 56, where the emission intensities for each molecule are converted to a relative scale. The vibrational energy distribution in the CN molecule shows behavior similar to that seen in OH, with the 4,4 bandhead at 351.1 nm ($v' = 4$) confined to a region much closer to the surface than the 0,0 bandhead at 388.3 nm (see Section 4.7). These intensity profiles were obtained by allowing the propellant to burn down through the collection volume, in essence allowing sequential data collection from progressively higher in the flame. The surface is defined as the point of first significant emission. This is only approximate since the presence of a non-emitting zone just above the surface would be missed. In AP propellant flames, however, emission extends from the surface- there is no "dark" zone. This data appears to contradict idealized flame models which show thin flame sheets at distances on the order of 100 μ m for the final flame and 10 μ m for the primary and monopropellant flames at typical pressures. If one assumes that the Na emission is a function of temperature, then the final flame, defined as the part of the flame that has reached the maximum flame temperature, is a rather large flame with a thickness on the order of centimeters. This is approximately the same size as the visible flame. Improved resolution would be desirable, however, to better resolve AP flame zones in both time and space. For this reason, LIF experiments were performed (see Section 5). Both control and burndown experiments were performed with Na emission to see if periodic fluctuations proportional to the combustion time of the constituent AP crystals could be seen. No such behavior was seen, which is not surprising since the emission was collected over a horizontal slice of the flame of at least 6 mm in width, averaging over many AP particles.

Table 11. Species seen in emission in AP1 propellant flame.

Emitting species	Wavelength/band	present/absent
CN	B-X, 0-0, 1-0, 0-1 band sequences	present at low P
NH	0-0 band sequence (336 nm)	present at low P
CH	A-X system, 430 nm system	present at low P
OH	A-X, 0-0 and 1-0 band sequences	present
Na	589.0, 589.6, 330.2-3 nm	present
Fe	386, 387.9, 388.7 nm, etc.	absent?
K	769.9, 766.5, 403.5, 404.4 nm	present
Ca	422.7 nm	present
CaCl	A-X, 0-0 bands	present
Cr	425.4, 427.5, 428.4 nm	present near ignition
Ni	lines from 337-353 nm	present near ignition
CaOH	554 nm system	present
NO	A-X (γ bands), 200-300 nm	absent
C ₂	A-X, 0-0, 1-0 bands	absent
ClO	A-X, 0-6, 1-7 bands	absent

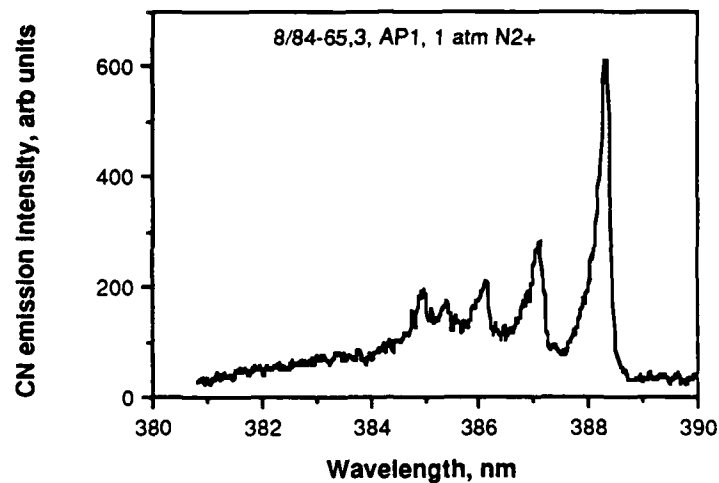


Figure 46. CN ($B^2\Sigma-X^2\Sigma$) emission spectrum. AP1 propellant, 1 atm N_2+ , Reticon detector, 700 pixels, 0.0175 nm/pixel dispersion, 0.24 s exp. time, 500/100 μm slits, $h=0$.

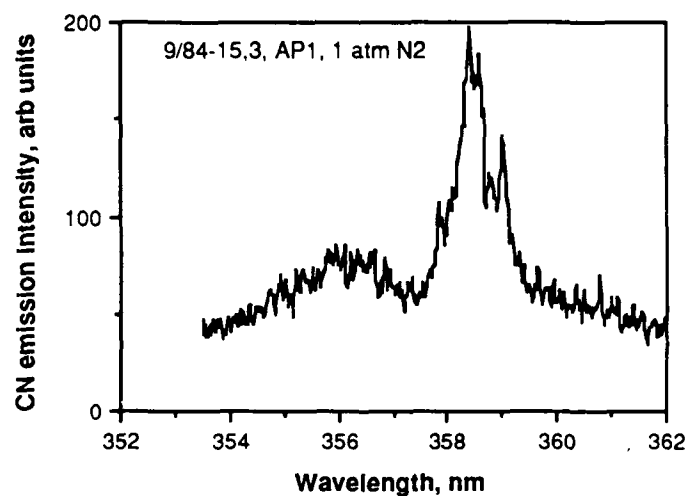


Figure 47. CN ($B^2\Sigma-X^2\Sigma$) emission spectrum. AP1 propellant, 1 atm N_2+ , Reticon detector, 700 pixels, 0.0175 nm/pixel dispersion, 0.24 s exp. time, 500/100 μm slits, $h=0$.

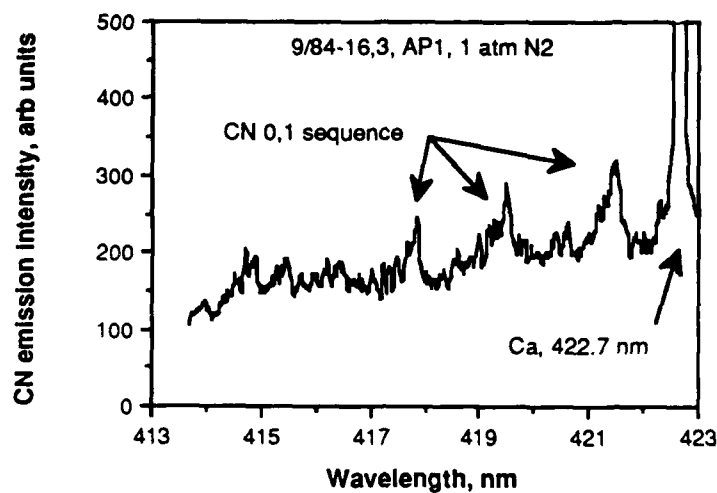


Figure 48. CN ($B^2\Sigma-X^2\Sigma$) emission spectrum. AP1 propellant, 1 atm N_2 +, Reticon detector, 700 pixels, 0.0175 nm/pixel dispersion, 0.24 s exp. time, 500/100 μm slits, $h=0$.

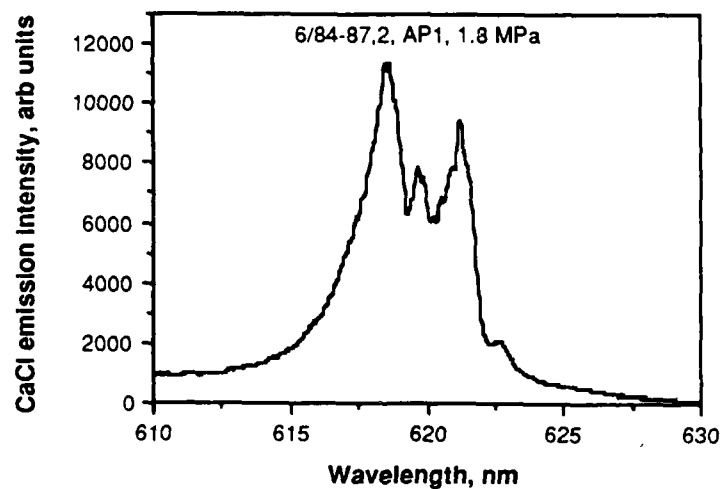


Figure 49. CaCl ($A^2\Pi-X^2\Sigma$) emission spectrum. AP1 propellant, 1.8 MPa, Reticon detector, 700 pixels, 0.035 nm/pixel dispersion, 0.07 s exp. time, 50/100 μm slits, $h=0$?

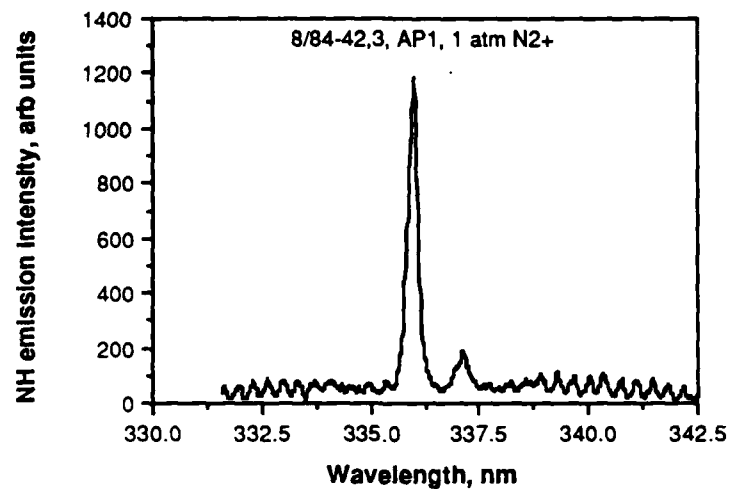


Figure 50. NH ($A^3\Pi-X^3\Sigma$) emission spectrum. AP1 propellant, 1 atm N_2+ , Reticon detector, 700 pixels, 0.0175 nm/pixel dispersion, 0.24 s exp. time, 500/100 μm slits, $h=1$ mm?

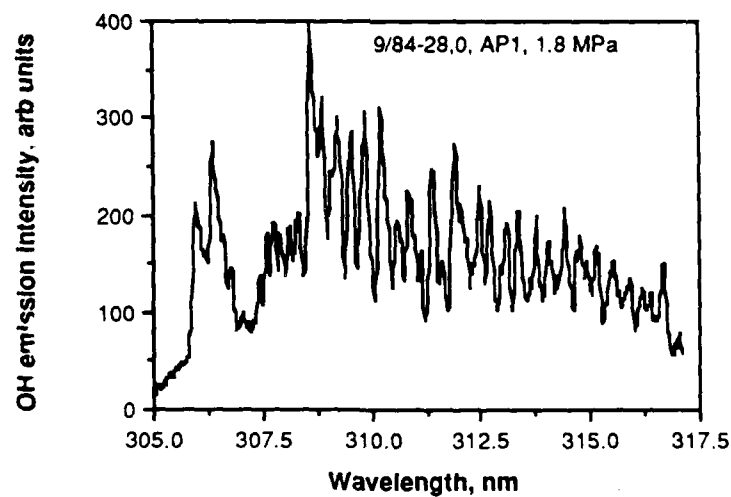


Figure 51. OH ($A^2\Sigma-X^2\Pi$) emission spectrum. AP1 propellant, 1.8 MPa, Reticon detector, 700 pixels, 0.0175 nm/pixel dispersion, 0.07 s exp. time, 100/100 μm slits, $h=10$ mm.

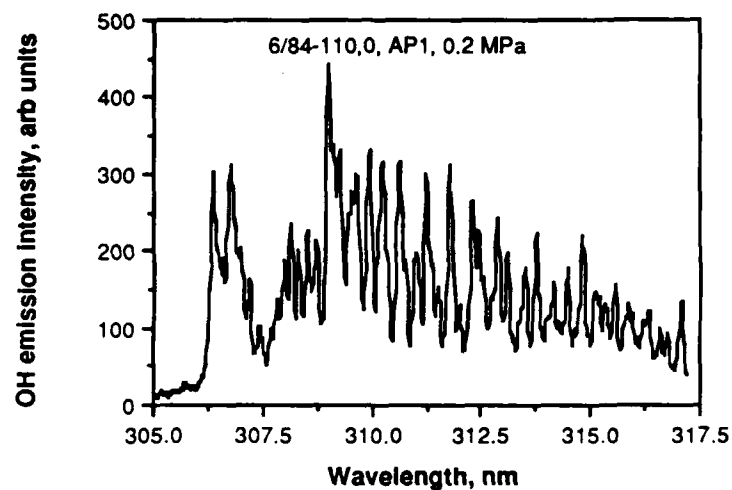


Figure 52. OH ($A^2\Sigma-X^2\Pi$) emission spectrum. AP1 propellant, 0.2 MPa, Reticon detector, 700 pixels, 0.0175 nm/pixel dispersion, 0.24 s exp. time, 100/100 μm slits, $h=0$.

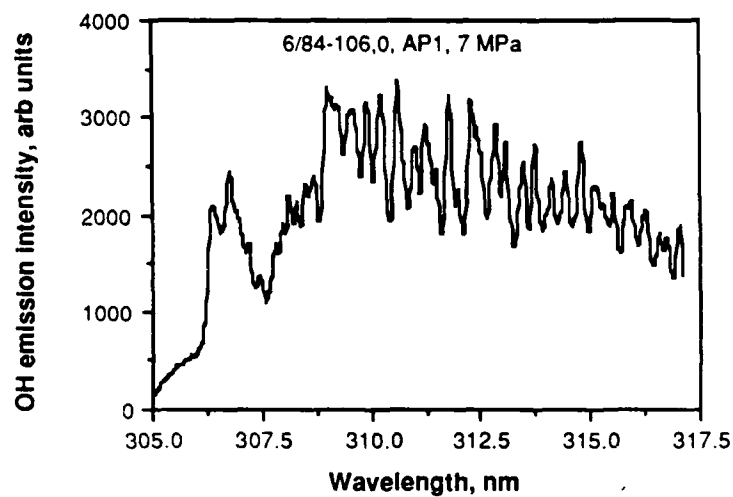


Figure 53. OH ($A^2\Sigma-X^2\Pi$) emission spectrum. AP1 propellant, 7 MPa, Reticon detector, 700 pixels, 0.0175 nm/pixel dispersion, 0.07 s exp. time, 100/100 μm slits, $h=0$?

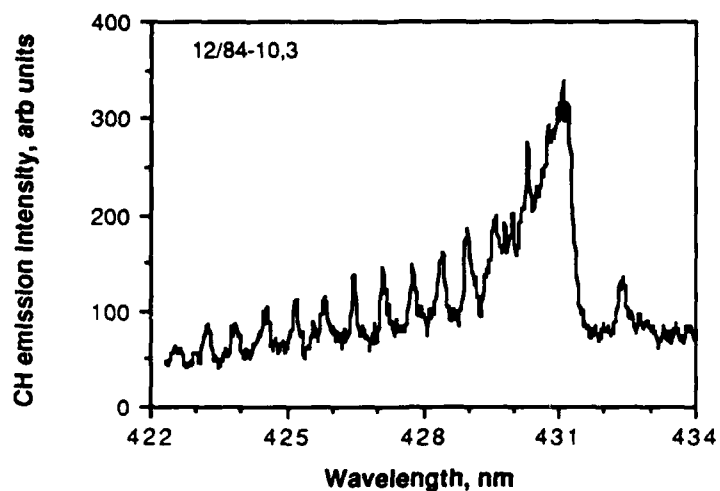


Figure 54. CH ($A^2\Delta-X^2\Pi$) emission spectrum. AP1 propellant, 1 atm N_2+ , Reticon detector, 700 pixels, 0.0175 nm/pixel dispersion, 0.24 s exp. time, 500/100 μm slits, $h=0?$.

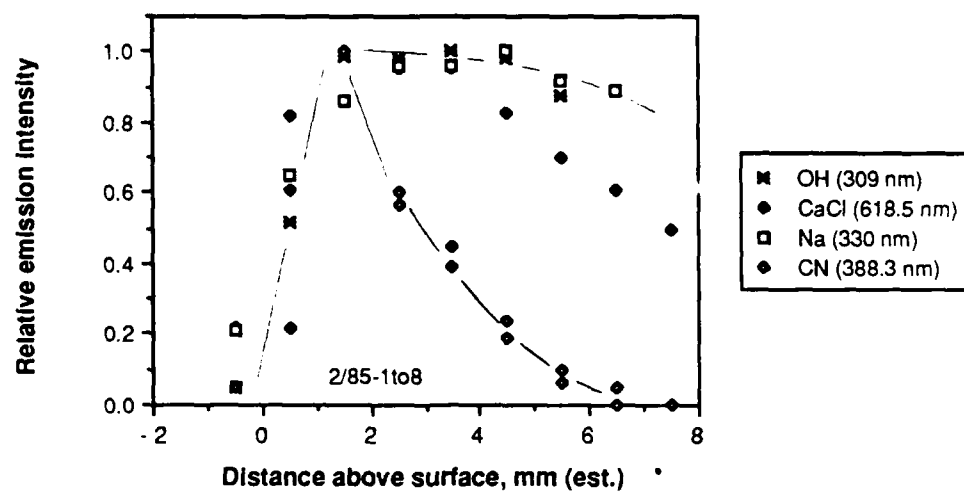


Figure 55. Emission intensity as a function of distance above surface. AP1 propellant, 1 atm N_2+ .

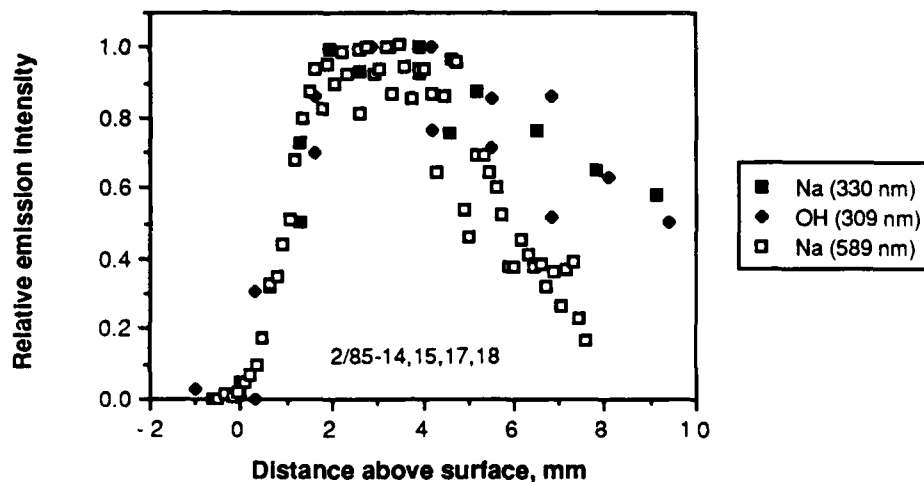


Figure 56. Emission intensity as a function of distance above surface. AP1 propellant, 1.8 MPa (filled symbols) and 3.5 MPa (open symbols).

4.4. AP2 PROPELLANT EMISSION STUDIES

Many solid propellants contain aluminum. The flame above such a metallized propellant would be expected to be especially inhospitable to laser diagnostics. For this reason, a brief study was made of the emission from AP2 propellant. The flame above this propellant was essentially opaque at 0.8 MPa (see Section 3.4), so laser diagnostics would be difficult to apply.

A survey was made of the possible emitting species at atmospheric pressure (under N_2) and at 0.8 MPa by allowing the propellant to burn down through the collection volume with the spectrometer set to the appropriate wavelength. Surprisingly (?), weak CN emission was the only molecular emission seen, although Na, Fe, and Al emission lines were seen. For example, see Figure 57. CN was seen only at atmospheric pressure, as in AP1 propellant. The results of the survey are summarized in Table 12. The most notable, and most obvious visual, aspect of the flame is the bright continuous background from burning aluminum particles.

The distribution of the CN and Al emission is illustrated in Figure 58. The most obvious characteristic is the extended CN emission profile (as compared to the non-aluminized AP1). The CN profiles from Figure 54 (AP1) and Figure 58 are compared in Figure 59, showing the extension of the CN profiles. This change in CN profile may be due to the "coolant" effect of unburned aluminum particles extending and attenuating the reaction zone, where reaction zone is here defined as the zone in the flame giving rise to the CN emission.

Na emission was also measured at 0.8 MPa with Na emission spectra and emission profiles shown in Figures 60 and 61, respectively. One interesting observation is the apparent self-absorption of the Na lines due to high Na concentration in the flame (see Section 3.1). The spectral distribution of the continuous background has also been measured, as shown in Figure 62. This background is quite similar to that from a tungsten lamp (GE FEL lamp), indicating that the background originated from hot aluminum particles.

Table 12. Species seen in emission in AP2 propellant flame.

Emitting species	Wavelength/band	present/absent
CN	B-X, 0,0 band sequence	present
Na	D lines (589.0, 589.6 nm)	present
Al	396.2, 394.4, 309.3, 308.2 nm	present
Fe	386 nm line	present
K	769.9, 766.5 nm	present
OH	A-X, 0,0 band	absent
NH	0,0 band sequence (336 nm)	absent
CH	A-X system, 0,0 band	absent
NO	A-X (γ bands), 200-200 nm	absent
AlCl	A-X, 0,0 band	absent
AlO	B-X, 0,0 band	absent
C ₂	A-X, 0,0 band	absent

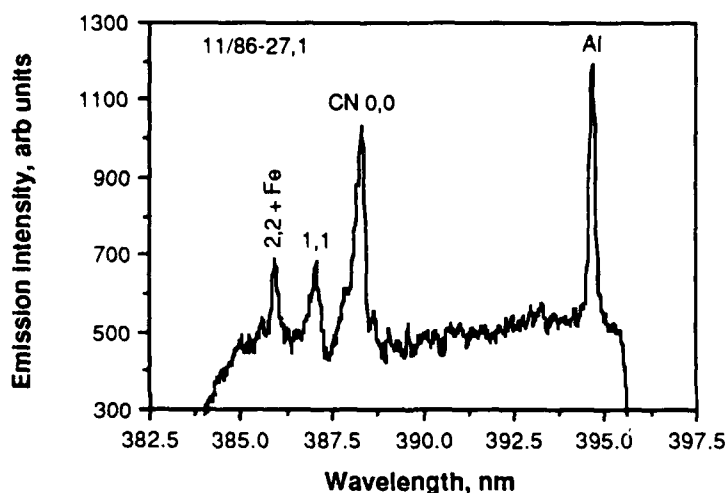


Figure 57. Emission spectra. AP2 propellant, 1 atm N₂+, Reticon detector, 700 pixels, 0.0175 nm/pixel dispersion, 0.36 s exp. time, 500/200 μ m slits, h=0?.

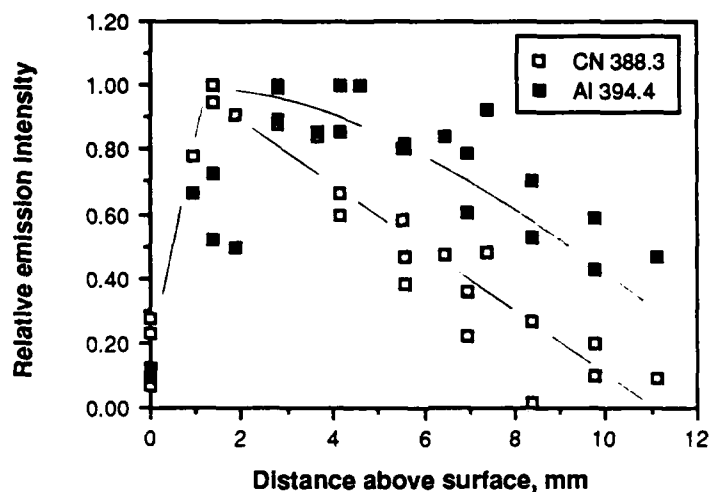


Figure 58. Emission intensity as a function of distance. AP2 propellant, 1 atm N_2^+ .

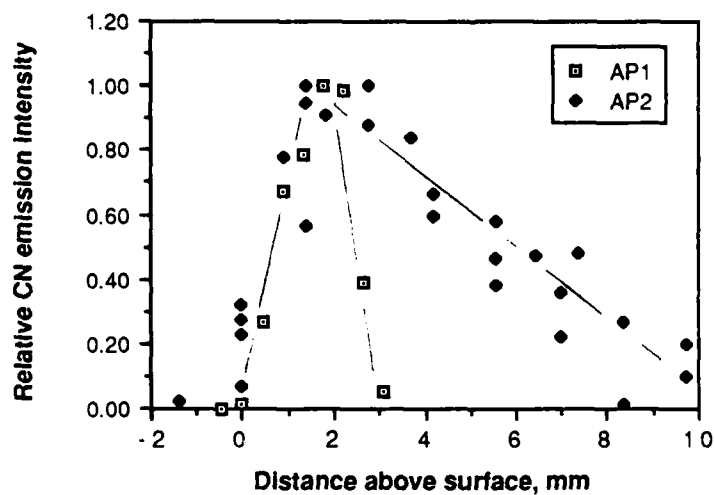


Figure 59. CN emission intensity profiles for two AP propellants (1 atm N_2^+).

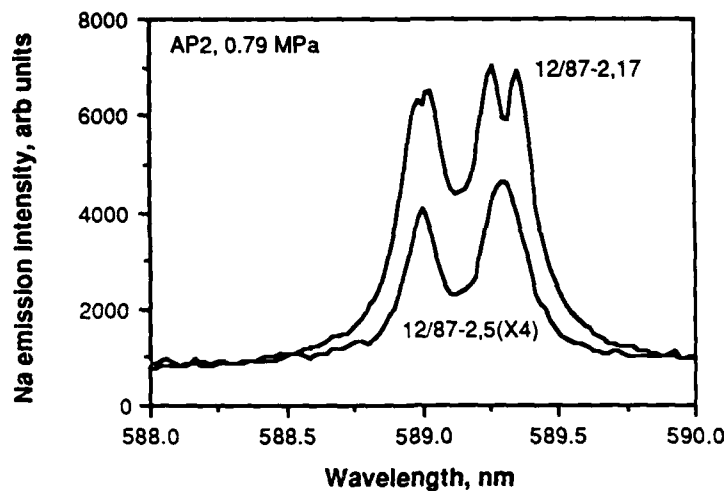


Figure 60. Na emission spectra. AP2 propellant, 0.79 MPa, Reticon detector, 700 pixels, 0.0175 nm/pixel dispersion, 0.05 s exp. time, 50/50 μ m slits, $h=0$ (bottom spectrum), $h=2$ mm (top spectrum).

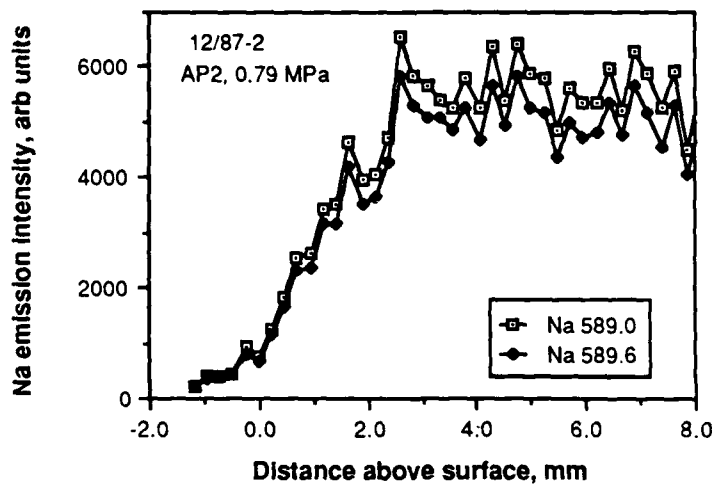


Figure 61. Na emission intensity as a function of distance. AP2 propellant, 0.79 MPa.

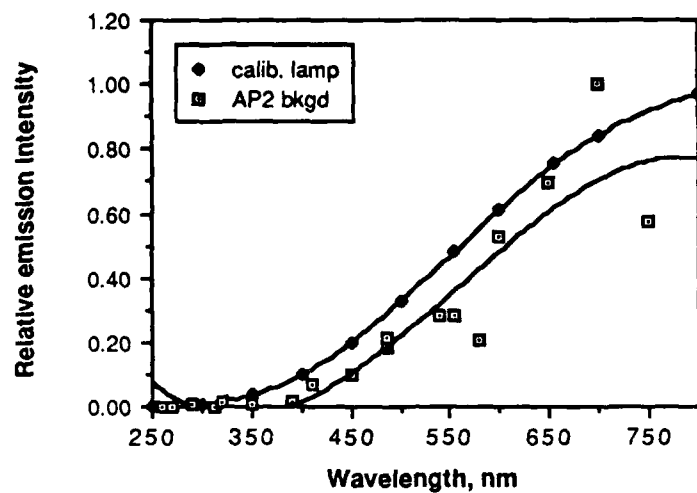


Figure 62. Comparison of continuous emission from AP2 propellant and a tungsten calibration source.

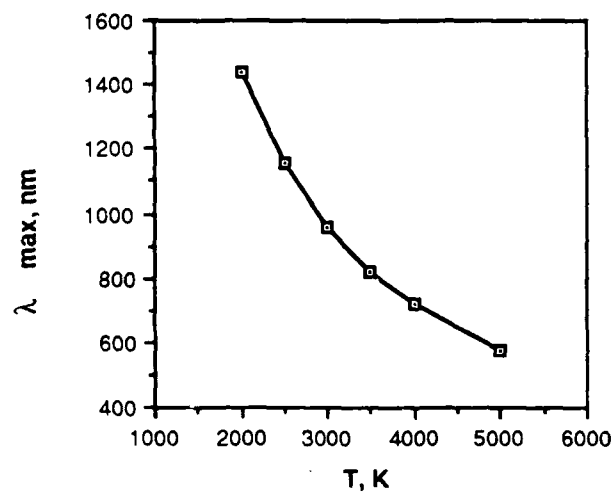


Figure 63. Black body predictions.

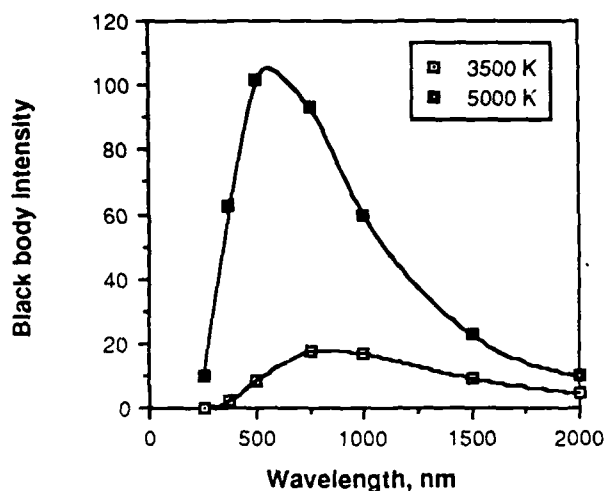


Figure 64. Black body predictions.

4.5. HMX PROPELLANT EMISSION STUDIES

The emission from the HMX flame is quite different from the AP propellant flame in several ways (see Figures 65 to 72 and Table 13). The molecular emission from CN and NH is seen at pressures up to 7 MPa (1000 psig). At 3.5 MPa, the ratio of emission intensities (maximum peak heights) is approximately CN/NH/OH=5/1/1. No CH or C₂ emission was detected at any pressure (Table 13). The presence of molecular emission at the highest pressures implies that the HMX propellant flame shows much more premixed character than the AP flame. As already discussed, this is basically due to the fuel-rich nature of the HMX. The continuum is much weaker in the HMX flame, which is probably due to the smaller amount of oxygen in the flame (see Table 6). The combustion behavior of the HMX propellants is significantly different from that of the AP propellants in another way. Unlike the AP propellants, the HMX propellants will not burn under nitrogen at atmospheric pressure. They will however burn quite well in air at atmospheric pressure, because of the diffusion of oxygen into the flame, which indicates that the combustion of HMX in air may be proceeding by a significantly different mechanism than the combustion of HMX in an inert atmosphere.

It is interesting to compare the emission seen in the HMX propellant flame to the emission seen in the flames of proposed intermediates in HMX combustion (Ref. 22,91-93,106). On the basis of low temperature decomposition studies, it has been suggested that the primary decomposition products of HMX are CH₂O and N₂O. CH₂O/N₂O flames have been studied (Ref. 145,155), with the primary emission species being OH, NH, NH₂. No CN, CH, or C₂ emission was seen. High temperature decomposition studies indicate that, under

conditions more similar to propellant deflagration, HCN is a major product (along with NO_2). An HCN/NO_2 flame should (analogous to HCN/O_2 flames (Ref. 87)) have CN and NH as intermediates, but not CH. Thus, it may be speculated that the strong CN emission and absence of CH emission is due to the predominance of HCN as the fuel species, at the expense of hydrocarbons or CH_2O . Note that the flame of the energetic plasticizer must also be considered. Multiply nitrated esters, such as TMETN, have been found to decompose into (mainly) NO_2 and aldehydes (Ref. 36). Aldehyde/ NO_2 flames show no CN or CH emission, while hydrocarbon/ NO_2 flames show both. Thus, the presence of the TMETN does not affect the observation of CN in the absence of CH emission. Our data, then, appears to confirm the importance of pathways other than $\text{CH}_2\text{O}/\text{N}_2\text{O}$ in HMX propellant combustion. LIF measurements underway on other radicals should give a much firmer basis for assignment of HMX flame reaction mechanisms.

Emission profiles for various species have been obtained in the HMX propellant flame at 3.5 MPa in the same manner as for the AP propellant flames. The main difference is CN and NH emission can be seen at these pressures in the HMX propellant flame. Typical emission profiles are shown in Figure 73. The profiles are similar to those seen in low pressure AP propellant flames. The "primary reaction zone" (characterized by CN and NH emission) is quite extended for such a high pressure, extending over several millimeters. The data indicates chemistry involving CN and NH occurring on a scale of millimeters, larger than would be expected from current HMX propellant combustion models. The temperature profile implied by the Na emission is similar to that found by Kubota, who used microthermocouples to follow the spatial variations in temperature in an HMX-based solid propellant (Ref. 22). These results, although not definitive because of the limitations of emission spectroscopy, are quite interesting, and the detailed study of the reaction zones in solid propellant flames using advanced combustion diagnostics that is now underway should yield important results.

Table 13. Species seen in emission in HMX1 propellant flame.

Emitting species	Wavelength/band	present/absent
CN	B-X, 0-0, 1-0, 0-1 band sequences	present
NH	0-0 band sequence (336 nm)	present
CH	A-X system, 430 nm system	absent
OH	A-X, 0-0 and 1-0 band sequences	present
Na	589.0, 589.6, 330.2-3 nm	present
Fe	386, 387.9, 388.7 nm, etc.	present
K	769.9, 766.5, 403.5, 404.4 nm	present
Ca	422.7 nm	present
Cr	425.4, 427.5, 428.4 nm	present
Ni	lines from 337-353 nm	present near ignition
Cu	324.8, 327.4 nm	present
Mg	285.2 nm	present
Sn	284.0, 286.3 nm	present
NO	A-X (γ bands), 200-300 nm	absent
C_2	A-X, 0-0, 1-0 bands	absent

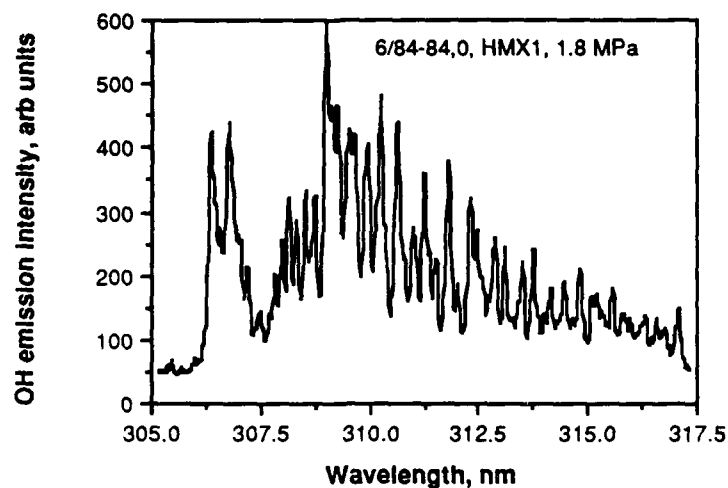


Figure 65. OH ($A^2\Sigma-X^2\Pi$) emission. HMX1 propellant, 1.8 MPa, Reticon detector, 700 pixels, 0.0175 nm/pixel dispersion, 0.24 s exp. time, 500/100 μm slits, $h=0$?

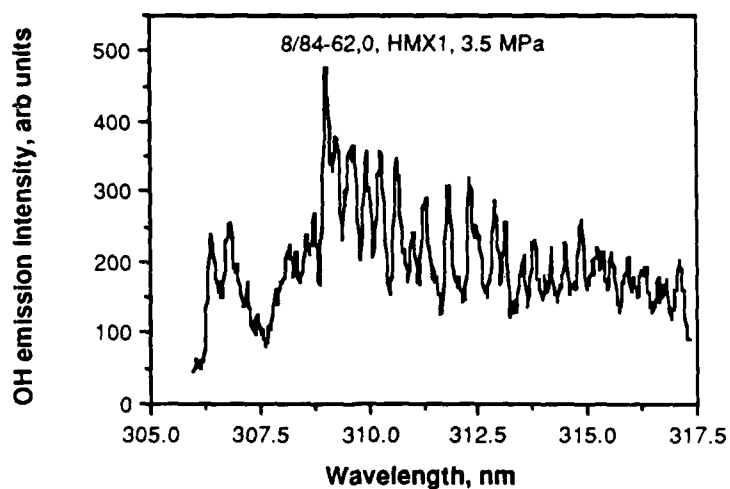


Figure 66. OH ($A^2\Sigma-X^2\Pi$) emission. HMX1 propellant, 3.5 MPa, Reticon detector, 700 pixels, 0.0175 nm/pixel dispersion, 0.24 s exp. time, 500/100 μm slits, $h=0$.

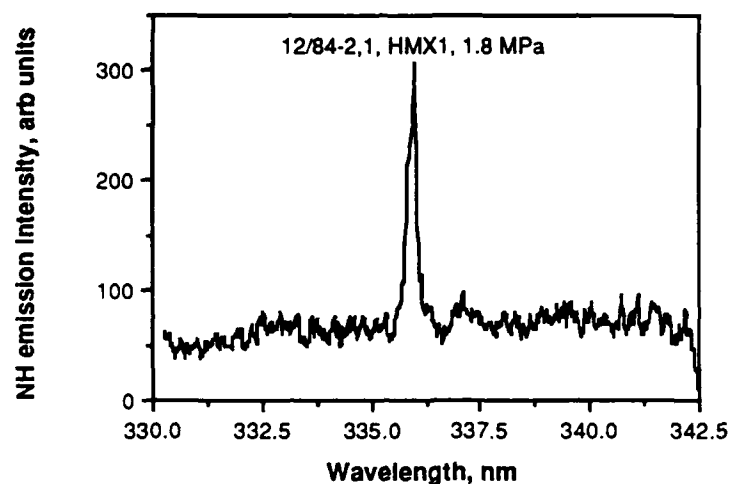


Figure 67. NH ($A^3\Pi-X^3\Sigma$) emission. HMX1 propellant, 1.8 MPa, Reticon detector, 700 pixels, 0.0175 nm/pixel dispersion, 0.24 s exp. time, 500/100 μm slits, $h=0?$.

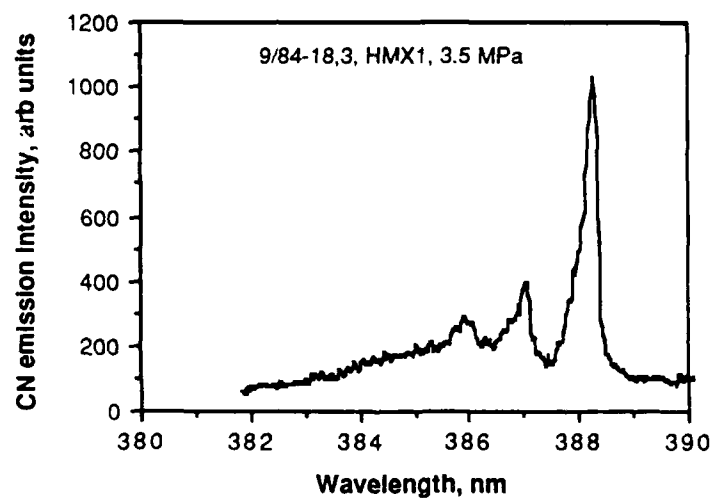


Figure 68. CN ($B^2\Sigma-X^2\Sigma$) emission. HMX1 propellant, 3.5 MPa, Reticon detector, 700 pixels, 0.0175 nm/pixel dispersion, 0.24 s exp. time, 500/100 μm slits, $h=1-2\text{mm}$.

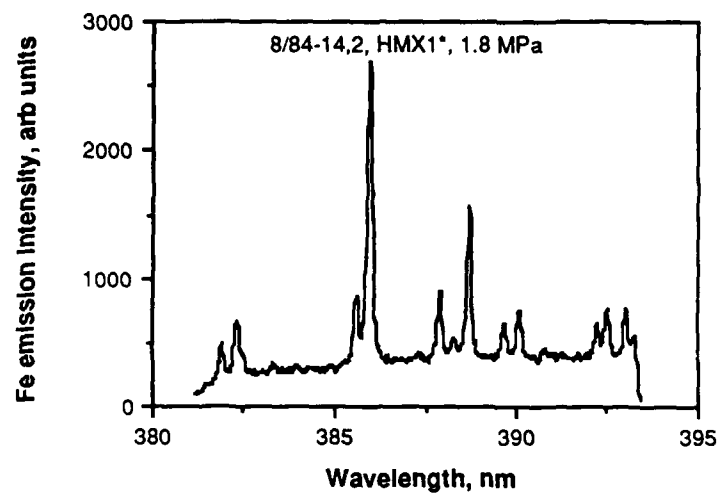


Figure 69. Fe emission. HMX1 propellant w/ 1% metal catalyst, 1.8 MPa, Reticon detector, 700 pixels, 0.0175 nm/pixel dispersion, 0.24 s exp. time, 500/100 μm slits, $h=10$ mm.

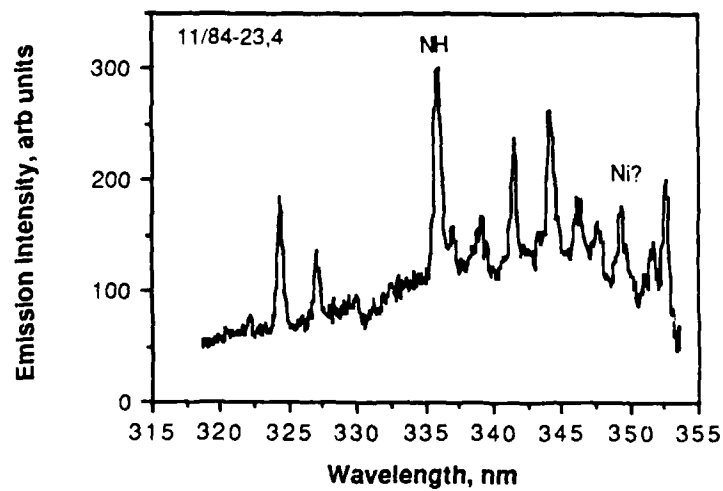


Figure 70. Emission. HMX1 propellant, 1.8 MPa, Reticon detector, 700 pixels, 0.07 nm/pixel dispersion, 0.18 s exp. time, 500/100 μm slits, $h=?$.

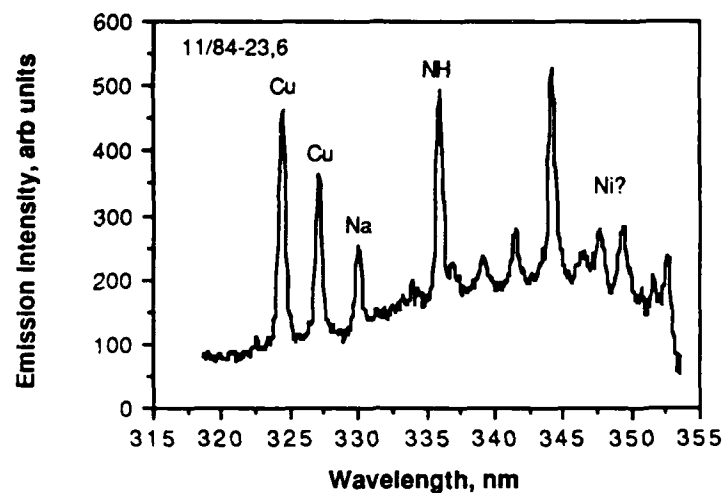


Figure 71. Emission. HMX1 propellant, 1.8 MPa, Reticon detector, 700 pixels, 0.07 nm/pixel dispersion, 0.18 s exp. time, 500/100 μ m slits, $h=?$.

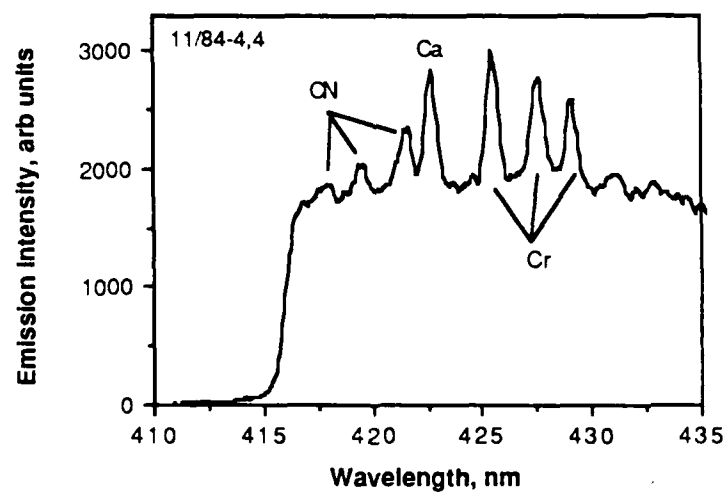


Figure 72. Emission. HMX1 propellant, 1.8 MPa, Reticon detector, 700 pixels, 0.07 nm/pixel dispersion, 0.18 s exp. time, 500/100 μ m slits, $h=0?$.

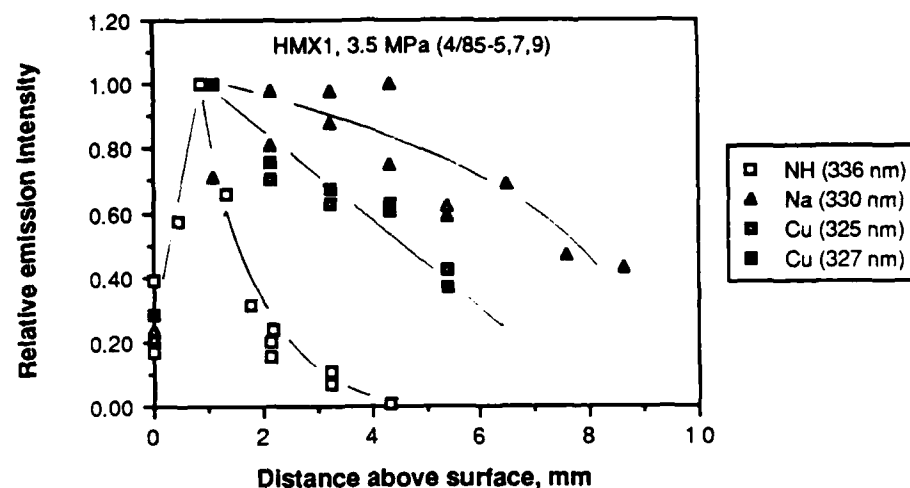


Figure 73. Relative emission intensity as a function of distance above surface. HMX1 propellant, 3.5 MPa.

4.6. EMISSION SPECTRA FROM OTHER PROPELLANTS

The other propellants listed in Table 3 were examined with emission spectroscopy, as was a pure GAP (glycidyl azide polymer)/TMETN gumstock. Emission from the "interesting" radicals (OH, CN, NH, CH, NO) was not seen in HMX2, DB1, DB2, AN1, or the GAP gumstock. The only exception was weak CN emission seen in the AN1 propellant flame. Emission was seen consistently from sodium, usually found in most propellants (Table 4), and, occasionally, other contaminant species. This illustrates one of the limitations of emission spectroscopy, relative to laser-induced fluorescence—a species may be present in high concentration (e.g., NO), but may not be observable in emission.

4.7. MODELING OF EMISSION SPECTRA-CN

It has long been recognized that the chemiluminescence (emission) spectra from flames can be analyzed to give rotational and vibrational temperatures (T_r and T_v) of the upper state of an emitting transition (Ref. 156). The temperature obtained is not a translational or gas kinetic temperature such as might be measured by a thermocouple, but is instead the equivalent temperature a molecule would show in purely thermal emission. Often, molecules are created in chemical reactions with excess vibrational and rotational energy, and so the vibrational or rotational temperature can be much higher than the gas kinetic temperature. For example, a $C_2N_2/O_2/H_2$ flame (Ref. 157) showed a CN ($B^2\Sigma^+$) T_v of 6300 K in the reaction zone, more than double the adiabatic flame temperature. Similarly, the CN ($B^2\Sigma^+$) rotational temperatures have also been measured in the reaction zones of C_2N_2 and C_2H_2/NO flames (Ref. 157-159), showing $T_r=5000-6000$ K for flames with equilibrium flame temperatures of 2000-2500 K. Thus, the vibrational and rotational temperatures in the flame reaction zone are more characteristic of the chemical environment of the flame than the actual gas kinetic temperatures.

OH chemiluminescence from solid propellant flames has previously been analyzed (Ref. 3). That work determined OH rotational temperatures in the pressure range of 0.2-7.0 MPa at several positions above the surface of AP1 propellant burning in a strand burner. Emission from other species has been seen in similar solid propellant flames, including CN, NH, CH, CaCl, CaOH, Na, K, Fe, Cr, and Al (Sections 4.3-4.6). This section describes the analysis of the CN ($B^2\Sigma^+ - X^2\Sigma^+$) chemiluminescence spectra in two such propellant flames. Modeling of NH emission spectra is discussed in Section 4.8. Studies of solid propellant chemiluminescence can yield important flame information in situations where other flame diagnostics, such as laser-induced fluorescence (LIF), are difficult or impossible. For example, in high pressure solid propellant flames the optical thickness of the flames can be so large that laser beams can not penetrate the flames, making LIF and absorption measurements impossible (Section 5). Analysis of the CN radical provides a good complement to the OH results since the CN is confined to the near surface "primary" reaction zone, whereas OH is found throughout the propellant flames (Sections 4.3, 4.4, 5.1).

In contrast to the OH emission spectrum (Ref. 3), the CN rotational lines are much closer and therefore not resolvable with the detection system, so a vibrational temperature is the only temperature that can be accurately computed. Because of the limited resolution of the detection system and the complicated nature of the CN vibrational structure, synthetic spectra were created to compare to the experimental spectra to obtain the vibrational temperature. The equations used are the standard spectroscopic equations for a $\Sigma-\Sigma$ transition (Ref. 160). Since the splitting of the rotational lines is not resolvable with the detection equipment used, the CN B-X transition is treated as a $^1\Sigma-^1\Sigma$ transition. The intensity of a given line is calculated by assuming a Boltzmann distribution: $I_{em}=CS_jA_vv''v^4\exp(-Fhc/kT_r)\exp(-Ghc/kT_v)$, where C is a constant, S_j is the rotational line strength ($=J'$ for the CN R branch and $=J'+1$ for the P branch (Ref. 160)), A_vv'' is the Franck-Condon factor (Ref. 161), and the term values for the rotation (F) and vibration (G) have been separated to allow for differing rotational and vibrational temperatures. Values for most of the spectroscopic constants were found in (Ref. 162). The vibrational constants for the $B^2\Sigma^+$ state are poorly fit by the standard equations (Ref. 162), so tabular values from (Ref. 163) were used. Once the line locations and

intensities were calculated (for $v'=0-7$ and $J'=1-95$), a synthetic spectrum was created by scanning (700 points, 0.0175 nm between points) a triangular slit function with a given bandpass over the 760 (8X95) calculated spectral lines. A bandpass of 0.125 nm (FWHM) was used, in agreement with the bandpass used in the analysis of the OH spectra (Ref. 3). The synthetic spectra were then calculated for a range of temperatures and the best match to the experimental spectra was selected. A sample model synthetic spectra is presented in Figure 74b. The best fit was determined by minimizing the differences between the experimental and theoretical spectra at the 10 indicated points. The spectra were fairly sensitive to the vibrational temperature, with the 3,3 and 4,4 bandheads disappearing at T_v 's less than approximately 3000 K.

An experimental CN spectra for the AP propellant burning at atmospheric pressure under nitrogen is shown in Figure 75a. The best match synthetic spectra for atmospheric pressure conditions represents an effective vibrational temperature of 4500 ± 500 K. The vibrational temperature in the AP propellant at atmospheric pressure resembles the spectrum in the $\text{CH}_4/\text{N}_2\text{O}$ flame, as can be seen by comparing Figures 4.7a and 75a. In contrast, the CN vibrational temperature in the HMX propellant flame is 2500 ± 500 K at pressures from 0.5 to 7 MPa (for example, Figure 75b), much closer to the adiabatic flame temperature. 0.5 MPa is the minimum nitrogen pressure under which the HMX propellant will burn, although the propellant will burn at 1 atm in air. The CN vibrational temperature obtained from burning of the HMX propellant in air is 2750 K, slightly higher than the higher pressure results but still substantially lower than the CN T_v in the AP propellant flame. The diffusion of atmospheric oxygen into the flame may well have perturbed the CN chemistry and/or the flame temperature in the propellant flame, but the large difference between the AP and HMX propellant flames still remains and is evidently not a pressure-related effect. The CN vibrational temperature in the AP propellant flame shows much more spatial dependence than the T_v in the HMX flames. The spectrum from Figure 75a is a typical spectrum near the peak of the CN emission intensity distribution. At larger distances from the surface, the spectra show a lower vibrational temperature, resembling the HMX spectra. This effect has also been seen in the $\text{CH}_4/\text{N}_2\text{O}$ flame, where the vibrational temperature decreases as the distance above the burner increases. This effect has also been noted in OH chemiluminescence in solid propellant flames (Ref. 3). As the pressure increases, the AP propellant flames show a rapid decrease in the intensity of the CN emission (and LIF) because of the transition between the premixed and diffusion flame regimes (Sections 4.3 and 5.2). It appears that this decrease in intensity is accompanied by a decrease in the CN vibrational temperature, although the spectra are weak enough at the higher pressures (0.5-0.8 MPa) that the higher vibrational bandheads may be obscured by detector noise. At atmospheric pressure, the emission from the weaker CN $\Delta v=-1$ band sequence can be observed in the AP propellant flame, although analysis of this band is difficult because of the presence of underlying CH A-X emission lines and the presence of the underlying CO+O continuum (Section 4.3). The corresponding $\Delta v=-1$ model spectrum shows a slightly higher vibrational temperature than the $\Delta v=0$ band sequence, although the fit is much less accurate because of the interfering emission. This interference is much less of a problem for the $\Delta v=0$ band sequence, although the HMX CN spectra are occasionally "contaminated" with emission from the 386.0 nm Fe line, interfering with the CN 2,2 bandhead. At pressures above about 2 MPa, the high intensity of the continuous background underlying the CN emission spectra

creates difficulties in background subtraction, but in general the $\Delta v=0$ band sequence was relatively free of interference problems.

The calculation of the synthetic spectra assumes a Boltzmann distribution of vibrational and rotational energies. Such a Boltzmann distribution would produce a linear plot of $I_{em}(\text{bandhead})/(A_v \nu''^4) (\nu^4)$ vs the vibrational energy $G'(v)$ (Ref. 156,159,160). However, when the resolution is not sufficient to resolve the contributions of other vibrational bands to the bandhead intensity, a linear relationship may not be produced. For this reason, synthetic spectra were matched to the experimental spectra, since the vibrational overlap would be the same in both. The bandhead peaks and the minima between the peaks were compared to obtain the best match. The model allows the possibility of differing T_v and T_r , although the best fit usually occurred with $T_v=T_r$. The model spectra could closely approximate the entire experimental spectra, although the 1,1 bandhead was typically slightly over-predicted and the 4,4+5,5 bandhead was slightly under-predicted in the AP propellant flames. Excluding the 1,1 peak from the fitting routine raised the best fit T_v by approximately 250 K, while excluding the 4,4+5,5 peak from the fit decreased the best fit temperature by about 250 K. In general, it appears that the CN emission from AP propellant flames is derived from a different chemical reaction from the CN emission from the HMX propellant flames because of the large difference in T_v . It is possible that the high pressure of the HMX propellant flames (the propellant will not burn at pressures below ~0.5 MPa) is causing the T_v in the CN* molecules to be reduced before radiating, although no effect of pressure was seen between 0.5 and 7 MPa and the 1 atm air experiments yielded the lower vibrational temperature seen in the high pressure experiments. Thus it seems likely that the difference in T_v is due to differences in flame chemistry.

The CN chemiluminescence in C_2N_2 and hydrocarbon/ NO_x flames is generally attributed to the exothermic reaction $C_2 + NO = CN^* + CO$ (Ref. 158,159,164,165). This reaction is believed to contribute also to the production of ground state CN (Ref. 159), although fuel nitrogen consumption generally proceeds through HCN as an intermediate (Ref. 87), with HCN the likely major precursor to ground state CN. It is interesting to speculate about why the C_2+NO reaction appears to be important in AP propellant flames and not in HMX propellant flames. Low (near-atmospheric) pressure AP propellant flames are similar to "typical" premixed flames (Ref. 113). The fuel is supplied by pyrolysis of the hydrocarbon binder (polybutadiene, $\sim C_4H_6$), while the oxidant is provided by the decomposition of the ammonium perchlorate (Ref. 122,166). One of the decomposition products of the AP is NO, while the presence of C_2 from the pyrolysis of a C_4H_6 hydrocarbon is to be expected. Thus, the presence of CN* is not surprising. In the case of HMX decomposition, the gas phase species are thought to arise from the decomposition of the HMX into some combination of HCN, CH_2O , NO_2 , and N_2O (Ref. 29,28). Studies of these type of flames are underway, with CH_2O/NO_2 (Ref. 82) and $C_2N_2/H_2/NO_2$ (Ref. 88) flame studies recently begun. The flame chemistry of HCN and NO are of much current interest from a pollution perspective (Ref. 87,89). CH_2O/NO_2 flames don't produce CN emission at all (Ref. 145), although the polyester binder in the HMX propellant may be a source of hydrocarbons which react with NO_2 . Hydrocarbon/ NO_2 flames do show vibrationally-excited CN chemiluminescence (Ref. 104,145), as do hydrocarbon/ N_2O flames (Figure 4.7a). $C_2N_2/H_2/O_2$ (and presumably $C_2N_2/H_2/NO_2$) flames also show vibrationally-excited CN chemiluminescence, although the

dissociation energy of C_2N_2 is so high that significant pyrolysis of C_2N_2 occurs before reaction (Ref. 167), so a mixture of $C_2N_2/H_2/NO_2$ may have a significantly different reaction mechanism than the stoichiometrically equivalent flame of HCN/NO_2 . Several possibilities follow from these observations : (1) the NO_2 , N_2O , and NO don't encounter hydrocarbons in the HMX propellant flame, and either (2) flames with HCN as a fuel don't produce vibrationally-excited CN chemiluminescence, or (3) HCN is not present in the HMX propellant flame and the $T_v=2500$ K CN emission comes from some fuel other than HCN or CH_2O . The knowledge of the reaction mechanisms in HMX propellant flames is insufficient to resolve this issue at present (Ref. 29), thus the rationale for model flame studies (Ref. 82,88) and propellant flame studies (Ref. 1-9).

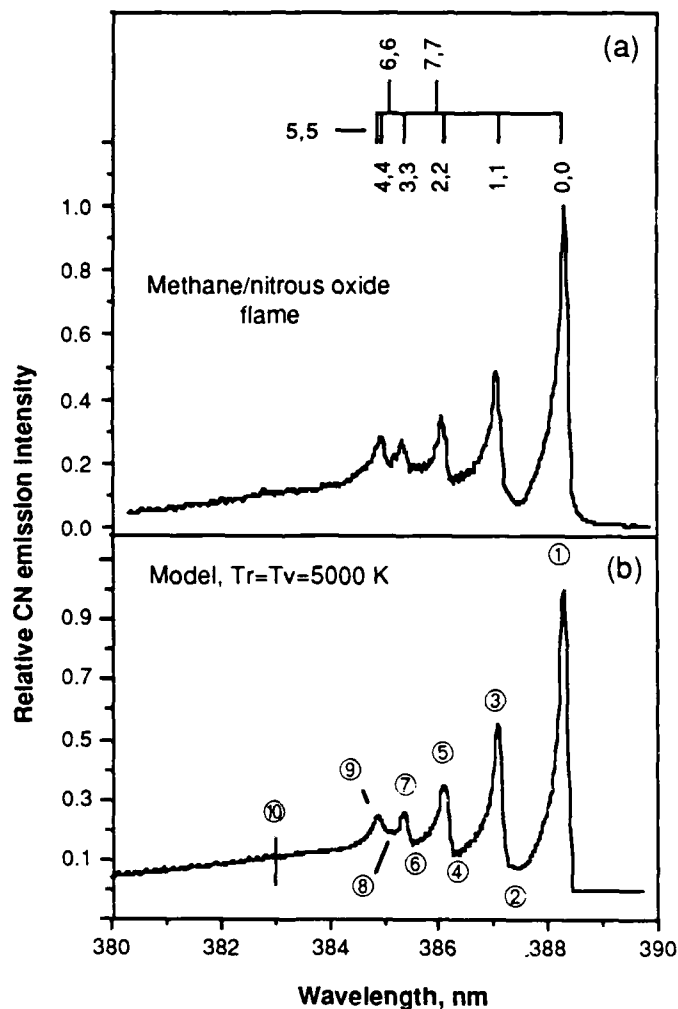


Figure 74. Sample CN ($B^2\Sigma-X^2\Sigma$) emission spectra. (a) CH_4/N_2O flame, 1 atm. (b): Model spectrum with $T_r=T_v=5000$ K.

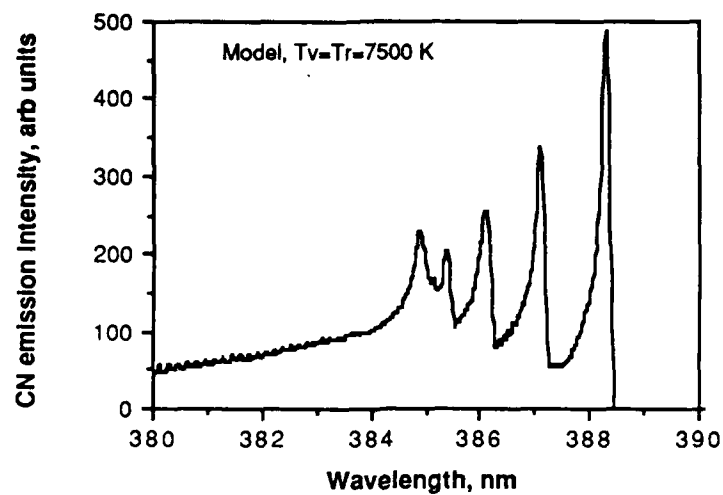


Figure 75. Model CN ($B^2\Sigma-X^2\Sigma$) emission spectrum. $T_r=T_v=7500$ K (0,0 band sequence).

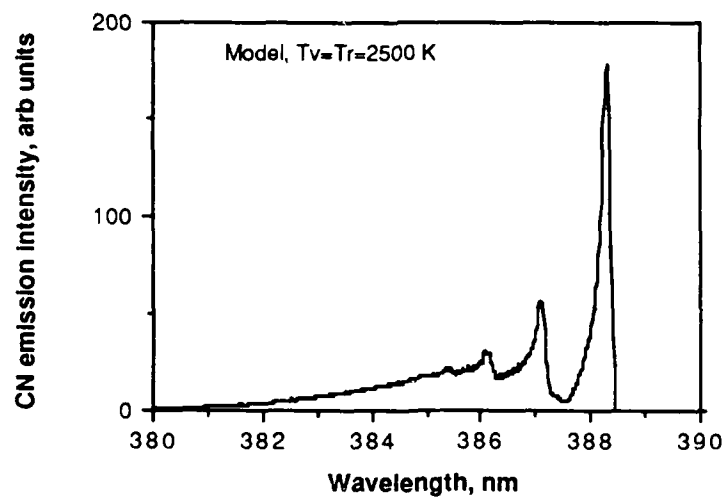


Figure 76. Model CN ($B^2\Sigma-X^2\Sigma$) emission spectrum. $T_r=T_v=2500$ K (0,0 band sequence).

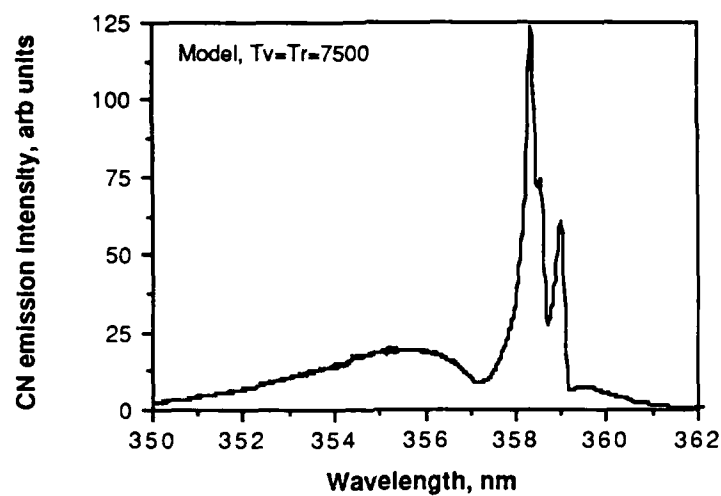


Figure 77. Model CN ($B^2\Sigma-X^2\Sigma$) emission spectrum. $T_r=T_v=7500$ K (1,0 band sequence).

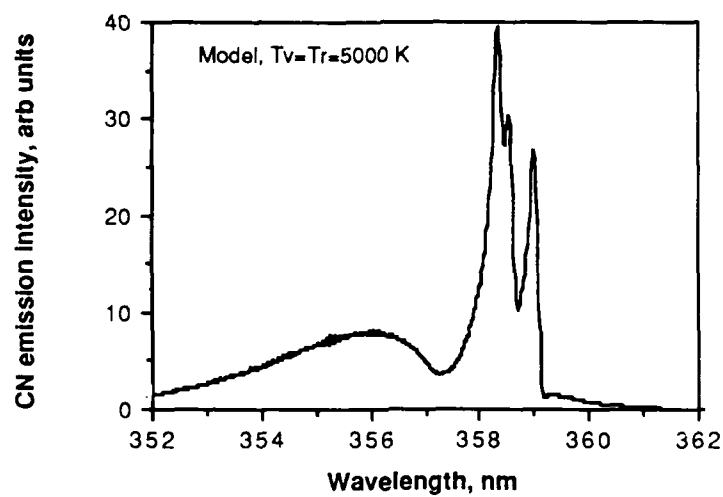


Figure 78. Model CN ($B^2\Sigma-X^2\Sigma$) emission spectrum. $T_r=T_v=5000$ K (1,0 band sequence).

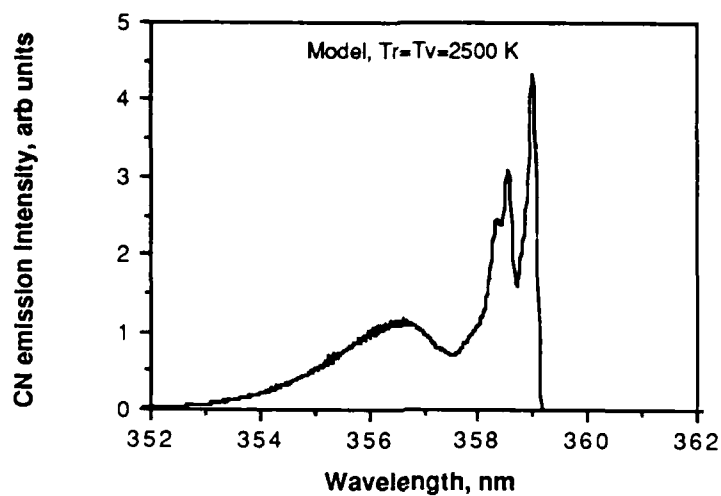


Figure 79. Model CN ($B^2\Sigma-X^2\Sigma$) emission spectrum. $T_r=T_v=2500$ K (1,0 band sequence).

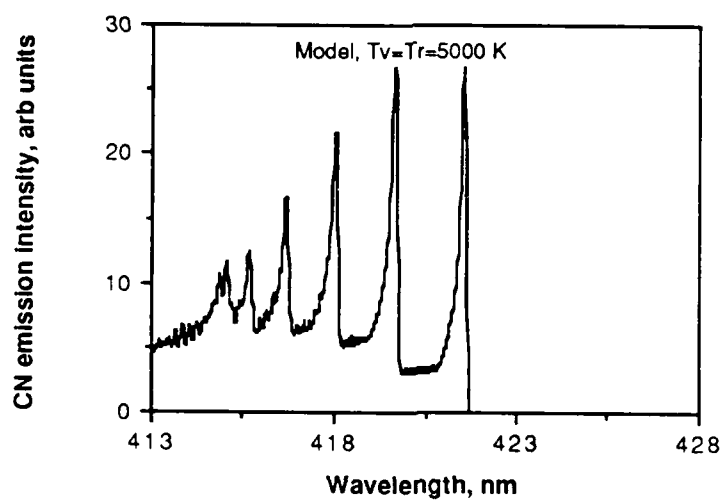


Figure 80. Model CN ($B^2\Sigma-X^2\Sigma$) emission spectrum. $T_r=T_v=5000$ K (0,1 band sequence).

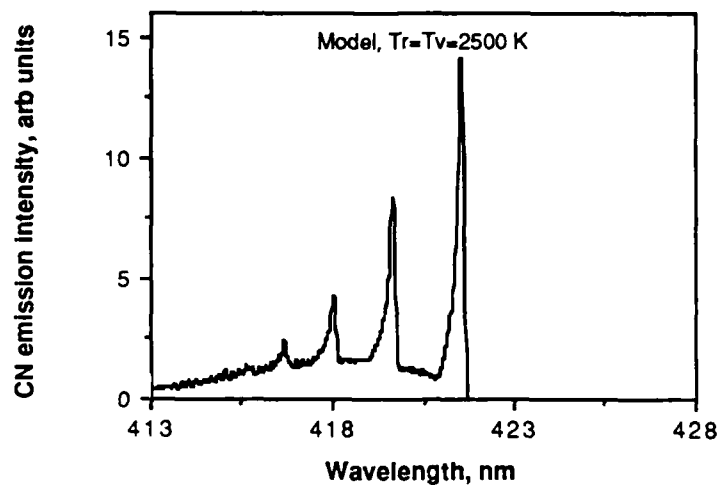


Figure 81. Model CN ($B^2\Sigma-X^2\Sigma$) emission spectrum. $T_r=T_v=2500$ K (0,1 band sequence).

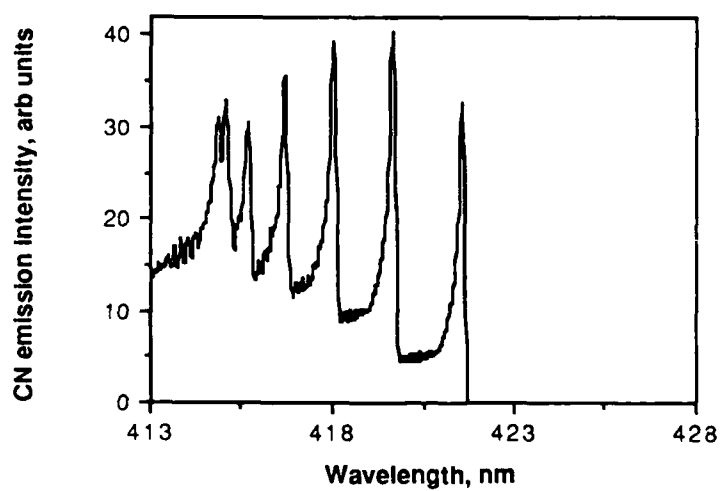


Figure 82. Model CN ($B^2\Sigma-X^2\Sigma$) emission spectrum. $T_r=T_v=7500$ K (0,1 band sequence).

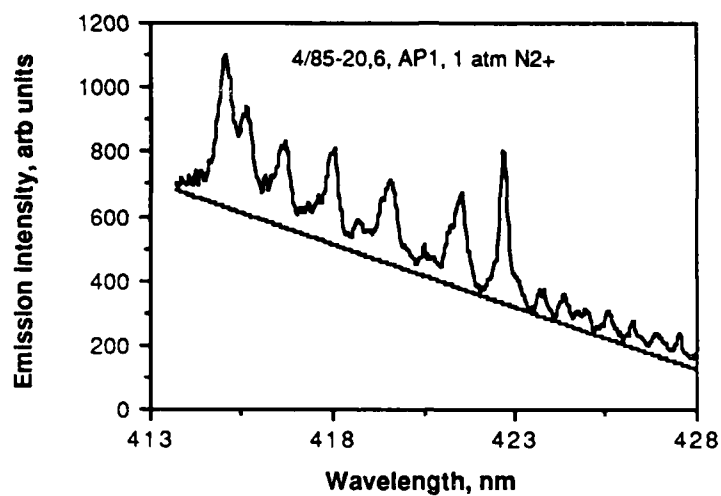


Figure 83. CN ($B^2\Sigma-X^2\Sigma$) emission spectrum in AP1 propellant flame. 1 atm N_2+ , showing underlying continuum and estimated background correction (line).

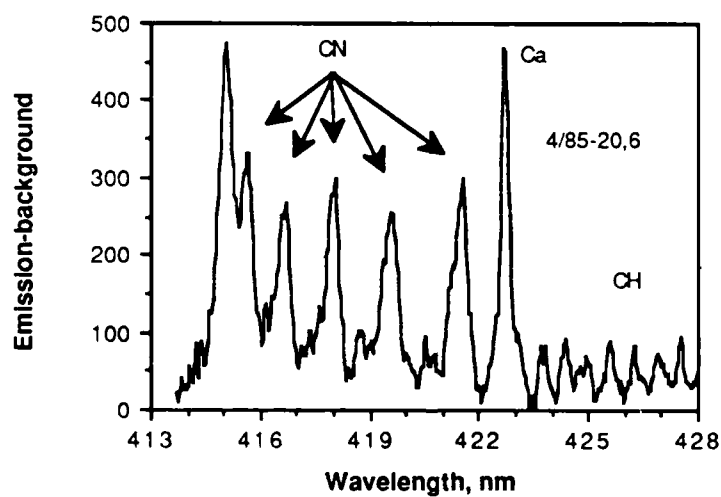


Figure 84. CN emission spectra in AP1 propellant flame. 1 atm N_2+ , after background subtraction.

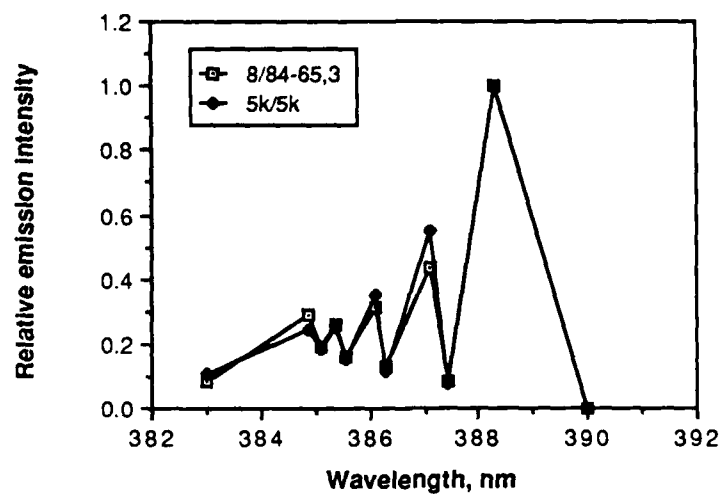


Figure 85. Comparison of model and experimental CN peak heights.

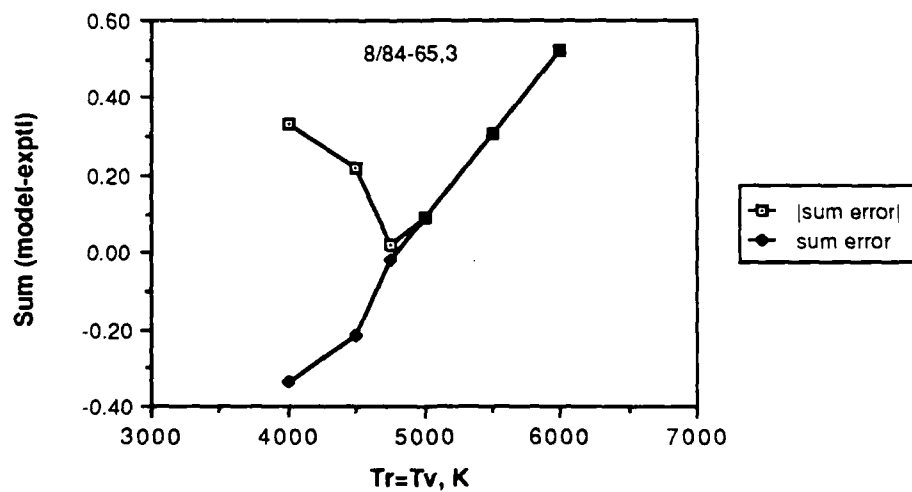


Figure 86. Comparison of model and experimental CN peak heights.

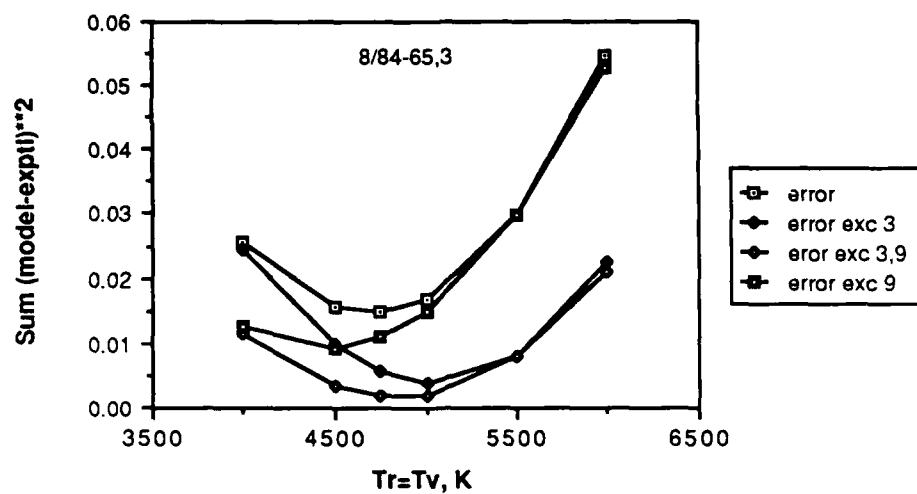


Figure 87. Comparison of model and experimental CN peak heights.

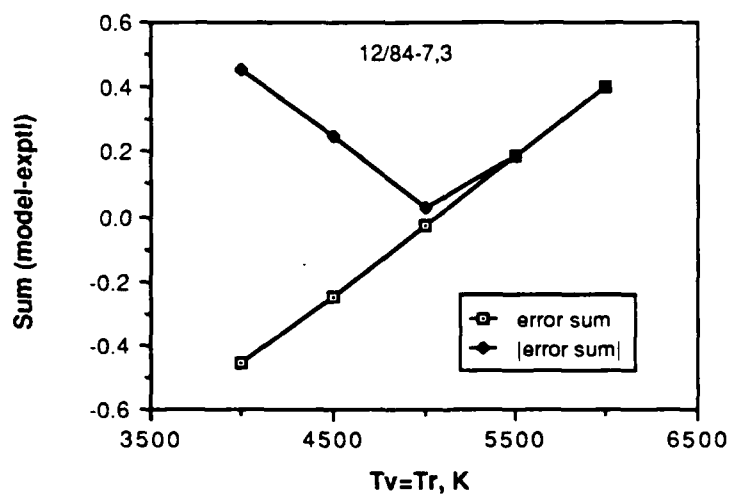


Figure 88. Comparison of model and experimental CN peak heights.

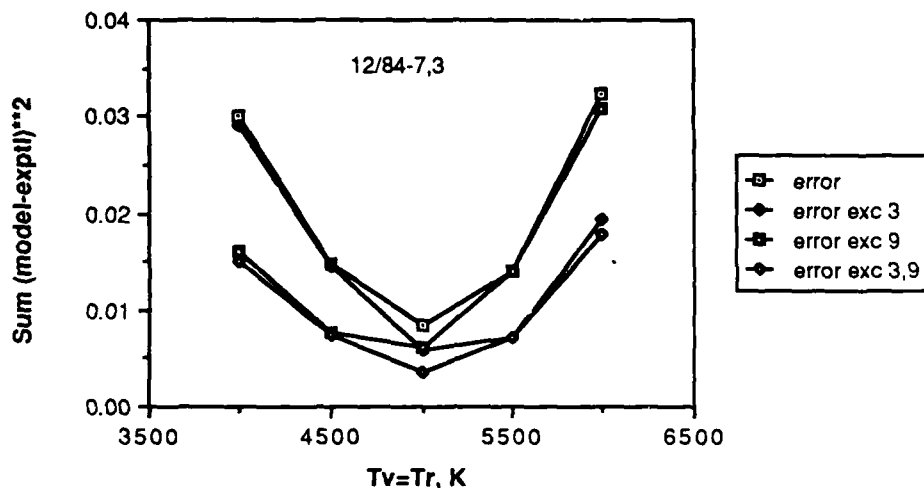


Figure 89. Comparison of model and experimental CN peak heights.

4.8. MODELING OF EMISSION SPECTRA-NH

Synthetic spectra for NH were constructed for the same reasons as the CN spectra. The equations and program are listed in Appendix 2. The most important difference between the two molecules is that NH has a more open rotational structure, thus splitting of the rotational lines must be taken into account. The standard equations used (Ref. 168-172) are listed in Appendix 2. For whatever reason (programming error, poor spectroscopic constants), the equations fit the NH line data (Ref. 169-171) with only fair precision. This is illustrated in Figures 90 to 96. To obtain a temperature from the ratio of the 0,0 and 1,1 Q bandheads (often the only visible NH features, for example Figures 4.1.5, 4.3.5, 4.5.3), the synthetic spectra must match the Q branches at low J', which the current program does not. This modeling work is incomplete, but preliminary estimates of the NH vibrational temperature were made by inputting the known NH 0,0 and 1,1 lines from (Ref. 169-171) as shown in the program listing in Appendix 2. When this was done (with the 2,2 lines calculated from the equations), the synthetic spectra shown in Figure 96 was obtained. This spectrum matches the experimental spectrum (Figure 4.1.5) fairly well and allows estimates of vibrational temperature to be made by calculating the ratio of the 0,0 and 1,1 bandheads. The calculated relationship between the bandhead ratio and the vibrational temperature is shown in Figure 97: the result is $T_v (=T_r \text{ in the model}), K = 14450(0,0:1,1 \text{ Q branch bandhead ratio})^{-0.8431}$. A preliminary analysis of the some experimental data yields the results shown in Table 14. One interesting fact emerged in the preliminary analysis-the NH T_v was quite variable in the propellant flames, as shown in Figure 98. Thus the average T_v in Table 14 is less relevant to the flame chemistry than the complete profile. This will be more thoroughly analyzed when the

NH spectral modeling is completed. The similarity between $T_{v,max}$ in the AP1 propellant flame and the adiabatic flame temperature (Table 6) is interesting and should be investigated further. In the HMX1 propellant flames, the NH intensity is less and the background is higher (see Figure 4.5.3), so the uncertainty in the bandhead ratio is greater. The background subtracted from the peaks was the minimum between the 0,0 and 1,1 peaks. The error may not appear to be larger, but the ratio does not appear to be a function of distance above the surface. Thus the indicated error is not a systematic error, but is rather a large random error reflecting the lower signal-to-noise ratio in the HMX flames. It appears, however, that the T_v in the HMX1 propellant flames is significantly higher than the adiabatic flame temperature. These results are preliminary since they are based on a relatively small number of data points.

The model can also be used to predict T_r by looking for an R branch bandhead at 328 nm, seen only at high T_r (Ref. 173). The model is somewhat inaccurate in this area since the tabulated line data only extends to $J=30$, which is in the bandhead region (see Figure 90). Thus, the bandhead may be larger than the model predicts since lines with $J>30$ would add to the bandhead intensity. Nevertheless, the model does show a bandhead at higher T_r , as shown in Figures 100 and 101. Such a bandhead has not been observed in either the propellant flames or the CH_4/N_2O calibration flame. For example, the 328 nm region of the CH_4/N_2O flame spectrum is shown in Figure 102. This indicates that $T_r=T_v$ is probably a fairly good approximation. Model predictions of the NH P branch are presented in Figures 103 to 108. These are compared to the NH excitation distribution in the NH LIF experiments in Section 5.3.

Table 14. Preliminary NH T_v results

Flame	Pressure	Q branch bandhead ratio	# of spectra analyzed	$T_v(=T_r)$, K
CH_4/N_2O	1 atm air	6.61 ± 0.48	6	2940
AP1	1 atm N_2+	7.26 ± 0.81	5	2720
HMX1	1.8 MPa	4.64 ± 0.92	5	3960
HMX1	3.5 MPa	4.59 ± 0.42	3	4000

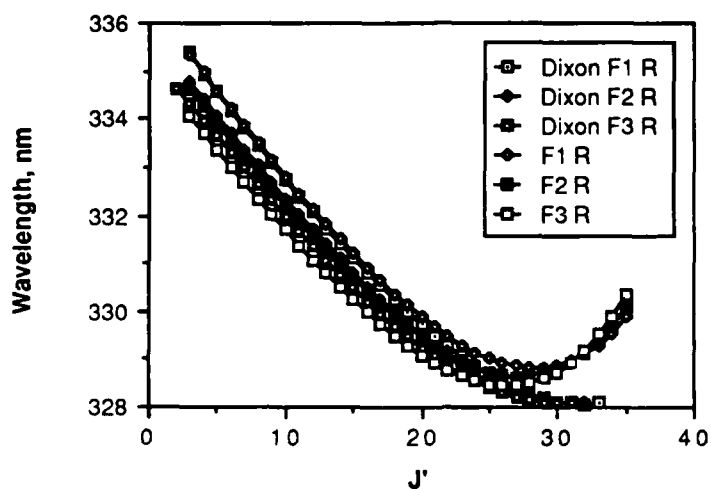


Figure 90. Comparison of theoretical (F1 R, F2 R, F3 R) NH 0,0 R branch lines with literature (Dixon) values.

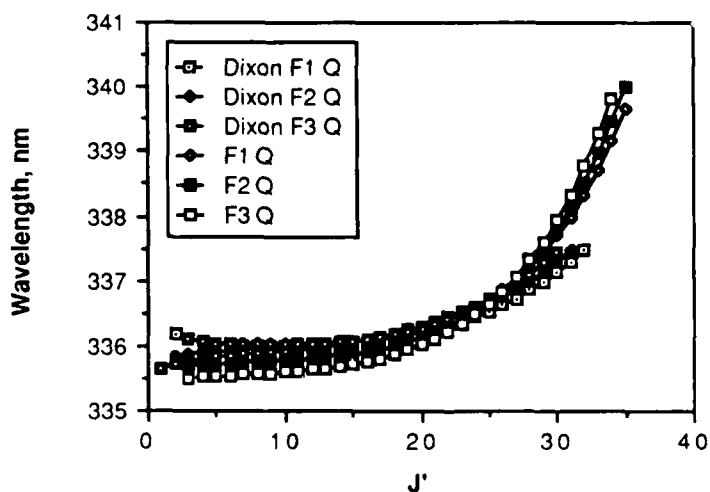


Figure 91. Comparison of theoretical (F1 Q, F2 Q, F3 Q) NH 0,0 Q branch lines with literature (Dixon) values.

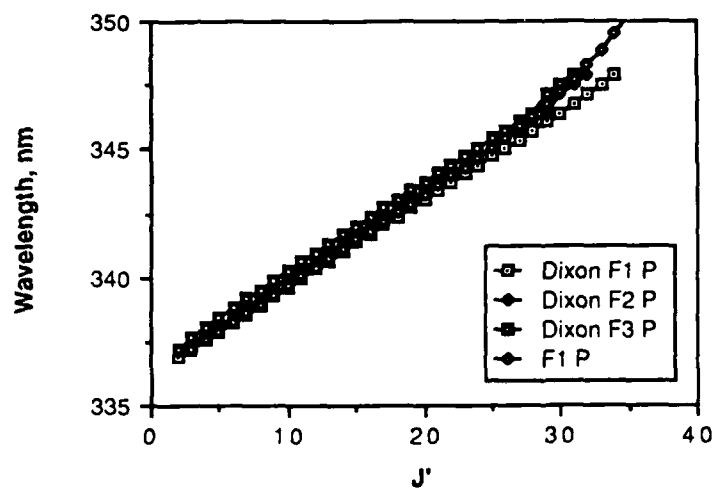


Figure 92. Comparison of theoretical (F1 P) NH 0,0 P branch lines with literature (Dixon) values.

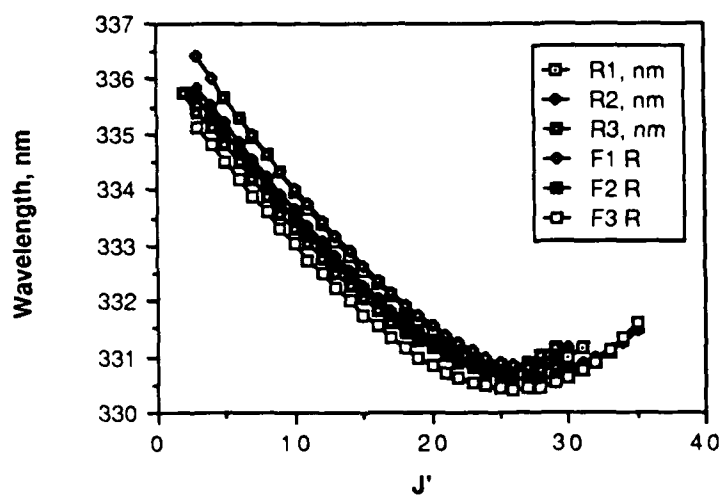


Figure 93. Comparison of theoretical (F1 R, F2 R, F3 R) NH 1,1 R branch lines with literature (Funke) values.

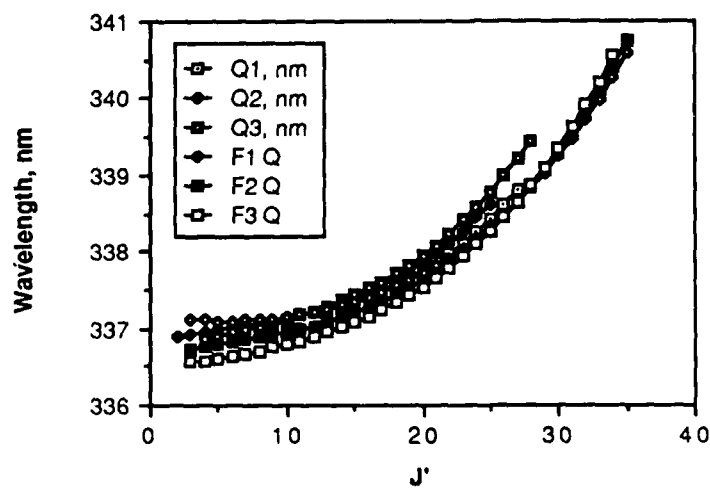


Figure 94. Comparison of theoretical (F1 O, F2 O, F3 O) NH 1,1 O branch lines with literature (Funke) values.

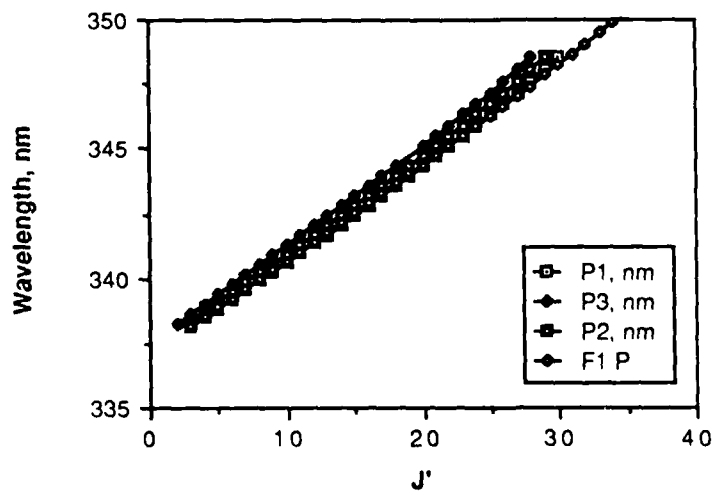


Figure 96. Comparison of theoretical (F1 P) NH 1,1 P branch lines with literature (Funke) values.

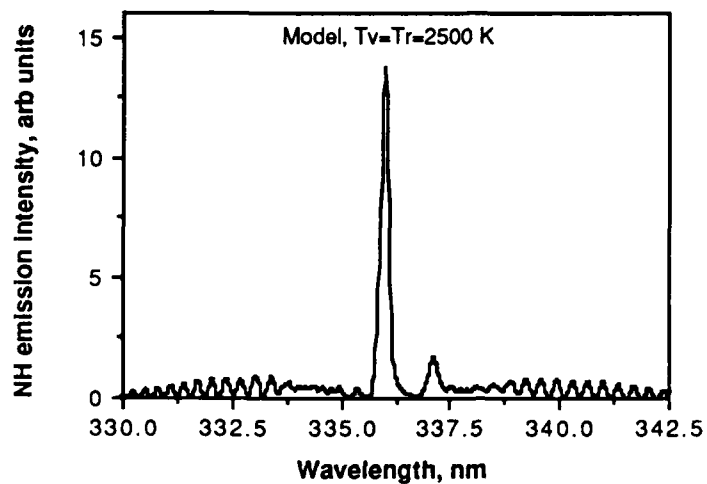


Figure 96. Model NH ($A^3\Pi-X^3\Sigma$) emission spectrum ($T_v=T_r=2500$ K).

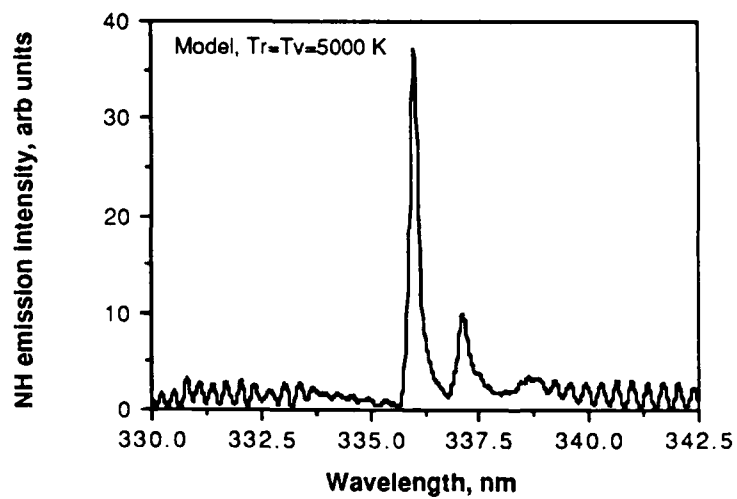


Figure 97. Model NH ($A^3\Pi-X^3\Sigma$) emission spectrum ($T_v=T_r=5000$ K).

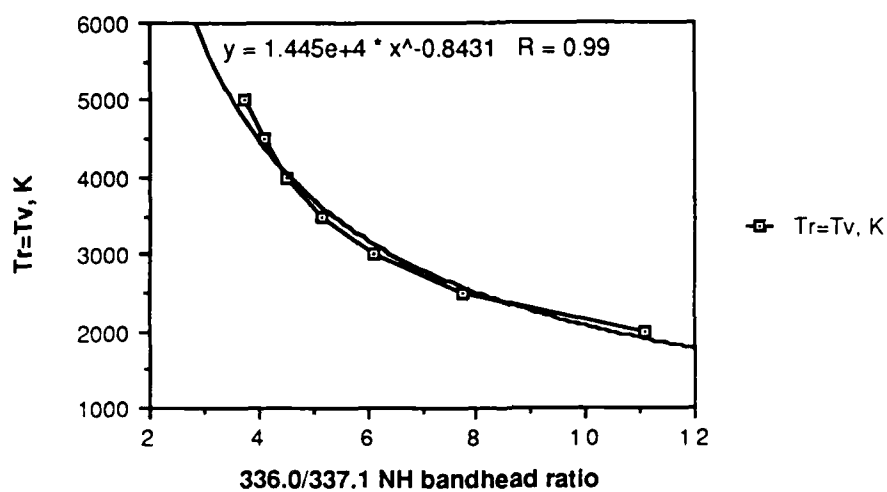


Figure 98. Fitting of model bandhead ratio data.

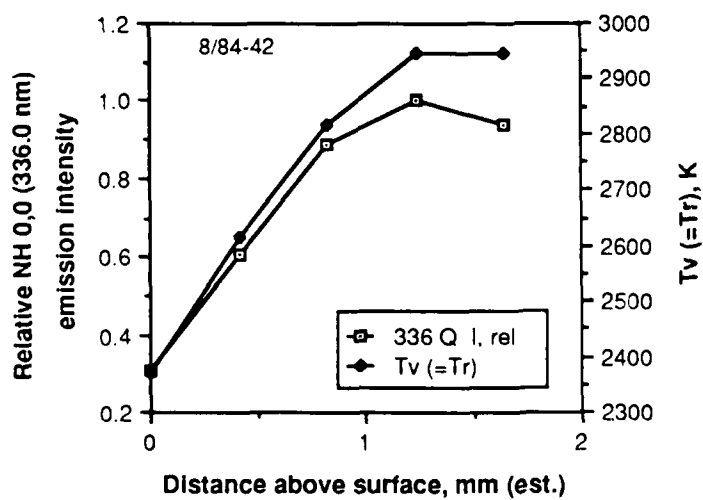


Figure 99. Variation of NH T_v in API propellant flame with distance above surface.

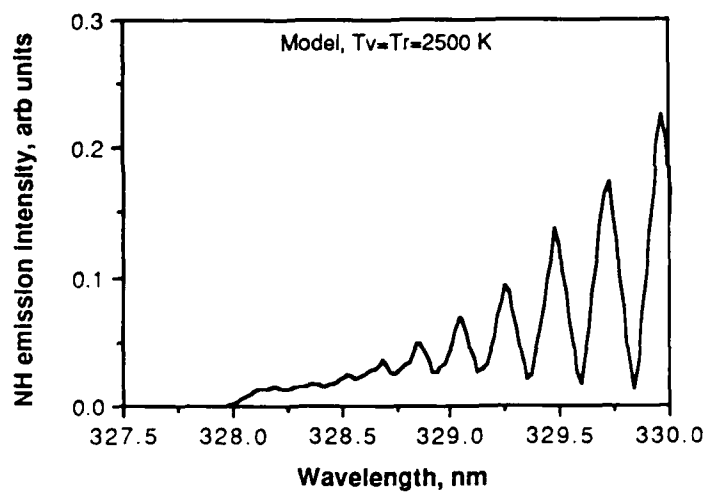


Figure 100. Model NH ($A^3\Pi-X^3\Sigma$) emission spectrum ($T_v=T_r=2500$ K).

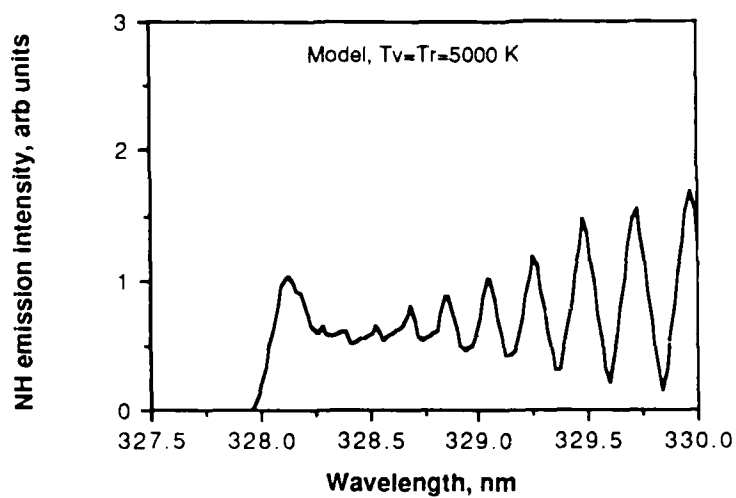


Figure 101. Model NH ($A^3\Pi-X^3\Sigma$) emission spectrum ($T_v=T_r=5000$ K).

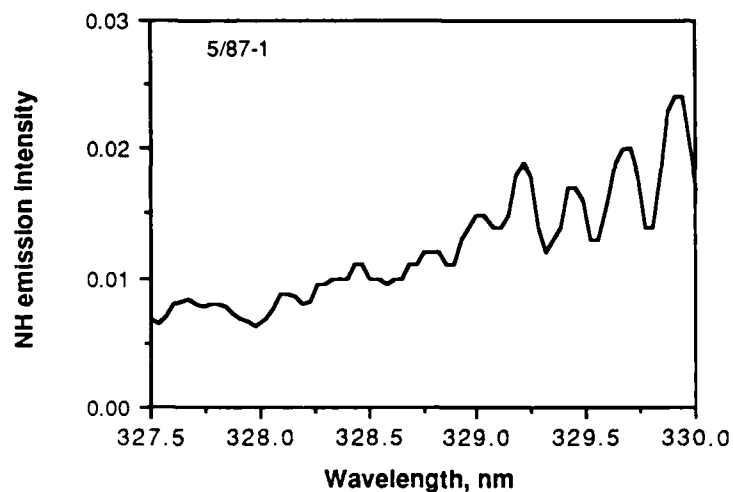


Figure 102. NH ($A^3\Pi-X^3\Sigma$) emission spectrum. CH_4/N_2O flame, same as Fig. 30 but replotted to emphasize 328 nm region.

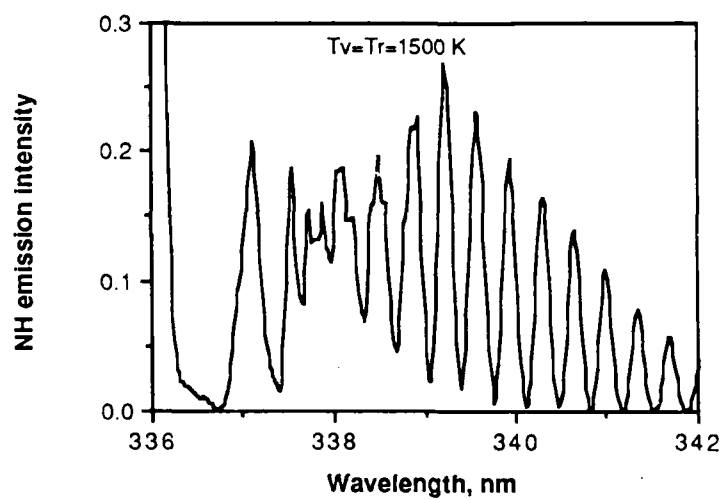


Figure 103. Model NH ($A^3\Pi-X^3\Sigma$) emission spectrum. P branch, with $T_v=T_r=1500$ K.

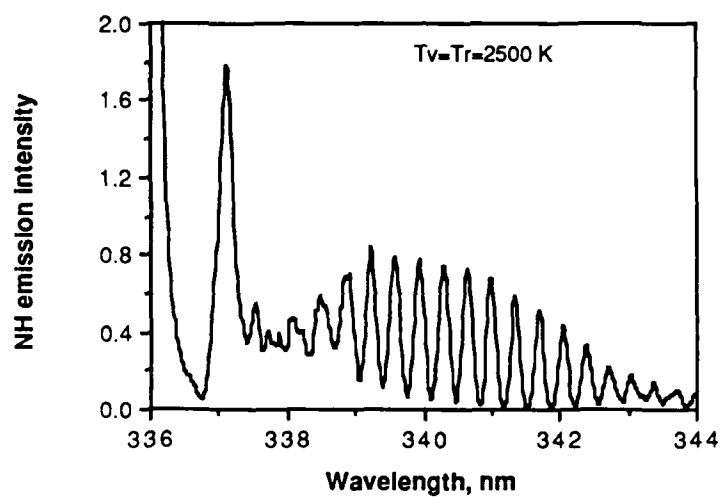


Figure 104. Model NH ($A^3\Pi-X^3\Sigma$) emission spectrum . P branch, with $T_v=T_r=2500$ K.

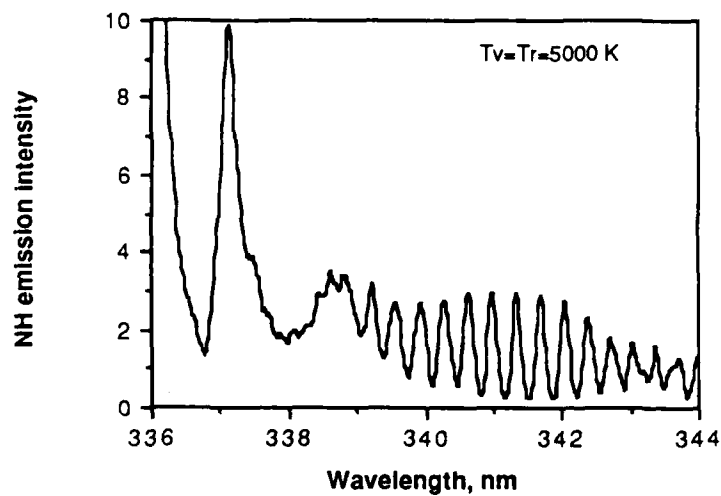


Figure 105. Model NH ($A^3\Pi-X^3\Sigma$) emission spectrum . P branch, with $T_v=T_r=5000$ K.

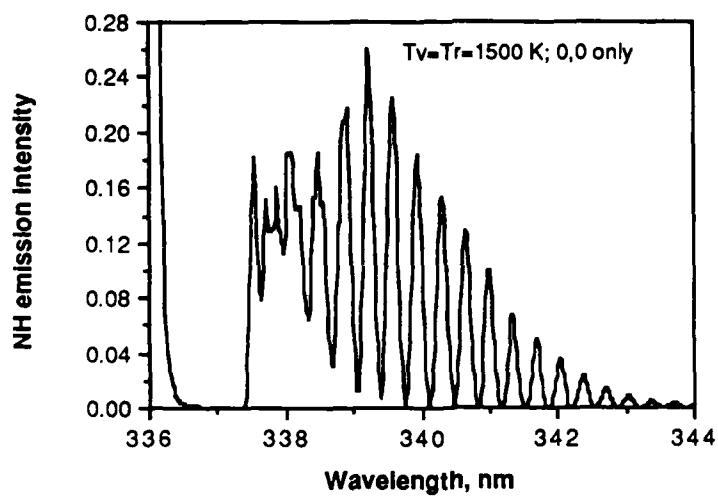


Figure 106. Model NH ($A^3\Pi-X^3\Sigma$) emission spectrum. 0,0 P branch, with $T_v=T_r=1500$ K.

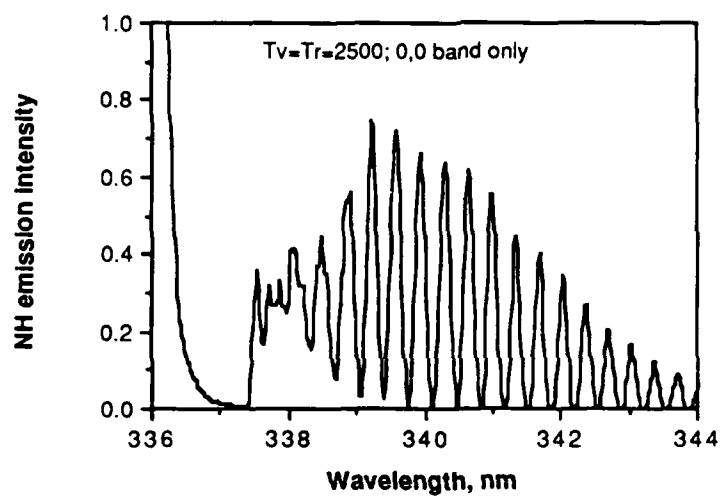


Figure 107. Model NH ($A^3\Pi-X^3\Sigma$) emission spectrum. 0,0 P branch, with $T_v=T_r=2500$ K.

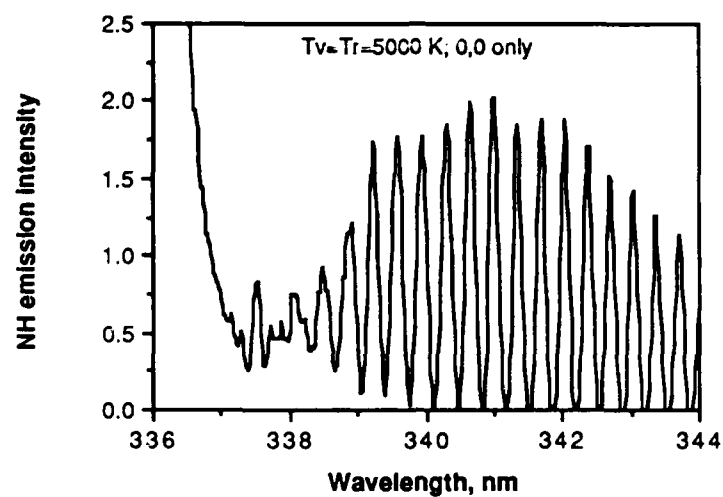


Figure 108. Model NH ($A^3\Pi-X^3\Sigma$) emission spectrum. 0,0 P branch, with $T_v=T_r=5000$ K.

5.0. LASER-INDUCED FLUORESCENCE EXPERIMENTS

Although emission spectroscopy has the attractive features of relatively low cost and simplicity, the drawbacks are important. Emission occurs from a chemically-excited upper state of a given molecule, so the emission is characteristic of that upper state of the molecule, not the much more prevalent (and thus kinetically important) ground state of the molecule. The spatial resolution of emission measurements may not be sufficient to resolve processes of interest, especially since the emission is collected as a line of sight measurement. The temporal resolution may also be insufficient. For all these reasons, modern laser-based combustion diagnostics are usually used when spatially and temporally resolved species concentration and temperature measurements are required. The temporal resolution for single-pulse experiments is on the order of the laser pulse width (typically tens of ns), while the spatial resolution is determined by the imaging of focussed laser beams (100 μm or less is possible). Species can also be probed that do not emit under flame conditions.

5.1. OH LIF EXPERIMENTS (PART 1)

The initial LIF measurements in solid propellant flames were performed with OH LIF. OH is not the most interesting species from a chemical standpoint in propellant flames since OH is found throughout the flame, but OH has several advantages. OH is the radical present in the highest concentration in most flames, with the possible exception of NO, and therefore will have the largest signal-to-noise ratio (all other factors being equal). OH is the most common radical studied with LIF, so the spectroscopy is well-known. The region of the spectrum where OH is found is conveniently accessible to frequency-doubled Nd:YAG-pumped dye lasers, which is what was available at the beginning of this part of the project. Thus, OH had many advantages. The information desired from this part of the project included the answers to the following questions:

- (1) Can laser-induced fluorescence measurements be made in the hostile environment of a solid propellant flame?
- (2) At what pressure do quenching and other pressure-dependent processes make LIF measurements in solid propellant flames impossible?
- (3) Can these pressure-dependent phenomena (quenching, self-absorption, etc.) be characterized in propellant flames?

For these initial experiments, the OH transition pumped was chosen by determining the strongest fluorescence (as seen on the Reticon) while tuning the laser from 306 to 309 nm (see Figs 109 to 122). In this way the pump wavelength was chosen as 306.42 nm, pumping the $R_1 7$ and $R_1 11$ transitions. An illustration of the resulting fluorescence in the methane/oxygen flame is shown in Fig. 123. For comparison purposes, an OH emission spectrum is shown in Fig. 4.1.10. As expected from pumping the $R_1 7$ and $R_1 11$ transitions, the $Q_1 8$, $Q_1 12$, $P_1 9$, and $P_1 13$ lines are accentuated in the fluorescence spectrum.

If the OH fluorescence is generated in an AP propellant flame at, for example, 2 mm above the surface at 0.8 MPa (100 psig), the spectrum shown in Fig. 124 is obtained. As can be seen, the scattering at the laser wavelength is greatly accentuated (2-3 orders of magnitude) over the value found in the methane/oxygen flame. As the surface of the strand is approached

the scattering increases still more, making data interpretation difficult. This scattering can be mostly eliminated by closing the intermediate slit of the filter stage of the Triplemate spectrometer. This yields the fluorescence spectrum shown in Fig. 125. This was successful in the AP1 propellant flame up to pressures of 2.2 MPa (Fig. 126). In the discussion that follows, the intensity of the fluorescence is usually characterized by the height of the peak at 310.6 nm when the Reticon was used. Using the 1/2 meter monochromator and photomultiplier tube to analyze the fluorescence from the propellant flame was more difficult because the scattered light rejection of the single monochromator was, understandably, much poorer than that of the Triplemate. This problem was alleviated somewhat by setting the spectrometer on the P_{13} peak (315.1 nm), as far removed as possible from the laser wavelength (306.42 nm). This arrangement generally minimized the scattered light at the laser wavelength reaching the detector, although measurements near the surface caused sufficient scattering to swamp the fluorescence signal. Gating the the detector on after the pulse passed through the collection volume reduced the amount of scattered laser light being detected, but also reduced the fluorescence signal significantly. A typical trace of the intensity of the 315.1 nm line as a function of time during the propellant burn is shown in Fig. 127. Fig. 127 shows a 10 pulse average of the fluorescence. Single-pulse measurements showed more scatter, demonstrating the necessity for a pulse-to-pulse laser output energy measurement to correct for pulse energy variations.

The OH fluorescence intensity is, not surprisingly, quite dependent on the type of solid propellant burned. The stoichiometry in a solid propellant flame can vary dramatically when an oxygen-rich ingredient like AP is replace by a more balanced ingredient like HMX or a fuel-rich ingredient like a typical binder. This is illustrated in Table 15, which shows the variation in calculated flame temperature and calculated equilibrium OH mole fraction between several propellants with varying compositions. In some early experiments, it was found that the fluorescent intensity in the flame tends to follow the trends in equilibrium OH concentration, a reasonable result given the relationship between OH concentration and OH fluorescence. The intensity of OH emission from these flames also follows this trend. The rest of this section describes experiments with AP1 propellant. One variable not held constant in these early experiments was the attenuation of the laser beam in the propellant flame due to scattering from the particulate matter in the flame (and thus reduction of the laser intensity reaching the collection volume). This is an important phenomenon since the scattering from propellant flames varies dramatically depending on the propellant composition and the pressure. For example, measurements of fluorescent intensity as a function of pressure for the AP1 propellant showed the attenuation of the laser beam was a fairly linear function of pressure as is shown in Fig. 128. This large attenuation at the higher pressures indicates that it would be difficult to achieve saturation of the fluorescence at these pressures. Actually, the data we have to date indicates that saturation cannot be achieved, even at 0.8 MPa. This data is shown in Fig. 129, where data from both detector systems is included. The best fit (linear regression) line has a y-intercept of 0.02. Thus the overall behavior is reasonable, although the reproducibility of the data leaves a lot to be desired. Saturated fluorescence is preferred for OH concentration measurements (Ref. 16,205). Whether the data scatter is a characteristic of the AP propellant flame or is due to inadequately optimized experimental technique remains to be determined. When fluorescence data taken at various pressures is scaled to the same laser intensity in the flame (with the aid of Fig. 129), the initially scattered data falls on a line. This

is illustrated in Fig. 130. This trend comes from a fairly small number of experiments (13) and thus must be considered preliminary. It is interesting nonetheless. Fluorescence has been detected at 3.5 MPa (500 psig), although the AP propellants burn erratically in the combustor at pressures much above 2 MPa (Ref. 1). Another important aspect of the propellant flame is the vertical distribution of fluorescence. In general, OH is not restricted to the primary reaction zone of a flame, but rather is found throughout the flame. This distribution was seen in OH emission in propellant flames (Ref. 2). Confirmation of this distribution was found with OH fluorescence, as is shown in Fig. 131. OH emission data from a similar pressure is included for comparison. This distribution should not be influenced by variations in scattering in the flame since previous measurements have shown the flame scattering to be fairly constant with height above the surface (except very near the surface) (Ref. 1). At the higher pressure of these experiments, self-absorption should be more important an effect than at the lower pressures (atmospheric and below) typically encountered in flame diagnostic experiments. To determine the influence of self-absorption, the laser focus was translated from one edge of the flame to the other and the fluorescence monitored. As shown in Fig. 132, the profile is symmetrical from one edge of the flame to the other, indicating little effect of self-absorption. This is rather surprising and awaits further analysis.

These results have several implications. Perhaps the most important is the large scattering and attenuation of the laser beam that occurs in the propellant flame. Thus the environment is much closer to a highly sooting flame than a typical laboratory flame. For this reason, any flame diagnostics that are to be applied to propellant flames must have some method of discriminating between the desired signal (Raman, LIF, etc.) and the scattered radiation. For example, two-dimensional imaging of fluorescence onto a Vidicon-type detector will be impossible without some sort of high quality filter (a spectrometer, perhaps?) to discriminate between the desired signal and spurious scattering. Another implication is that careful attention must be paid to the attenuation of the laser during an experiment, since saturation is difficult and the signal is proportional to the actual laser intensity in the collection volume.

Table 15. Influence of propellant composition on OH LIF intensity

Propellant	AP1	A	B	C	HMX1
Composition, wt %					
AP	87	80	67	0	0
HMX	0	0	0	62	73
binder	non-energetic	non-energetic	energetic	energetic	energetic
Adiabatic flame T, K	2900	2200	2900	2400	2600
Mole fraction OH at T	2×10^{-2}	8×10^{-5}	2×10^{-2}	4×10^{-4}	1×10^{-3}
OH LIF intensity (rel)*	1.0	0.1	0.7	0.15	0.08
OH emis. intens. (rel)*	1.0	0.002	0.98	0.02	0.004

*at 0.8 MPa and 1.5 mm above surface

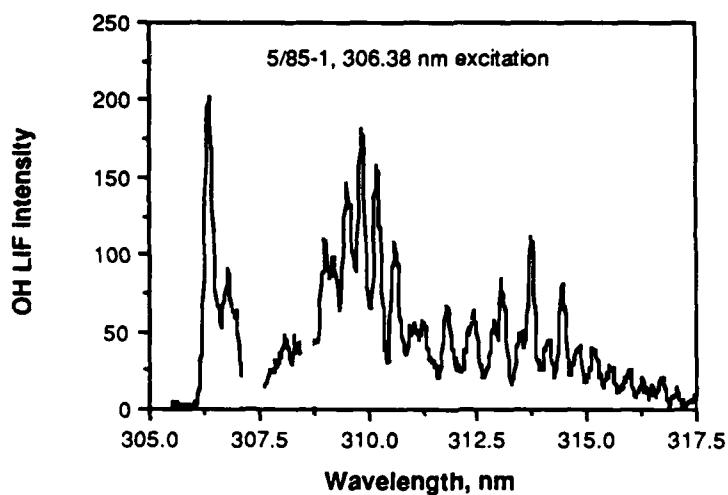


Figure 109. OH ($A^2\Sigma-X^2\Pi$) LIF, CH_4/O_2 flame, 306.38 nm excitation. 3-4 mJ/pulse in flame, Reticon detector, 700 pixels, 0.0175 nm pixel dispersion, 500/100 μ m slits, 12 pulse signal accumulation, 5 μ s gate width on Reticon pulser.

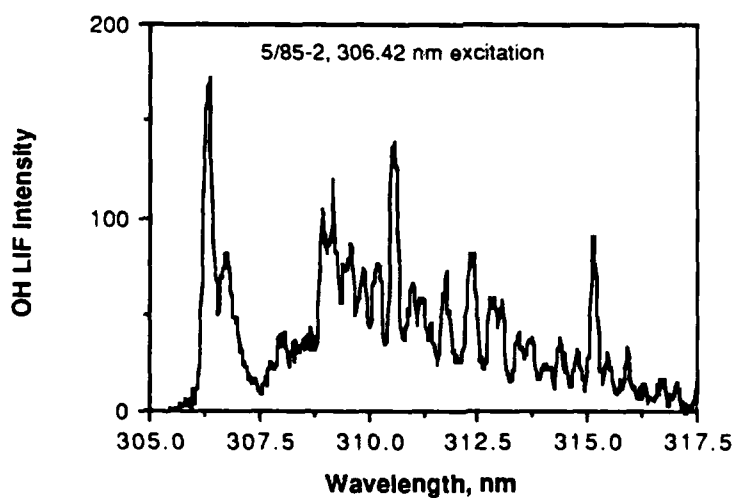


Figure 110. Same as Figure 109, 306.42 nm excitation.

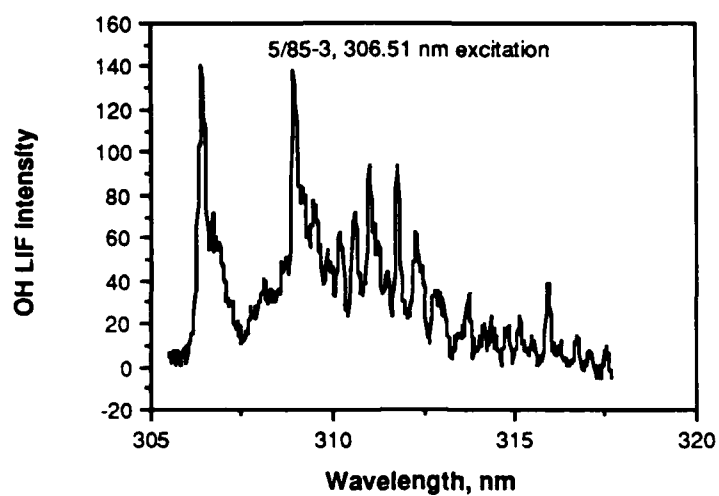


Figure 111. Same as Figure 109, 306.51 nm excitation.

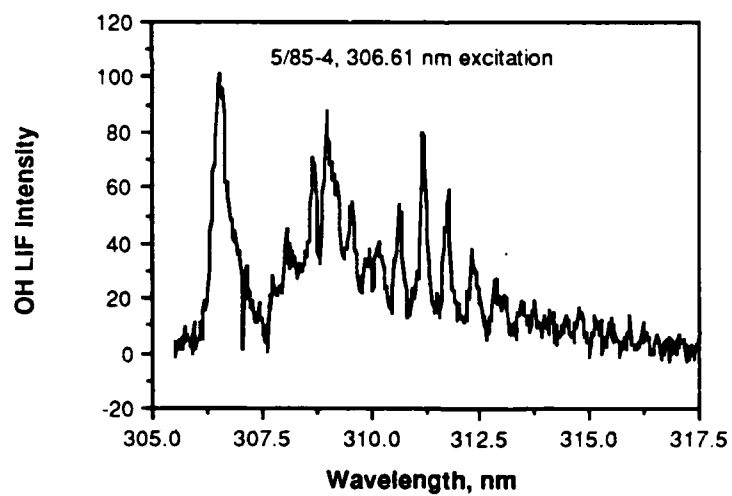


Figure 112. Same as Figure 109, 306.61 nm excitation.

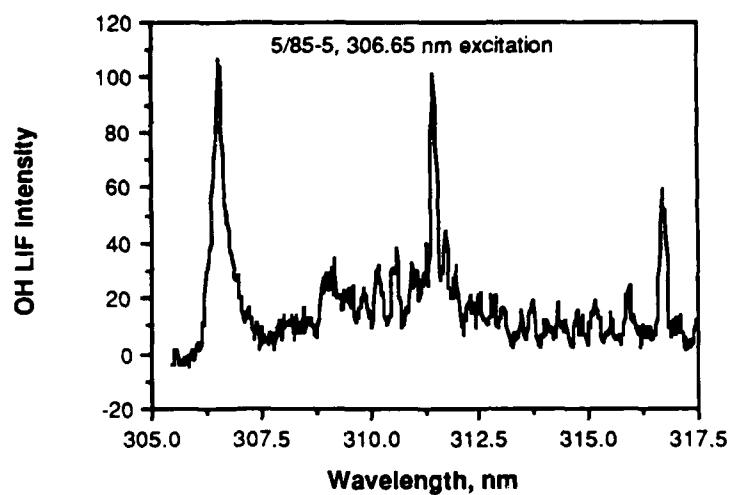


Figure 113. Same as Figure 109, 306.65 nm excitation.

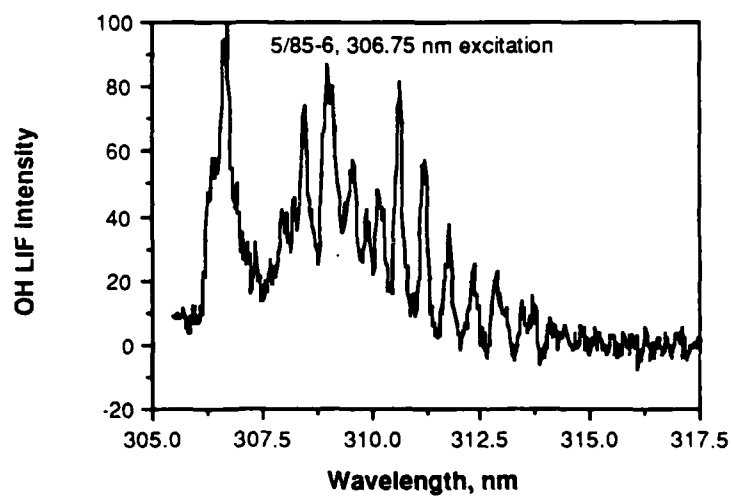


Figure 114. Same as Figure 109, 306.75 nm excitation.

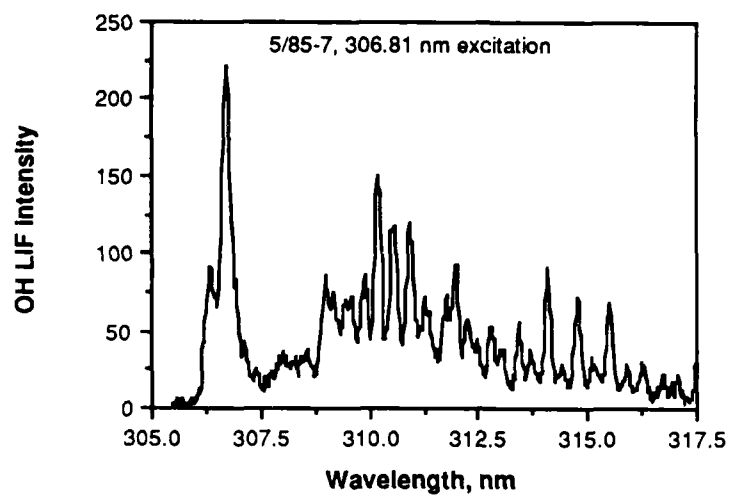


Figure 115. Same as Figure 109, 306.81 nm excitation.

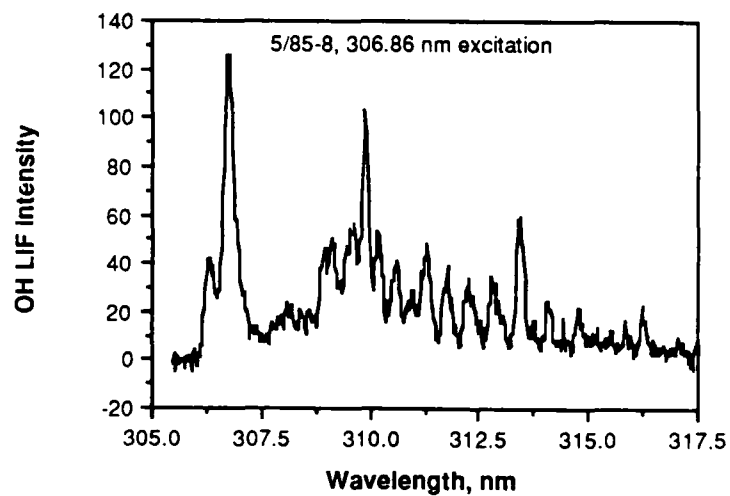


Figure 116. Same as Figure 109, 306.86 nm excitation.

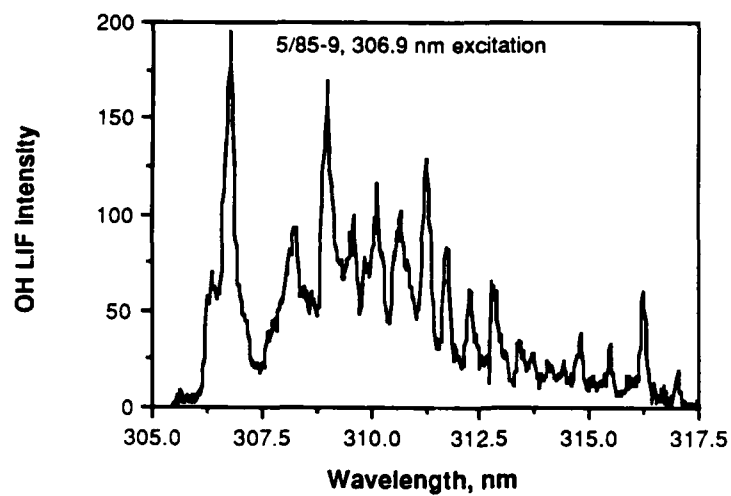


Figure 117. Same as Figure 109, 306.9 nm excitation.

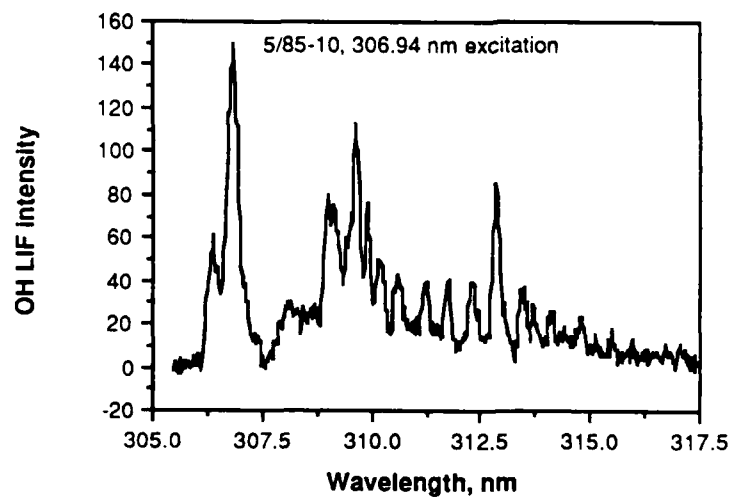


Figure 118. Same as Figure 109, 306.94 nm excitation.

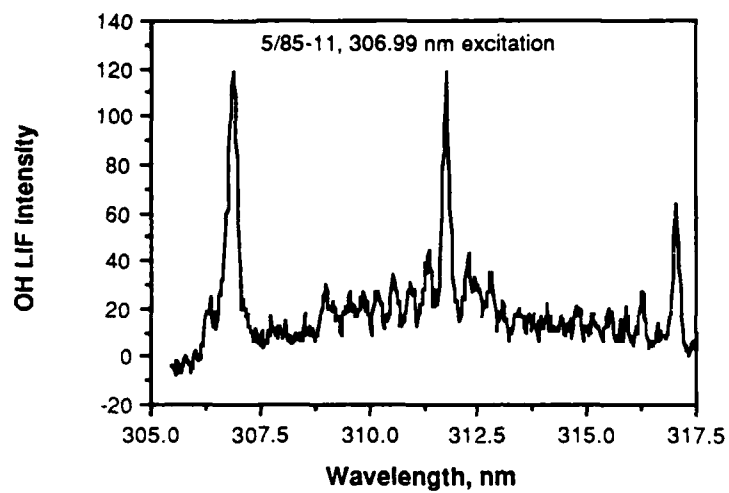


Figure 119. Same as Figure 109, 306.99 nm excitation.

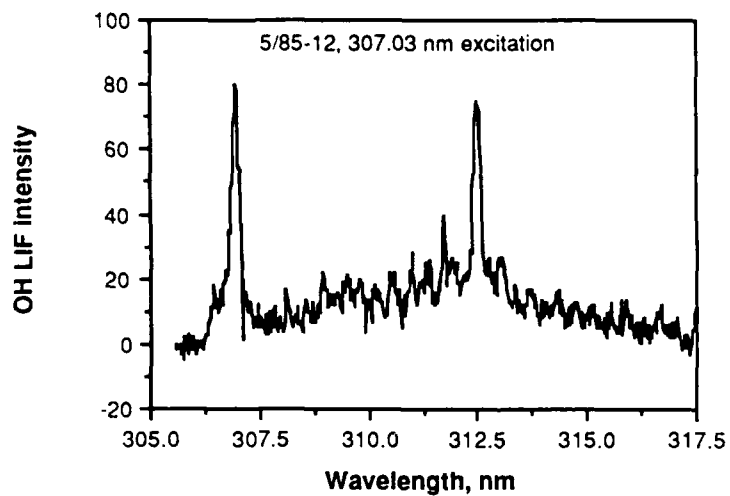


Figure 120. Same as Figure 109, 307.03 nm excitation.

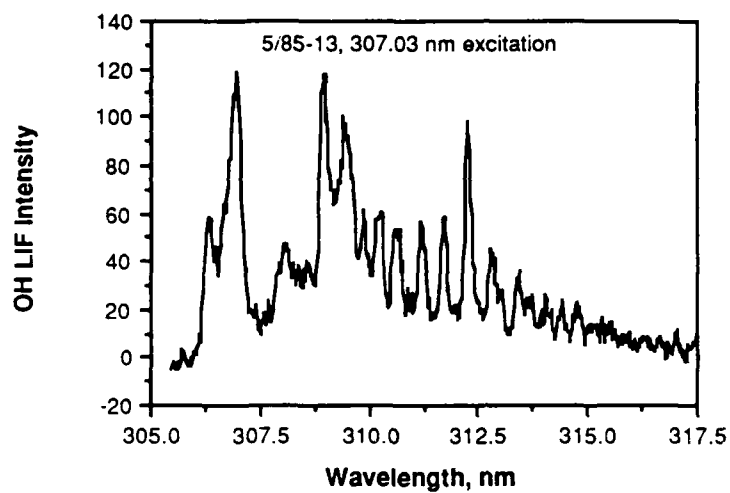


Figure 121. Same as Figure 109, 307.03 nm excitation.

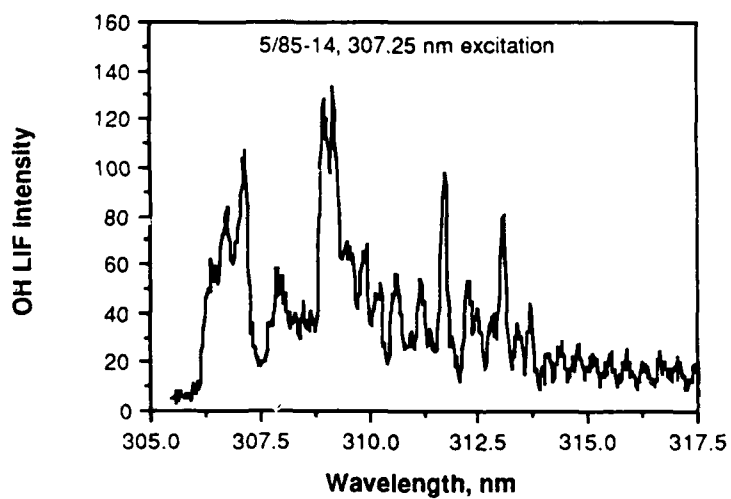


Figure 122. Same as Figure 109, 307.25 nm excitation.

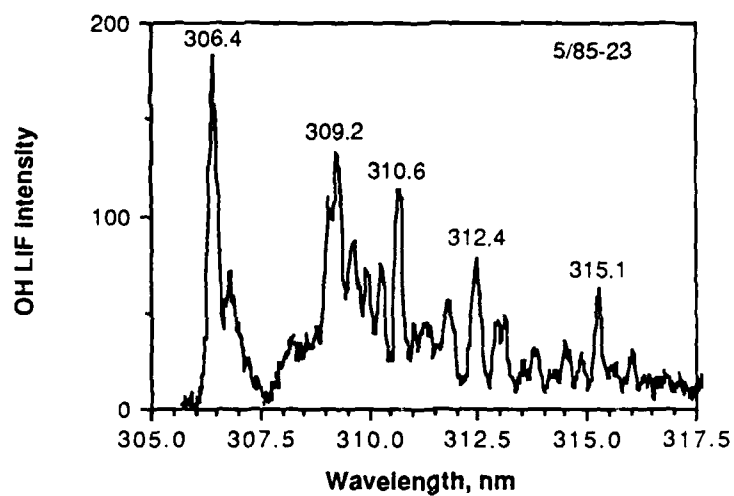


Figure 123. Replication of Figure 109.

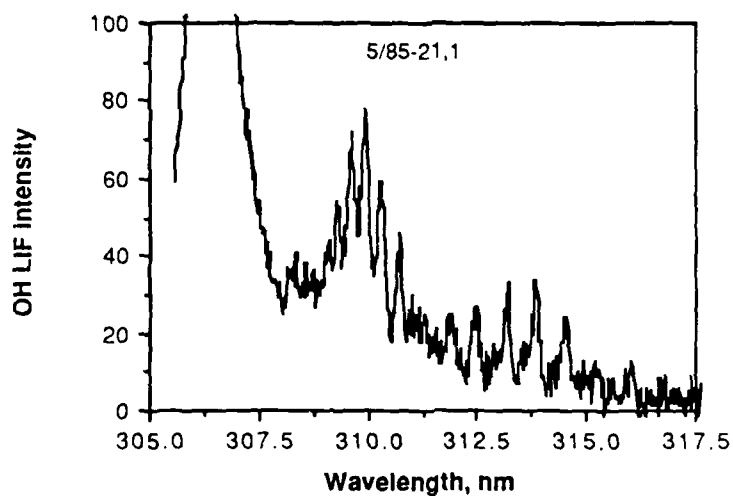


Figure 124. OH ($A^2\Sigma-X^2\Pi$) LIF, AP1 propellant flame. 4 mm above surface, 306.38 nm excitation, 3.5 mJ/pulse in flame (est.), Reticon detector, 700 pixels, 0.0175 nm pixel dispersion (laser line intensity=8000 on Y axis), 500/200 μm slits, intermediate slit on Tripletmate=8 mm.

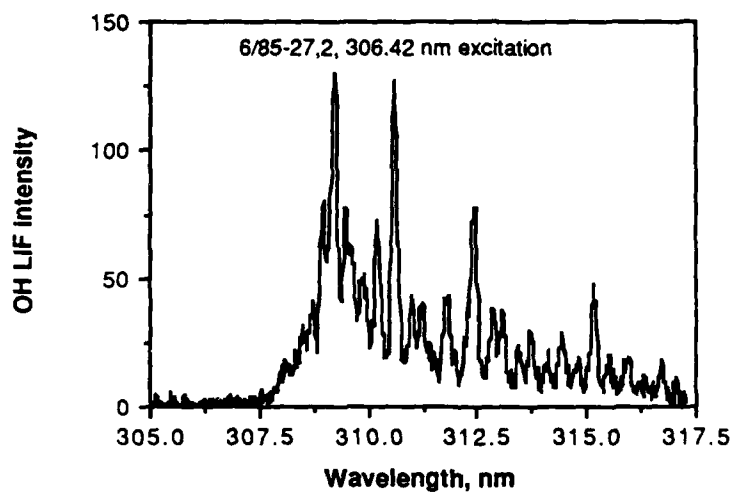


Figure 125. OH ($A^2\Sigma-X^2\Pi$) LIF, AP1 propellant flame. 0.45 MPa, 1.5 mm above surface, 306.42 nm excitation, 3.5 mJ/pulse in flame, Reticon detector, 700 pixels, 0.0175 nm pixel dispersion, 12 pulse signal accumulation, 500/200 μ m slits, intermediate slit on Triplemate=6 mm.

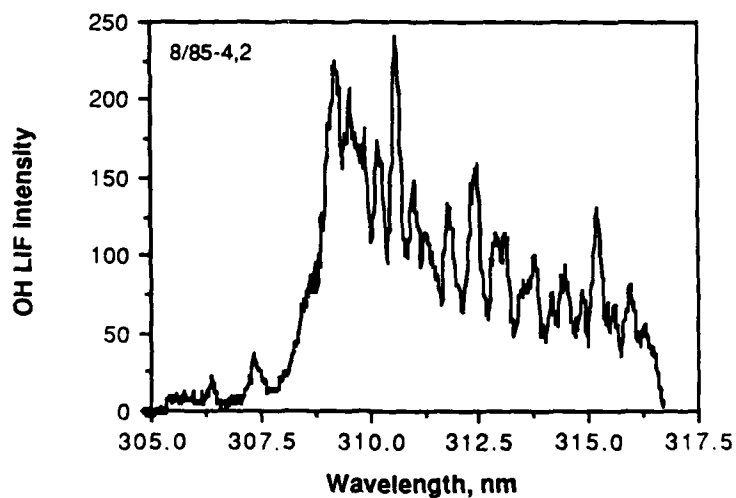


Figure 126. Same conditions as Figure 125 except AP1 propellant, 2.2 MPa, 4 mm above surface.

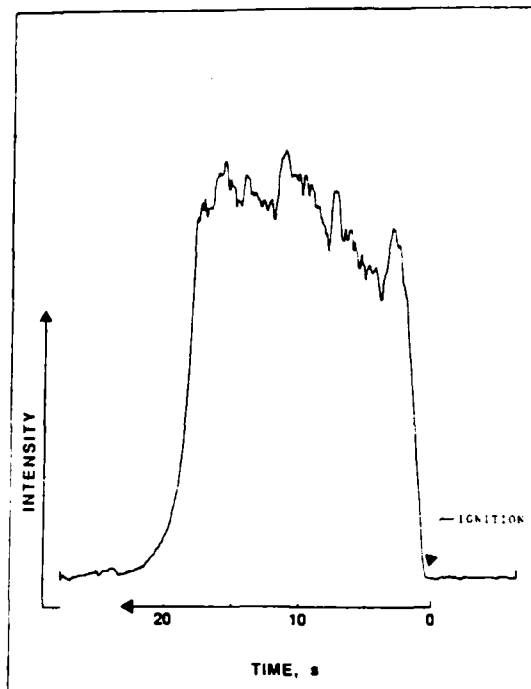


Figure 127. OH ($A^2\Sigma-X^2\Pi$) LIF, AP1 propellant flame. 0.8 MPa, 4 mm above surface, 306.42 nm excitation, 315.1 nm observed, 4.3 mJ/pulse in flame, PMT detector, 10 pulse averaging.

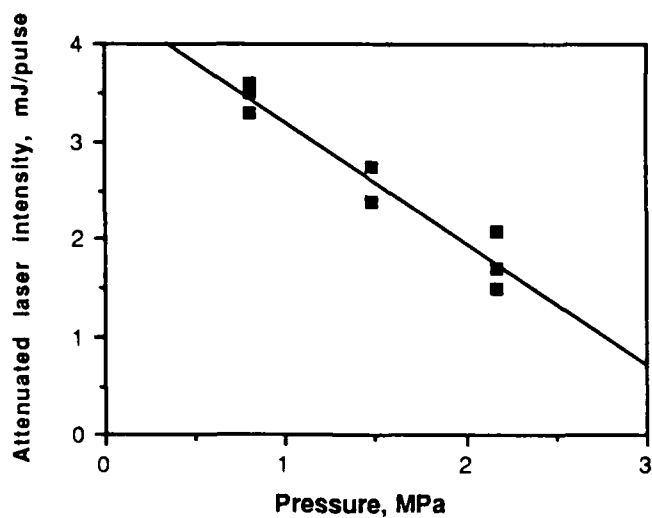


Figure 128. Laser transmittance through flame as a function of pressure. AP1 propellant, $h=4$ mm, laser intensity (in absence of flame): 4.3 mJ/pulse.

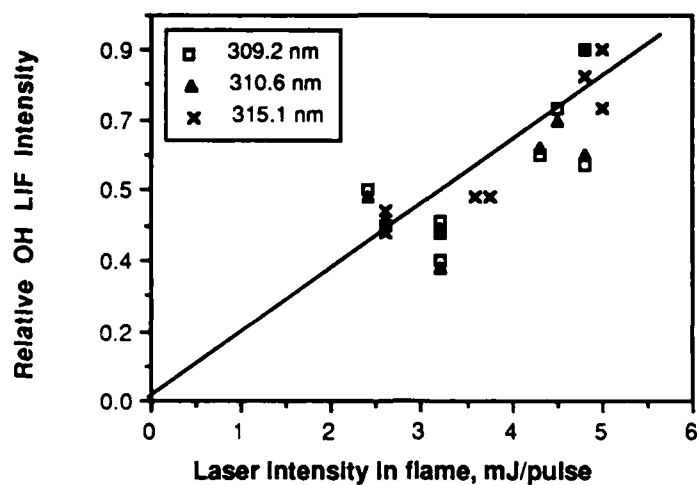


Figure 129. OH LIF intensity as a function of laser power. AP1 propellant, $h=4$ mm, 0.8 MPa. 309.2 and 310.6 nm data points are average of 5 scans/experiment on Reticon; 315.1 nm points are average intensity on PMT during experiment.

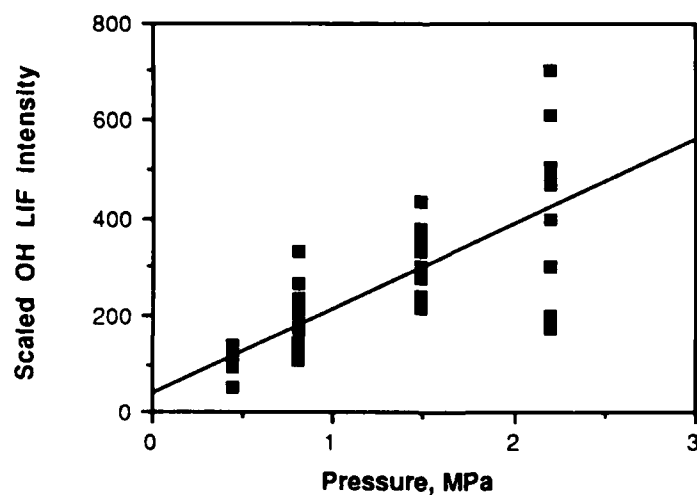


Figure 130. OH LIF intensity (scaled to 3.5 mJ/pulse attenuated laser energy in flame) as a function of pressure. AP1 propellant, $h=4$ mm, 306.42 nm excitation.

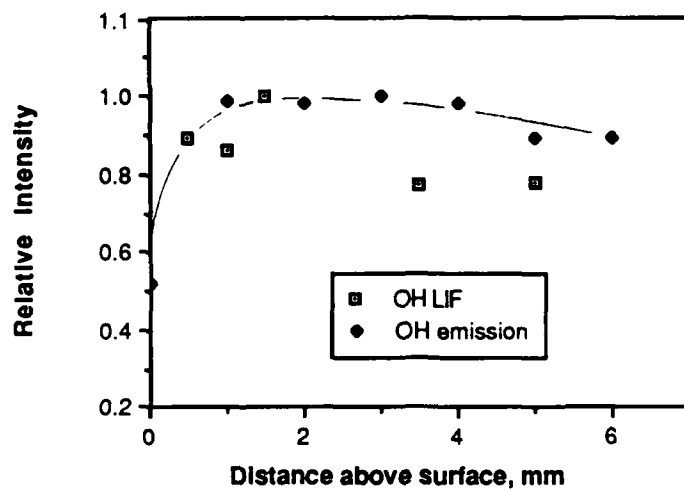


Figure 131. OH LIF and emission intensities as a function of distance above surface. LIF: 0.8 MPa; emission, 0.2 MPa.

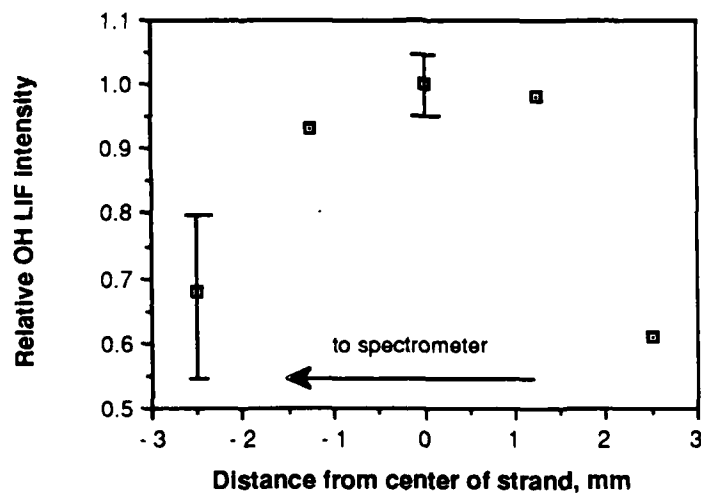


Figure 132. OH LIF intensity as a function of horizontal position in flame. AP1 propellant, 0.8 MPa, 4.3 mJ/pulse, 315.1 nm LIF line monitored on PMT.

5.2. CN LIF EXPERIMENTS (Ref. 7,8)

The CN systems chosen for excitation and detection were selected primarily to minimize the interference of the large Mie scattering signal with the detected LIF signal. The LIF experiments involved exciting the bandhead of the 0,1 band of the CN B-X transition and observing the resulting LIF in the 0,0 band. There are advantages and disadvantages to this scheme. The main advantage is that the excitation wavelength (421.5 nm, see Figure 133) is well removed spectrally from the detected LIF wavelength (typically 388.3 nm). A filter (Ealing 35-3110, 390 nm center wavelength, 11.5 nm bandwidth, 30% peak transmission) was used in the CN LIF experiments in propellant flames to aid in the rejection of scattered laser light. CN fluorescence obtained in a $\text{CH}_4/\text{N}_2\text{O}$ flame by exciting the CN 0,1 bandhead is illustrated in Figures 134 and 135 for the PMT detector. The bandwidth of the laser was larger than the CN line separation in the 0,1 bandhead region (Ref. 163,174), so several lines near the bandhead were being excited. The prominent lines excited in the R branch are R(20)-R(23), indicating that P(22)-P(25) in the 0,1 band are being excited (the bandhead is P(23) (Ref. 174)). A corresponding CN LIF spectrum is shown in Figure 136 for the Reticon detector. A similar spectrum in an AP1 propellant flame is shown in Figure 137. The corresponding emission spectrum is shown in Figure 138. Note the lower resolution, as compared to Figure 4.3.1. The signal levels were low enough that propellant experiments required maximum signal, which was obtained at lowest resolution. Only AP1 propellant yielded intense enough CN LIF signals to be analyzed with the Reticon. Experiments with the Reticon were typically performed by controlling the surface position and measuring the CN LIF intensity at a given point above the surface. The results of these early experiments are shown in Figure 139. The reproducibility of these experiments was not high and the PMT detector was used for most of the subsequent CN LIF experiments. Typically, propellant experiments using the PMT detector were performed by setting the spectrometer on the 388.3 nm P branch bandhead peak and monitoring the fluorescence as the propellant burned down through the collection volume, as illustrated in Figures 140 and 141. The temporal resolution of such a system is directly related to the speed at which data can be collected, so single-pulse data acquisition and high laser repetition rates were desirable.

The concept of exciting and observing different band systems has been used in several previous LIF studies, especially those involving two-dimensional imaging (Ref. 17,175,176). Imaging of liquid propellant combustion also requires this type of excitation-detection scheme to minimize the scattering from liquid droplets (Ref. 177). One of the disadvantages of such a scheme is that the transition probability is smaller than the transition probability for a "excite 0,0 - detect 0,0" experiment such as the OH LIF just described. Another disadvantage to exciting the 0,1 band is that the $v''=1$ population is more sensitive to temperature than the $v''=0$ population. Future CN LIF experiments in propellants will probably involve the excitation of the 0,0 bandhead and the observation of the LIF in the 0,1 band. A discussion of the relative merits of several LIF methods can be found in (Ref. 175). The discussion of CN LIF results in propellant flames is divided up into sections by the propellant studied.

AP1 propellant

The study of the AP propellant flame with CN LIF had several goals. The initial goals were to determine if the CN molecule was indeed confined to a small region near the surface and to determine if this region could be successfully probed in solid propellant flames. Another goal was to determine if the disappearance of the CN emission with increasing pressure corresponded to the disappearance of the CN molecule itself or was due to some other effect. Initially, the CN LIF experiments were performed with the Reticon detector. As previously discussed, the weakness of the CN LIF signal meant that the signal had to be integrated on the detector for 10-20 laser pulses, thus only experiments in which the surface was maintained at a constant level could be performed. In Figure 139, the results of a series of such experiments is illustrated. At a constant pressure of 1 atm (nitrogen), the CN LIF intensity was seen to extend from the surface to about 1 mm. The distance scale on the figure is the set value of the control system and variations in control of surface position lead to errors in this value. Fluctuations in surface position undoubtedly account for much of the spread in the data seen in Figure 139. Because of the poor data quality and the poor time resolution, the distribution of CN was studied more thoroughly with the more sensitive PMT system. The surface control problem was skirted by taking single pulse data as the propellant burned down through the collection volume, in essence collecting a CN profile in a single experiment. Such an experiment is illustrated in Figure 140. Two channels of data are collected in such an experiment (see Figure 2.1.2). The 1/2-meter monochromator was set to the peak of the peak of the 0,0 LIF spectrum (~ 388.3 nm) and one data channel was the intensity of this LIF peak as a function of time. The second data channel was the split-off portion of the laser beam after passing through the combustor. As illustrated in Figure 140, this data channel yields the (approximate) position of the surface since the transmission of the laser beam is zero while the propellant surface is above the collection volume (and the laser beam). Near the propellant surface, the laser beam is partially obscured by the surface. This effect is similar to the "vignetting" of the laser beam caused by the burner surface in gas flame experiments. In these propellant experiments, vignetting of the beam would be seen in the transmission curve as a non-instantaneous change from 0 to 100% transmission as the surface passes through the collection volume. Referring to Figure 140, this "rise time" distance is approximately equivalent to one-half of the beam diameter at the edge of the propellant strand, or ~ 100 μm . A related problem would be caused by a non-planar propellant surface (or a non-planar laser beam). In certain cases, a non-planar surface would cause the LIF signal to be delayed in time from the initial transmission of the laser beam across the surface, while in other cases, a non-planar surface would cause the disappearance of the LIF signal altogether. Inhibition of the sides of the propellant strands helps to minimize non-planar burning, but in general, replication of experiments was deemed to be the best way to minimize the influence of this problem. Yet another problem with laser diagnostics in propellant flames is the roughness of the surface itself. This roughness is especially prominent in AP propellants, where surface features on the order of the AP particle size (100's of μm) have been seen in SEM studies of quenched propellant surfaces (Ref. 178). This roughness could also delay in time the transmission of the laser beam relative to the LIF signal, as well as obscure the LIF signal itself. With that background in mind, the results of such an experiment with AP propellant burning at 1 atm under nitrogen is shown in Figure 141. With an AP propellant burn rate of 1.7 mm/s under these conditions, the 75 Hz data collection rate corresponds to a surface regression of

approximately 23 μm between data points. Theoretically, the surface is precisely located at the point where the first transmission occurs, which first becomes non-zero when the propellant surface initially passes through the collection volume (and LIF beam). However, in many such experiments, the initial LIF signal is seen to occur "below" the surface, indicating that the LIF laser beam is probably slightly non-level. In experiments where the $\text{CH}_4/\text{N}_2\text{O}$ flame on the 0.25-inch tubing burner was moved down through the collection volume, the same effect was seen when the flame was inside the combustor, but was not evident when the combustor head was removed. Apparently the first combustor window that the laser beam passes through is not perfectly perpendicular to the beam and causes the beam to be deflected slightly downward, causing the apparent subsurface CN LIF. This is not a serious problem, since the surface is located well enough to analyze the results. The results of a series of these experiments gave a reaction zone thickness (defined in Figure 139) of $\sim 600 \mu\text{m}$ for the AP propellant at 1 atm. Figure 141 can be compared to Figure 6, showing the improvement in tracing out the CN profile obtainable with this technique (with both techniques limited, as previously stated, by difficulties within $\sim 100 \mu\text{m}$ of the surface). Pulse averaging could be performed to improve the appearance of the CN profile data, as shown in Figure 142 where the gated integrator was (inadvertently) set to collect the data as a 10 pulse average, although pulse averaging decreases the temporal resolution of the system and was not commonly employed. The influence of pressure on the CN distribution was investigated with the Reticon and PMT systems, with the results confirming the rapid disappearance of the CN at pressures above atmospheric. This is illustrated in Figure 143. It must be emphasized that the interpretation of this data is complicated by effects such as self-absorption (see later discussion), although we believe the disappearance of the CN molecule is real and due to changes in the propellant flame structure with pressure (diffusion flame structure replacing premixed flame structure as pressure increases).

Saturation of the LIF has not been obtained yet in these experiments. The $\text{CH}_4/\text{N}_2\text{O}$ flame could easily be saturated at $\sim 2 \text{ mJ/pulse}$. However, the propellant experiments were typically performed at maximum laser power ($\sim 8\text{-}10 \text{ mJ/pulse}$ inside the combustor) with no evidence of saturation. As a comparison, a CN LIF signal equivalent in intensity to that seen in Figure 141 could be obtained in the inner cone of a slightly rich, premixed $\text{CH}_4/\text{N}_2\text{O}$ flame with 0.1 mJ/pulse . This is graphic evidence of how much weaker the CN LIF signal is in the solid propellants examined, probably indicating a much lower CN concentration. A rough estimate would be that the CN concentration is probably about a factor of 100 less than that seen in the $\text{CH}_4/\text{N}_2\text{O}$ flame (estimated to be $\sim 10^{12} \text{ cm}^{-3}$ (Ref. 179)), or very approximately 10^{10} cm^{-3} . This is a rough estimate because the chemical environment encountered by the CN radical is quite different in the propellant and premixed gas flames and because the $\text{CH}_4/\text{N}_2\text{O}$ flame in our laboratory was probably operated under somewhat different conditions than the burner in (Ref. 179).

The intensity of the CN LIF (as measured by the peak in the CN LIF distribution) decreased rapidly with pressure, although the thickness of the reaction zone was not similarly affected. This can be seen in Figure 143, confirming the earlier CN emission results. As previously discussed, the influence of pressure on LIF is not well understood, so the behavior shown in Figure 143 is only indicative of a trend, not an absolute measure of the CN concentration decrease. However, OH LIF results (and CN LIF results in other propellants) at

pressures up to 3.5 MPa imply that the trend shown in Figure 143 is indicative of CN concentration and not an artifact of the LIF process. Thus, two different diagnostic techniques have confirmed the rapid disappearance of the CN radical at pressures below about 0.5 MPa. These results may be compared to the experimental data of Kubota, et al (Ref. 45,180,181), where temperature traces (very fine thermocouples) have shown that AP/HTPB propellants appear to require more than 400 μm to reach the maximum flame temperature, a distance that can be reduced by replacing the HTPB binder with a polyester or CMDDB binder. The connection between temperature and radical distributions is not clear in the AP flame at this point, although in most flames the maximum temperature is reached in the luminous flame zone which follows the primary reaction zone, not in the primary reaction zone itself (Ref. 46,104).

The characteristics of the radicals examined thus far in AP composite propellants (CN, NH, CH, and OH) are not particularly surprising in light of past and current modeling of AP combustion (Ref. 107,113,182). The flame structure above the surface of an AP composite propellant is thought to consist of multiple flames: the "monopropellant" flame between (among) the decomposition products of the AP itself (NH_3 , ClO , OH , O_2), the "primary" flame between the oxidizers in the AP and the fuel-rich decomposition products of the binder, and the "final" flame where the leftovers of the first two flames complete the combustion. The relative importance of these flames varies dramatically with pressure. At low pressures, flame reaction rates are slow and diffusion is fast, leading to the formation of a premixed flame above the surface. As pressure is increased, the reaction rate increases and diffusion slows to the extent that the primary flame between the oxidizer decomposition products and the fuel decomposition products becomes a diffusion flame. At still higher pressures, the (always premixed) monopropellant flame becomes controlling. The chemical character of premixed flames and diffusion flames is quite different (Ref. 46,104). In a premixed flame, the reactant molecules are largely broken up by radical attack. In contrast, in a diffusion flame the initial reactant molecules (especially the fuel) are significantly degraded by pyrolysis before reaching the flame front. Thus, while a CH_4/O_2 premixed flame shows emission from CH and C_2 radicals (characteristic of radical attack on CH_4), a CH_4/O_2 diffusion flame shows only OH and $\text{CO} + \text{O}$ emission, indicating that the fuel has been significantly degraded to carbon before being attacked by oxidizers (Ref. 46,104). Thus, the AP propellant experimental data indicates that the transition of the primary flame from premixed to diffusion flame is essentially complete at 0.5-0.8 MPa (50-100 psig). The lack of emission from the monopropellant flame (NH emission might reasonably be expected) may be due to the low monopropellant flame temperature (1400 K). Note that the primary flames of the largest particles are probably already diffusion-controlled at atmospheric pressure, thus the observed CN is probably from the primary flames above the small AP particles (Ref. 113). These radical distributions are somewhat larger than the distributions implied by most solid propellant models, if one takes the peak of the CN concentration to correspond to the flame height. For example, Beckstead, et al (Ref. 115) calculate a "heat transfer distance" of $\sim 300 \mu\text{m}$ for a 200 μm AP propellant at 1 atm. Alternatively, the "flame standoff distance" (x^*) for a kinetically limited flame can be calculated for the AP propellant flame to be $\sim 150 \mu\text{m}$ (Ref. 115). The link between the CN radical distribution and the heat transfer-based concepts of standoff distance and heat transfer distance is somewhat tenuous. Indeed, one of the (long-term) goals of this work is to link the flame chemistry to the heat transfer processes in the propellant flame to allow the creation of more effective propellant combustion models.

This work has several implications for future AP composite propellant research. First, examination of AP propellant flames at atmospheric pressure probably has little application to propellant combustion at higher pressures since the combustion chemistry and physics of premixed flames are so totally different from that seen in diffusion flames. Additionally, 1 atm experiments in air are doubly suspect (Ref. 37), since the diffusion of oxygen into the flame at these pressures is so rapid that the O/F ratio in the flame bears little resemblance to that encountered in a "real" situation, such as in a rocket motor. A second conclusion is that the most common radical diagnostics used in premixed flames may have little importance as AP composite propellant diagnostics. Thus, the study of high pressure diffusion-flame controlled AP propellant combustion with OH, CN, or NH LIF shows little promise, since the species either aren't present in the diffusion flame (CN, NH (?)) or are not an important primary flame constituent (OH). The species of most importance in the study of diffusion flame structure and thus propellant decomposition chemistry are probably the small hydrocarbons such as C_2H_2 , which are produced in copious amounts in typical polymer pyrolysis (e.g., (Ref. 119) for butadiene pyrolysis). The study of these molecules requires a technique such as laser-Raman scattering or CARS (Ref. 25). The study of binder chemistry is of much current interest in AP composite propellant research (e.g., see (Ref. 183)). The ultimate goal is not to create detailed reaction models along the lines of those for hydrocarbons such as butane (Ref. 184), containing 400+ reactions and requiring large investments of computer time, but to create simpler models which have much smaller reaction sets but have other features which allow the modeling of more complex systems (such as models for the combustion of iso-octane (Ref. 185)).

Another aspect of AP propellant combustion that has important diagnostic implications is the heterogeneous nature of the propellant flame itself, and the associated difficulty of relating a gas-phase diagnostic measurement to the associated surface beneath. In other words, a radical concentration measurement is difficult to interpret if one doesn't know if the measurement was taken above a large AP particle, above a small particle, above the interface between binder and AP, or whatever. Without this correlation between gas phase and surface, diagnostic measurements like those described in this section can only show average flame structures (averaged across many possible surfaces) or relative differences in flame structure between different formulations. For this reason, the CN LIF measurements in the AP propellants were taken with 2 mm horizontal resolution, averaging over many possible surface structures to create an "average" CN distribution. Laser diagnostics have the temporal and spatial resolution to resolve individual particle phenomena (at least for moderate-sized AP particles), if one could find a way to link the gas phase measurement to the surface. The temporal resolution of 30 ns is much smaller than the particle burn times (Ref. 138), and the spatial extent of LIF measurements can be limited to 20-50 μm in all three spatial dimensions (subject, of course, to signal-to-noise limitations), but the problem of linking the gas phase measurement to the surface still remains. A possibility to surmount this difficulty is to construct model systems that have a well-defined, time-invariant flame structure, such as sandwich propellants (Ref. 111), although these model systems have difficulties of their own.

The question remains, is the trend shown in Figure 143 real? It seems unlikely that quenching in the AP propellant flame is vigorous enough that the disappearance of CN is due

only to quenching, for two reasons. First, CN LIF has been seen in the HMX flame at 3.5 MPa (500 psig) and it seems unlikely that the quenching environment in the AP propellant flame is that dramatically different. In addition, OH LIF showed dramatically different pressure behavior in the AP propellant flame (Section 5.1). When the LIF intensity was scaled to correct for flame attenuation of the laser beam, the OH LIF intensity increased linearly with pressure between 0.4 and 2.2 MPa. The (flat) OH concentration distribution in the portion of the propellant flame examined is not pressure dependent, so flame structure changes shouldn't affect the OH results. An estimate of the influence of self-absorption was made by moving the collection volume from one edge of the flame to the other, with the result that little influence of self-absorption was seen at 0.8 MPa (100 psig). Thus, three main effects should have an influence on the OH LIF signal: quenching (LIF \downarrow as P \uparrow), total density changes (LIF \uparrow as P \uparrow), and chemistry changes (radical formation, reaction and recombination ? as P \uparrow). The relationship of these three variables with the LIF intensity is complex, but it seems unlikely that the processes for CN are so different from those for OH that CN quenching should dominate CN LIF at pressures near 0.5 MPa. Thus, we conclude that the decrease in CN LIF intensity with pressure in the AP propellant flame (Figure 143) does in fact reflect a corresponding decrease in CN concentration.

HMX and AN propellants

The HMX propellant has a very different flame structure from the AP propellant (Ref. 6). CN and NH have been seen in emission up to 7 MPa, and the structure of the flame (as seen in 2-D imaging experiments (Ref. 5)) is a much different function of pressure. The CN LIF intensity of the HMX propellant was significantly less than that of the AP propellant, so only PMT experiments will be described. Similar experiments to those leading to Figure 141 have been performed in the HMX1 and HMX2 propellant flame at various pressures. For example, the results of an HMX propellant experiment at 0.8 MPa (115 psia) are shown in Figure 144. A pulse-averaged experiment performed under the same conditions is shown in Figure 145. The slight misalignment of the laser is evident in Figure 145 but, after adjustment of the collection optics, has disappeared in Figure 144. The reasons for this are not totally clear, but adjusting the collection optics could change the position of the collection volume inside the laser beam, altering the relationship between transmission and LIF. A notable difference between the results in Figures 141 and 144 is the increased number of data points in the reaction zone. However, the much lower burn rate of the HMX propellant (see Section 3.2) translates into a similar reaction zone thickness of $\sim 500 \mu\text{m}$ for the HMX propellant under these conditions. At higher pressures, on the order of 1 MPa and higher, interference from Mie scattering began to be apparent. The type of interference seen is apparent in Figure 146, where a typical experiment along the lines of Figures 141 and 144 was performed at 1.8 MPa, but with the laser "detuned" so that no LIF was possible. Note the short (3-5 data points) "spikes" present. For a propellant with a reaction zone that is (for example) 100 data points thick under these conditions, these spikes could probably be easily separated from the LIF data. For example, the corresponding CN LIF experiment is illustrated in Figure 147. The reaction zone is still evident. However, as pressure is further increased, the propellant reaction zone (proportional to P^{-1} for premixed flames (Ref. 46)) shrinks and the propellant burn rate increases (Section 3.2). Thus, the number of data points in the reaction zone, a measure of the ease of separating interference from the LIF signal, is doubly decreased by increasing pressure.

For example, for a propellant with a burn rate of 5 mm/s and a reaction zone thickness of 500 μm , the 75 Hz data collection rate of this system implies that the reaction zone thickness (as defined in Figure 139) is ~ 7 data points. The difficulty of differentiating between such an LIF signal and the scattering seen in Figure 146 is evident. In addition, the optical thickness of propellant flames increases swiftly with increasing pressure (Sections 3.3, 5.1), leading to much more intense Mie scattering at pressures on the order of 3.5 MPa (500 psi). The amount of scattering present is quite dependent on the propellant formulation and stoichiometry, with certain propellants having much "sootier" flames than others. The combination of all these difficulties has (thus far) limited the use of this technique to pressures at or below 3.5 MPa.

A second HMX propellant flame has been examined with CN LIF, an 80% HMX propellant quite similar to one studied by Kubota (propellant HTPS in (Ref. 22)). An interesting difference between the two propellants is that propellant HMX2 has a "dark zone" or "preparation zone" while propellant HMX1 does not. The dark zone is an induction zone usually indicative of the presence of NO (Ref. 29). Kubota has shown that, in certain cases, the length of the dark zone has no influence on the propellant burn rate (Ref. 22), but the chemistry of the dark zone is still of interest (Ref. 29,186). Propellant HMX2 is much more fuel-rich than HMX1, with a correspondingly lower flame temperature (see Section 3.3). Whether or not this causes the larger dark zone remains to be determined. Kubota's data indicates that the dark zone for propellants similar to HMX2 is 2-2.5 mm at 1.8 MPa (18 atm, 265 psia) (Ref. 22,187). In contrast, the dark zone for HMX CMDDB propellants is essentially zero for HMX concentrations greater than $\sim 35\%$ (Ref. 187). Thus, the observation that the addition of TMETN to HMX composite propellants eliminates the dark zone is not surprising, since TMETN is a nitrate ester as was the double-base matrix of Kubota's HMX CMDDB propellant. A typical CN distribution for propellant HMX2 is shown in Figures 148. The HMX2 flame shows several obvious differences from the HMX1 flame. The CN signal is much smaller at the same pressure (probably indicating a lower CN concentration), the CN is distributed over a much larger distance, and it appears that the CN profile begins at a point about 1 mm above the surface, rather than right at the surface for the AP and HMX1 CN distributions. The data shown in Figure 148 was taken after the optical system was readjusted to prevent the appearance of CN LIF before the initial transmission across the surface, thus Figure 148 is not directly comparable to Figures 143 and 144. However, the much larger "reaction zone" in the HMX2 propellant is a real effect. The reasons for the scatter in the data are not yet clear. Perhaps more important is that the HMX1 "reaction zone" apparently does not shrink as pressure is increased as one would expect for a premixed-type flame (Ref. 46). The implication of these results is that the flame chemistry is quite different from what one would expect on the basis of comparison to a premixed flame. This behavior should become more clear as more data is collected, both for CN and for other reaction zone radicals such as NH.

When the CN distributions for the two HMX propellants are placed on the same scale (Figure 149), an interesting comparison emerges. Propellant HMX2 has been studied with microphotography (Ref. 22), with the dark zone length reported as 2-2.5 mm at 1.8 MPa. Apparently, then, the observed CN in the HMX2 flame is seen in the upper end of the dark zone, coinciding with the rapid temperature rise (and resulting NO consumption) seen in (Ref. 22). The dark zone is usually considered to contain only NO, H_2 , and CO as the reactive

species (Ref. 29,76), at least for double-base propellants. In spectroscopic studies of flames containing NO, H₂, and CO (Ref. 46), no CN was seen in emission. Indeed, the reaction mechanisms for NO supported flames do not involve CN unless hydrocarbons are present (Ref. 82,89). How, then, can the dark zone CN be explained? Kubota (Ref. 22) has reported that significant amounts of hydrocarbons and N₂O are found in the dark zone of HMX propellants. Hydrocarbon/N₂O flames have been studied extensively, and CN is an active part of the flame chemistry (Ref. 179). In fact, a CH₄/N₂O flame is used in these CN LIF experiments to adjust the laser wavelength to the CN transition because of the (relatively) large amount of CN present. Thus, these results are in agreement with Kubota's data. It was expected that CN would be found in the first-stage reaction zone (next to the surface), but the relatively low signal levels in propellant HMX2 make it difficult to determine at this time whether or not CN is found in this flame zone. All that can be stated is that the CN concentration in the first-stage reaction zone is apparently less than that in the upper part of the preparation (dark) zone. Experiments are underway to determine if CN can be found in the zone next to the surface. In propellant HMX1, much stronger CN LIF signals can be seen near the surface, but it can't be determined at this time whether this CN is from the first-stage reaction zone or is the dark zone CN from a much smaller (or closer to the surface) dark zone. In any case, the complexity of the reactions preceding the first-stage reaction zone (Ref. 29,53) mean the analysis of the first-stage reactions will be a difficult undertaking, requiring data on other molecules in addition to CN.

An AN propellant (Ref. 188) was examined with emission spectroscopy and CN LIF to study the flame structure. Interestingly, no emission could be seen from CH, NH, and OH and only weak emission from CN was seen under conditions where both the AP and HMX propellants had shown strong emission. The reasons for this are not clear at this point (lower flame temperature?), although the chemistry in the AN propellant is undoubtedly quite different from that in the AP and HMX flames. The AN propellant was quite sooty, with visible glowing particles in the flame. This sootiness was evident in CN LIF experiments, where the increasing scattering in the flame was evidenced by many "spikes" in the data. These spikes occur when particles pass through the collection volume and are struck by the laser beam, causing large signals at the laser wavelength. These signals are large enough to overcome the filtering in the collection system and appear in the LIF data. An example of such an experiment is shown in Figure 150. Because of the sootiness of the AN1 propellant flame, only 0.8 MPa (115 psia) CN LIF results have been successfully obtained so far. The average reaction zone thickness of the AN1 propellant at 0.8 MPa was ~600 μ m. This is a rough answer made by estimating the background underlying the large number of spikes. Obviously, this propellant is not easily accessible with laser diagnostics.

An interesting comparison to make between the various propellants is suggested by the data presented in (Ref. 46), where reaction zone thicknesses for premixed flames are compared at various pressures and burning velocities (flame stoichiometries). It was found that the reaction zone thickness was inversely proportional to pressure and to flame speed. The burn rate of a solid propellant is not strictly analogous to the flame velocity of a premixed flame, since it is possible to change the propellant burn rate without changing the propellant stoichiometry and vice versa, but a comparison in terms of burn rate is enlightening. The available propellant data is shown in Figure 150. The lack of a trend (especially for the HMX

propellants) may indicate serious departures from premixed-flame-type behavior, but more probably is indicative of the fact that CN is found in several flame zones and that care must be taken to assure that consistent comparisons are made in the complex propellant flames. As a comparison, the same data is plotted as a function of pressure in Figure 151. We anticipate that more meaningful correlations of flame structure properties can be made when more LIF data becomes available, especially for other species such as NH. It has been found experimentally that radicals such as CH, CN, and NH often have quite different distributions in nitrogen-containing flames (Ref. 82).

The width of the transition region (defined in Figure 139) can also be measured from these transmission traces. This quantity should be a function of the optical system (same for all propellant experiments) and the propellant surface roughness. One would expect that the diffusion-flame dominated propellants (AP1 and AN1) would tend to have rougher surfaces than the HMX propellants. The average transition region thicknesses are plotted in Figure 151 as a function of propellant burn rate, and the thickest transition zones are indeed in the AP1 and AN1 propellants, although the differences are small compared to the data scatter (as shown in Figure 152).

Absolute CN concentrations have not yet been determined from these LIF measurements for several reasons. Saturation of the fluorescence is necessary to minimize the influence of quenching on the LIF signal (Ref. 150,190), but has not yet been achieved for CN (or OH (Section 5.1)) in the propellant flame. However, even in the absence of saturation, concentration profiles should agree with the LIF intensity profiles at a given pressure (e.g. Figure 141). The influence of pressure on quenching, and thus on LIF intensity, is much more difficult to assess (Ref. 10-12,191). This is particularly true when other pressure dependent phenomena (such as self-absorption (Ref. 13,175), line broadening (?), and flame structure changes) are superimposed on the changes in LIF signal due to quenching. For this reason, the reaction zone thickness is the quantity used to assess the CN distribution, rather than the absolute CN LIF intensity. The determination of a reaction zone thickness is not dependent on the absolute LIF intensity and thus should be relatively independent of quenching. This type of semi-quantitative analysis is fairly common (Ref. 89).

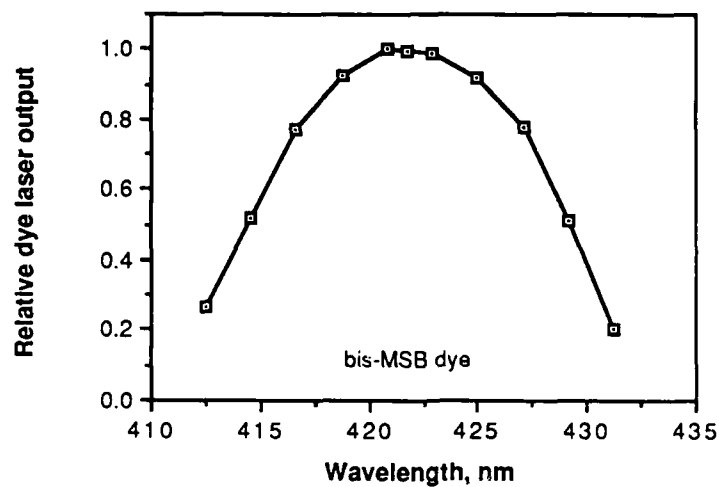


Figure 133. Dye laser output as a function of wavelength (Lambdachrome LC 4200 bis-MSB dye).

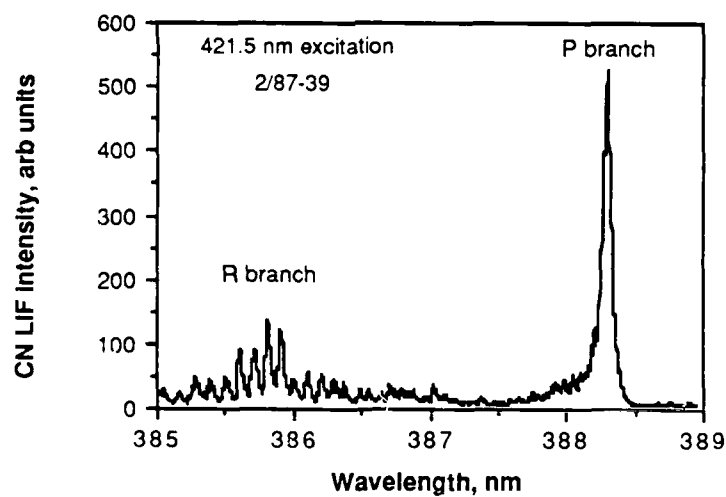


Figure 134. CN ($B^2\Sigma-X^2\Sigma$) LIF, CH_4/N_2O flame. Inner cone, 421.5 nm excitation, 0.09 mJ/pulse in flame, PMT detector, 10 μ m slits.

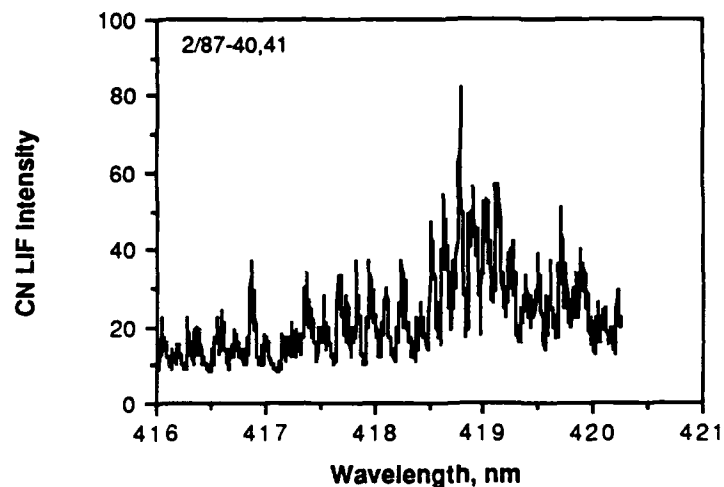


Figure 135. CN ($B^2\Sigma-X^2\Sigma$) LIF, CH_4/N_2O flame. Inner cone, 421.5 nm excitation, 1.25 mJ/pulse in flame, PMT detector, 20 μ m slits.

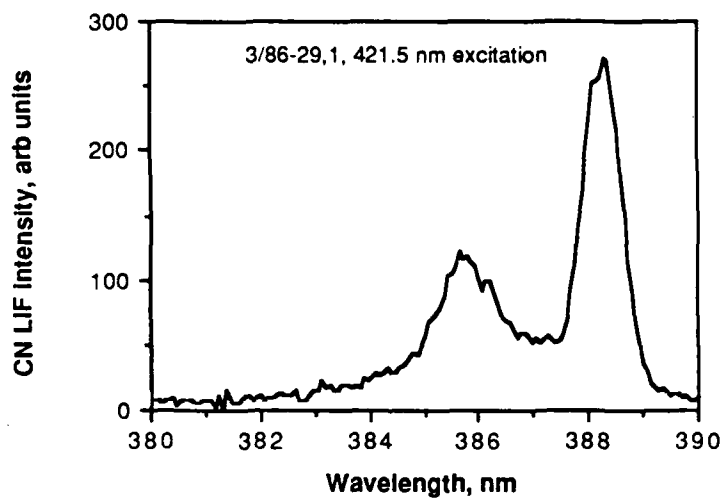


Figure 136. CN ($B^2\Sigma-X^2\Sigma$) LIF, CH_4/N_2O flame. Inner cone, 421.5 nm excitation, 10 mJ/pulse in flame (est.), Reticon detector, 200 pixels, 0.07 nm pixel dispersion, 500/200 μ m slits, 5 pulse/0.5 s signal accumulation (10 Hz laser repetition rate).

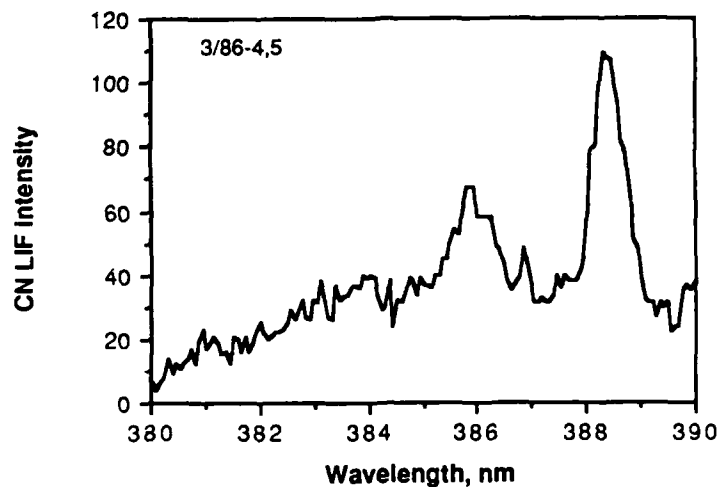


Figure 137. CN ($B^2\Sigma-X^2\Sigma$) LIF, AP1 propellant flame. 1 atm N_2+ , 421.5 nm excitation, 8 mJ/pulse in flame, Reticon detector, 200 pixels, 0.07 nm pixel dispersion, 500/200 μm slits, $h \approx 200 \mu\text{m}$, 10 pulse/0.5 s signal accumulation (20 Hz laser repetition rate).

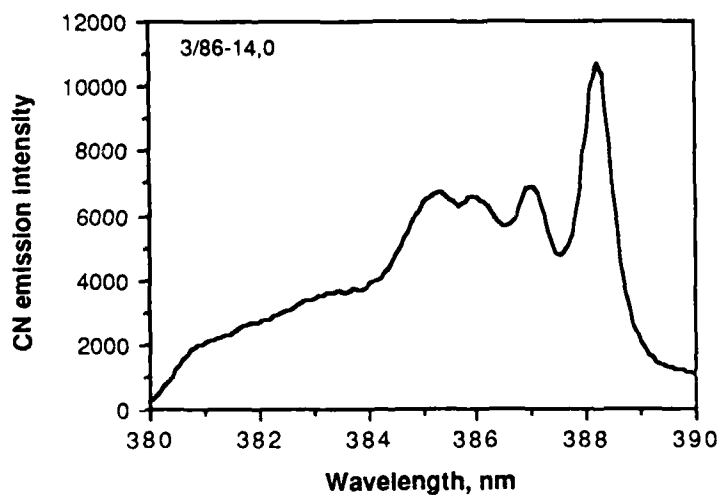


Figure 138. CN ($B^2\Sigma-X^2\Sigma$) emission, AP1 propellant flame. 1 atm N_2+ , Reticon detector, 200 pixels, 0.07 nm pixel dispersion, 50/200 μm slits, 0.5 s exposure time.

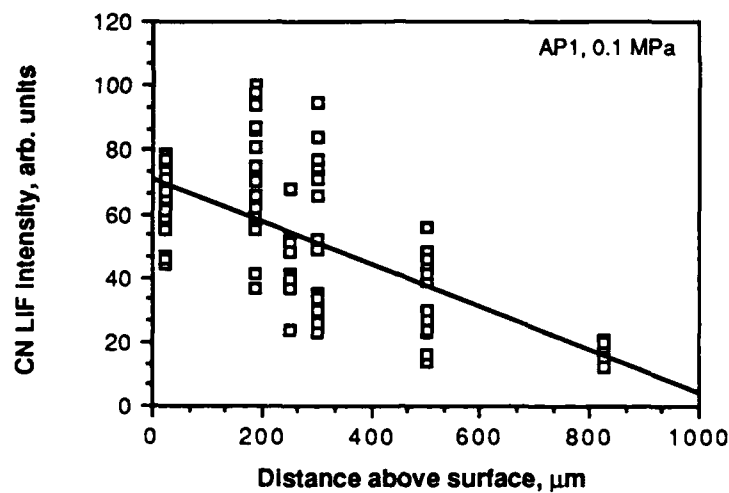


Figure 139. Relationship between CN LIF intensity and (nominal) distance above the propellant surface. AP1 propellant, 1 atm N_2^+ , Reticon detector.

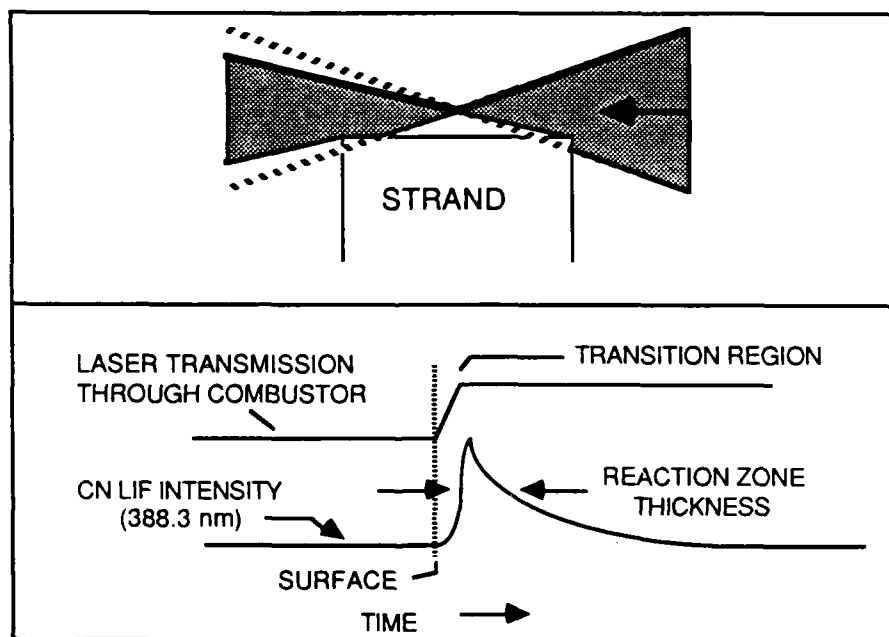


Figure 140. Schematic of CN LIF experiments with PMT detector.

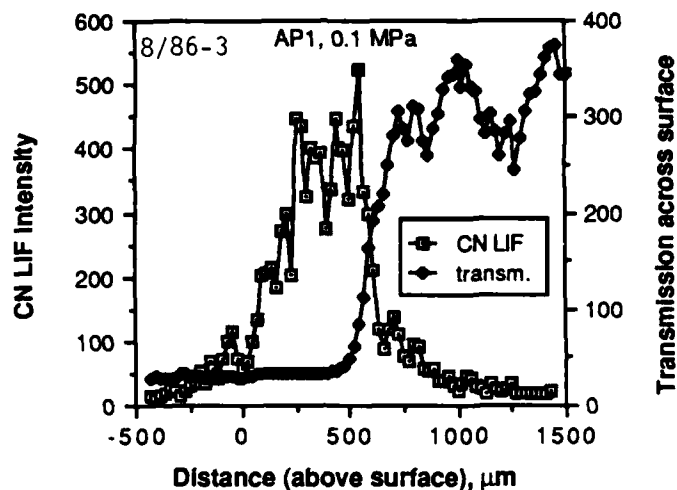


Figure 141. CN LIF, AP1 propellant. 1 atm N_2 +, 421.5 nm excitation, 10 mJ/pulse in flame, PMT detector, 20 μm slits.

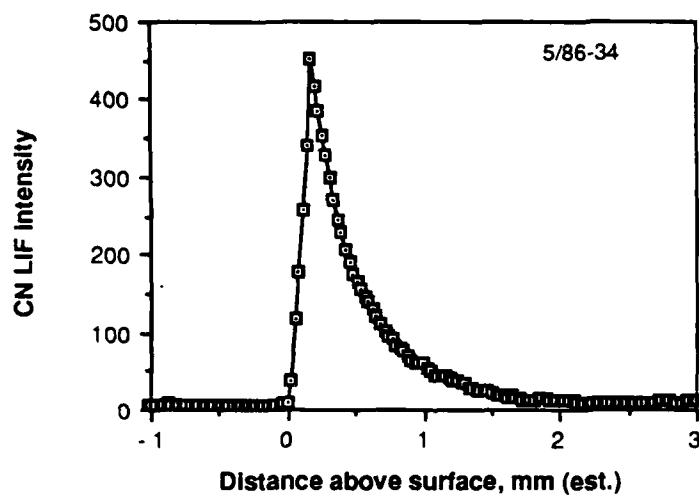


Figure 142. Same conditions as Figure 140; but CN LIF collected as 10 pulse running average, 3 mJ/pulse in flame.

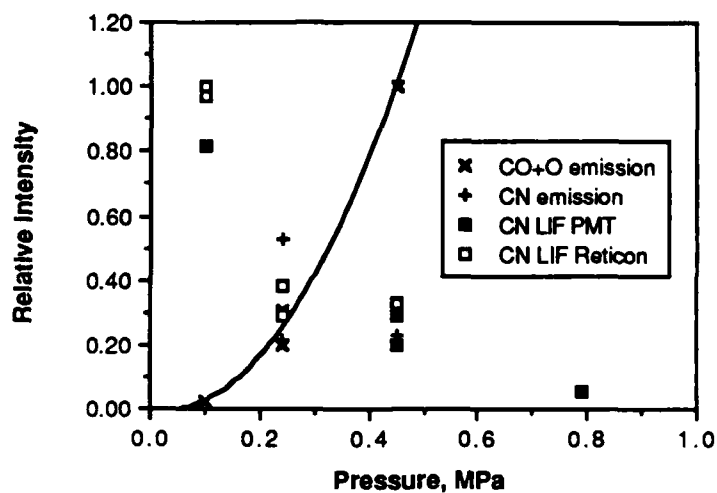


Figure 143. Influence of pressure on AP1 propellant flame quantities.

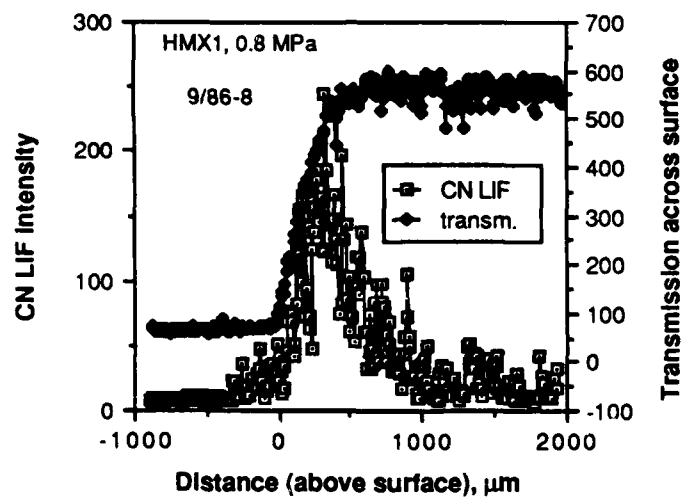


Figure 144. CN LIF, HMX1 propellant flame. 0.8 MPa, 421.5 nm excitation, 3.8 mJ/pulse in flame, PMT detector, 20 μm slits.

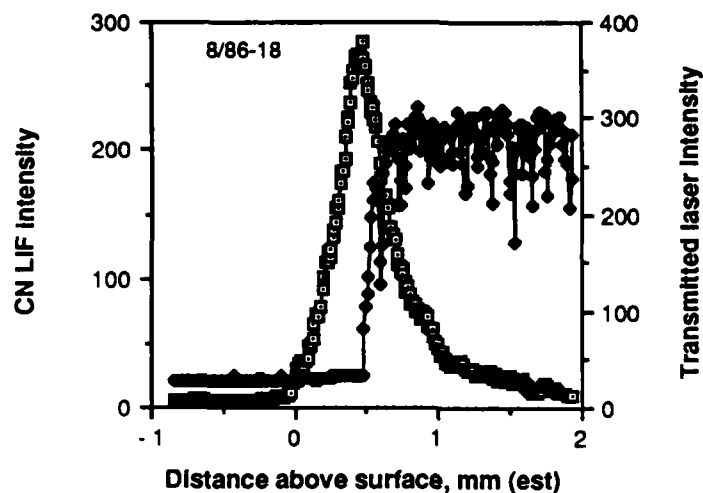


Figure 145. Same conditions as Figure 143; but 10 pulse running average on CN LIF channel, 5 mJ/pulse in flame.

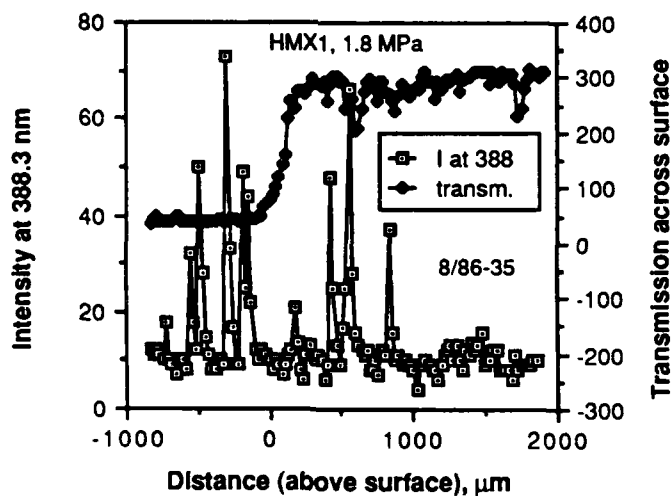


Figure 146. CN LIF, HMX1 propellant flame. 1.8 MPa, laser detuned from CN 421.5 nm bandhead, 4.5 mJ/pulse in flame (est.), PMT detector, 20 μm slits.

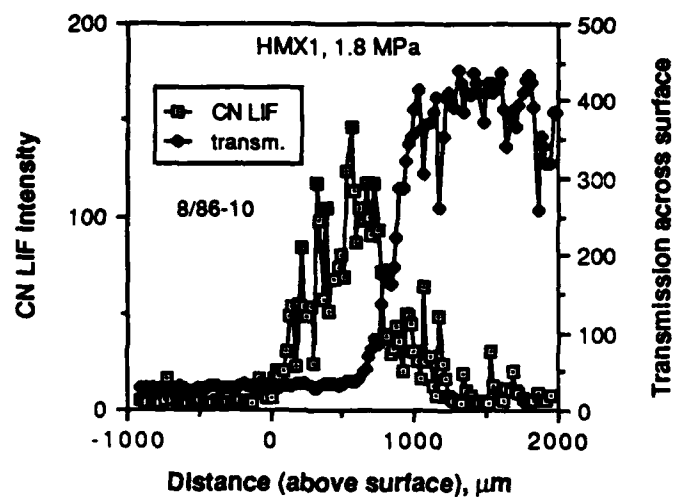


Figure 147. CN LIF, HMX1 propellant flame. 0.8 MPa, 421.5 nm excitation, 5 mJ/pulse in flame, PMT detector, 20 μ m slits.

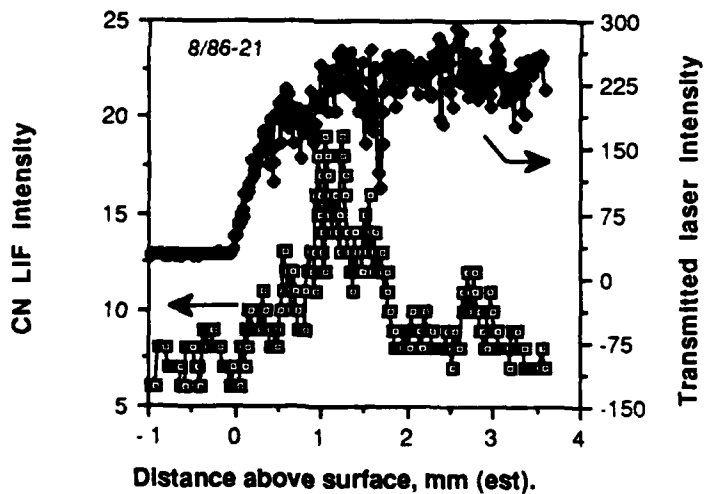


Figure 148. CN LIF, HMX2 propellant flame. 1.8 MPa, 421.5 nm excitation, 5 mJ/pulse in flame, PMT detector, 20 μ m slits.

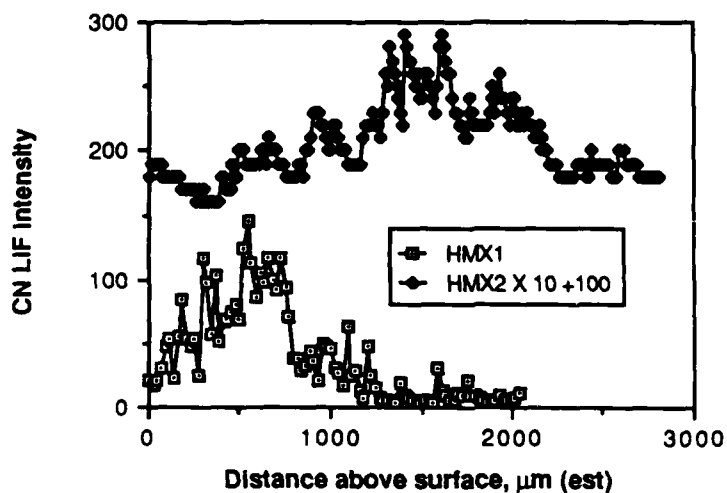


Figure 149. Comparison of CN LIF intensity profiles for propellants HMX1 and HMX2 at 1.8 MPa.

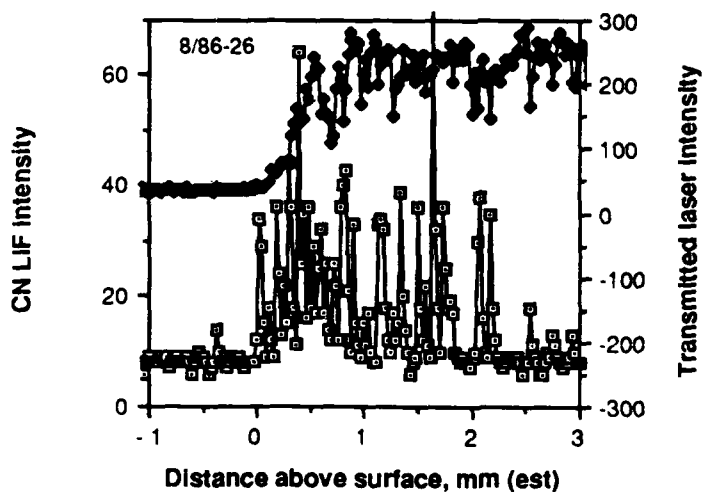


Figure 150. CN LIF, AN1 propellant flame. 0.8 MPa, 421.5 nm excitation, 4.5 mJ/pulse in flame (est.), PMT detector, 20 μm slits.

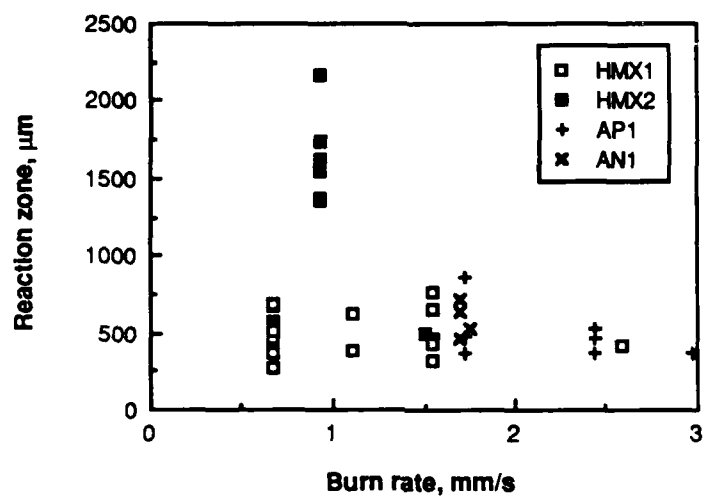


Figure 151. Reaction zone thickness as a function of propellant burn rate.

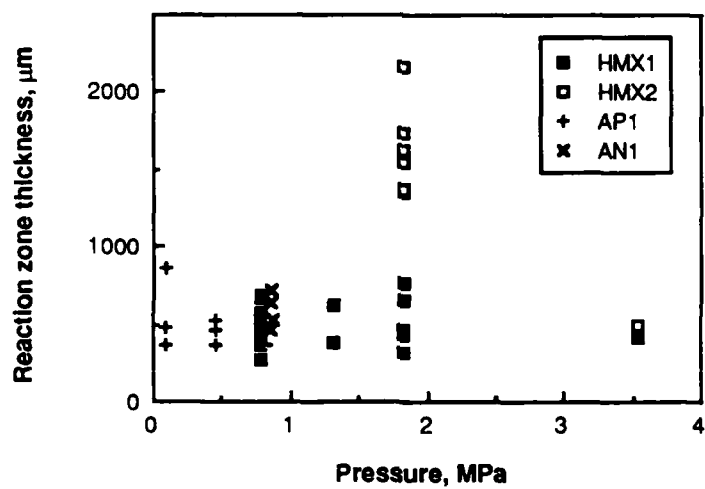


Figure 152. Reaction zone thickness as a function of pressure.

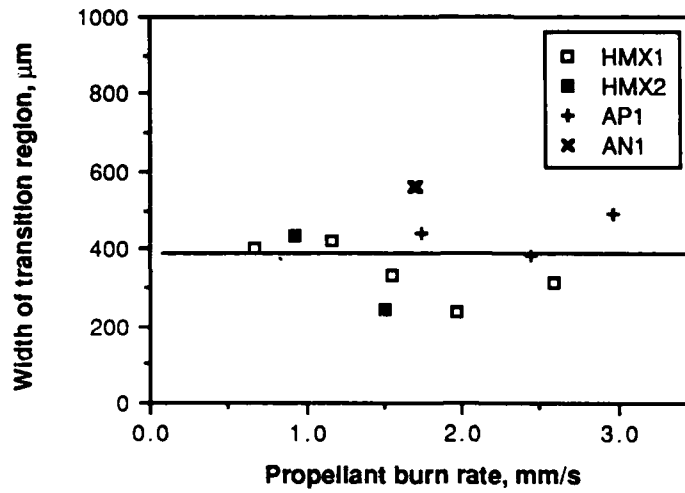


Figure 153. Relationship between width of transition region (defined in Figure 139) and propellant burn rate.

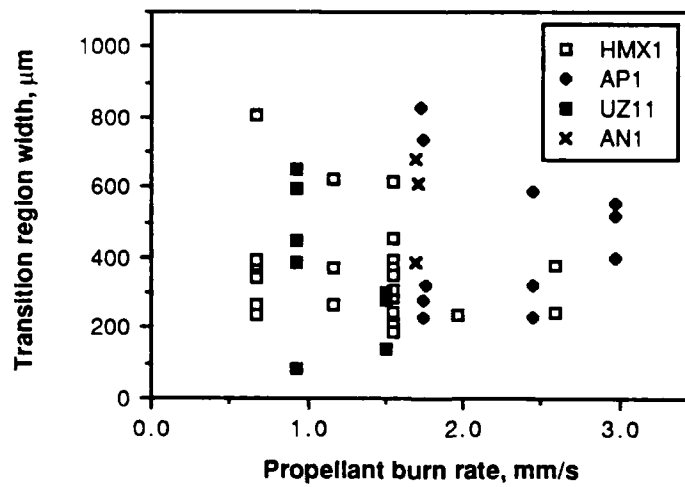


Figure 154. Relationship between width of transition region (defined in Figure 139) and propellant burn rate.

An attempt was made to excite the CN 1,2 bandhead at 419.7 nm. The resulting spectrum is shown in Figure 155. Excitation of the 1,2 bandhead should lead to the observation of the 1,1 bandhead (387.1 nm). This may be the case in Figure 155, although the 1,1 bandhead is not strongly excited. This type of experiment has little relevance to the propellant flames, but is interesting nonetheless.

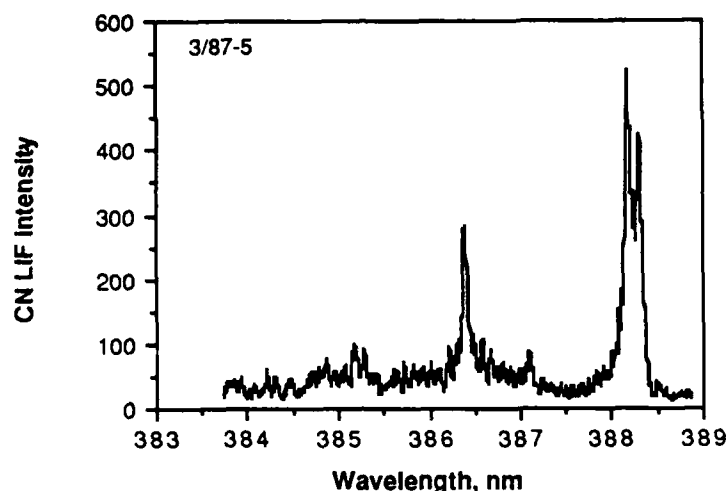


Figure 155. CN LIF, CH₄/N₂O flame. Inner cone, 419.7 nm excitation, 0.75 mJ/pulse in flame (est.), PMT detector, 50 μ m slits.

5.3. NH LIF EXPERIMENTS

NH is an important combustion radical like CN. There are some spectroscopic differences between the two, however. Unlike CN and OH, the "off-diagonal" bands of NH (the bands where $v' \neq v''$) are much weaker than those where $v' = v''$ (Ref. 17,203). The importance of this is that the transition probability between the 0,0 band sequence and the off-diagonal bands is small, which leads to much weaker signals in experiments similar to the CN experiments where the 0,1 or 1,0 bands are excited and the 0,0 and/or 1,1 bands are observed (or vice-versa). As shown in Table 16, these type of experiments have been done, although the signal levels are much lower than for similar experiments with OH and CN. On the plus side, the excited and observed lines are well removed spectrally and the rejection of scattered laser light shouldn't be a problem. An alternative is to excite one line in the NH 0,0 spectrum and observe another 0,0 line well removed from the laser wavelength. These experiments have also been done, as shown in Table 16. Whether or not scattered laser light can be rejected in the environment of a propellant flame was one of the subjects of this research.

The dye used in most of the NH LIF experiments was p-terphenyl (Lambdachrome 3400), with the output curve shown in Figure 156. The key to the "excite 0,0-observe 0,0"

NH LIF experiments was to determine if the separation between the filter transmission and dye output curves could be utilized to accomplish successful NH LIF measurements in high pressure propellant flames. NH LIF could be generated throughout the dye curve, as shown in Figure 157. It would be expected that the LIF signal divided by the laser intensity would be proportional to the NH population in the particular state being excited. Thus, one would expect that the NH model (Section 4.8) could produce a spectrum with a distribution similar to that shown in Figure 157. However, comparison of Figures 4.8.14-19 shows that the distribution of Figure 157, with its peak at about 338 nm, does not match either the 0,0 or the combined model at reasonable temperatures. What may be occurring is that the NH lines crowd together in the 338 nm region and the laser linewidth is exciting more lines at 338 nm than at 341 nm, for example. Excitation wavelengths of 341-342 nm were chosen for the propellant experiments to maximize signal and maximize the separation of the laser wavelength from the observed NH LIF 0,0 Q branch bandhead at 336.0 nm. Example NH LIF spectra for various wavelengths are shown in Figures 158 to 163.

An NH LIF experiment directly comparable to that shown in Figure 5.2.8 is shown in Figure 164. Note the obvious difficulty in rejecting laser light scattered from the surface of the propellant, as shown by the presence of signal before the surface passes through the collection volume. A possible NH LIF profile is observable in Figure 164, with a "reaction zone thickness" (as defined in Figure 5.2.7) of approximately 500 μm . However, it was very difficult to obtain a clean enough profile to analyze-usually the signal profile at 336 nm was dominated by "spikes" indicative of laser scattering, rather than NH LIF. Pulse averaging could be performed, as illustrated in Figure 165, although the profile obtained is so broad that it seems likely that both NH LIF and laser scattering are being averaged together, yielding a profile of questionable relevance. Typically (especially in experiments at higher pressures), the profiles resembled Figure 166, where no "reaction zone" was visible at all. Thus, it appears that propellant experiment using this type of LIF probe will require either a better spectrometer to separate the laser scattering from the NH LIF or will require that off-diagonal lines be excited.

As a first step in studying the possibility of improved separation of laser scattering and LIF, the Triplemate/Reticon system was used, analogous to the experiment described in Section 5.2. The resulting NH LIF spectrum is shown in Figure 167. The corresponding experiment in an HMX1 propellant flame (in air) is shown in Figure 168. Closing the intermediate slit on the Triplemate (as described in Section 5.1) lead to the NH LIF spectrum shown in Figure 169. The laser line has been filtered out, exactly as in the OH LIF experiments with the Reticon. This indicates that it may be possible to use such a spectrometer to improve the rejection in propellant LIF experiments, although the problems with using the Reticon (reduced sensitivity, longer pulse widths) remain. Despite the longer pulse widths used with the Reticon, the signal seen is LIF, as shown by an identical experiment where the laser is blocked (Figure 170). If any flame emission was contaminating the LIF spectrum, it would show in Figure 169. It was very difficult to obtain any NH LIF signal in the propellant flames with the Reticon system due to low signal levels. The best result is shown in Figure 171. This signal required the accumulation of many pulses, thus the spatial/temporal resolution is poor. It does indicate, however, that a multiple-stage spectrometer can be used to

separate the laser scattering from the NH LIF more successfully than the single stage spectrometer used in the PMT NH LIF experiments.

A brief study was made of NH 0,1 band excitation. This is accomplished by frequency doubling 610 nm laser light (see Section 5.4 for details since this is the same scheme for exciting OH LIF). Because of laser problems, the energy at 305 nm was low, so propellant experiments were postponed until after laser repair. A propellant experiment would involve exciting the NH 0,1 bandhead at 305 nm and observing the resulting NH LIF at either the 0,0 (336.0 nm) or 1,1 (337.1 nm) bandheads. For example, the resulting NH LIF from the excitation of the NH 0,1 bandhead at 305 nm is shown in Figure 172.

Table 16. Previous NH LIF schemes

Author	Excited		Observed		Ref
	Line/wavelength	Band	Line/wavelength	Band	
Parr, et al	305.06	1,0	1,1+0,0 broadband	0,0	17
Salmon, et al	P ₁ 7,5,11	0,0	R ₁ 5,3,9	0,0	192
Jeffries, et al	various	0,0, 1,0, 2,1	336.0	0,0	193
Morley	336.0	0,0	336.0	0,0	194
Anderson, et al	350.7	0,0	336.0?	0,0	195

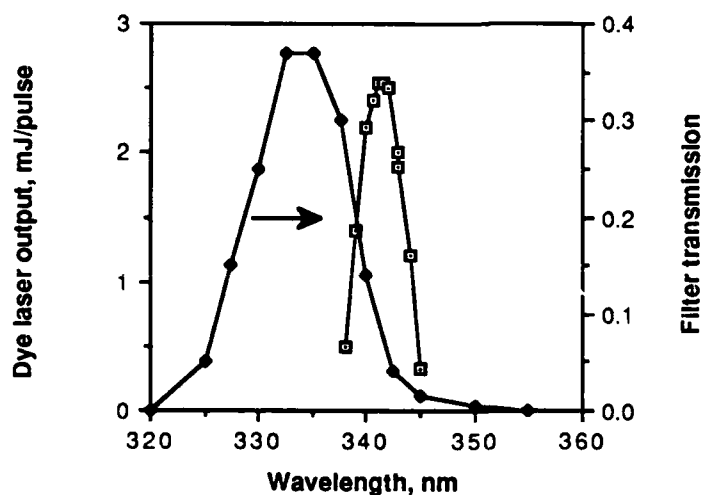


Figure 156. Comparison of dye output (PTP dye) and filter transmission (Ealing 35-9224 filter) curves.

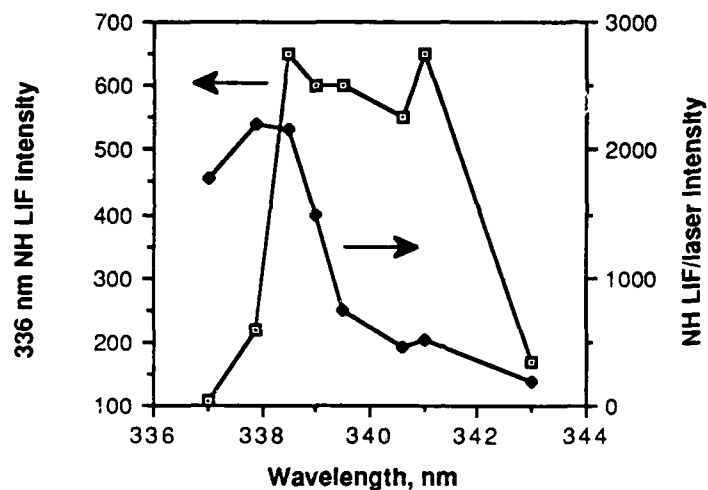


Figure 157. NH ($A^3\Pi-X^3\Sigma$) LIF intensity as a function of excitation wavelength; $\text{CH}_4/\text{N}_2\text{O}$ flame, inner cone, PMT detector.

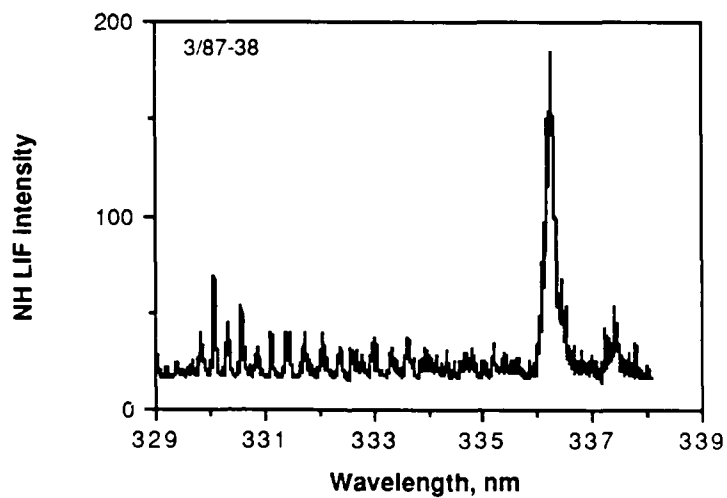


Figure 158. NH ($A^3\Pi-X^3\Sigma$) LIF, 343 nm excitation. 1.1 mJ/pulse in flame, $\text{CH}_4/\text{N}_2\text{O}$ flame, inner cone, PMT detector, 30 μm slits.

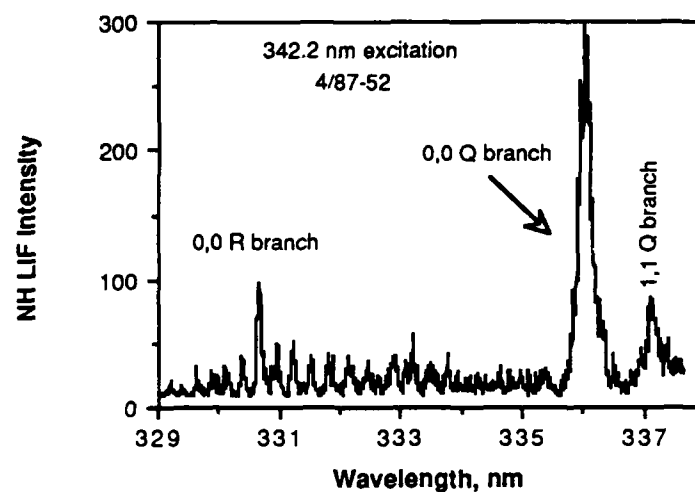


Figure 159 NH LIF, 342.2 nm excitation. 0.4 mJ/pulse in flame, $\text{CH}_4/\text{N}_2\text{O}$ flame, inner cone, PMT detector, 30 μm slits.

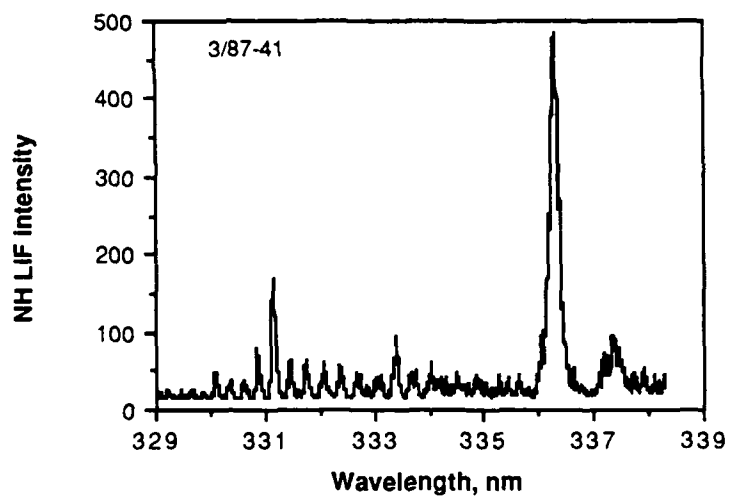


Figure 160. NH LIF, 341.8 nm excitation. 0.8 mJ/pulse in flame, $\text{CH}_4/\text{N}_2\text{O}$ flame, inner cone, PMT detector, 30 μm slits.

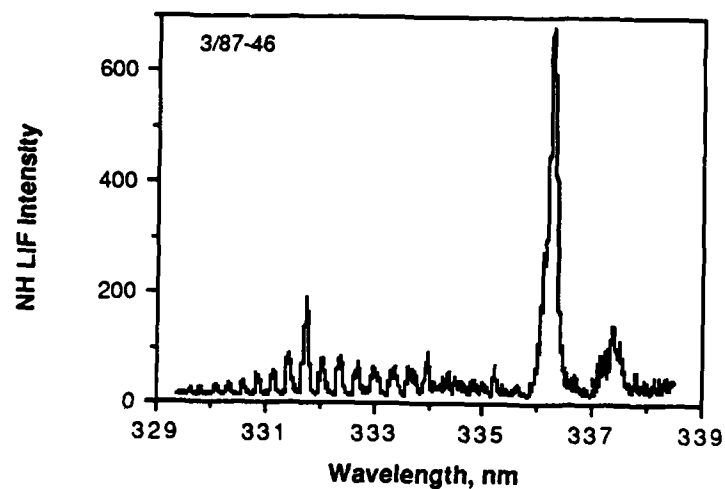


Figure 161. NH LIF, 341.0 nm excitation. 0.5 mJ/pulse in flame, CH₄/N₂O flame, inner cone, PMT detector, 30 μ m slits.

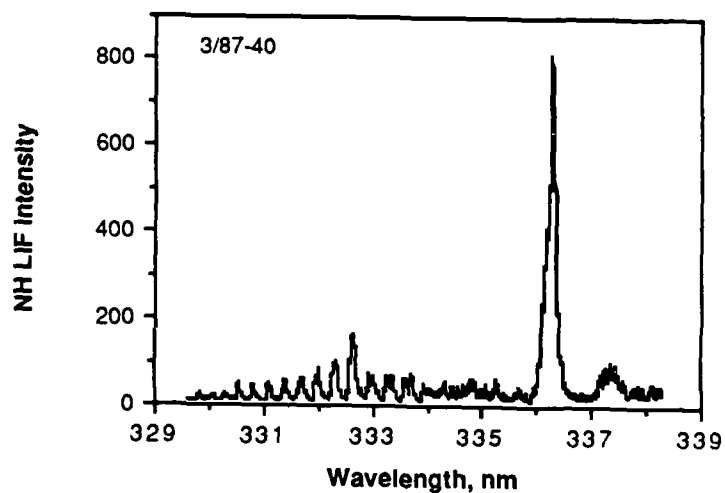


Figure 162. NH LIF, 340 nm excitation. 0.8 mJ/pulse in flame, CH₄/N₂O flame, inner cone, PMT detector, 30 μ m slits.

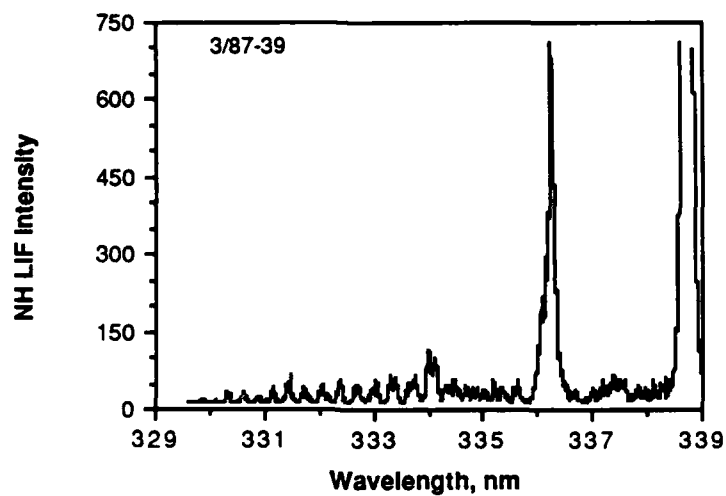


Figure 163 NH LIF, 338.5 nm excitation. 0.1 mJ/pulse in flame, CH₄/N₂O flame, inner cone, PMT detector, 30 μ m slits.

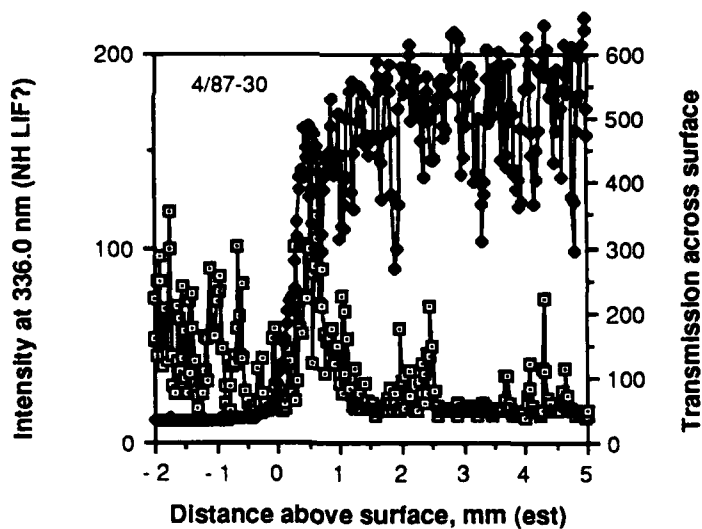


Figure 164. NH ($A^3\Pi-X^3\Sigma$) LIF, AP1 propellant. 341 nm excitation, 2 mJ/pulse (est.) in flame, 1 atm N₂+, 50 μ m slits, 1 pulse average both channels, PMT detector.

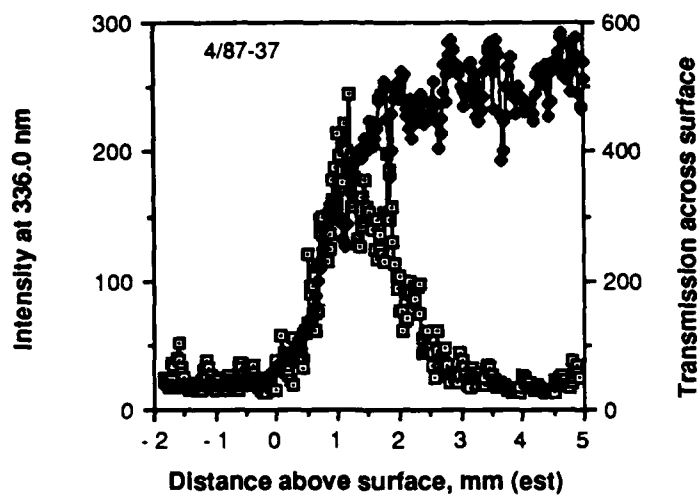


Figure 165. NH LIF, AP1 propellant. 341 nm excitation, 2.4 mJ/pulse in flame, 1 atm N_2 +, PMT detector, 3 pulse average on both channels, 50 μ m slits.

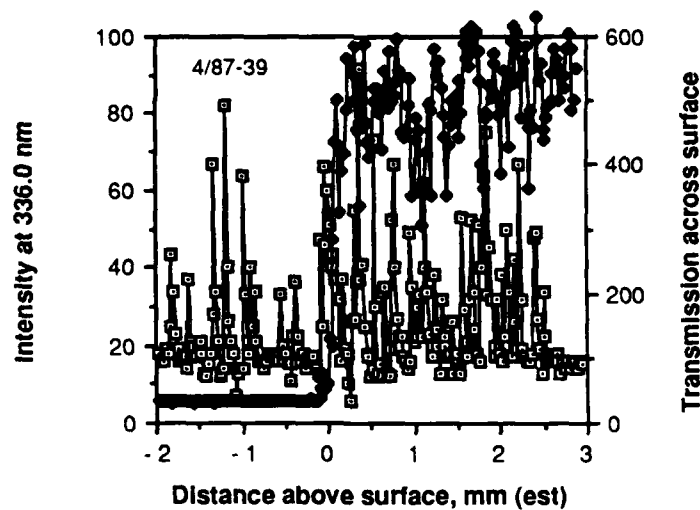


Figure 166. Same conditions as Figure 165; but HMX1, 1.8 MPa, 1 pulse average both channels.

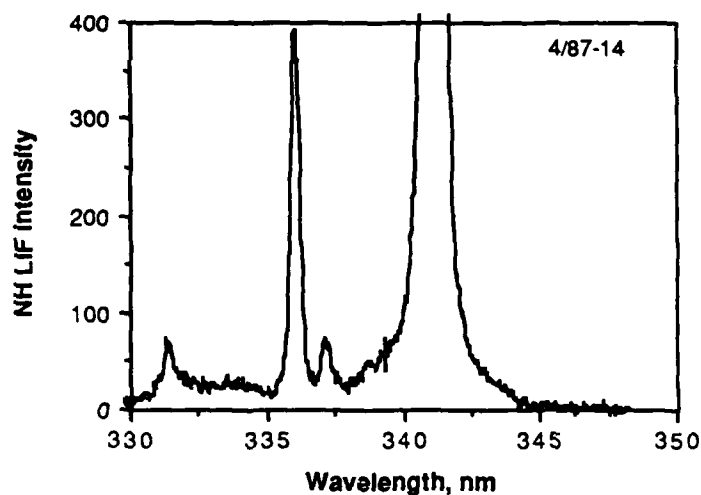


Figure 167. NH ($A^3\Pi-X^3\Sigma$) LIF, Reticon detector. 341 nm excitation, 3.8 mJ/pulse in flame, $\text{CH}_4/\text{N}_2\text{O}$ flame, inner cone, 0.035 nm/pixel dispersion, 500/200 μm slits, 93 pulse/2.32 s signal accumulation (40 Hz laser repetition rate).

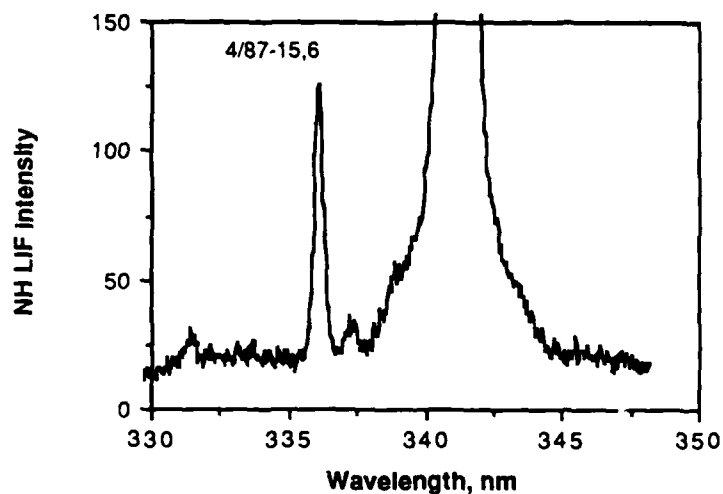


Figure 168. NH LIF, Reticon detector, HMX1 propellant flame. 341 nm excitation, 3.8 mJ/pulse in flame, 1 atm air, $h=?$, 0.035 nm/pixel dispersion, 500/200 μm slits, 58 pulse/1.17 s signal accumulation (50 Hz laser repetition rate).

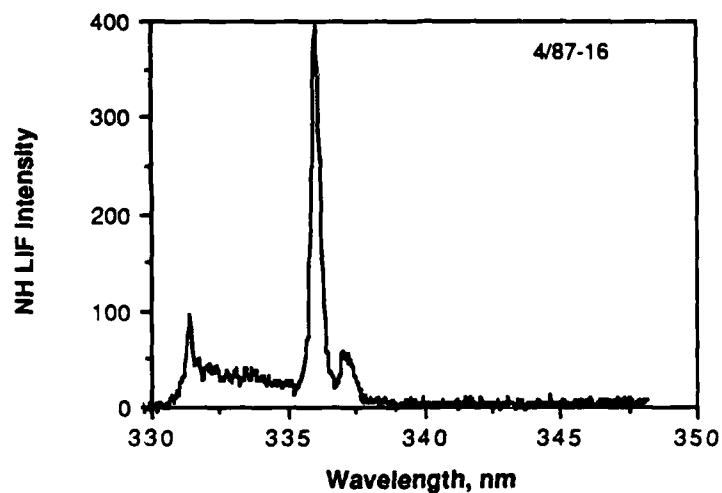


Figure 169. Same conditions as Figure 167; but intermediate slit on Triplemate=1.1 mm and 116 pulse/2.32 s signal accumulation (50 Hz laser repetition rate).

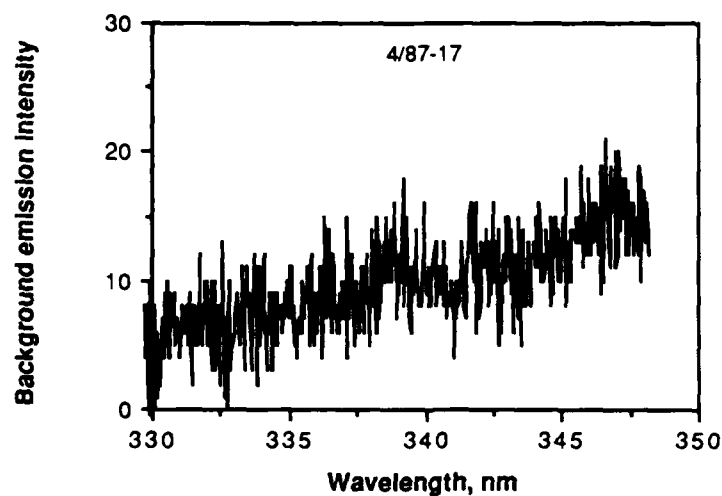


Figure 170. Same conditions as Figure 167 but laser blocked. Shows absence of emission even with relatively wide gate width (2.5 μ s).

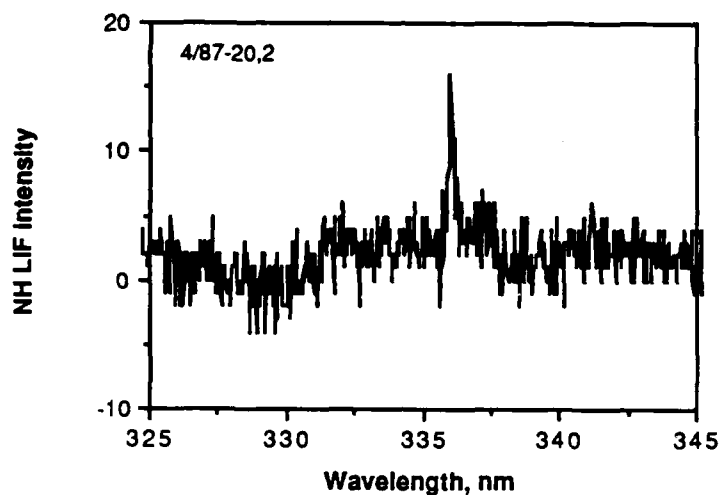


Figure 171. NH LIF, Reticon detector, AP1 propellant. 341 nm excitation, 3.2 mJ/pulse in flame (est.), 1 atm N_2+ , $h=0?$, 500/200 μm slits, 30 pulse/0.59 s signal accumulation (50 Hz laser repetition rate).

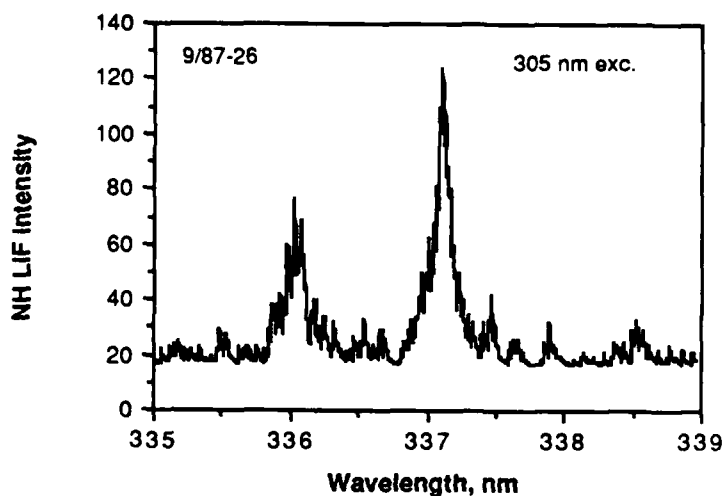


Figure 172. $NH(A^3\Pi-X^3\Sigma)$ LIF, 305 nm exc. (NH 1.0 band). 0.15 mJ/pulse in flame, CH_4/N_2O flame, inner cone, PMT detector, 30 μm slits.

5.4. OH LIF EXPERIMENTS (PART 2)

In this section, OH LIF experiments utilizing the excimer pumped dye laser are described. The main advance is the ability to digitally collected data at high repetition rates on the PMT detector. Early OH LIF PMT results were limited to chart recorder output (Figure 127) and thus temporal resolution available with the laser was limited by the chart recorder response time constant. For these experiments, the dye laser output with Rhodamine B (LC 6100) dye was frequency doubled down in to the OH region of the spectrum, as illustrated in Figure 173 and 174. The laser needed routine maintenance so the power output was rather low, however, the high concentration of OH in typical flames (often 1% or more) allowed OH LIF to be excited even with low laser power. One problem with these experiments is the lack of a suitable filter to use to aid in the rejection of unwanted scattering at the laser wavelength (as described in the NH LIF Section). It was expected that this would create problems near the propellant surface.

The OH 0,0 band extends from 306.4--320 nm. OH LIF could be excited over much of this range, as illustrated in Figures 175 to 177. Weak OH LIF in the off-diagonal bands could also be observed, as illustrated in Figure 179 and 180 (compare to 178, taken on same day). In Figure 179, The OH 1,0 R_1 bandhead at 281.1 nm and the 1,0 Q_2 bandhead at 282.9 nm are (weakly) visible, as are the OH 0,1 R_1 bandhead at 342.8 nm and the OH 0,1 Q_2 bandhead at 347.2 nm in Figure 180. Better examples of OH LIF in these bands can be found in Section 5.5. Propellant experiments were typically performed by exciting LIF at 306.4 nm and observing the large OH LIF peak at 313.8 nm (see Figure 174). Even with low laser power, saturation could be achieved in the CH_4/N_2O flame, as shown in Figure 181. Note that the 306 nm line shows less saturation because of the included laser scattering. The effect on the saturation behavior of changing the gate width of the collection electronics was briefly explored, as shown in Figure 182. The effect was not large. Reducing the gate width to 3 ns didn't have a large effect either, as shown in Figure 183.

An example of the OH LIF experiment analogous to the CN LIF experiment in Figure 5.2.8 is shown in Figure 184. Another OH LIF profile is compared to the CN LIF profile in the same propellant flame in Figure 185. The CN is confined to the "reaction zone" near the surface, while the OH is distributed throughout the flame. This is typical of OH and CN in premixed flames (Ref. 46,104). Results in propellants other than AP1 at atmospheric pressure were very difficult to obtain. This is not surprising considering the large variations in stoichiometry in the various propellant flames, as shown by the wide range of equilibrium OH concentrations in Table 17. Without a filter to aid in rejection of scattered laser light, there was typically large scattering signals near the propellant surface. This is illustrated in Figure 186, where a large signal is visible "below" the surface of the propellant as indicated by the transmission trace in the DB1 propellant flame. This is very probably just spurious scattering off the propellant strand. If the 313.8 nm data channel of Figure 185 is smoothed, the resulting profiles could perhaps be considered to be OH (Figure 187), but is probably just scattering from the flame. A similar experiment in the HMX1 propellant flame is shown in Figure 188. The scattering off the strand is even more obvious, as is the lack of OH LIF. In summary, it appears that successful OH LIF experiments in propellant flames will have to employ either or both of two modifications of the current techniques. Off-diagonal

excitation/observation, such as exciting the OH 1,0 band at 281 nm and observing the 0,0 and 1,1 band, could be used with a narrow band filter to aid in the rejection of the scattered laser light. Alternatively, a spectrometer with much better rejection, such as a double spectrometer, could be used to aid in the separation of the LIF from the scattered laser light.

The excimer laser was recently upgraded to allow scanning of the dye laser wavelength. The scanning can be synchronized with the rotation of the frequency doubling crystal. For example, the results of an OH LIF excitation scan experiment are shown in Figure 189. In this experiment, the spectrometer is set to a particular wavelength (the 310 nm OH LIF line in this case) and the laser is scanned. This type of excitation experiment can be used to determine the temperature of a molecule at a given point in this flame by relating the total fluorescence to the molecular line excited (Ref. 48). It might be possible to use this technique in the propellant flames (already attempted at atmospheric pressure (Ref. 17)), although the laser scattering in the flame would be difficult to filter out of the fluorescence.

Table 17. Equilibrium OH concentrations

Propellant	Mole % OH at equilibrium (3.5 MPa)
AP1	1.42
AP2	0.80
HMX1	0.066
HMX2	0.000008
AN1	0.01
DB1	<0.000001
DB2	<0.005

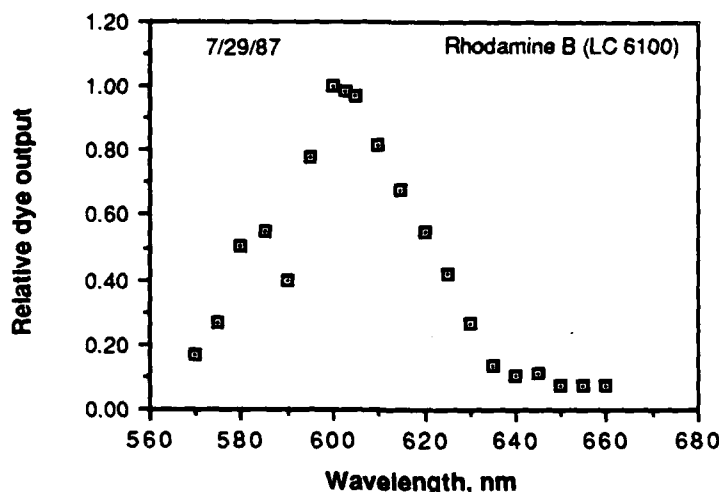


Figure 173. Excimer-pumped dye laser output with Rhodamine B (LC 6100) dye.

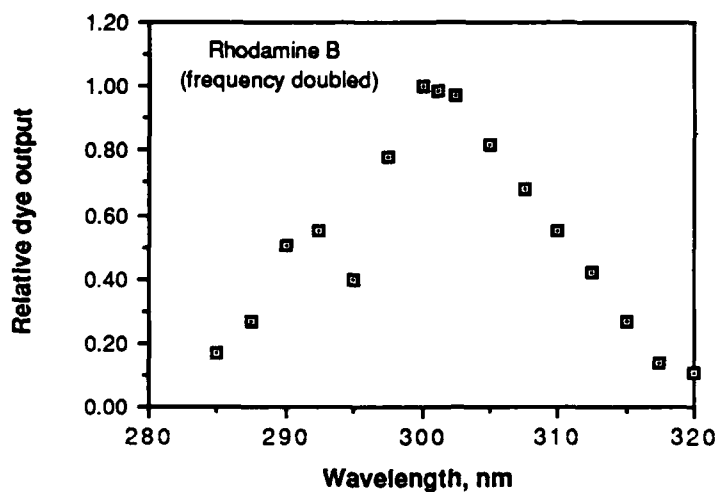


Figure 174. Estimated frequency-doubled excimer-pumped dye laser output with Rhodamine B dye.

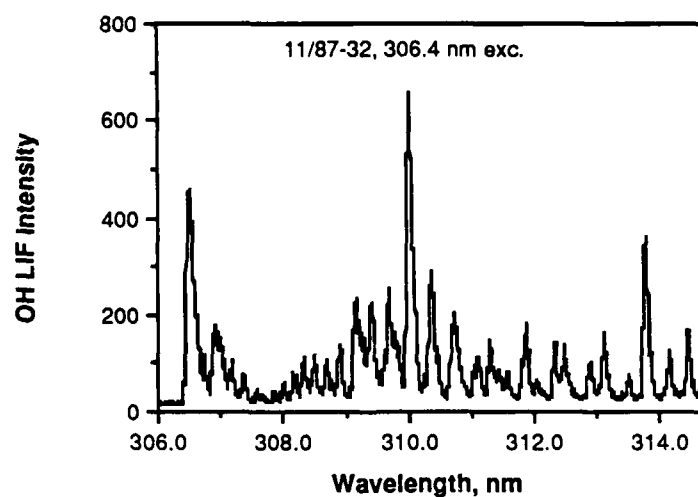


Figure 175. OH ($A^2\Sigma-X^2\Pi$) LIF, CH₄/N₂O flame, outer cone, 306.4 nm excitation, 0.002 mJ/pulse in flame (est), 30 μ m slits, PMT detector.

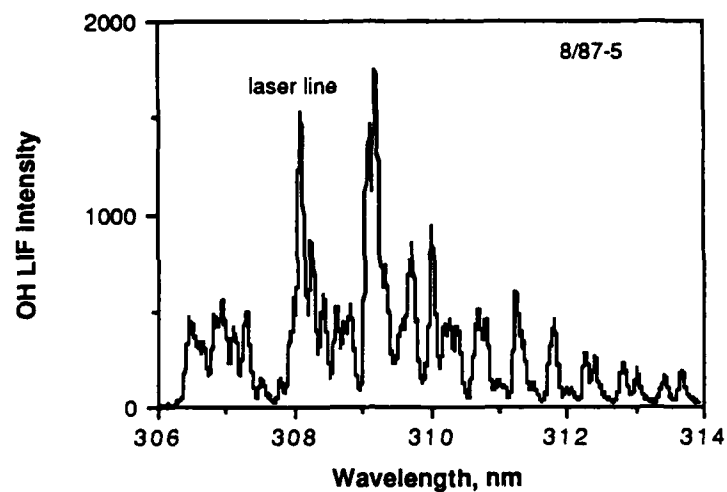


Figure 176. OH ($A^2\Sigma-X^2T$) LIF, 308.0 nm excitation. CH_4/N_2O flame, outer cone, 0.05 mJ/pulse in flame (est), 30 μ m slits, PMT detector.

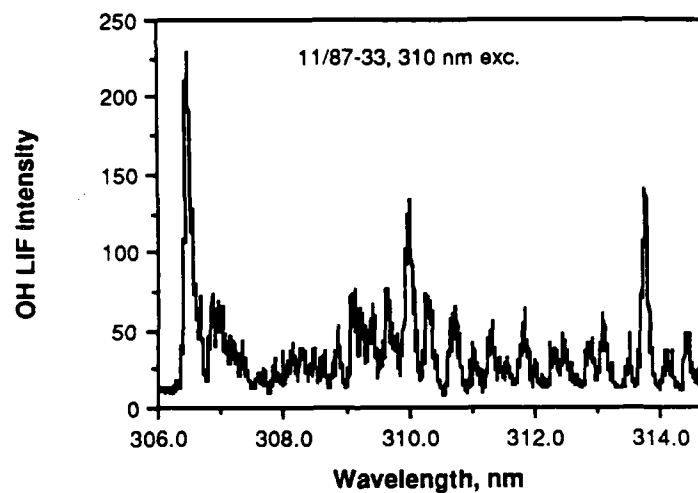


Figure 177. OH LIF, 310.0 nm excitation. CH_4/N_2O flame, outer cone, 0.002 mJ/pulse in flame (est), 50 μ m slits, PMT detector

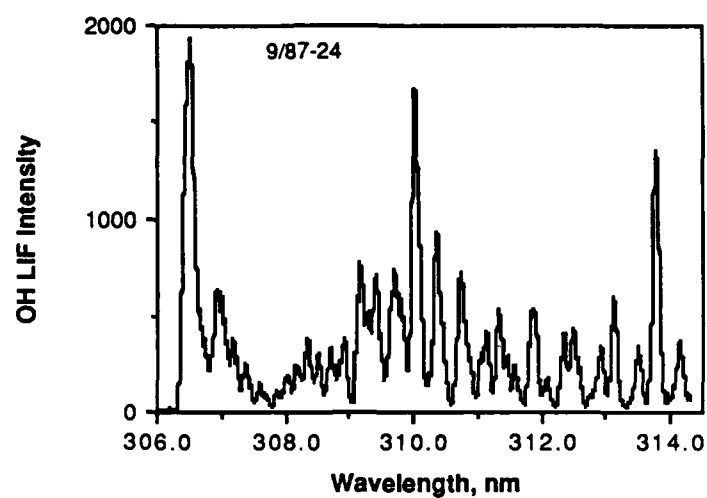


Figure 178. OH LIF, 306.4 nm excitation. $\text{CH}_4/\text{N}_2\text{O}$ flame, outer cone, 0.06 mJ/pulse in flame (est), 30 μm slits, PMT detector.

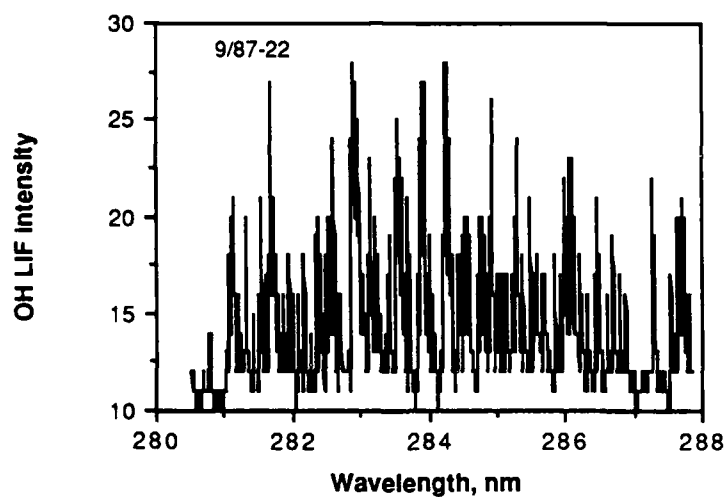


Figure 179. OH LIF, 306.4 nm excitation. $\text{CH}_4/\text{N}_2\text{O}$ flame, outer cone, 0.06 mJ/pulse in flame (est), 30 μm slits, PMT detector.

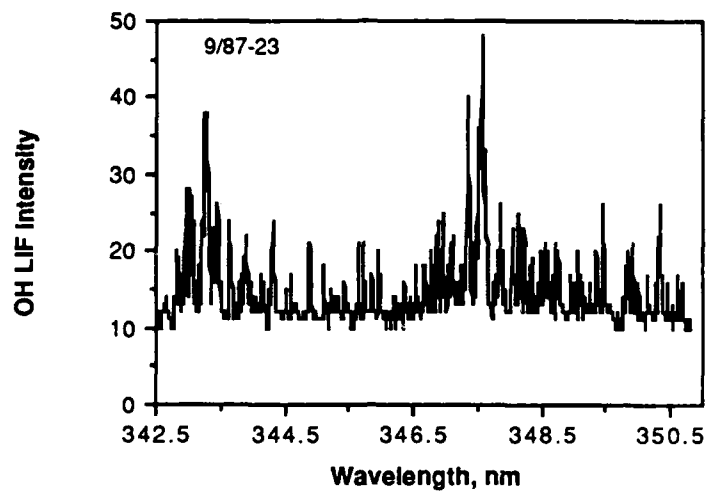


Figure 180. OH LIF, 306.4 nm excitation. CH₄/N₂O flame, outer cone, 0.06 mJ/pulse in flame (est), 30 μ m slits, PMT detector.

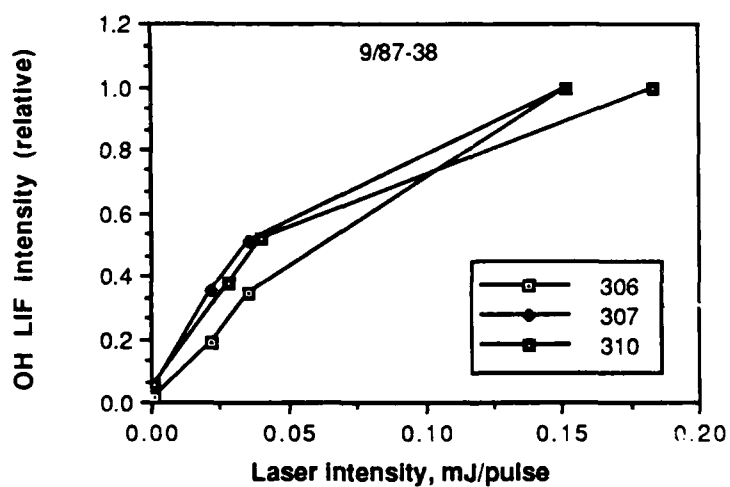


Figure 181. Saturation results for OH (A-X) LIF experiments, using excimer pumped dye laser. PMT detector, 306.4 nm excitation, 30 ns gate, 30 μ m slits, CH₄/N₂O flame, outer cone.

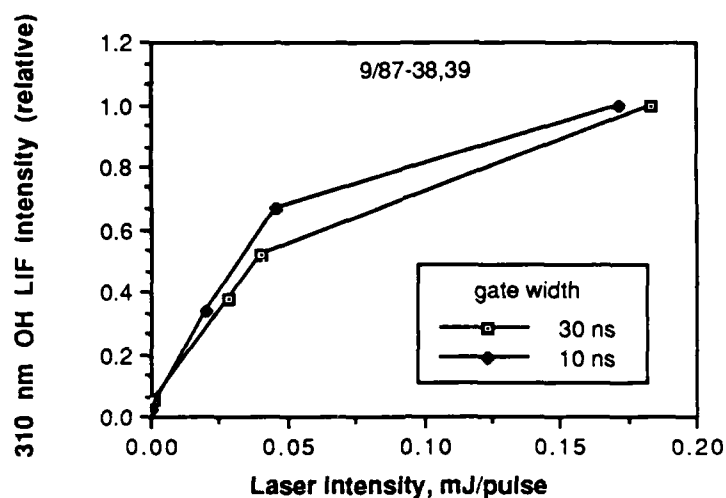


Figure 182. Saturation results for OH (A-X) LIF experiments using excimer pumped dye laser. PMT detector, 306.4 nm excitation, 30 ns gate, 30 μ m slits, CH₄/N₂O flame, outer cone.

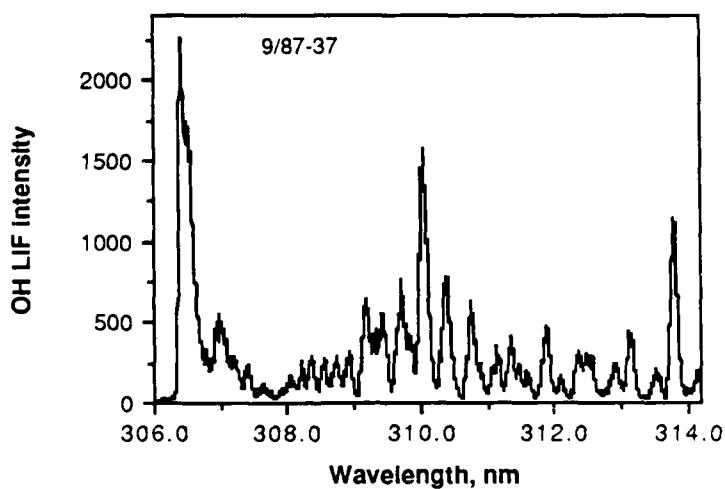


Figure 183. Same conditions as Figure 178 but 3 ns gate width.

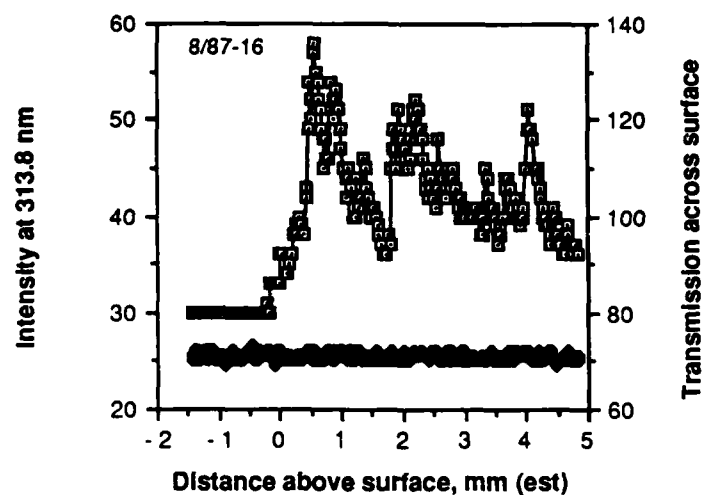


Figure 184. OH ($A^2\Sigma-X^2\Pi$) LIF, AP1 propellant flame. 1 atm N_2+ , 306.4 nm exc., 30 μ m slits, 0.003 mJ/pulse in flame, 313.8 nm channel collected as 10 pulse average, PMT detector.

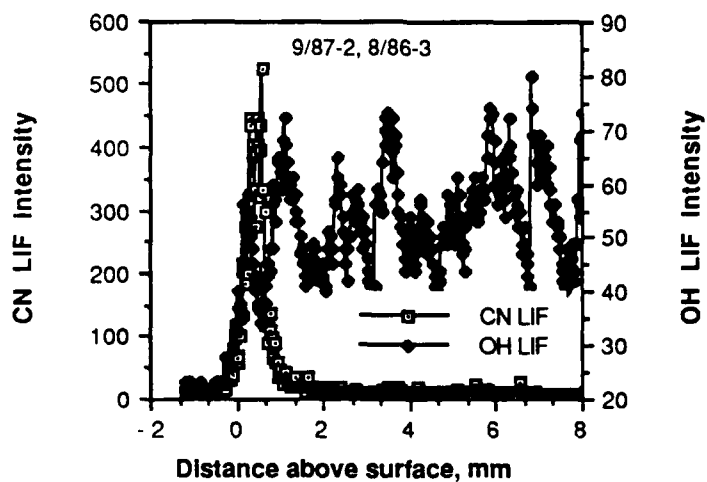


Figure 185. Comparison of OH LIF and CN LIF profiles in AP1 propellant flame. 1 atm N_2+ , PMT detector. OH LIF conditions same as Figure 183; CN LIF conditions shown in Figure 5.2.8.

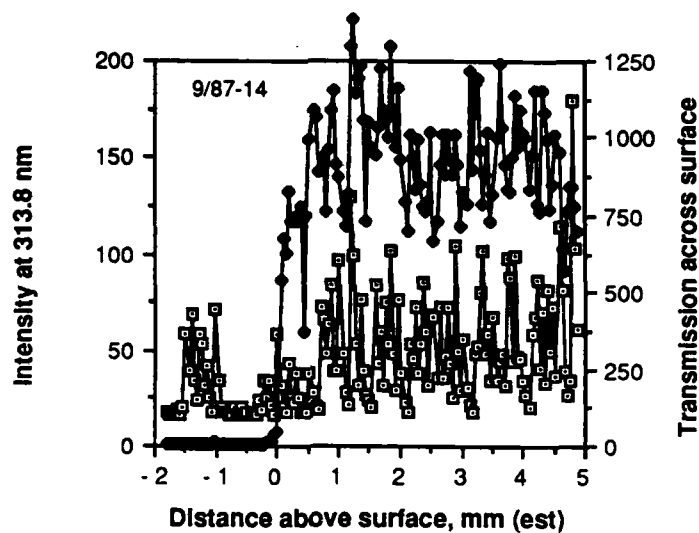


Figure 186. OH LIF, DB1 propellant flame. 1.8 MPa, 306.4 nm excitation, 0.2 mJ/pulse in flame (est), 30 μ m slits, PMT detector.

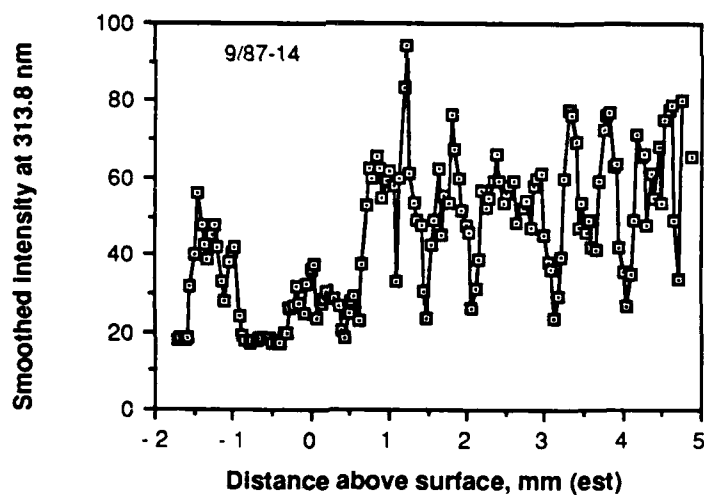


Figure 187. 313.8 nm channel of Figure 185 smoothed (3 pulse running average applied to collected data).

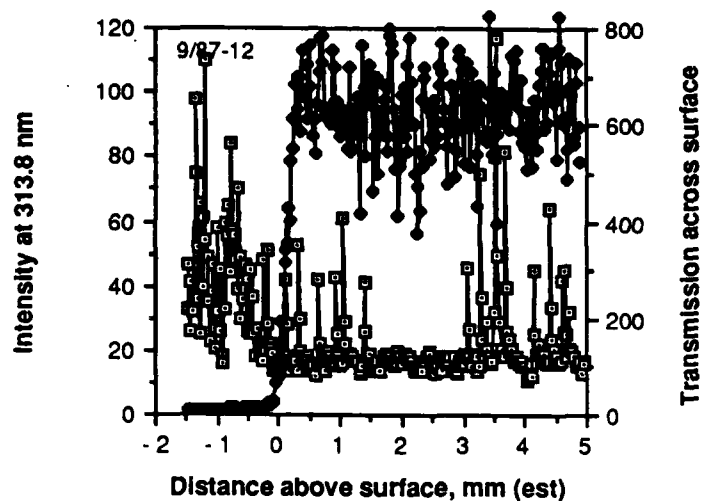


Figure 188 OH LIF, HMX1 propellant flame. 1.8 MPa, 306.4 nm excitation, 0.06 mJ/pulse in flame (est), 30 μ m slits, PMT detector.

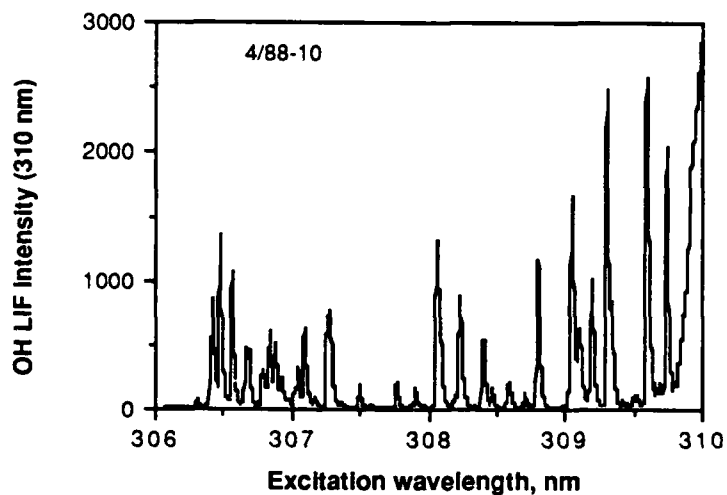


Figure 189. OH LIF excitation spectrum. $\text{CH}_4/\text{N}_2\text{O}$ flame, 310.0 nm observed, 0.15 mJ/pulse in flame (est), 30 μ m slits, PMT detector.

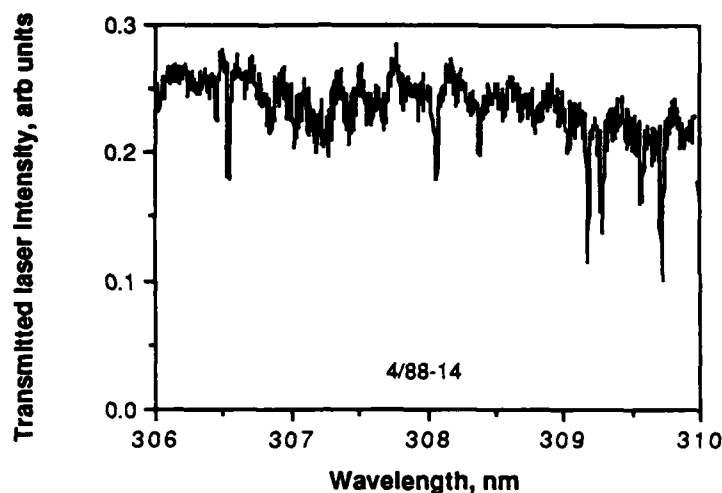


Figure 190. OH absorption spectrum. $\text{CH}_4/\text{N}_2\text{O}$ flame, 0.1 mJ/pulse in flame (est), PMT detector.

5.5. RAMAN SCATTERING UTILIZING 308 nm LIGHT

It was desired to use laser-Raman scattering for temperature and major species measurements in the propellant flames. One problem with this diagnostic probe is the presence of LIF interferences. Raman scattering is a relatively weak process in comparison to LIF, so fluorescence interference was anticipated to be a problem. LIF from C_2 and other molecules has been observed in Raman scattering experiments using 532 nm lasers (Ref. 196). It was anticipated that LIF interferences would also be present with the 308 nm excimer beam, with OH LIF previously observed (Ref. 82,197,198). In fact, the 308 nm radiation excited LIF in several molecules in the calibration $\text{CH}_4/\text{N}_2\text{O}$ flame, including OH, NH, CN, and C_2 .

OH LIF was the strongest fluorescence observed with the 308 nm beam. For example, the OH LIF in the R branches of the A-X 0,0 band is illustrated in Figure 191. This LIF is so strong that many of the other OH bands can also be observed. For example, LIF in the 1,0 band sequence and in the $^5\text{R}_{12}$ band of the 0,0 transition is shown in Figure 192 and 193. LIF from the 0,1 band sequence was also seen (Figure 194). The relative intensity of the bandheads was 0,0 R_1 (306.4 nm) : 1,0 R_1 (281.1 nm) : Q_2 0,1 (347.2 nm) : 0,0 $^5\text{R}_{21}$ (302.1 nm) = 82:2:16:1. NH LIF was also strong from the reaction zone of the $\text{CH}_4/\text{N}_2\text{O}$ flame when the 308 nm beam was used. The resulting LIF is shown in Figure 195. This spectrum can be compared to the corresponding emission spectrum of NH (Figure 30), showing the abnormal excitation of the 1,1 and 2,2 bandheads. This is perhaps not surprising since the 308 nm beam is apparently exciting the NH 2,1 Q branch, which has a red-degraded bandhead at 307.6 nm (Ref. 172,173). Relatively weak CN LIF could be observed at 388.3 nm (Figure 196) and C_2 LIF at 516.5 nm (Figure 197), with the overall ratio of LIF intensities being OH

(306.4 nm) : NH (336.0 nm) : CN (388.3 nm) = 82:33:5.5. The C_2 (and perhaps the CN) is probably being produced by some photochemical (Ref. 193) or collisional (Ref. 199) process in the flame. "Photofragmentation" of molecules to form fluorescing species is used as a diagnostic (Ref. 200), but here it is a drawback to the technique. This LIF has also been observed with the Reticon system. For example, OH LIF can be seen in Figure 198 (highest resolution), and both OH and NH LIF can be seen in Figure 199 (lowest resolution).

The observed LIF is a strong interference for Raman studies. For example, N_2 Stokes Raman is overlain by the NH LIF spectrum, and N_2 anti-Stokes Raman is overlain by OH 1,0 LIF. The problem is the relative intensity of the Raman and LIF effects. For example, Figure 200 presented a comparison of the intensities of NH LIF in the reaction zone of a CH_4/N_2O flame and N_2 Raman in air. The intensities are comparable. In a real flame, however, the N_2 Raman signal would be several orders of magnitude smaller and would be swamped by the NH LIF signal. In an NH-free flame, N_2 Raman with a 380 nm beam might be successful. No common solid propellant flame fits this category since all contain nitrogen and most have been observed to have NH emission. Note that higher pressure increases the Raman signal by increasing the concentration of the subject molecules, so (in the absence of LIF interference) high pressure Raman experiments might have significant promise. Possible LIF interferences with other Raman species are presented in Table 17. Using a tunable dye laser beam pumped by the excimer laser may have better prospects for success since the laser could be tuned to minimize LIF interference, although the laser energy will be much less. Note that the 2-line nature of the excimer beam is evident in the low temperature N_2 Raman spectrum in Figure 200 and would complicate temperature measurements.

Raman measurements were attempted in several propellant flames. In an AP1 propellant flame at atmospheric pressure (N_2), a spectrum very similar to that obtained in the CH_4/N_2O flame was obtained. As shown in Figure 200, both NH and OH LIF are observed, as is some Na (and probably OH) emission, visible due to the wide pulse width (100 μs) of the Reticon pulser. A comparable emission spectrum is shown in Figure 201. Similar Raman experiments in HMX1 propellant flames were unsuccessful--the propellant extinguished consistently when the 308 nm beam impinged on the surface. This radiative extinguishment was reproducible and not observed with AP1 propellant. This is good evidence that the 308 nm radiation is significantly perturbing the chemistry in the propellant flames.

Table 18. Interferences with Raman measurements using 308 nm laser light

Species	Raman shift (Ref. 15) cm ⁻¹	Raman (relative to 308 nm), nm	
		Stokes	anti-Stokes
H ₂	4169	353.4	273.0
N ₂	2331	331.8	287.4
NO	1876	326.9	291.2
O ₂	1556	323.5	293.9
OH	3665	347.2	276.8
CH ₄	2916	338.4	282.6
C ₂ H ₂	3372	343.7	279.0
CO ₂	1388	321.8	295.4
H ₂ O	3657	347.1	276.8
HCN	3311	343.0	279.5
CO	2143	329.8	288.9

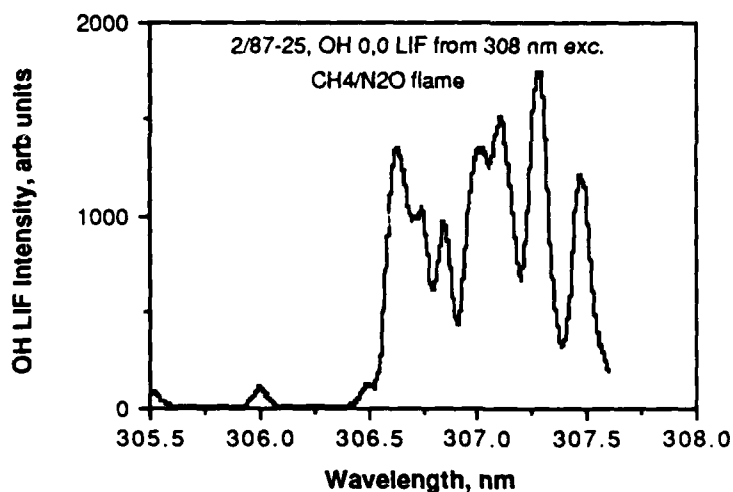


Figure 191. OH ($A^2\Sigma-X^2\Pi$) LIF from 308 nm excitation. CH₄/N₂O flame, inner cone, 15 mJ/pulse in flame, PMT detector, 30 μ m slits.

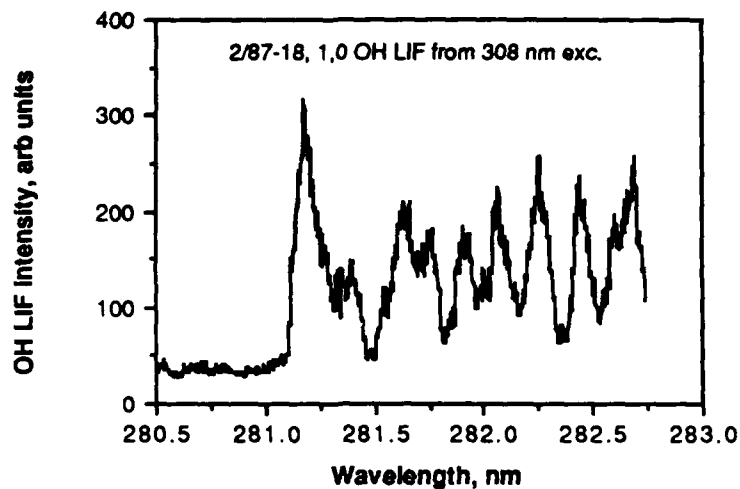


Figure 192. OH (A²Σ-X²Π, 1,0 band) LIF from 308 nm excitation. CH₄/N₂O flame, inner cone, 4 mJ/pulse in flame (est.), PMT detector, 10 μm slits.

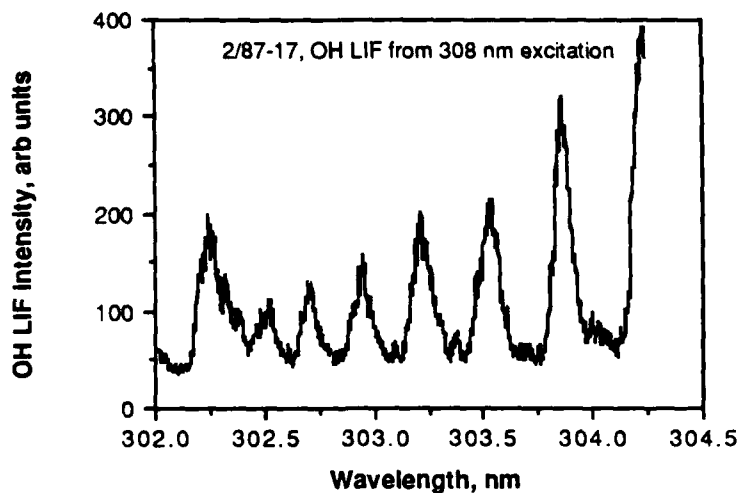


Figure 193. OH (A²Σ-X²Π, 5R₂₁ band) LIF from 308 nm excitation. CH₄/N₂O flame, inner cone, 4 mJ/pulse in flame (est.), PMT detector, 10 μm slits.

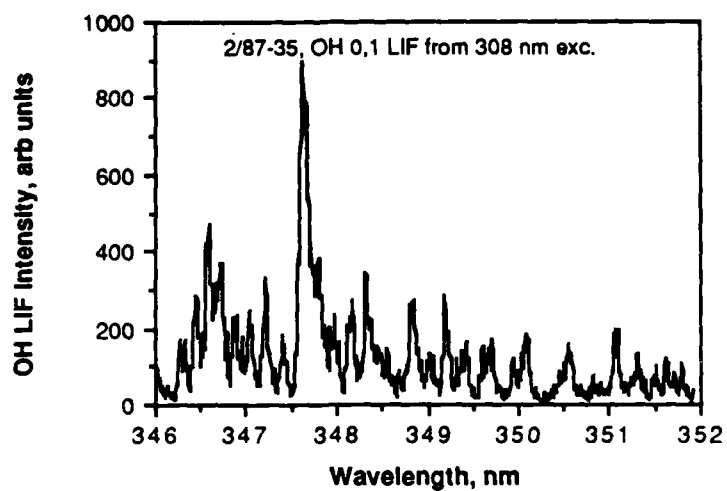


Figure 194. OH ($A^2\Sigma-X^2\Pi$, 0,1 band) LIF from 308 nm excitation. $\text{CH}_4/\text{N}_2\text{O}$ flame, inner cone, 12 mJ/pulse in flame (est.), PMT detector, 30 μm slits.

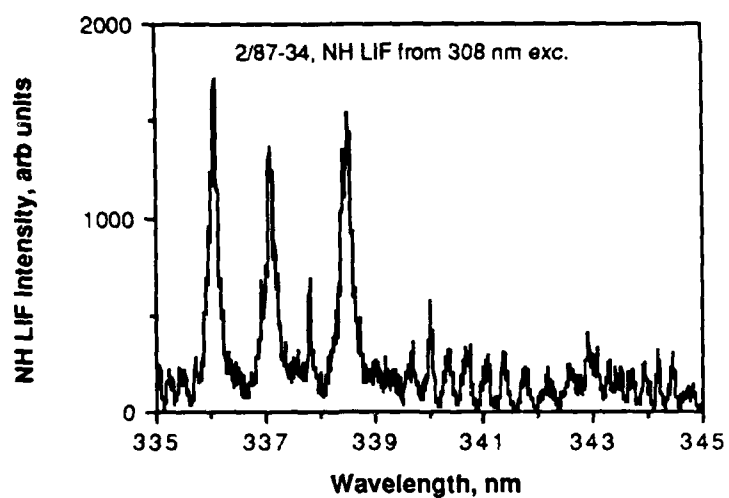


Figure 195. NH ($A^3\Pi-X^3\Sigma$, 0,0 band sequence) LIF from 308 nm excitation. $\text{CH}_4/\text{N}_2\text{O}$ flame, inner cone, 12 mJ/pulse in flame (est.), PMT detector, 30 μm slits.

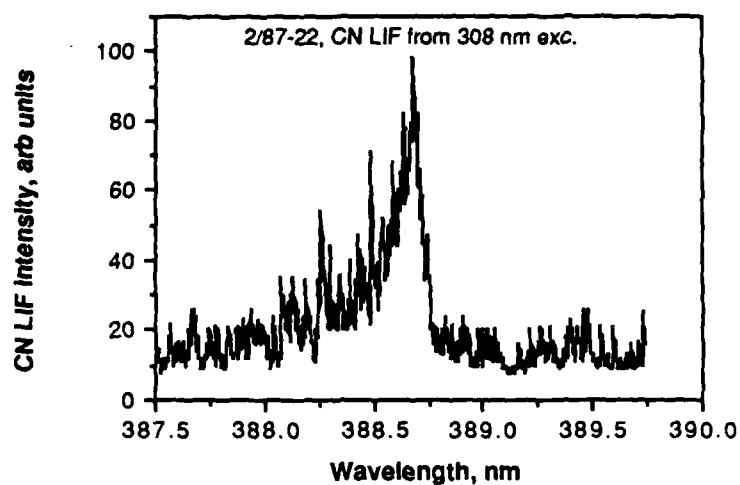


Figure 196. CN ($A^2\Sigma-X^2\Sigma$, 0.0 band) LIF from 308 nm excitation. $\text{CH}_4/\text{N}_2\text{O}$ flame, inner cone, 12 mJ/pulse in flame, PMT detector, 30 μm slits.

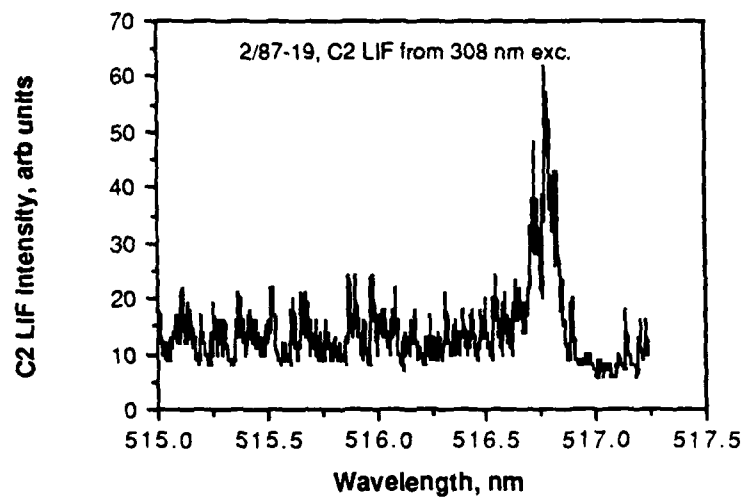


Figure 197. C_2 ($A^2\Sigma-X^2\Pi$, 0.0 band) LIF from 308 nm excitation. $\text{CH}_4/\text{N}_2\text{O}$ flame, inner cone, 12 mJ/pulse in flame, PMT detector, 30 μm .

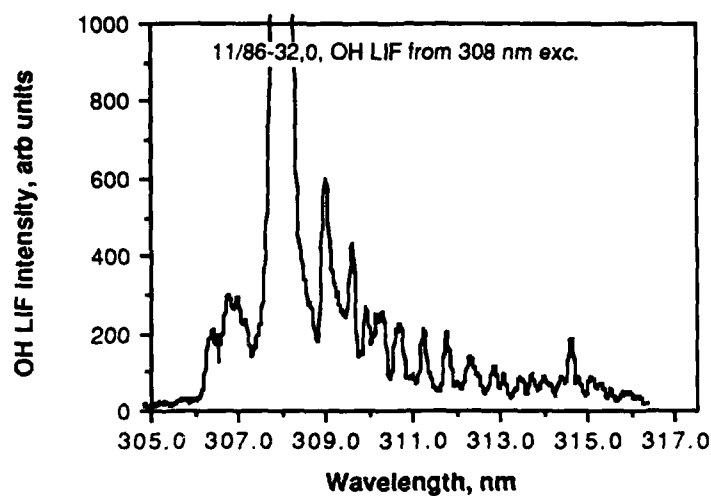


Figure 198. OH ($A^2\Sigma-X^2\Pi$, 0,0 band) LIF from 308 nm excitation. CH_4/N_2O flame, inner cone, 15 mJ/pulse in flame (est.), Reticon detector, 700 pixels, 0.0175 nm/pixel dispersion, 500/200 μm slits, 7 pulse signal accumulation, 5 μs gate width.

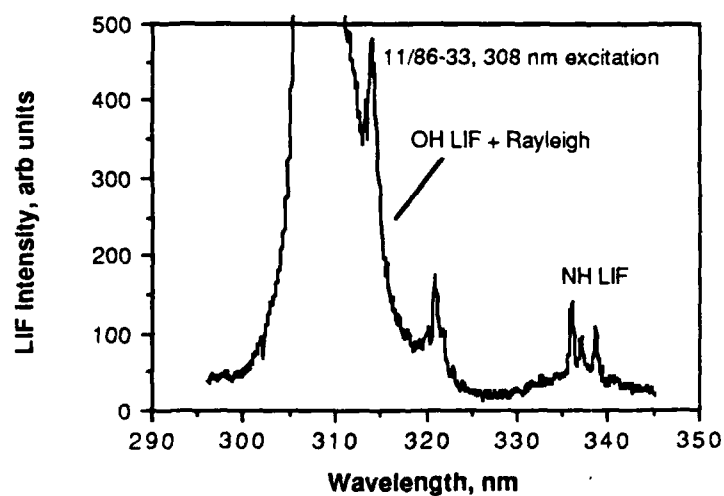


Figure 199. OH ($A^2\Sigma-X^2\Pi$, 0,0 band) LIF from 308 nm excitation. CH_4/N_2O flame, inner cone, 15 mJ/pulse in flame (est.), Reticon detector, 700 pixels, 0.07 nm/pixel dispersion, 500/200 μm slits, 7 pulse signal accumulation, 5 μs gate width.

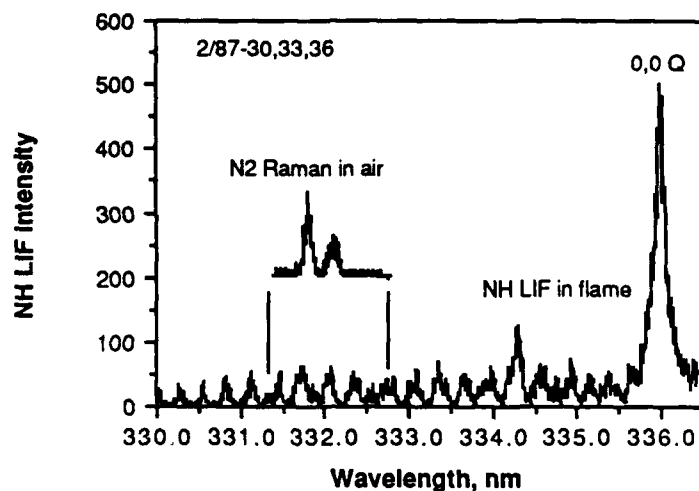


Figure 200. NH LIF and N₂ Raman from 308 nm excitation. LIF: CH₄/N₂O flame, inner cone, 12 mJ/pulse in flame (est.), PMT detector, 30 μ m slits; Raman, 1 atm air, 12 mJ/pulse in flame (est.), PMT detector, 30 μ m slits.

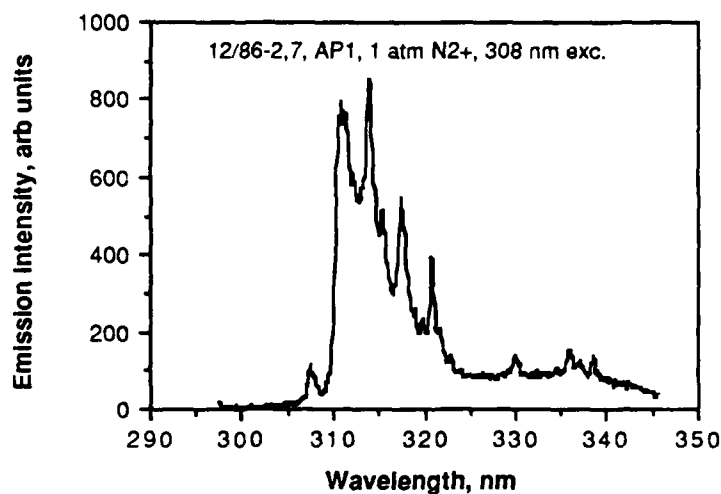


Figure 201. OH and NH LIF from 308 nm excitation. AP1 propellant flame, 1 atm N₂, 15 mJ/pulse in flame (est.), Reticon detector, 500/200 μ m slits, 44 pulse signal accumulation, 5 μ s gate width.

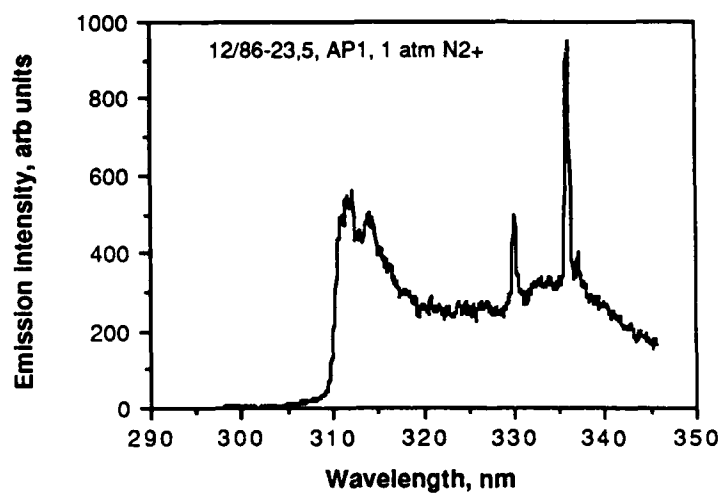


Figure 202. Emission from AP1 propellant flame. 1 atm N_2+ , Reticon detector, 500/200 μm slits, 0.59 s exp. time, $h=??$.

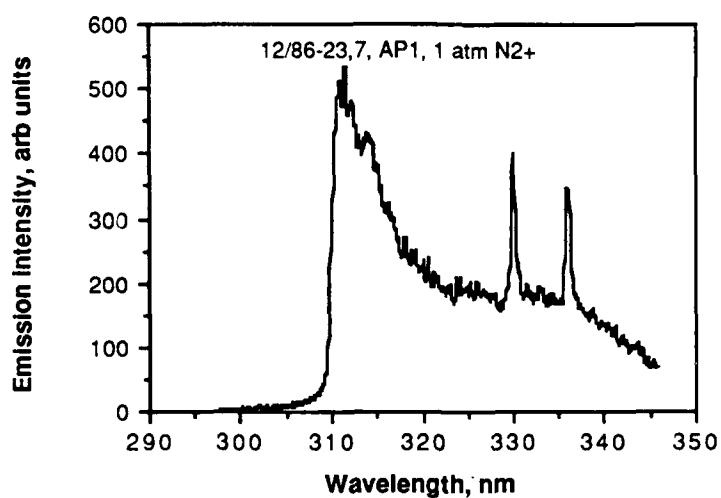


Figure 203. Emission from AP1 propellant flame. 1 atm N_2+ , Reticon detector, 500/200 μm slits, 0.59 s exp. time, $h=??$.

6.0 SUMMARY, CONCLUSIONS, RECOMMENDATIONS

In this section I hope to summarize the status of species and temperature measurements in solid propellant flames (much more briefly than in the Introduction), give some conclusions about the applicability of current techniques to this area, and make some observations and recommendations about future approaches and goals. More detailed information can be found in documents generated from recent workshops in this area (Ref. 201).

From the data presented in the previous sections, it is apparent that some atoms and molecules can be probed in solid propellant flames up to moderate pressures (20-30 atm) using emission spectroscopy (relatively low resolution) and laser-based techniques such as LIF and laser-Raman scattering. These diagnostics techniques are limited to a relatively small number of molecules. For example, LIF can be used to measure CN, NH, OH, CH, NO, and several other small molecules, while laser-Raman scattering could be used to measure N_2 , CO, CO_2 and some of the hydrocarbon molecules such as C_2H_2 . These molecules can be very enlightening when compared to the predictions from detailed kinetic modeling as described in the introduction, but large gaps still remain in the knowledge of the early reactions very close to the propellant surface. The initial breakup products of the solid propellant ingredients are still relatively unknown, although much progress has been made. Mass spectrometer studies have identified many larger molecules and will probably retain an important role in experimental studies. It may turn out that the importance of these earliest reactions is their role in the production of the smaller, reactive radicals which may control the chemistry of the propellant flame. This was found to be good approximation in the combustion of larger hydrocarbons, where it was found that the main influence of the large (C_8) molecules was in the relative amounts of the C_1 and C_2 radicals that were formed during the breakup of the parent molecule (Ref. 185). In any case, the breakup of these larger molecules needs further study, especially for the polymeric binder constituents found in typical propellant binders. Temperature measurements are also important, but seem to relatively straightforward.

One area that particularly needs further study is that of high pressure combustion kinetics. Current kinetic modeling of solid propellant flames (Ref. 74,94,95) utilizes kinetic data and mechanism understanding developed in atmospheric and lower pressure flames and reactors. There is a important need to verify the applicability of this low pressure data to the high pressures encountered in solid propellant combustion. The appropriate place to accomplish this verification is not in the very complex and poorly understood environment of a high pressure solid propellant flame, but in a simpler system such as a high pressure gas flame of (for example) fuel/ NO_2 . The current understanding of these flames at atmospheric pressure appears to be good, and predicting the behavior of these flames at higher pressures would be a good test of the ability to extend the current understanding of combustion chemistry to the higher pressures of solid propellant combustion. The experimental difficulties would not be trivial, however, since the problems of small dimensions encountered in propellant flames would also be present in the high pressure gas flames. A diffusion flame might be required to get around this limitation, although the chemistry in a diffusion flame is quite different from that in a premixed flame of the same ingredients. Of course, a diffusion flame is a more accurate representation of many solid propellant flame situations. More research in the high pressure combustion kinetic area appears to be warranted.

7.0. REFERENCES

1. Edwards, T., Weaver, D. P., Campbell, D. H., and Hulsizer, S., "A High Pressure Combustor for the Spectroscopic Study of Solid Propellant Combustion Chemistry," Review of Scientific Instruments, Vol. 56, No. 11, pp. 2131-2137, 1985.
2. Edwards, T., Weaver, D. P., Campbell, D. H., and Hulsizer, S., "Investigation of High Pressure Solid Propellant Combustion Chemistry using Emission Spectroscopy," Journal of Propulsion and Power, Vol. 2, No. 3, pp. 228-236, 1986.
3. Campbell, D. H., Hulsizer, S., Edwards, T. and Weaver, D. P., "High Pressure Solid Propellant Combustion Zone Structure from Analysis of Hydroxyl Radical Chemiluminescence," Journal of Propulsion and Power, Vol. 2, No. 5, pp. 414-422, 1986.
4. Edwards, T., Weaver, D. P., and Campbell, D. H., "Laser-Induced Fluorescence in High Pressure Solid Propellant Flames," Applied Optics, Vol. 26, No. 17, pp. 3496-3509, 1987.
5. Hulsizer, S., Campbell, D. H., and Edwards, T., 2-D Imaging of High Pressure Solid Propellant Flames, Paper presented at Spring 1985 Western States/Central States Sections Combustion Institute Spring Meeting, San Antonio, Texas, April 1985 (Paper WSS/CI 85-5-6A).
6. Edwards, T., Weaver, D. P., Campbell, D. H., and Hulsizer, S., Laser-Induced Fluorescence in High Pressure Solid Propellant Flames, Paper presented at AIAA 24th Aerospace Sciences Meeting, Reno, Nevada, Jan. 1986 (AIAA Paper 86-0295).
7. Edwards, T., Weaver, D. P., Campbell, D. H., and Frederick, F., "CN Radical Distributions in Solid Propellant Flames," 23rd JANNAF Combustion Meeting, CPIA Publication 457, Volume I, pp. 181-195, Oct. 1986.
8. Edwards, T., Weaver, D. P., Campbell, D. H., and Frederick II, F., Laser-Induced Fluorescence of CN in Solid Propellant Flames, Paper presented at Fall 1986 Western States Section/Combustion Institute Meeting, Tucson, Arizona (Paper WSS/CI 86-18).
9. Edwards, T., "Modeling and Experimental Measurements of Solid Propellant Flame Structure," 24th JANNAF Combustion Meeting, CPIA Publication 476, Volume I, pp. 235-242, 1987.
10. Campbell, D. H., "Vibrational Level Relaxation Effects on Laser Induced Fluorescence Measurements of Hydroxide Number Density in a Methane-Air Flame," Applied Optics, Vol. 21, No. 16, pp. 2912-2919, 1982.
11. Campbell, D. H., "Collisional effects on laser-induced fluorescence measurements of hydroxide concentrations in a combustion environment. 1: Effects for $v'=0$ excitation," Applied Optics, Vol. 23, No. 5, pp. 689-703, 1984.
12. Campbell, D. H., "Collisional effects on laser-induced fluorescence measurements of hydroxide concentrations in a combustion environment. 2: Effects for $v'=1$ excitation," Applied Optics, Vol. 23, No. 9, pp. 1319-1327, 1984.
13. Campbell, D. H., Self-Absorption Effects in Emission and Laser-Induced Fluorescence Diagnostics, Paper presented at Fall 1985 Western States Section/Combustion Institute Meeting, Davis, CA, Oct. 1985 (Paper WSS/CI 85-14).
14. Kuo, K., and Summerfield, M.(eds), Fundamentals of Solid Propellant Combustion, AIAA Progress in Astronautics and Aeronautics Series, Volume 90, AIAA, New York, 1984.

15. Eckbreth, A. C., Bonczyk, P. A., and Verdick, J. F., "Combustion Diagnostics by Laser Raman and Fluorescence Techniques," Progress in Energy and Combustion Science, Vol. 5, pp. 253-322, 1979. See also Eckbreth, A. C., "Recent Advances in Laser Diagnostics for Temperature and Species Concentration in Combustion," 18th Symposium (Int'l) on Combustion, Combustion Institute, Pittsburgh, 1981, pp. 1471-1488.
16. Eckbreth, A. C., Laser Diagnostics for Combustion Temperature and Species, Abacus Press, Cambridge, 1988
17. Parr, T. and Hanson-Parr, D., "Species and Temperature Profiles in Ignition and Deflagration of HMX," Paper presented at Spring 1987 Western States Section/Combustion Institute Meeting, Salt Lake City, Utah, April 1987 (Paper WSS/CI 87-8). Also, "The Application of Imaging Laser-Induced Fluorescence to the Measurement of HMX and Aluminized Propellant Ignition and Deflagration Flame Structure," 23rd JANNAF Combustion Meeting, CPIA Publication 457, Volume I, pp. 249-267, 1986. Also, "Temperature and Species Profiles in Propellant Ignition and Combustion," 24th JANNAF Combustion Meeting, CPIA Publication 476, Volume I, pp. 367-382, 1987.
18. Harris, L. E., CARS Spectroscopy of the Reaction Zone of Methane-Nitrous Oxide and RDX Propellant Flame, ARAED-TR-85007, Army Armament Research and Development Center, Dover, NJ, Jan. 86. Also, Chemical Physics Letters, Vol. 103, pp. 413-???, 1984; Chemical Physics Letters, Vol. 109, pp. 110-113, 1984.
19. Vanderhoff, J. A., Peterson, R. B., and Kotlar, A. J., "The Feasibility of Using CARS for the Study of Muzzle Flash," 23rd JANNAF Combustion Meeting, CPIA Publication 457, Volume II, pp. 263-271, Oct. 1986.
20. Wilmot, G. B., Barber, W. H., Fleming, J. W., and Baronavski, A. P., "Application of Coherent Anti-Stokes Raman Spectroscopy to Solid Propellant Combustion Diagnostics," 20th JANNAF Combustion Meeting, CPIA Publication 383, Volume II, pp. 1-4, Oct. 1983.
21. Haw, T. E., Darrah, S., and Harris, L. E., "Single-Shot H₂ CARS Spectrometry of Propellant Ignition and Combustion, Under Pressure," 22nd JANNAF Combustion Meeting, CPIA Publication 432, Volume I, pp. 55-64, Oct. 1985.
22. Kubota, N., "Physicochemical Processes of HMX Propellant Combustion," 19th Symposium (Int'l) on Combustion, Combustion Institute, Pittsburgh, 1983, pp. 777-785.
23. Lengelle, G., Bizot, A., Duterque, J., and Trubert, J. F., "Steady-State Burning of Homogeneous Propellants," Chapter 7 (pp. 361-408) in Fundamentals of Solid Propellant Combustion (Kuo, K., and Summerfield, M.(eds)), AIAA Progress in Astronautics and Aeronautics Series, Volume 90, AIAA, New York, 1984.
24. Jacox, M. E., "Vibrational and Electronic Spectra of the H + HCN Reaction Products Trapped in Solid Argon," Journal of Physical Chemistry, Vol. 91, pp. 6595-6600, 1987.
25. Farrow, R. L., Lucht, R. P., Flower, W. L., and Palmer, R. E., "Coherent Anti-Stokes Raman Spectroscopic Measurements of Temperature and Acetylene Spectra in a Sooting Diffusion Flame," 20th Symposium (Int'l) on Combustion, Combustion Institute, Pittsburgh, 1986, pp. 1307-1312.

26. Cool, T, Profiles of HCO and CH₃ in Flames by Resonance Ionization, presentation at JANNAF workshop on "Kinetic and Related Aspects of Propellant Combustion Chemistry," Laurel, MD, May 1988.
27. Brill, T. and co-workers, "Thermal Decomposition of Energetic Materials," series of papers, e.g., Combustion and Flame, Vol. 62, pp. 213-224, 1985; Vol. 66, pp. 9-16, 1986; Vol. 67, pp. 121-126, 1987; Vol. 68, pp. 209-216 (1987).
28. Boggs, T. L., "The Thermal Behavior of Cyclotrimethylenetrinitramine (RDX) and Cyclotetramethylenetetranitramine (HMX)," Chapter 3 (pp. 121-176) in Fundamentals of Solid Propellant Combustion (Kuo, K., and Summerfield, M.(eds)), AIAA Progress in Astronautics and Aeronautics Series, Volume 90, AIAA, New York, 1984.
29. Fifer, R. A., "Chemistry of Nitrate Ester and Nitramine Propellants," Chapter 4 (pp. 177-238) in Fundamentals of Solid Propellant Combustion (Kuo, K., and Summerfield, M.(eds)), AIAA Progress in Astronautics and Aeronautics Series, Volume 90, AIAA, New York, 1984.
30. Chemical Propulsion Acronyms, Codes, and Trade Names, Feb. 1988 list, published by CPIA (no CPIA #).
31. Rekers, R. G., and Villars, D. S., "Flame Zone Spectroscopy of Solid Propellants," Review of Scientific Instruments, Vol. 25, No. 5, pp. 424-429, 1954.
32. Waesche, R. H. W., Spectroscopic Studies of Solid Propellant Flames, Rohm and Haas Special Report S-111, Rohm and Haas, Huntsville, AL, Oct. 1966 (AD 376283).
33. Waesche, R. H. W., A Spectrographic Technique for the Study of Solid Propellant Combustion, Rohm and Haas Special Report S-75, Rohm and Haas, Huntsville, AL, July 1965.
34. Povinelli, L.A., "A Study of Composite Solid-Propellant Flame Structure Using a Spectral Radiation Shadowgraph Technique," AIAA Journal, Vol. 3, No. 9, pp. 1593-1598, 1965.
35. Povinelli, L. A., Effect of Oxidizer Particle Size on Additive Agglomeration, NASA TN D-1438, NASA Lewis Research Center, Cleveland, OH, Nov. 1962.
36. Powling, J., and Smith, W. A. W., "The Combustion of the Butane-2,3- and 1,4-Diol Dinitrates and Some Aldehyde-Nitrogen Dioxide Mixtures," Combustion and Flame, Vol. 2, pp. 157-170, 1958.
37. Summerfield, M., Sutherland, G. S., Webb, M. J., Taback, H. J., and Hall, K. P., "Burning Mechanism of Ammonium Perchlorate Propellants," ARS Progress in Astronautics and Rocketry Series, Volume 1: Solid Propellant Rocket Research, edited by M. Summerfield, Academic Press, Inc., New York, 1960, pp. 141-182.
38. Mal'tsev, V. M., Stasenko, A. G., Selezner, V. A., and Pokhil, P. F., "Spectroscopic Investigation of Combustion Zones of Flame Flares of Condensed Systems," Fizika Goreniya y Vzryva, Vol. 9, No. 2, pp. 186-190, 1973.
39. Korobeinichev, O. P., Kuibida, L. V., Orlov, V. N., Tereshchenko, A. G., Kutsenogii, K. P., Mavliev, R. A., Ermolin, N. E., Fomin, V. M., Emel'yanov, I. D., "Mass Spectrometric Probe Study of the Flame Structure and Kinetics of Chemical Reactions in Flames," Mass-Spectrum. Khim. Kinet., pp. 73-93, 1985 (English translation supplied by C. Melius, SNLL).
40. Korobeinichev, O. P., Tereshchenko, A. G., Emel'yanov, I. D., Rudnitskii, A. L., Fedorov, S. Yu., Kuibida, L. V., and Lotov, V. V., "Substantiation of the Probe

- Mass-Spectrometric Method for Studying the Structure of Flames with Narrow Combustion Zones," Fizika Goreniya i Vzryva, Vol. 21, No. 5, pp. 22-28, 1985.
41. Tereshchenko, A. G., and Korobeinichev, O. P., "Correctness of Mass-Spectrometric Probe Measurements when Investigating the Flame Structure of Condensed Systems," Fizika Goreniya i Vzryva, Vol. 18, No. 6, pp. 39-45, 1982.
 42. Hertzberg, M., Laser-Induced Combustion of Pure AP and the Structure of its Composite Propellant Flames, NASA-CR-66919, NASA Langley Research Center, , Hampton, VA, 1969.
 43. Kubota, N., Ohlemiller, T. J., Caveny, L. H., and Summerfield, M., The Mechanism of Super-Rate Burning of Catalyzed Double-Base Propellants, Princeton Technical Report AMSR 1087, Princeton University, 1973 (Kubota's PhD thesis).
 44. Aoki, I., and Kubota, N., "Combustion Wave Structures of High and Low Energy Double-Base Propellants," AIAA Journal, Vol. 20, No. 1, pp. 100-105, 1982.
 45. Kubota, N., Kuwahara, T., Miyazaki, S., Uchiyama, K., and Hirata, N., "Combustion Wave Structures of Ammonium Perchlorate Composite Propellants," Journal of Propulsion and Power, Vol. 2, No. 4, pp. 296-300, 1986.
 46. Gaydon, A. G., and Wolfhard, H. G., Flames: Their Structure, Radiation, and Temperature, 4th Edition, Chapman and Hall, London, 1979.
 47. Bradshaw, S. D., Omenetto, N., Zizak, G., Bower, J. N., and Winefordner, J. D., "Five laser-excited fluorescence methods for measuring spatial flame temperatures. 1: Theoretical basis," Applied Optics, Vol. 19, No. 16, pp. 2709-2716, 1980.
 48. Crosley, D.R., and Smith, G. P., "Rotational Energy Transfer and LIF temperature Measurements," Combustion and Flame, Vol. 44, pp. 27-34, 1982.
 49. Stufflebeam, J. H., Shirley, J. A., CARS Diagnostics of High Pressure Combustion-II, Report on Contract DAAG 29-83-C-0001, United Technologies Research Center, Hartford, CT, 1985.
 50. Stufflebeam, J. H., Progress of CARS Applications to Solid Propellant Combustion, presentation at JANNAF workshop on "Kinetic and Related Aspects of Propellant Combustion Chemistry," Laurel, MD, May 1988.
 51. Lapp, M., and Penney, C. M., eds., Laser Raman Gas Diagnostics, Plenum Press, New York, 1973.
 52. Boggs, T. L., Crump, J. E., Kraeutle, K. L., and Zurn, D. E., "Cinephotomicrography and Scanning Electron Microscopy as Used to Study Solid Propellant Combustion," in Boggs, T. L., and Zinn, B. T. (eds), Experimental Diagnostics in the Combustion of Solids, AIAA Progress in Astronautics and Aeronautics Series, Volume 63, AIAA, New York, 1978, pp. 20-48.
 53. Shackleford, S. A., Coolidge, M. B., Goshgarian, B. B., Loving, B. A., Rogers, R. N., Janney, J. L., and Ebinger, M. H., "Deuterium Isotope Effects in Condensed-Phase Thermochemical Decomposition Reactions of Octahydro-1,3,5,7-tetranitro-1,3,5,7-tetrazocine," Journal of Physical Chemistry, Vol. 89, pp. 3118-3126, 1985.
 54. Cohen, N. S., Lo, G. A., and Crowley, J. C., "Model and Chemistry of HMX Combustion," AIAA Journal, Vol. 23, No. 2, pp. 276-282, 1985 (AIAA Paper 83-1195).
 55. Cohen, N. S., Crowley, J. C., and Lo, G. A., "Effects of HMX Addition on the Combustion of Energetic Binders," 21st JANNAF Combustion Meeting, CPIA Publication 412, Volume I, pp. 423-432, 1984.

56. Miller, R. R., Jones, M. L., Foster, R. L., and Condon, J. A., Ballistic Control of Solid Propellants, AFRPL-TR-81-058, Volume I, Air Force Rocket Propulsion Laboratory, Edwards AFB, CA, April 1982.
57. Heller, C. A., and Gordon, A. S., "Structure of the Gas Phase Combustion Region of a Solid Double Base Propellant," Journal of Physical Chemistry, Vol. 59, 773-777, 1955.
58. Beckstead, M. W., "Model for Double-Base Propellant Combustion," AIAA Journal, Vol. 18, No. 8, pp. 980-985, 1980.
59. Kubota, N., "Survey of Rocket Propellants and Their Combustion Characteristics," Chapter 1 (pp. 1-52) in Fundamentals of Solid Propellant Combustion (Kuo, K., and Summerfield, M.(eds)), AIAA Progress in Astronautics and Aeronautics Series, Volume 90, AIAA, New York, 1984.
60. Glazkova, A. P., Catalysis of Explosive Combustion, Nauka, Moscow, 1976 (English translation FTD-ID(RS)T-0267-78).
61. Armstrong, R. C., and Koszykowski, M. L., "A Theoretical and Numerical Study of Radiative Ignition and Deradiative Extinction in Solid Propellants," Combustion and Flame, Vol. 72, pp. 13-26, 1988.
62. Margolis, S. B., Williams, F. A., and Armstrong, R. C., "Influence of Two-Phase Flow in the Deflagration of Homogeneous Solids," Combustion and Flame, Vol. 67, pp. 249-258, 1987.
63. Cohen, N. S., Analysis of Double-Base Propellant Combustion, Paper presented at AIAA 19th Aerospace Sciences Meeting, St. Louis, MO, Jan. 1981 (AIAA Paper 81-0120).
64. Cohen, N. S., and Lo, G. A., "Modeling Effects of Composition on the Burn Rates of Nitrate Ester-Based Energetic Binders," 20th JANNAF Combustion Meeting, CPIA Publication 383, Volume I, pp. 621-628, 1983.
65. Cohen, N. S., and Lo, G. A., Combustion Chemistry of Nitrate Ester-Based Propellants, Paper presented at AIAA/SAE/ASME 19th Joint Propulsion Conference, Seattle, WA, June 1983 (AIAA Paper 83-1198).
66. Bizot, A., A Model for Double-Base Propellant Combustion, Paper presented at Spring 1987 Western States Section/Combustion Institute Meeting, Salt Lake City, Utah, April 1987 (Paper WSS/CI 87-22).
67. Kuo, K. K., Principles of Combustion, John Wiley & Sons, New York, 1986, Chapter 5.
68. Zeldovich, Ya. B., Berenblatt, G. I., Librovich, V. B., Makhilvadze, G. M., The Mathematical Theory of Combustion and Explosions, Nauka, Moscow, 1980 (English translation by Consultants Bureau, Plenum, NY, 1985); Zeldovich, Ya. B., Leipunskii, O. I., Librovich, V. B., The Theory of the Non-Stationary Burning of Powders, Nauka, Moscow, 1975 (not read, referenced in 68); Novozhilov, B. V., Nonstationary Combustion of Solid Rocket Fuels, Nauka, Moscow, 1973 (not read, referenced in 68).
69. Williams, F. A., Combustion Theory, 2nd edition, Benjamin/Cummings, Menlo Park, 1985, Chapter 5.
70. Glazkova, A. P., "Some General Catalytic Regularities in the Deflagration of Condensed Systems: The Effects of Catalysts on the Combustion of Styphnic Acid and

- the Nitroso-Analog of RDX," 17th Symposium (Int'l) on Combustion, Combustion Institute, Pittsburgh, 1979, pp. 1425-1434.
71. Kubota, N., "Determination of Plateau Burning Effect of Catalyzed Double-Base Propellant," 17th Symposium (Int'l) on Combustion, Combustion Institute, Pittsburgh, 1979, pp. 1435-1441.
 72. Ermolin, N. E., Korobeinichev, Tereschenko, A. G. , and Fomin, V. M., "Measurement of the Concentration Profiles of Reacting Components and Temperature in an Ammonium Perchlorate Flame," Fizika Goreniya i Vzryva, Vol. 18, No. 1, pp. 46-49, 1982.
 73. Cohen, N. S., and McGrath, D. K., "Nonequilibrium Thermochemistry of Ammonium Nitrate and Nitramine Propellants," 23rd JANNAF Combustion Meeting, CPIA Publication 457, Volume II, pp. 63-71, 1986.
 74. Hatch, R. L., "Chemical Kinetics Combustion Model of the NG/Binder System," 23rd JANNAF Combustion Meeting, CPIA Publication 457, Volume I, pp. 157-165, 1986.
 75. Branch, M. C., "Chemical Kinetics of Gas Phase Decomposition Products of Nitramine Propellants," 21st JANNAF Combustion Meeting, CPIA Publication 412, Volume I, pp. 409-415, 1984.
 76. Sotter, J. G., "Chemical Kinetics of the Cordite Explosion Zone," 10th Symposium (Int'l) on Combustion, Combustion Institute, Pittsburgh, 1965, pp. 1405-1411.
 77. Symposium on Kinetics of Propellants, Journal of Physical Chemistry, Vol. 54, pp. 847-954, 1950.
 78. Korobeinichev, O. P., and Khlevnoi, S. S., "Mass-Spectrometer Study of the Thermal Decomposition of Nitroglycerine Powder at High Temperatures," Fizika Goreniya i Vzryva, Vol. 6, No. 3, pp. 404-406, 1970.
 79. Bent, H. A., and Crawford, B., "Infrared Studies of Propellant Flames," Journal of Physical Chemistry, Vol. 63, pp. 941-952, 1959.
 80. Rekers, R. G., and Villars, D. S., "Flame Zone Spectroscopy of Solid Propellants II. Double Base Propellants JPN," Journal of the Optical Society of America, Vol. 46, pp. 534-537, 1956.
 81. Heath, G. A., and Hirst, R., "Some Characteristics of the High Pressure Combustion of Double-Base Propellant," 8th Symposium (Int'l) on Combustion, Williams and Wilkins, London, 1960, pp. 711-720.
 82. Branch, M. C., Alfarayedhi, A., and Sadeqi, M., Structure of Flames Associated with Nitramine Solid Propellants, Paper presented at Spring 1987 Western States Section/Combustion Institute Meeting, Salt Lake City, Utah, April 1987 (Paper WSS/CI 87-20). Also Branch, M. C., and Sadeqi, M., "Structure of Laminar Premixed Flames of $\text{CH}_2\text{O}/\text{NO}_2/\text{O}_2$," 24th JANNAF Combustion Meeting, CPIA Publication 476, Volume I, pp. 343-351, 1987.
 83. Cohen, N. S., and Fleming, R. W., Role of Binders in Solid Propellant Combustion, AFRPL-TR-72-96, Air Force Rocket Propulsion Laboratory, Edwards AFB, CA, Oct. 1972.
 84. Bamford, C. H., and Tipper, C. F. H. (eds), Comprehensive Chemical Kinetics, Volume 14: Degradation of Polymers, Elsevier Science Publishing Company, New York, 1975.

85. Melius, C., and Binkley, J. S., "Quantum Mechanical Calculations of the Decomposition of Nitramines: Thermochemistry and Reaction Pathways, 23rd JANNAF Combustion Meeting, CPIA Publication 457, Volume I, pp. 241-248, 1986.
86. Umstead, M. E., Lloyd, S. A., and Lin, M. C., "Kinetic Modeling of Dimethylnitramine Thermal Decomposition--A Mechanistic Extrapolation to RDX Decomposition in the Gas Phase," 22nd JANNAF Combustion Meeting, CPIA Publication 432, Volume I, pp. 515-521, 1983.
87. Miller, J. A., Branch, M. C., McLean, W. J., Chandler, D. W., Smooke, M. D., and Kee, R. J., "The Conversion of HCN to NO and N₂ in H₂-O₂-HCN-Ar Flames at Low Pressure," 20th Symposium (Int'l) on Combustion, Combustion Institute, Pittsburgh, 1984, pp. 673-684.
88. Smith, O. I., and Thorne, L. R., "The Structure of Cyanogen-Nitrogen Dioxide Premixed Flames," Paper presented at Fall 1986 Western States Section/Combustion Institute Paper Meeting, Tucson, AZ, Oct. 1986 (Paper WSS/CI 86-34).
89. Thorne, L. R., Branch, M. C., Chandler, D. W., Kee, R. J., and Miller, R. J., "Hydrocarbon-Nitric Oxide Interactions in Low-Pressure Flames," Paper presented at Spring 1986 Western States Section/Combustion Institute Meeting, Banff, Alberta, April 1986 (Paper WSS/CI 86-29).
90. Miller, J. A., and Fisk, G. A., "Combustion Chemistry," Chemical and Engineering News, August 31, 1987, pp. 22-46.
91. Summerfield, M., Combustion of Nitramine Propellants, ARBRL-CR-00507, Army Armament Research and Development Command, Aberdeen Proving Ground, MD, March 1983.
92. Ben Reuven, M., and Caveny, L. H., HMX Deflagration and Flame Characterization, AFRPL TR-79-94, Air Force Rocket Propulsion Laboratory, Edwards AFB, CA, Oct. 1980.
93. Ben Reuven, M., and Caveny, L. H., "Nitramine Flame Chemistry and Deflagration Interpreted in Terms of a Flame Model," AIAA Journal, Vol. 19, No. 10, pp. 276-1285, 1981.
94. Hatch, R. L., "Chemical Kinetics Modeling of HMX Combustion," 24th JANNAF Combustion Meeting, CPIA Publication 476, Volume I, pp. 383-391, 1987.
95. Melius, C., "Theoretical Studies of the Chemical Reactions Involved in the Ignition of Nitramines," 24th JANNAF Combustion Meeting, CPIA Publication 476, Volume I, pp. 359-366, 1987.
96. Beckstead, M. W., "A Model for Solid Propellant Combustion", 18th Symposium (Int'l) on Combustion, Combustion Institute, Pittsburgh, 1981, pp. 175-185.
97. Beckstead, M. W., Derr, R. L., and Price, C. F., "The Combustion of Solid Monopropellants and Composite Propellants," 13th Symposium (Int'l) on Combustion, 1047-1056 (1971).
98. Beckstead, M. W. and McCarty, K. P., "Modeling Calculations for HMX Composite Propellants," AIAA Journal, Vol. 20, No. 1, pp. 106-115, 1982.
99. Kumar, R. N., and Strand, L. D., "Theoretical Combustion Modeling Study of Nitramine Propellants," Journal of Spacecraft and Rockets, Vol. 14, No. 7, pp. 427-433.

100. Ermolin, N. E., Korobeinichev, O. P., Kuibida, L. V., and Fomin, V. M., "Study of the Kinetics and Mechanism of Chemical Reactions in Hexogen Flames," Fizika Goreniya i Vzryva, Vol. 22, No. 5, pp. 54-56, 1986.
101. Korobeinichev, O. P., Kuibida, L. V., "Mass Spectrometry of Flame Structure for Condensed Systems with Molecular-Beam Sampling," Fizika Goreniya i Vzryva, Vol. 17, No. 2, pp. 86-89, 1981.
102. Emel'yanov, I. D., Korobeinichev, O. P., Tereshchenko, A. G., and Kuibida, L. V., "Heat Transfer Between Flame and Probe in Mass-Spectrometric Research on Flame Structure," Fizika Goreniya i Vzryva, Vol. 22, No. 2, pp. 45-51, 1986.
103. Dobbs, G., report in preparation on spectral analysis of HCN CARS, United Technologies Research Center, Hartford, CT, May 1988.
104. Gaydon, A. G., The Spectroscopy of Flames, 2nd Edition, Chapman and Hall, London, 1974.
105. Garo, A., Westmoreland, P. R., Howard, J. B., and Longwell, J. P., "Analysis of Fuel-Lean Combustion Using Chemical Mechanisms," Combustion and Flame, Vol. 72, pp. 271-286, 1988.
106. Schroeder, M. A., "Critical Analysis of Nitramine Decomposition Data: Update, Some Comments on Pressure and Temperature Effects, and Wrap-up Discussion of Chemical Mechanisms," 21st JANNAF Combustion Meeting, CPIA Publication 412, Volume II, pp. 595-614, Oct. 1984.
107. Cohen, N.S., "Review of Solid Propellant Burn Rate Modeling," AIAA Journal, Vol. 18, pp. 277-293, 1980.
108. Renie, J. P., and Osborn, J. R., Combustion Response Calculations for Composite Solid Propellants, AFRPL-TR-81-25, Air Force Rocket Propulsion Laboratory, Edwards AFB, CA, Dec. 1981.
109. Renie, J. P., Condon, J. A., and Osborn, J. R., "Oxidizer Size Distribution Effects on Propellant Combustion," AIAA Journal, Vol. 17, No. 8, pp. 877-883, 1979.
110. Cor, J. J., and Renie, J. P., A Continuous Surface Regression Model for the Combustion of Composite Solid Propellants, Paper presented at Spring 1987 Western States Section/Combustion Institute Meeting, Salt Lake City, Utah, April 1987 (Paper WSS/CI 87-17).
111. Price, E. W., Sambamurthi, J. K., Sigman, R. K., and Panyam, R. R., "Combustion of Ammonium Perchlorate-Polymer Sandwiches," Combustion and Flame, Vol. 63, pp. 381-413, 1986.
112. Steinz, J. A., Stang, P. L., and Summerfield, M., The Burning Mechanism of Ammonium Perchlorate-Based Composite Solid Propellants, Princeton Department of Aerospace and Mechanical Sciences Report 830, Princeton University, Princeton, NJ, Feb. 1969.
113. Von Elbe, G., King, M. K., McHale, E. T., and Macek, A., Chemical Kinetic and Physical Processes in Composite Solid Propellant Combustion, NASA CR 66307, NASA Langley Research Center, Hampton, VA, Jan. 1967.
114. Smyth, K. C., Miller, J. H., Dorfman, R. C., Mallard, W. G., and Santoro, R. J., "Soot Inception in a Methane/Air Diffusion Flame as Characterized by Detailed Species Profiles," Combustion and Flame, Vol. 62, pp. 157-181, 1985.

115. Beckstead, M. W., Derr, R. L., and Price, C. F., "A Model of Composite Solid-Propellant Combustion Based on Multiple Flames," AIAA Journal, Vol. 8, No. 12, pp. 2200-2207, 1970.
116. Hepler, W. A., and Smith, O. I., Numerical Simulation Study of a Hydrazine/Nitrogen Dioxide Diffusion Flame in a Burke-Schumann Burner, Paper presented at Spring 1987 Western States Section/Combustion Institute Meeting, Salt Lake City, Utah, April 1987 (Paper WSS/CI 87-23).
117. Chen, J.-Y., "A General Procedure for Constructing Reduced Reaction Mechanisms with Given Independent Relations," Combustion Science and Technology, Vol. 57, pp. 89-94, 1988.
118. Dryer, F. L., and Rabitz, H., Lumped Model Generation and Evaluation: Sensitivity Analysis and Lie Algebraic Techniques with Application to Combustion, Abstract in Proceedings of AFOSR/ONR Contractors Meeting on Combustion and Rocket Propulsion held at Pennsylvania State University, University Park, PA, June 22-26, 1987.
119. Brezinsky, K., Burke, E. J., and Glassman, I., "The High-Temperature Oxidation of Butadiene," 20th Symposium (Int'l) on Combustion, Combustion Institute, Pittsburgh, 1984, pp. 613-622.
120. Ermolin, N. E., Korobeinichev, Tereshchenko, A. G. , and Fomin, V. M., "Kinetic Calculations and Mechanism Definition for Reactions in an Ammonium Perchlorate Flame," Fizika Goreniya i Vzryva, Vol. 18, No. 2, pp. 61-70, 1982.
121. Friedman, R., "Experimental Techniques for Solid-Propellant Combustion Research," AIAA Journal, Vol. 5, No. 7, pp. 1217-1223, 1967.
122. Jacobs, P. W. M., and Whitehead, H. M., "Decomposition and Combustion of Ammonium Perchlorate," Chemical Reviews, Vol. 69, No. 9, pp. 551-590, 1969.
123. Heatli, G.A., and Pearson, G.S., "Perchloric Acid Flames: Part III. Chemical Structure of Methane Flames," 11th Symposium (Int'l) on Combustion, Combustion Institute, Pittsburgh, 1967, pp. 967-977.
124. Jacobs, P. W. M., and Stevenson, J., "The Gas-Phase Reaction of Perchloric Acid with Ethylene," Combustion and Flame, Vol. 20, pp. 51-57, 1973.
125. Korobeinichev, Orlov, V. N., and Shifon, N. Ya., "Mass-Spectrometric Investigation of the Chemical Structure of the Flames of Chloric Acid in a Stoichiometric Mixture with Methane," Fizika Goreniya i Vzryva, Vol 17, No. 6, pp. 55-62, 1981; Korobeinichev, Orlov, V. N., and Shifon, N. Ya., "Mass-Spectrometric Study of the Chemical Structures of Flames of Perchloric Acid in Lean and Rich Mixtures with Methane," Fizika Goreniya i Vzryva, Vol. 18, No. 5, pp. 77-83, 1982.
126. Pearson, G. S., "Perchloric Acid Flames V - Ethylene-Rich Flames," Combustion and Flame, Vol. 11, pp. 97-102, 1967.
127. Pearson, G. S., "Perchloric Acid Flames IV - Methane-Rich Flames," Combustion and Flame, Vol. 11, pp. 89-96, 1967.
128. Pearson, G. S., "Perchloric Acid Flames VI - Ethane-Rich Flames," Combustion and Flame, Vol. 11, pp. 103-108, 1967.
129. Pearson, G. S., "Perchloric Acid Flames VII - Mixed Fuel-Rich Flames," Combustion and Flame, Vol. 11, pp. 471-482, 1967.
130. Pearson, G. S., "Perchloric Acid Flames VIII. - Methane-Rich Flames with Oxygen," Combustion and Flame, Vol. 12, pp. 54-62, 1968; Hall, A. R., and Pearson, G. S.,

- "Perchloric Acid Flames: IX. Two-Flame Structure with Hydrocarbons," 12th Symposium (Int'l) on Combustion, Combustion Institute, Pittsburgh, 1969, pp. 1025-1033.
131. Combourieu, J. and Moreau, R., "A Study of $\text{ClO}_2\text{-CH}_4$, $\text{ClO}_2\text{-O}_2\text{-CH}_4$, and $\text{ClO}_2\text{-N}_2$ (or Ar)- CH_4 Flames at Low Pressures," 12th Symposium (Int'l) on Combustion, Combustion Institute, Pittsburgh, 1969, pp. 1015-1023.
 132. Combourieu, J., and Moreau, G., "A Study of $\text{ClO}_2\text{-C}_2\text{H}_2$ Flames at Low Pressures," Combustion and Flame, Vol. 24, pp. 381-390, 1975.
 133. Laffitte, P., Combourieu, J., Hajal, I., Ben Caid, M., and Moreau, R., "Characteristics of Chlorine Dioxide Decomposition Flames at Reduced Pressures," 11th Symposium (Int'l) on Combustion, Combustion Institute, Pittsburgh, 1967, pp. 941-950.
 134. Combourieu, J., Moreau, G., Moreau, R. and Pearson, G. S., "Ammonium Perchlorate Combustion Analogue: Ammonia-Chlorine Dioxide Flames," AIAA Journal, Vol. 8, No. 3, pp. 594-597, 1970.
 135. Combourieu, J., Moreau, R., Hall, A. R., and Pearson, G. S., "Chlorine Dioxide and Perchloric Acid Flames," Combustion and Flame, Vol. 13, pp. 596-604, 1969.
 136. Madorsky, S. L., Thermal Degradation of Organic Polymers, Wiley, New York, 1964.
 137. Andersen, W. H., Bills, K. W., Mishuck, E., Moe, G., and Schultz, R. D., "A Model Describing Combustion of Solid Composite Propellants Containing Ammonium Nitrate," Combustion and Flame, Vol. 3, pp. 301-318, 1959.
 138. Miller, R. R., "A Framework for a Totally Statistical Composite Propellant Combustion Model," 19th JANNAF Combustion Meeting, CPIA Publication 366, Volume II, pp. 81-92, Oct. 1982.
 139. Miller, R. R., Donohue, M. T., and Martin, J. R., "Control of Solids Distribution I. Ballistics of Non-Aluminized HTPB Propellants," 13th JANNAF Combustion Meeting, CPIA Publication 281, Volume II, pp. 1-36, 1976.
 140. Eldredge, H. B., Beckstead, M. W., and White, S. C., "Solid Propellant Diffusion Flame Structure," 19th JANNAF Combustion Meeting, CPIA Publication 366, Volume I, 99-108 (1982) and 18th JANNAF Combustion Meeting, CPIA Publication 347, Volume III, pp. 285-295, 1981.
 141. Beckstead, M. W., "Combustion Mechanisms of Composite Solid Propellants," 19th JANNAF Combustion Meeting, CPIA Publication 366, Volume II, pp. 93-100, 1982.
 142. Price, E. W., "Combustion of Metalized Propellants," pp. 479-514 in Fundamentals of Solid Propellant Combustion (Kuo, K., and Summerfield, M.(eds)), AIAA Progress in Astronautics and Aeronautics Series, Volume 90, AIAA, New York, 1984.
 143. Geisler, R. L., "Summary Report on 1977 JANNAF Aluminum Combustion Workshop," 14th JANNAF Combustion Meeting, CPIA Publication 292, Volume I, pp. 181-193, 1977.
 144. Fontijn, A., "Temperature Dependence of the Kinetics of Elementary Combustion Reactions of Refractory Species," Combustion Science and Technology, Vol. 50, pp. 151-???, 1986.
 145. Gaydon, A. G., and Wolfhard, H. G., "Spectroscopic Studies of Low-Pressure Flames," 3rd Symposium (Int'l) on Combustion, Williams and Wilkins, London, 1948, pp. 504-518.

146. Wolfhard, H. G., and Parker, W. G., "Spectra and Combustion Mechanism of Flames Supported by the Oxides of Nitrogen," 5th Symposium (Int'l) on Combustion, Williams and Wilkins, London, 1955, pp. 718-728.
147. CRC Handbook of Chemistry and Physics, Chemical Rubber Company, 57th Edition, CRC Press, Cleveland Ohio, 1976-1977 edition.
148. Solid Propellant Ingredients Manual, CPIA/M3, Chemical Propulsion Information Agency, Laurel, MD, Jan. 1986.
149. Vanderhoff, J. A., Beyer, R. A., Kotlar, A. J., and Anderson, W. R., "Kr⁺ and Ar⁺ laser-excited fluorescence of CN in a flame," Applied Optics, Vol. 22, No. 13, pp. 1976-1979, 1983.
150. Lucht, R. P., Sweeney, D. W., and Laurendeau, N. M., "Laser-Saturated Fluorescence Measurements of OH in Atmospheric Pressure CH₄/O₂/N₂ Flames Under Sooting and Non-Sooting Conditions," Combustion Science and Technology, Vol. 42, pp. 259-281, 1985.
151. Cohen-Nir, E., "Combustion Characteristics of Advanced Nitramine-Based Propellants," 18th Symposium (Int'l) on Combustion, Combustion Institute, Pittsburgh,, 1981, pp. 195-206.
152. Miller, R. R., Grigor, A. F., Musso, R. C., and Yount, R. A., Combustion Mechanism of Low Burning Rate Propellant, AFRPL TR 69-130, Air Force Rocket Propulsion Laboratory, Edwards AFB, CA, May 1969.
153. Slack, M. and Grillo, A., "High Temperature Rate Coefficient Measurement of CO + O Chemiluminescence," Combustion and Flame, Vol. 59, No. 2, pp. 189-196, 1985.
154. Cummings, G. A. McD., and Hall, A. R., "Perchloric Acid Flames. I. Premixed Flames with Methane and Other Fuels," 10th Symposium (Int'l) on Combustion, Combustion Institute, Pittsburgh, 1965, pp. 1365-1372.
155. McCarty, K. P., HMX Propellant Combustion Studies, AFRPL TR-79-61, Air Force Rocket Propulsion Laboratory, Edwards AFB, CA, Nov. 1979.
156. Ornstein, L. S., and Brinkmann, H., "Temperature Determination from bandspectra. I. Vibrational energy distribution and vibrational transition probabilities in the Cyanogen 2Σ-2Σ bandsystem," Proceedings of the Netherlands Academy of Sciences, Vol 34, pp. 3-41, 1931.
157. Bulewicz, E. M., Padley, P. J., Smith, R. E., "Elementary Combustion Processes in Cyanogen+Oxygen+Hydrogen Flames: Spectroscopic Studies," 14th Symposium (Int'l) on Combustion, Combustion Institute, Pittsburgh, 1973, pp. 329-341.
158. Quang, L. N., and Vanpee, M., "A Spectroscopic Investigation of the Premixed Acetylene-Nitric Oxide Flame," 19th Symposium (Int'l) on Combustion, Combustion Institute, Pittsburgh, 1982, pp. 293-301.
159. Guillaume, P., and Van Tiggelen, P. J., "Spectroscopic Investigation of Acetylene-Nitrous Oxide Flames," 20th Symposium (Int'l) on Combustion, Combustion Institute, Pittsburgh, 1984, pp. 751-760.
160. Herzberg, G., Molecular Spectra and Molecular Structure I. Spectra of Diatomic Molecules, Van Nostrand Reinhold, New York, 1950.
161. Nicholls, R. W., "Franck-Condon Factors to High Vibrational Quantum Numbers III: CN," Journal of Research of the National Bureau of Standards A, Vol. 68A, No. 1, pp. 75-78, 1964.

162. Huber, K. P., and Herzberg, G., Molecular Spectra and Molecular Spectra IV. Constants of Diatomic Molecules, Van Nostrand Reinhold, New York, 1979.
163. Engleman, R., "The $\Delta v=0$ and $+1$ Sequence Bands of the CN Violet System Observed During the Flash Photolysis of BrCN," Journal of Molecular Spectroscopy, Vol. 49, pp. 106-116, 1974.
164. Reisler, H., Mangir, M., and Wittig, C., "The kinetics of free radicals generated by IR laser photolysis. I. Reactions of $C_2(a^3\Pi_u)$ with NO, vinyl cyanide, and ethylene," Journal of Chemical Physics, Vol. 71, No. 5, pp. 2109-2117, 1979.
165. Quang, N. L., and Vanpee, M., "Free Radical Concentration Measurements in Nitric Oxide-Acetylene Flames," Combustion and Flame, Vol. 62, pp. 193-210, 1985.
166. Kishore, K., and Gayathri, V., "Chemistry of Ignition and Combustion of Ammonium-Perchlorate Based Propellants," pp 53-120 in Fundamentals of Solid Propellant Combustion (Kuo, K., and Summerfield, M.(eds)), AIAA Progress in Astronautics and Aeronautics Series, Volume 90, AIAA, New York, 1984.
167. Thomas, N., Gaydon, A. G., and Brewer, L., "Cyanogen Flames and the Dissociation Energy of N_2 ," Journal of Chemical Physics, Vol. 20, No. 3, pp. 369-374, 1952.
168. Malicet, J., Brion, J., Guenebaut, "Contribution a L'Etude Spectroscopique de la Transition $A(^3\Pi_i)-X(^3\Sigma^-)$ du Radical NH," J. Chim. Phys., Vol. 67, pp. 25-30, 1970.
169. Funke, G., "Die NH-Banden bei λ 3360," Z. Physik, Vol. 96, pp. 787-798, 1935.
170. Funke, G., "Das Absorptionsspektrum des NH," Z. Physik, Vol. 101, pp. 104-112, 1936.
171. Dixon, R. N., "The 0-0 and 1-0 Bands of the $A(^3\Pi_i)-X(^3\Sigma^-)$ System of NH," Canadian Journal of Physics, Vol. 37, pp. 1171-1186, 1959.
172. Lents, J. M., "An Evaluation of Molecular Constants and Transition Probabilities for the NH Free Radical," Journal of Quantitative Spectroscopy and Radiative Transfer, Vol. 13, pp. 297-310, 1977.
173. Pearse, R. W. B., and Gaydon, A. G., The Identification of Molecular Spectra, 4th edition, Chapman and Hall, London, 1976.
174. Jevons, W., "The More Refrangible Band System of Cyanogen as Developed in Active Nitrogen," Proceedings of the Royal Society, Series A, Volume 112, pp. 407-442, 1926.
175. Laurendeau, N. M., and Goldsmith, J. E. M., "Comparison of Laser-Induced Fluorescence Methods for Measurement of Hydroxyl Concentration in Flames," Paper presented at Spring 1986 Western States Section/Combustion Institute Meeting, Banff, Alberta, April 1986 (Paper WSS/CI 86-27).
176. Cattolica, R. J., and Vosen, S. R., "Two-Dimensional Measurements of the OH in a Constant Volume Combustion Chamber," 20th Symposium (Int'l) on Combustion, Combustion Institute, Pittsburgh, 1984, pp. 1273-1282.
177. Bowman, C. T., Hanson, R. K., Vandsburger, U., Allen, M. G., and McManus, K. R., "Effects of Fuel Spray Characteristics and Vaporization on Energy Release Rates and Flow Field Structure in a Dump Combustor," 23rd JANNAF Combustion Meeting, CPIA Publication 457, Vol I, pp. 545-550, 1986.
178. Boggs, T. L., Derr, R. L., and Beckstead, M. W., "Surface Structure of Ammonium Perchlorate Composite Propellants," AIAA Journal, Vol. 8, No. 2, pp. 370-372, 1970.

179. Vanderhoff, J. A., Anderson, W. R., Kotlar, A. J., and Beyer, R. A., "Raman and Fluorescence Spectroscopy in a Methane-Nitrous Oxide Flame," 20th Symposium (Int'l) on Combustion, Combustion Institute, Pittsburgh, 1984, pp. 1299-1306.
180. Kuwahara, T., and Kubota, N., "Combustion of RDX/AP Composite Propellants at Low Pressures," Journal of Spacecraft and Rockets, Vol. 21, No. 5, pp. 502-507, 1984.
181. Kubota, N., and Masamoto, T., "Flame Structures and Burning Rate Characteristics of CMDDB Propellants," 16th Symposium (Int'l) on Combustion, Combustion Institute, Pittsburgh, 1977, pp. 1201-1209.
182. Ramohalli, K. N. R., "Steady State Burning of Composite Propellants under Zero Cross-Flow Situation," Chapter 8 (409-478) in Fundamentals of Solid Propellant Combustion (Kuo, K., and Summerfield, M.(eds)), AIAA Progress in Astronautics and Aeronautics Series, Volume 90, AIAA, New York, 1984.
183. Fong, C. W., and Hamshire, B. L., "The Mechanism of Burning Rate Catalysis in Composite HTPB-AP Propellant Combustion," Combustion and Flame, Vol. 65, pp. 61-69, 1986.
184. Pitz, W., Westbrook, C., Proscia, W., and Dryer, F., "A Comprehensive Chemical Kinetic Mechanism for the Oxidation of N-Butane," 20th Symposium (Int'l) on Combustion, Combustion Institute, Pittsburgh, 1984, pp. 831-843.
185. Axelsson, E. I., Brezinsky, K., Dryer, F. L., Pitz, W. J., and Westbrook, C. K., "Chemical Kinetic Modeling of the Oxidation of Large Alkane Fuels: n-Octane and iso-Octane," 21st Symposium (Int'l) on Combustion, Combustion Institute, Pittsburgh, 1986, pp. 783-793.
186. Kubota, N., and Okuhara, H., Burning Rate Temperature Sensitivity of HMX Propellants, Paper presented at AIAA/SAE/ASME/ASEE 22nd Joint Propulsion Conference, Huntsville, AL, June 1986 (AIAA Paper 86-1593).
187. Kubota, N., and Hirata, N., "Super-Rate Burning of Catalyzed HMX Propellants," 21st Symposium (Int'l) on Combustion, Combustion Institute, Pittsburgh, 1986, pp. 1943-1951.
188. Ferguson, D. C., Roberto, F. Q., Murrell, T., and Resnick, P., "Hydrogen Chloride-Free Propellant," 21st JANNAF Combustion Meeting, CPIA Publication 412, Volume II, pp. 13-22, 1984.
189. Pokhil, P. F., Belyaev, A. F., Frolov, Yu. V., Logachev, V. S., Korotkov, A. I., Combustion of Powdered Metals in Active Media, Nauka, Moscow, 1972 (English translation FTD-MT-24-551-73 (AD 769-576)).
190. Bonczyk, P. A., and Shirley, J. A., "Measurement of CH and CN Concentration in Flames by Laser-Induced Saturated Fluorescence," Combustion and Flame, Vol. 34, pp. 253-264, 1979.
191. Crosley, D. R., "Collisional effects on laser-induced fluorescence flame measurements," Optical Engineering, Vol. 20, No. 4, pp. 511-521, 1981.
192. Salmon, J. T., Lucht, R. P., Sweeney D. W., and Laurendeau, N. M., "Laser-Saturated Fluorescence Measurements of NH in a Premixed Subatmospheric CH₄/N₂O/Ar Flame," 20th Symposium (Int'l) on Combustion, Combustion Institute, Pittsburgh, 1984, pp 1187-1193.

193. Goldsmith, J. E. M., "Photochemical Effects in Two-Photon-Excited Fluorescence Detection of Atomic Oxygen in Flames," Applied Optics, Vol. 26, No. 17, pp. 3566-3572, 1987.
194. Morley, C., "The Application of Laser Fluorescence to Detection of Species in Atmospheric Pressure Flames. Relative Quenching Rates of OH by H₂O, H₂, and CO," Combustion and Flame, Vol. 47, pp. 67-81, 1982.
195. Anderson, W. R., Decker, L. J., and Kotlar, A. J., "Concentration Profiles of NH and OH in a Stoichiometric CH₄/N₂O Flame by Laser Excited Fluorescence and Absorption," Combustion and Flame, Vol. 48, pp. 179-190, 1982.
196. Masri, A. R., Bilger, R. W., and Dibble, R. W., "Fluorescence Interference with Raman Measurements in Nonpremixed Flames of Methane," Combustion and Flame, Vol. 68, pp. 109-119, 1987.
197. Gutmark, E., Parr, T. P., Hanson-Parr, D. M., and Schadow, K. C., "Azimuthal Structure of Circular Diffusion Flame," Paper presented at Spring 1987 Western States Section/Combustion Institute Meeting, Salt Lake City, Utah, April 1987 (Paper WSS/CI 87-40).
198. Williams, W. D., Jones, J. H., Curry, B. P., and Lewis, J. W. L., Raman Scattering Diagnostics Development Using an Excimer/Dual Dye Laser System, AEDC TR 83-15, Arnold Engineering Development Center, Arnold Air Force Station, TN, July 1983.
199. Jeffries, J. B., Copeland, R. A., Smith, G. P., and Crosley, D. R., "Multiple Species Laser-Induced Fluorescence in Flames," 21st Symposium (Int'l) on Combustion, Combustion Institute, Pittsburgh, 1988, pp. 1709-1718.
200. Wehry, E. L., Hohmann, R., Gates, J. K., Guilbault, L. F., Johnson, P. M., Schendel, J. S., and Radspinner, D. A., "Fragmentation-fluorescence spectrometric determination of non-fluorescent compounds," Applied Optics, Vol. 26, No. 17, pp. 3559-3565, 1987.
201. Cor, J., workshop report in preparation from workshop on "Gas Phase Reactions in Propellant Combustion" held at 24th JANNAF Combustion Meeting, Monterey, CA, Oct. 1987.
202. Behrens, R., "Simultaneous Thermogravimetric Modulated Beam Mass Spectrometry and Time-of-Flight Velocity Spectra Measurements of the Thermal Decomposition Products from HMX and RDX," Paper presented at Spring 1987 Western States Section/Combustion Institute Meeting, Salt Lake City, Utah, April 1987 (Paper WSS/CI 87-19). See also Review of Scientific Instruments, Vol. 58, No. 3, pp. 451-461, 1987.
203. Smith, W. H., and Liszt, H. S., "Franck-Condon Factors and Absolute Oscillator strengths for NH, SiH, S₂, and SO," Journal of Quantitative Spectroscopy and Radiative Transfer, Vol. 11, pp. 45-54, 1971.
204. Guirao, C., and Williams, F. A., "A Model for Ammonium Perchlorate Deflagration between 20 and 100 Atm.," AIAA Journal, Vol. 9, No. 7, pp. 1345-1356, 1971.
205. Lucht, R. P., Sweeney, D. W., and Laurendeau, N. M., "Laser-Saturated Fluorescence Measurements of OH Concentration in Flames," Combustion and Flame, Vol. 50, pp. 189-205, 1983.
206. Glassman, I., Combustion, 2nd ed., Academic Press, New York, 1987, pp. 67-106.

207. Hucknall, D. J., Chemistry of Hydrocarbon Combustion, Chapman and Hall, London, 1985.
208. Summerfield, M., ed., Solid Propellant Rocket Research, ARS Progress in Astronautics and Rocketry, Volume 1, Academic Press, New York, 1960.
209. Williams, F. A., Barrere, M., Huang, N. C., Fundamental Aspects of Solid Propellant Rockets, AGARDograph 116, NATO Advisory Group for Aerospace Research and Development (AGARD), 1969.
210. Cohen, A., Miller, M. S., Holmes, H. E., and Funk, C. M., "Heats of Explosion for LOVA Propellants," 24th JANNAF Combustion Meeting, CPIA Publication 476, Volume III, pp. 115-120, 1987.

APPENDIX A. LISTING OF CN TEMPERATURE FITTING PROGRAM

The equations used in the synthetic spectra are the standard equations as given in (Ref. 160). Since the splitting of the rotational lines is not resolvable with the detection equipment used, the CN B-X transition is treated as a $1\Sigma-1\Sigma$ transition. The term values of the emission lines are calculated with the standard formulas for a vibrating rotator (Ref. 160), where the ' refers to the excited state (the initial level of the emitting molecule) and the " refers to the ground state:

$$T=F(J,v) + G(v) + T_e$$

where

$$\begin{aligned} F(J,v) &= B_v(v)J(J+1) - D_v(v)J^2(J+1)^2 \\ G(v) &= \omega_e(v+0.5) - \omega_e x_e(v+0.5)^2 + \omega_e y_e(v+0.5)^3 \\ B_v(v) &= B_e - \alpha_e(v+0.5) + \gamma_e(v+0.5)^2 \\ D_v(v) &= D_e - \beta_e(v+0.5) \end{aligned}$$

The wavelength of the emission lines is then calculated as $\lambda = T' - T''$. The intensity of a given line is calculated by assuming a Boltzmann distribution:

$$I_{em} = CS_j A_{v'v''} n^4 \exp(-F'hc/kT_{rot}) \exp(-G'hc/kT_{vib})$$

where C is a constant, S_j is the rotational line strength ($=J'$ for the CN R branch and $=J'+1$ for the P branch (Ref. 160)), $A_{v'v''}$ is the Franck-Condon factor (Ref. 161), and the term values for the rotation and vibration have been separated to allow for differing rotational and vibrational temperatures. Values for ω_e , $\omega_e x_e$, $\omega_e y_e$, B_e , α_e , γ_e , D_e , β_e can be found in (Ref. 162). However, the B_v , D_v , and G values for the B $2\Sigma^+$ state are poorly fit by the preceding equations, so tabular values from (Ref. 163) were used. Once the line locations and intensities were calculated (for $v'=0-7$ and $J=1-95$), a synthetic spectrum was created by scanning a triangular slit function with a given bandpass over the 760 (8X95) calculated spectral lines. A bandpass of 0.125 nm (FWHM) was used, in agreement with the bandpass used in the analysis of the OH spectra (Ref. 3). The synthetic spectra were then calculated for a range of temperatures and the best match to the experimental spectra was selected.

The program was run with the Microsoft Fortran 2.2 compiler for the Macintosh. The two subroutines at the end of the program ("Cricket" and "Fastsave") convert the data file, containing two columns with the wavelength and CN emission intensity data, into a file that can be rapidly opened by the CricketGraph 1.1 software. Text files can be opened by CricketGraph, but these large files are more conveniently opened in "fast format". The program reads input data from a startup file (START), with the input data being the rotational (TROT) and vibrational (TVIB) temperature, the initial wavelength to start the scanning (WINIT), the number of model data points to use (NDATA, usually 700 to match the Reticon's array size), the resolution of the scanning (RES, defined as the FWHM of the triangular slit function), and the $v'-v''$ of the band sequence (DELTV, works for $v'-v''=0, \pm 1$). The program then calculates the line locations and writes the information to disk in the "LINES" file. Then, the triangular slit function is scanned over the calculated CN lines and the resulting spectrum is written to the "DATA" file in fast format. The program could be used to model more resolved spectra by changing RES.

```

PROGRAM BOLTZM
C   CALCULATES BOLTZMANN DISTRIBUTION IN MOLECULE
C   AS A FUNCTION OF QUANTUM NUMBER.
    DIMENSION WAYER(100,100), ER(100,100), VR(100,100)
    DIMENSION WAVEP(100,100), EP(100,100), VP(100,100)
    DIMENSION VZERO(8,8), FC(8,8), BV1(8,8), BV2(8,8)
    DIMENSION ENET(2000), EINCR(2000), WSCAN(2000), ESUM(2000)
    DIMENSION DV1(8), DV2(8), G1(9), G2(9), BG(8)
    DIMENSION FR(100), BFR(100), FP(100), BFP(100)
    INTEGER*2 N,COLUMNS
    INTEGER*2 NDATA,DELTV
    REAL WSCAN(2000), ENET(2000), ESUM(2000)
    OPEN(UNIT=23, FILE='START', FORM='FORMATTED',STATUS='OLD')
    READ (23,250) TROT,TVIB,WINIT,RES,NDATA,DELTV
250  FORMAT(3F9.3,F6.3,2I4)
    C
    C   CAN WRITE MOLECULE INFO IF DESIRED
    C
    WRITE(9,300)
    FORMAT('MOLECULE IS CN')
300  WRITE(9,400) TROT,TVIB
    FORMAT('BOLTZMANN DISTRIBUTION FOR TROT,TVIB=',F9.3,',',F9.3)
400  WRITE(9,450) WINIT,RES,NDATA,DELTV
    FORMAT('WINIT=',F9.3,5X,'RES=',F6.3,5X,'NDATA=',I4,5X,
450  1 'DELTV=',I4)
    CLOSE(UNIT=23)
    OPEN(UNIT=23, FILE='LINES', FORM='FORMATTED',STATUS='NEW')
    C   TO CALCULATE BAND ORIGINS, NEED ACCURATE G' DATA FROM
    C   ENGLEMAN--DATA IS G'(V)=G1(N1) BUT USE G1(NV1) TO AVOID ZEROS
    C
    G1(1)=1076.9
    G1(2)=3200.5
    G1(3)=5283.9
    G1(4)=7324.9
    G1(5)=9320.9
    G1(6)=11269.2
    G1(7)=13166.9
    G1(8)=15011.5
    G2(1)=1031.0
    G2(2)=3073.4
    G2(3)=5089.5
    G2(4)=7079.4
    G2(5)=9042.8
    G2(6)=10979.9
    G2(7)=12890.4
    G2(8)=14774.4
    G2(9)=16631.9
    V00=25752
    C
    C   VZERO DATA FROM JEVONS PRS (A) (POOR), ENGLEMAN FOR 0,0 AND 1,0
    C
    C   NOTE!!!!!! NEED DUMMY VARIABLES SINCE ARRAYS CANT HAVE ZEROS!
    C   SO NV1=NV2=1 FOR 0,0 BAND, ETC, AND N1=0, SO USE N1 IN CALCS
    C
    VZERO(1,1)=25797.81
    C   VZERO(2,2)=25879.01
    C   VZERO(3,3)=25946.34
    C   VZERO(4,4)=25997.57

```

```

C      VZERO(5,5)=26030.17
C      VZERO(6,6)=26041.36
C      VZERO(7,7)=26028.05
C      VZERO(8,8)=25987.13
C
C      0,1 SEQUENCE DATA CALCULATED SINCE JEVONS' DATA POOR
C
C      VZERO(1,2)=23755.5
C      VZERO(2,3)=23863.0
C      VZERO(3,4)=23956.5
C      VZERO(4,5)=24034.1
C      VZERO(5,6)=24093.0
C      VZERO(6,7)=24130.8
C      VZERO(7,8)=24144.5
C      VZERO(8,9)=24131.6
C
C      1,0 SEQUENCE DATA FROM ENGLEMAN
C
C      VZERO(2,1)=27921.42
C      VZERO(3,2)=27962.43
C      VZERO(4,3)=27987.35
C      VZERO(5,4)=27993.57
C      VZERO(6,5)=27978.32
C      VZERO(7,6)=27938.60
C      VZERO(8,7)=27871.16
C
C      FC(NV1,NV2)=FRANCK-CONDON FACTORS, WHERE NV1=V'+1, NV2=V''+1
C
C      FC(1,1)=0.90861
C      FC(2,2)=0.75682
C      FC(3,3)=0.64884
C      FC(4,4)=0.57392
C      FC(5,5)=0.52453
C      FC(6,6)=0.49543
C      FC(7,7)=0.48301
C      FC(8,8)=0.48479
C
C      FC(1,2)=0.083968
C      FC(2,3)=0.13506
C      FC(3,4)=0.16365
C      FC(4,5)=0.17684
C      FC(5,6)=0.17943
C      FC(6,7)=0.17463
C      FC(7,8)=0.16456
C      FC(8,9)=0.15062
C
C      FC(2,1)=0.08908
C      FC(3,2)=0.15573
C      FC(4,3)=0.20419
C      FC(5,4)=0.23950
C      FC(6,5)=0.26442
C      FC(7,6)=0.28056
C      FC(8,7)=0.28863
C
C      DO 2600 NV1=1,8
C
C      HERE IS WHERE THE BAND SEQUENCES ARE INPUT--0,0->NV1=NV2--

```



```

C      THUS DELTV=0,+1,-1 FOR 0,0;0,1; AND THE 1,0 SEQUENCES
      NV2=NV1-DELT
      IF (NV2.EQ.0) GO TO 2600

C
      VZERO(NV1,NV2)=V00+G1(NV1)-G2(NV2)

C
C      N1,N2 ARE ACTUAL N
C
      N1=NV1-1
      N2=NV2-1

C
C      CAN WRITE MOLECULE INFO IF DESIRED
C
      WRITE(9,350) N1,N2
350    FORMAT (/,'BAND IS',I3,',',I3)
      WRITE(9,375) VZERO(NV1,NV2),FC(NV1,NV2)
375    FORMAT ('BAND ORIGIN IS',F12.4,' CM-1', ' FC=',F8.4)
      WRITE(23,500)
500    FORMAT (2X,'J1',1X,'V',2X,'V"',4X,'WAVER',10X,'ER',
1      7X,'WAVEP',10X,'EP')

C
C      CALCULATE B: BE", BE', FE", FE', V" AND V' MUST BE GIVEN
C      BUT USE TABULAR VALUES FOR BV1 SINCE DATA HARD TO FIT
C      BV1 DATA FROM ENGLEMAN
      BE2=1.89974
      FE2=0.017369
      GE2=-0.0003107
      BV2(NV1,NV2)=BE2-FE2*(N2+0.5)+GE2*(N2+0.5)**2

C
      BV1(1,1)=1.95874
      BV1(2,2)=1.93800
      BV1(3,3)=1.91629
      BV1(4,4)=1.89427
      BV1(5,5)=1.87062
      BV1(6,6)=1.84531
      BV1(7,7)=1.81978
      BV1(8,8)=1.78989

C
      BV1(2,1)=1.93784
      BV1(3,2)=1.91621
      BV1(4,3)=1.89338
      BV1(5,4)=1.87028
      BV1(6,5)=1.84484
      BV1(7,6)=1.81888
      BV1(8,7)=1.79028

C
C      SINCE NO BV DATA FOR 0,1 SEQUENCE, USE 0,0 BV DATA
C
      BV1(1,2)=BV1(1,1)
      BV1(2,3)=BV1(2,2)
      BV1(3,4)=BV1(3,3)
      BV1(4,5)=BV1(4,4)
      BV1(5,6)=BV1(5,5)
      BV1(6,7)=BV1(6,6)
      BV1(7,8)=BV1(7,7)
      BV1(8,9)=BV1(8,8)

C
C      SAME FOR DV--USE TABULAR DATA FROM ENGLEMAN

```

```

C      DV1(1)=6.58E-06
      DV1(2)=6.69E-06
      DV1(3)=6.82E-06
      DV1(4)=6.98E-06
      DV1(5)=7.19E-06
      DV1(6)=7.43E-06
      DV1(7)=7.72E-06
      DV1(8)=8.03E-06

C      DE2=6.40E-06
      BETAE2=1.2E-08
      DV2(NV2)=DE2+BETAE2*(N2+1)

C      J2=1
      DO 2500 J1=1,95
C      J1=J', J2=J" AND J" IS J IN TABLES
C      R BRANCH CALCULATIONS, J1-J2=1
C
C      VIBRATIONAL TERMS FOR VIBRATIONAL LEVELS=G(NV1)
C      G(NV1)=OMEGAE(V'+0.5)-OMEGAE*XE(V'+0.5)**2+
C      OMEGAE*YE(V'+0.5)**3
C
C      WORKS FOR GROUND STATE, BUT FIT IS POOR FOR B STATE
C      SO USE ENGLEMAN'S DELTA G DATA AND HERZBERG'S DATA TO
C      CALCULATE GZERO
C
C      OMEGAE=2163.9
C      XE=0.009335
C      G1ZERO=OMEGAE*0.5-(OMEGAE*XE)*0.5**2
C      G1(1)=G1ZERO
C      G1(2)=G1(1)+2123.57
C      G1(3)=G1(2)+2083.42
C      G1(4)=G1(3)+2041.00
C      G1(5)=G1(4)+1996.01
C      G1(6)=G1(5)+1948.15
C      G1(7)=G1(6)+1897.25
C      G1(8)=G1(7)+1843.11
C
C      VIBRATIONAL BOLTZMANN FACTOR=BG(NV1)
C
C      BG(NV1)=EXP(-1.43836*G1(NV1)/TVIB)
C
C      R BRANCH CALCULATIONS, ER=INTENSITY OF LINE AND
C      VR=LOCATION (CM-1) OF LINE, J1-J2=+1
C
C      JR1=J1
C      JR2=JR1-1
C      SJR=JR1
C
C      ROTATIONAL TERMS FOR ROTATIONAL LEVELS=FR(JR1)
C
C      FR(JR1)=BV1(NV1,NV2)*JR1*(JR1+1)
1 -DV1(NV1)*(JR1**2)*((JR1+1)**2)
C
C      BF=ROT BOLTZMANN FACTOR, SJ=LINE STRENGTH
C
C      BFR(JR1)=EXP(-1*1.43836*FR(JR1)/TROT)

```

```

ER(JR1,NV1)=2*SJR*FC(NV1,NV2)*BFR(JR1)*BG(NV1)
VR(JR1,NV1)=VZERO(NV1,NV2)+BV1(NV1,NV2)*JR1*(JR1+1)-
1 BV2(NV1,NV2)*JR2*(JR2+1)
2 -DV1(NV1)*JR1**2*(JR1+1)**2
3 +DV2(NV2)*JR2**2*(JR2+1)**2
WAVER(JR1,NV1)=1.0E07*(VR(JR1,NV1)**-1)/1.000282

C
C P BRANCH CALCULATIONS, J1-J2=-1
C
JP1=J1
JP2=JP1+1
SJP=JP1+1

C
C ROTATIONAL TERMS FOR ROTATIONAL LEVELS=FP(JP1)
C
FP(JP1)=BV1(NV1,NV2)*JP1*(JP1+1)
1 -DV1(NV1)*(JP1**2)*((JP1+1)**2)

C
C BF=ROT. BOLTZMANN FACTOR, SJ=LINE STRENGTH
C
BFP(JP1)=EXP(-1*1.43836*FP(JP1)/TROT)
EP(JP1,NV1)=2*SJR*FC(NV1,NV2)*BFP(JP1)*BG(NV1)
VP(JP1,NV1)=VZERO(NV1,NV2)+BV1(NV1,NV2)*JP1*(JP1+1)-
1 BV2(NV1,NV2)*JP2*(JP2+1)
2 -DV1(NV1)*JP1**2*(JP1+1)**2
3 +DV2(NV2)*JP2**2*(JP2+1)**2
WAVEP(JP1,NV1)=1.0E07*(VP(JP1,NV1)**-1)/1.000282

C
C NOW WRITE LINE DATA IF DESIRED
C
WRITE(23,1000) J1,N1,N2,WAVER(JR1,NV1),ER(JR1,NV1),
1 WAVEP(JP1,NV1),EP(JP1,NV1)
1000 FORMAT(3I3,4F12.4)
C WRITE(9,1100) J1
C1100 FORMAT(I3)
C
2500 CONTINUE
2600 CONTINUE
WRITE(9,2700)
2700 FORMAT('LINE CALCULATIONS COMPLETE - SCANNING UNDERWAY')
CLOSE(UNIT=23)

C
C NOW START SCANNING OVER LINES
C
DO 3000 I=1,NDATA
3000 WSCAN(I)=0.000
WSCAN(0)=WINIT
DO 5000 K=1,NDATA
DO 3100 I2=1,NDATA
3100 EINCR(I2)=0.000
DO 3200 I3=1,NDATA
3200 ENET(I3)=0.000
M=K-1
WSCAN(K)=WSCAN(M)+0.0175
DO 4200 NV1=1,8
DO 4000 J1=1,100
WDELT=WSCAN(K)-WAVER(J1,NV1)
DELTA=ABS(WDELT)

```

```

        IF (DELTA.GT.RES) GO TO 3900
        FRAC=(RES-DELTA)/RES
        GO TO 3950
3900    FRAC=0.000
3950    EINCR(J1)=FRAC*ER(J1,NV1)
        ENET(K)=ENET(K)+EINCR(J1)
4000    CONTINUE
        DO 4100 J1=1,100
        WDELTA=WSCAN(K)-WAVEP(J1,NV1)
        DELTA=ABS(WDELTA)
        IF (DELTA.GT.RES) GO TO 4025
        FRAC=(RES-DELTA)/RES
        GO TO 4050
4025    FRAC=0.000
4050    EINCR(J1)=FRAC*EP(J1,NV1)
        ENET(K)=ENET(K)+EINCR(J1)
        ESUM(K)=ENET(K)
4100    CONTINUE
4200    CONTINUE
C
C      NOW WRITE DATA TO FILE IF DESIRED
C
C          WRITE(23,4950) WSCAN(K),CHAR(9),ENET(K)
C      4950    FORMAT (F8.3,A1,F8.2)
C          WRITE (9,4975) K
C      4975    FORMAT (I4)
C
        IF (K.EQ.175) GO TO 4900
        IF (K.EQ.350) GO TO 4960
        IF (K.EQ.525) GO TO 4970
        GO TO 5000
4900    WRITE (9,4950)
4950    FORMAT ('175 DATA POINTS')
4951    GO TO 5000
4960    WRITE (9,4965)
4965    FORMAT ('350 DATA POINTS')
4966    GO TO 5000
4970    WRITE (9,4975)
4975    FORMAT ('525 DATA POINTS')
4976    GO TO 5000
5000    CONTINUE
        WRITE (9,5100)
5100    FORMAT ('SCANNING COMPLETE - POST-PROCESSING UNDERWAY')
        OPEN(UNIT=23, FILE='DATA', FORM='FORMATTED', STATUS='NEW')

C
C      NOW CHANGE DATA TO FAST FORMAT
C      SUBROUTINES WRITTEN BY FRANK FREDERICK II
C
        COLUMNS=2
        WRITE(23)COLUMNS
        CALL FASTSAVE('Wavelength, nm ',NDATA,WSCAN)
        CALL FASTSAVE('CN intensity ',NDATA,ESUM)
        CALL CRICKET('DATA')
8200    CLOSE (UNIT=23)
8300    END
C
C REAL FASTSAVE SUBROUTINE

```

```

C      SUBROUTINE FASTSAVE(TITLE, NUM, L )
C      CHARACTER*15 TITLE
C      INTEGER*2 NUM
C      REAL L( NUM )
C      CHARACTER*32 BUFFER

C      INTEGER*2 COUNT
C      CHARACTER*16 TITLEP

C      determine the output data size in bytes
C
C      COUNT = NUM * 11
C
C      change the column title to a pascal string
C      TITLEP = char(len(trim(TITLE))//TITLE
C      WRITE( 23 )TITLEP
C      WRITE( 23 )COUNT

C
C      DO 300 I=1, NUM, 1
C      write integer data to string buffer so ascii character
C      WRITE( BUFFER, 200 )L( I )
C      200  FORMAT( F10.3 )
C      WRITE( 23 )trim( BUFFER )//char( 13 )
C      300  CONTINUE
C
C      RETURN
C      END

C
C      This subroutine changes the File whose name is passed
C      to the type and creator of a Cricket Graph Fast Format
C      file.
C
C      SUBROUTINE CRICKET( NAME )
C
C      character*(*) NAME
C      INTEGER*4 toolbx
C      CHARACTER*256 FILENAME
C      INTEGER PTR
C      PARAMETER (PTR=Z'C0000000')

C
C      include XP 20:FORTTRAN:INCLUDE FILES:file.inc
C      include XP 20:FORTTRAN:INCLUDE FILES:params.inc
C
C      change the file name to a PASCAL string
C      FILENAME = char(len(TRIM( NAME))//TRIM(NAME )
C
C      set the toolbox parameters to call PBGETFILEINFO
C      ionameptr = toolbx(PTR, FILENAME )
C      iocompletion = 0
C      ioofdirindex = -1
C      iocompletion = 0
C      iovrefnum = 0
C      ioofversnum = 0
C
C      toolbox routine to get file info

```

```
CALL toolbox(PBGETFILEINFO, toolbox(PTR, params))
C
C Cricket Graph Fast Format type and Creator
fdtype = 'STWK'
fdcreator = 'CGRF'
C
C toolbox routine to set file info
CALL toolbox(PBSETFILEINFO, toolbox(PTR, params))
C
RETURN
END
```

APPENDIX B. LISTING OF NH TEMPERATURE FITTING PROGRAM

The same general scheme for calculating CN synthetic spectra was used for NH synthetic spectra, i.e.,

$$T = F(J, \nu) + G(\nu) + T_e$$

The wavelength of the emission lines is then calculated as $\lambda = T' - T''$. The intensity of a given line is calculated by assuming a Boltzmann distribution:

$$I_{em} = CS_j A_{\nu' \nu''} n^4 \exp(-F'hc/kT_{rot}) \exp(-G'hc/kT_{vib})$$

For the NH ($A^3\Pi-X^3\Sigma$) transition, the $F(J, \nu)$ equations are quite different from the equations used for CN, especially since the more open NH rotational structure required that the triplet splitting of the lines be taken into account. For a $^3\Sigma$ state, Schlapp's equations were used (Ref. 160,168,172):

$$F_1(K) = B_v K(K+1) + (2K+3)B_v - \lambda - (\text{Ref. } (2K+3)^2 B_v^2 + \lambda^2 - 2\lambda B_v)^{0.5} + \gamma(K+1)$$

$$F_2(K) = B_v K(K+1)$$

$$F_3(K) = B_v K(K+1) - (2K-1)B_v - \lambda - (\text{Ref. } (2K-1)^2 B_v^2 + \lambda^2 - 2\lambda B_v)^{0.5} - \gamma K$$

where F_1 , F_2 , and F_3 refer to the level with $J=K+1$, $J=K$, and $J=K-1$, respectively.

For $^3\Pi$ state, Gilbert's equations were used (Ref. 160,168,172):

$$F_1(J) = B_v (\text{Ref. } J(J+1) - Z_1^{0.5} - 2Z_2) - D_v (J-0.5)^4$$

$$F_2(J) = B_v (\text{Ref. } J(J+1) + 4Z_2) - D_v (J+0.5)^4$$

$$F_3(J) = B_v (\text{Ref. } J(J+1) + Z_1^{0.5} - 2Z_2) - D_v (J+1.5)^4$$

where

$$Z_1 = \Lambda^2 Y(Y-4) + 4/3 + 4J(J+1)$$

$$Z_2 = (1/3 Z_1) (\text{Ref. } \Lambda^2 Y(Y-1) - 4/9 - 2J(J+1))$$

$$Y = A/B_v$$

$$\nu(J', \nu') = \nu_{00} + F_1'(\nu', J') - F_1''(\nu'', K'')$$

where the relationship of J' and K'' was calculated by first calculating the relationship between J' and J'' (R branch: $J'' = J' - 1$, Q branch: $J'' = J'$, P branch: $J'' = J' + 1$) and then substituting $J'' = K'' + 1$, $J'' = K''$, and $J'' = K'' - 1$ for the F_1 , F_2 , and F_3 components, respectively.

The necessary spectroscopic data was taken from Malicet, et al (Ref. 168), with other sources available (Ref. 169-172). The data for $G(v)$ was also taken from (Ref. 168). The values used can be found in the program listing. The initial version of this program produced poor results for the Q branch bandheads (as discussed in Section 4.8), so the actual wavelengths of the 0,0 and 1,1 bands (Ref. 169-171) were temporarily input into the program, rather than calculating the lines. Future improvements in the program will allow the equations to be used exclusively. This will allow the program to create synthetic NH spectra for $J>30$, which might be important if higher temperatures are modeled.

NH Boltzmann program listing:

```

7      PROGRAM NHTEMP
C
C      CALCULATES BOLTZMANN DISTRIBUTION IN MOLECULE
C      AS A FUNCTION OF ROTATIONAL AND VIBRATIONAL
C      TEMPERATURE (TROT, TVIB RESPECTIVELY)
C
      DIMENSION WAVE1R(60,3), WAVE2R(60,3), WAVE3R(60,3)
      DIMENSION WAVE1P(60,3), WAVE2P(60,3), WAVE3P(60,3)
      DIMENSION WAVE1Z(60,3), WAVE2Z(60,3), WAVE3Z(60,3)
      DIMENSION VF1Z(60,3), VF2Z(60,3), VF3Z(60,3)
      DIMENSION VF1R(60,3), VF2R(60,3), VF3R(60,3)
      DIMENSION VF1P(60,3), VF2P(60,3), VF3P(60,3)
      DIMENSION F11(60,3), F12(60,3), F13(60,3)
      DIMENSION F21(60,3), F22(60,3), F23(60,3)
      DIMENSION BF11(60,3), BF12(60,3), BF13(60,3)
      DIMENSION E11(60,3), E12(60,3), E13(60,3)
      DIMENSION Z1(60,3), Z2(60,3), Z3(60,3)
      DIMENSION DELTA1(60,3), DELTA3(60,3)
      DIMENSION VZERO(8,8), FC(8,8), BV1(8), BV2(8)
      DIMENSION ENET(2000), EINCR(2000), WSCAN(2000), ESUM(2000)
      DIMENSION DV1(8), DV2(8), G1(9), G2(9), BG(8)
      DIMENSION HV1(8), HV2(8), Y(8)
      DIMENSION SJR(60), SJP(60), SJZ(60)
      DIMENSION GAMMA(3), LAMBDA(3), A(3)
      INTEGER*2 N,COLUMNS
      INTEGER*2 NDATA,DELTV
      REAL WSCAN(2000), ENET(2000), ESUM(2000)
C
C      FIRST, READ IN DATA FOR SYNTHETIC SPECTRA
C
C      JINIT=LOWER END OF WAVELENGTH RANGE FOR SCANNING
C      RES=SCANNING RESOLUTION (FWHM)
C      NDATA=NUMBER OF MODEL POINTS IN SYNTHETIC SPECTRUM
C      DELTV=0 FOR 0,0 SEQUENCE, -1 FOR 0,1 SEQUENCE, ETC
C
      OPEN(UNIT=23, FILE='START', FORM='FORMATTED', STATUS='OLD')
      READ (23,250) TROT,TVIB,WINIT,RES,NDATA,DELTV,SCALE1,SCALE2
250    FORMAT(3F9.3,F6.3,2I4,2F6.3)
C
C      CAN WRITE MOLECULE INFO IF DESIRED
C
      WRITE(9,300)
300    FORMAT ('MOLECULE IS NH')

```



```

WRITE(9,400) TVIB,TROT
400  FORMAT ('BOLTZMANN DISTRIBUTION FOR TVIB,TROT=',F9.3,',',F9.3)
WRITE(9,450) WINIT,RES,NDATA,DELTV,SCALE1,SCALE2
450  FORMAT('WINIT=',F9.3,5X,'RES=',F6.3,5X,'NDATA=',I4,5X,
1    'DELTV=',I4,/, 'SCALE1=',F6.3, '    SCALE2=',F6.3)
CLOSE(UNIT=23)

C
C    NOW CALCULATE LINE LOCATIONS AND INTENSITIES
C
OPEN(UNIT=23, FILE='LINES', FORM='FORMATTED',STATUS='NEW')

C
C    TO CALCULATE BAND ORIGINS, NEED TO CALCULATE G1 AND G2
C
C    DATA FROM MALICET J CHIM PHYS 67, 25-30 (1970)
C
A(1)=-34.72
A(2)=-34.74
A(3)=-34.6
BV1(1)=16.317
BV1(2)=15.567
BV1(3)=14.786
DV1(1)=1.780E-3
DV1(2)=1.762E-3
DV1(3)=1.765E-3
BV2(1)=16.342
BV2(2)=15.691
BV2(3)=15.046
DV2(1)=1.694E-3
DV2(2)=1.644E-3
DV2(3)=1.627E-3
WE1=3231.0
WEXE1=98.5
WE2=3203.2
WEXE2=78.3
WEYE1=0.0
WEYE2=0.0
FC(1,1)=1.000
FC(2,2)=0.999
FC(3,3)=0.996
LAMBDA(1)=0.928
LAMBDA(2)=0.948
LAMBDA(3)=0.955
GAMMA(1)=-0.053
GAMMA(2)=-0.047
GAMMA(3)=-0.044
HV2(1)=1.021E-7
HV2(2)=0.0
HV2(3)=0.0
HV1(1)=8.26E-8
HV1(2)=0.0
HV1(3)=0.0
HAT=1

C
C    NOTE THAT ARRAYS CANT HAVE ZEROS, SO NEED DUMMY VARIABLE
C    NV1=V'+1, AND HAVE N1=V'
C
DO 2600 NV1=1,3
NV2=NV1

```

```

N1=NV1-1
N2=NV2-1

C
C
C   CALCULATIONS OF NH LINES FOR V'=0,1,2
C
G1(NV1)=WE1*(N1+0.5)-WE1E1*(N1+0.5)**2+WEYE1*(N1+0.5)**3
G2(NV2)=WE2*(N2+0.5)-WE1E2*(N2+0.5)**2+WEYE2*(N2+0.5)**3

C
V00=29776.76

C
VZERO(NV1,NV2)=V00+G1(NV1)-G2(NV2)

C
C   ACTUALLY, THIS LEADS TO POOR RESULTS SO USE MALICET G DATA
C   DELTAG'(1/2)=3033.9, DELTAG'(3/2)=2836.8,
C   DELTAG"(1/2)=3125.49, DELTAG"(3/2)=2968.89
C
VZERO(2,2)=VZERO(1,1)+3033.9-3125.49
VZERO(3,3)=VZERO(2,2)+2836.8-2968.89

C
C
WRITE(9,550) N1,N2
550  FORMAT(/,'BAND IS',I3,',',I3)
WRITE(9,575) VZERO(NV1,NV2),FC(NV1,NV2)
575  FORMAT('BAND ORIGIN IS',F12.4,' CM-1', ' FC=',F8.4)
WRITE(23,600)
600  FORMAT(' WAVER1 ', ' WAVER2 ',
1    ' WAVER3 ', ' WAVEQ1 ', ' WAVEQ2 ', ' WAVEQ3 ',
2    ' WAVE1P ')

C
C   VIBRATIONAL BOLTZMANN FACTOR=BG(NV1)
C
BG(NV1)=EXP(-1.43836*G1(NV1)/TVIB)

C
C   NOW CALCULATE F" FOR ARBITRARY K AND THEN SUBSTITUTE
C   K1R FOR K IN WAVELENGTH CALCULATION
C
DO 700 K2=1,35
DELTA1(K2,NV2)=((2*K2+3)*BV2(NV2)-LAMBDA(NV2)-((2*K2+3)**2*
1 BV2(NV2)**2+LAMBDA(NV2)**2-2*LAMBDA(NV2)*BV2(NV2))**0.5
2 +GAMMA(NV2)*(K2+1))/SCALE2
DELTA3(K2,NV2)=(BV2(NV2)*(1-2*K2)-LAMBDA(NV2)+
1 ((2*K2-1)**2*BV2(NV2)**2+LAMBDA(NV2)**2
2 -2*LAMBDA(NV2)*BV2(NV2))**0.5-GAMMA(NV2)*K2)/SCALE2
F21(K2,NV2)=BV2(NV2)*K2*(K2+1)-DV2(NV2)*
1 (K2*(K2+1))**2+HV2(NV2)*(K2*(K2+1))**3+DELTA1(K2,NV2)
F22(K2,NV2)=BV2(NV2)*K2*(K2+1)-DV2(NV2)*
1 (K2*(K2+1))**2+HV2(NV2)*(K2*(K2+1))**3
F23(K2,NV2)=BV2(NV2)*K2*(K2+1)-DV2(NV2)*
1 (K2*(K2+1))**2+HV2(NV2)*(K2*(K2+1))**3+DELTA3(K2,NV2)
700  CONTINUE

C
C   NOW CALCULATE F'(J') AND F"(J')
C
DO 2500 J1=3,35

C
C   FIRST, CALCULATE QUANTUM NUMBER RELATIONSHIPS
C   J1=J', K2=K", K21R=K" FOR F1 R BRANCH
C   R BRANCH: J"=J'-1, Q BRANCH: J"=J', P BRANCH: J"=J'+1

```

```

C      F1: J=K+1, F2: J=K, F3: J=K-1
C
      K21R=J1-2
      K22R=J1-1
      K23R=J1
      K21Z=J1-1
      K22Z=J1
      K23Z=J1+1
      K21P=J1
      K22P=J1+1
      K23P=J1+2
C
C      NOW CALCULATE F' (J') (=F11 FOR F1')
C
      Y(NV1)=A(NV1)/BV1(NV1)
      Z1(J1,NV1)=(HAT**2*Y(NV1)*(Y(NV1)-4)+4/3+4*J1*(J1+2))/SCALE1
      Z2(J1,NV1)=(1/(Z1(J1,NV1)*3)*(HAT**2*Y(NV1)*(Y(NV1)-1)-
1 4/9-2*J1*(J1+1)))/SCALE1
      F11(J1,NV1)=BV1(NV1)*(J1*(J1+1)-Z1(J1,NV1)**0.5-
1 2*Z2(J1,NV1))-DV1(NV1)*(J1-0.5)**4
      F12(J1,NV1)=BV1(NV1)*(J1*(J1+1)+4*Z2(J1,NV1))-
1 DV1(NV1)*(J1+0.5)**4
      F13(J1,NV1)=BV1(NV1)*(J1*(J1+1)+Z1(J1,NV1)**0.5-
1 2*Z2(J1,NV1))-DV1(NV1)*(J1+1.5)**4
C
C      NOW CALCULATE WAVELENGTHS FOR F1 R BRANCH (WAVE1R) ETC
C
      VF1R(J1,NV1)=VZERO(NV1,NV2)+F11(J1,NV1)-F21(K21R,NV2)
      VF1P(J1,NV1)=VZERO(NV1,NV2)+F11(J1,NV1)-F21(K21P,NV2)
      VF1Z(J1,NV1)=VZERO(NV1,NV2)+F11(J1,NV1)-F21(K21Z,NV2)
C
      VF2R(J1,NV1)=VZERO(NV1,NV2)+F12(J1,NV1)-F22(K22R,NV2)
      VF2P(J1,NV1)=VZERO(NV1,NV2)+F12(J1,NV1)-F22(K22P,NV2)
      VF2Z(J1,NV1)=VZERO(NV1,NV2)+F12(J1,NV1)-F22(K22Z,NV2)
C
      VF3R(J1,NV1)=VZERO(NV1,NV2)+F13(J1,NV1)-F22(K23R,NV2)
      VF3P(J1,NV1)=VZERO(NV1,NV2)+F13(J1,NV1)-F22(K23P,NV2)
      VF3Z(J1,NV1)=VZERO(NV1,NV2)+F13(J1,NV1)-F22(K23Z,NV2)
C
      WAVE1R(J1,NV1)=1.0E07*(VF1R(J1,NV1)**-1)/1.00028
      WAVE2R(J1,NV1)=1.0E07*(VF2R(J1,NV1)**-1)/1.00028
      WAVE3R(J1,NV1)=1.0E07*(VF3R(J1,NV1)**-1)/1.00028
C
      WAVE1P(J1,NV1)=1.0E07*(VF1P(J1,NV1)**-1)/1.00028
      WAVE2P(J1,NV1)=1.0E07*(VF2P(J1,NV1)**-1)/1.00028
      WAVE3P(J1,NV1)=1.0E07*(VF3P(J1,NV1)**-1)/1.00028
C
      WAVE1Z(J1,NV1)=1.0E07*(VF1Z(J1,NV1)**-1)/1.00028
      WAVE2Z(J1,NV1)=1.0E07*(VF2Z(J1,NV1)**-1)/1.00028
      WAVE3Z(J1,NV1)=1.0E07*(VF3Z(J1,NV1)**-1)/1.00028
C
C      NOW CALCULATE LINE INTENSITIES
C
      SJR(J1)=(J1+1)/4
      SJZ(J1)=(2*J1+1)/4
      SJP(J1)=J1/4
C
C      BF=ROT. BOLTZMANN FACTOR, SJ=LINE STRENGTH

```

```

C      BF11(J1,NV1)=EXP(-1*1.43836*F11(J1,NV1)/TROT)
      BF12(J1,NV1)=EXP(-1*1.43836*F12(J1,NV1)/TROT)
      BF13(J1,NV1)=EXP(-1*1.43836*F13(J1,NV1)/TROT)
C
      E11(J1,NV1)=FC(NV1,NV2)*BF11(J1,NV1)*BG(NV1)
      E12(J1,NV1)=FC(NV1,NV2)*BF12(J1,NV1)*BG(NV1)
      E13(J1,NV1)=FC(NV1,NV2)*BF13(J1,NV1)*BG(NV1)
C
C      NOW WRITE LINE DATA IF DESIRED
C
      WRITE(23,1000) WAVE1R(J1,NV1),WAVE2R(J1,NV1),
1     WAVE3R(J1,NV1),WAVE1Z(J1,NV1),WAVE2Z(J1,NV1),
2     WAVE3Z(J1,NV1),WAVE1P(J1,NV1)
1000  FORMAT(7F10.4)
C      WRITE(9,1100) J1
C1100  FORMAT(I3)
C
2500   CONTINUE
2600   CONTINUE
C
C      Q BRANCH FIT POORLY, SO INPUT Q BRANCH LINES FOR 0,0
C      FROM DIXON, CAN J PHYS 37, 1171 (1959)
C
C      WAVELENGTH DATA INPUT AS F1 COMPONENT OF Q BRANCH=
C      WAVE1Z(J',V'+1), ETC
C
      WAVE1Z(2,1)=336.174
      WAVE1Z(3,1)=336.102
      WAVE1Z(4,1)=336.054
      WAVE1Z(5,1)=336.034
      WAVE1Z(6,1)=336.014
      WAVE1Z(7,1)=336.004
      WAVE1Z(8,1)=336.004
      WAVE1Z(9,1)=336.004
      WAVE1Z(10,1)=336.004
      WAVE1Z(11,1)=336.014
      WAVE1Z(12,1)=336.024
      WAVE1Z(13,1)=336.034
      WAVE1Z(14,1)=336.054
      WAVE1Z(15,1)=336.074
      WAVE1Z(16,1)=336.094
      WAVE1Z(17,1)=336.124
      WAVE1Z(18,1)=336.154
      WAVE1Z(19,1)=336.184
      WAVE1Z(20,1)=336.234
      WAVE1Z(21,1)=336.274
      WAVE1Z(22,1)=336.334
      WAVE1Z(23,1)=336.394
      WAVE1Z(24,1)=336.464
      WAVE1Z(25,1)=336.544
      WAVE1Z(26,1)=336.634
      WAVE1Z(27,1)=336.734
      WAVE1Z(28,1)=336.854
      WAVE1Z(29,1)=336.984
      WAVE1Z(30,1)=337.134
      WAVE1Z(31,1)=337.293

```

C

WAVE1Z (32,1)=337.474

WAVE2Z (2,1)=335.844
 WAVE2Z (3,1)=335.884
 WAVE2Z (4,1)=335.904
 WAVE2Z (5,1)=335.914
 WAVE2Z (6,1)=335.924
 WAVE2Z (7,1)=335.944
 WAVE2Z (8,1)=335.954
 WAVE2Z (9,1)=335.964
 WAVE2Z (10,1)=335.974
 WAVE2Z (11,1)=335.994
 WAVE2Z (12,1)=336.014
 WAVE2Z (13,1)=336.034
 WAVE2Z (14,1)=336.054
 WAVE2Z (15,1)=336.084
 WAVE2Z (16,1)=336.114
 WAVE2Z (17,1)=336.144
 WAVE2Z (18,1)=336.184
 WAVE2Z (19,1)=336.234
 WAVE2Z (20,1)=336.274
 WAVE2Z (21,1)=336.334
 WAVE2Z (22,1)=336.404
 WAVE2Z (23,1)=336.474
 WAVE2Z (24,1)=336.554
 WAVE2Z (25,1)=336.644
 WAVE2Z (26,1)=336.754
 WAVE2Z (27,1)=336.864
 WAVE2Z (28,1)=336.994
 WAVE2Z (29,1)=337.144
 WAVE2Z (30,1)=337.303
 WAVE2Z (31,1)=337.484

C

WAVE3Z (1,1)=335.654
 WAVE3Z (2,1)=335.734
 WAVE3Z (3,1)=335.774
 WAVE3Z (4,1)=335.804
 WAVE3Z (5,1)=335.834
 WAVE3Z (6,1)=335.854
 WAVE3Z (7,1)=335.874
 WAVE3Z (8,1)=335.894
 WAVE3Z (9,1)=335.914
 WAVE3Z (10,1)=335.924
 WAVE3Z (11,1)=335.954
 WAVE3Z (12,1)=335.974
 WAVE3Z (13,1)=336.004
 WAVE3Z (14,1)=336.034
 WAVE3Z (15,1)=336.064
 WAVE3Z (16,1)=336.104
 WAVE3Z (17,1)=336.144
 WAVE3Z (18,1)=336.184
 WAVE3Z (19,1)=336.244
 WAVE3Z (20,1)=336.294
 WAVE3Z (21,1)=336.364
 WAVE3Z (22,1)=336.434
 WAVE3Z (23,1)=336.524
 WAVE3Z (24,1)=336.614
 WAVE3Z (25,1)=336.714

WAVE3Z (26,1)=336.834
WAVE3Z (27,1)=336.964
WAVE3Z (28,1)=337.114
WAVE3Z (29,1)=337.274
WAVE3Z (30,1)=337.463

C

WAVE1R(3,1)=335.364
WAVE1R(4,1)=334.954
WAVE1R(5,1)=334.564
WAVE1R(6,1)=334.184
WAVE1R(7,1)=333.814
WAVE1R(8,1)=333.445
WAVE1R(9,1)=333.095
WAVE1R(10,1)=332.745
WAVE1R(11,1)=332.395
WAVE1R(12,1)=332.065
WAVE1R(13,1)=331.735
WAVE1R(14,1)=331.415
WAVE1R(15,1)=331.115
WAVE1R(16,1)=330.815
WAVE1R(17,1)=330.526
WAVE1R(18,1)=330.245
WAVE1R(19,1)=329.976
WAVE1R(20,1)=329.726
WAVE1R(21,1)=329.486
WAVE1R(22,1)=329.256
WAVE1R(23,1)=329.046
WAVE1R(24,1)=328.856
WAVE1R(25,1)=328.686
WAVE1R(26,1)=328.536
WAVE1R(27,1)=328.396
WAVE1R(28,1)=328.276
WAVE1R(29,1)=328.186
WAVE1R(30,1)=328.126
WAVE1R(31,1)=328.086
WAVE1R(32,1)=328.076
WAVE1R(33,1)=328.096

C

WAVE2R(3,1)=334.764
WAVE2R(4,1)=334.414
WAVE2R(5,1)=334.074
WAVE2R(6,1)=333.725
WAVE2R(7,1)=333.375
WAVE2R(8,1)=333.025
WAVE2R(9,1)=332.685
WAVE2R(10,1)=332.355
WAVE2R(11,1)=332.025
WAVE2R(12,1)=331.705
WAVE2R(13,1)=331.395
WAVE2R(14,1)=331.085
WAVE2R(15,1)=330.795
WAVE2R(16,1)=330.506
WAVE2R(17,1)=330.226
WAVE2R(18,1)=329.966
WAVE2R(19,1)=329.716
WAVE2R(20,1)=329.476
WAVE2R(21,1)=329.256
WAVE2R(22,1)=329.046

WAVE2R(23,1)=328.856
WAVE2R(24,1)=328.686
WAVE2R(25,1)=328.536
WAVE2R(26,1)=328.396
WAVE2R(27,1)=328.286
WAVE2R(28,1)=328.196
WAVE2R(29,1)=328.136
WAVE2R(30,1)=328.096
WAVE2R(31,1)=328.096
WAVE2R(32,1)=328.126

C

WAVE3R(2,1)=334.644
WAVE3R(3,1)=334.324
WAVE3R(4,1)=333.984
WAVE3R(5,1)=333.655
WAVE3R(6,1)=333.315
WAVE3R(7,1)=332.975
WAVE3R(8,1)=332.645
WAVE3R(9,1)=332.315
WAVE3R(10,1)=331.995
WAVE3R(11,1)=331.675
WAVE3R(12,1)=331.365
WAVE3R(13,1)=331.065
WAVE3R(14,1)=330.775
WAVE3R(15,1)=330.486
WAVE3R(16,1)=330.216
WAVE3R(17,1)=329.956
WAVE3R(18,1)=329.707
WAVE3R(19,1)=329.476
WAVE3R(20,1)=329.246
WAVE3R(21,1)=329.046
WAVE3R(22,1)=328.856
WAVE3R(23,1)=328.686
WAVE3R(24,1)=328.536
WAVE3R(25,1)=328.396
WAVE3R(26,1)=328.286
WAVE3R(27,1)=328.196
WAVE3R(28,1)=328.136
WAVE3R(29,1)=328.096
WAVE3R(30,1)=328.096
WAVE3R(31,1)=328.126

C

WAVE1P(2,1)=336.914
WAVE1P(3,1)=337.204
WAVE1P(4,1)=337.534
WAVE1P(5,1)=337.873
WAVE1P(6,1)=338.223
WAVE1P(7,1)=338.573
WAVE1P(8,1)=338.923
WAVE1P(9,1)=339.273
WAVE1P(10,1)=339.633
WAVE1P(11,1)=339.983
WAVE1P(12,1)=340.333
WAVE1P(13,1)=340.683
WAVE1P(14,1)=341.022
WAVE1P(15,1)=341.362
WAVE1P(16,1)=341.702
WAVE1P(17,1)=342.042

WAVE1P(18,1)=342.382
WAVE1P(19,1)=342.712
WAVE1P(20,1)=343.042
WAVE1P(21,1)=343.372
WAVE1P(22,1)=343.702
WAVE1P(23,1)=344.032
WAVE1P(24,1)=344.361
WAVE1P(25,1)=344.701
WAVE1P(26,1)=345.031
WAVE1P(27,1)=345.361
WAVE1P(28,1)=345.701
WAVE1P(29,1)=346.051
WAVE1P(30,1)=346.401
WAVE1P(31,1)=346.761
WAVE1P(32,1)=347.131
WAVE1P(33,1)=347.511
WAVE1P(34,1)=347.911

C

WAVE2P(3,1)=337.343
WAVE2P(4,1)=337.723
WAVE2P(5,1)=338.103
WAVE2P(6,1)=338.483
WAVE2P(7,1)=338.843
WAVE2P(8,1)=339.213
WAVE2P(9,1)=339.573
WAVE2P(10,1)=339.933
WAVE2P(11,1)=340.293
WAVE2P(12,1)=340.643
WAVE2P(13,1)=340.992
WAVE2P(14,1)=341.342
WAVE2P(15,1)=341.682
WAVE2P(16,1)=342.032
WAVE2P(17,1)=342.372
WAVE2P(18,1)=342.702
WAVE2P(19,1)=343.042
WAVE2P(20,1)=343.372
WAVE2P(21,1)=343.702
WAVE2P(22,1)=344.032
WAVE2P(23,1)=344.361
WAVE2P(24,1)=344.701
WAVE2P(25,1)=345.031
WAVE2P(26,1)=345.371
WAVE2P(27,1)=345.711
WAVE2P(28,1)=346.061
WAVE2P(29,1)=346.411
WAVE2P(30,1)=347.151
WAVE2P(31,1)=347.531
WAVE2P(32,1)=347.930

C

WAVE3P(2,1)=337.224
WAVE3P(3,1)=337.633
WAVE3P(4,1)=338.023
WAVE3P(5,1)=338.403
WAVE3P(6,1)=338.783
WAVE3P(7,1)=339.163
WAVE3P(8,1)=339.523
WAVE3P(9,1)=339.893
WAVE3P(10,1)=340.253

WAVE3P (11,1)=340.613
 WAVE3P (12,1)=340.962
 WAVE3P (13,1)=341.312
 WAVE3P (14,1)=341.662
 WAVE3P (15,1)=342.012
 WAVE3P (16,1)=342.352
 WAVE3P (17,1)=342.692
 WAVE3P (18,1)=343.032
 WAVE3P (19,1)=343.362
 WAVE3P (20,1)=343.702
 WAVE3P (21,1)=344.032
 WAVE3P (22,1)=344.361
 WAVE3P (23,1)=344.701
 WAVE3P (24,1)=345.031
 WAVE3P (25,1)=345.371
 WAVE3P (26,1)=345.711
 WAVE3P (27,1)=346.061
 WAVE3P (28,1)=346.411
 WAVE3P (29,1)=347.151
 WAVE3P (30,1)=347.531
 WAVE3P (31,1)=347.941

C
 C
 C

1,1 Q BRANCH FIT POORLY SO USE FUNKE DATA

WAVE3P (2,2)=338.215
 WAVE3P (3,2)=338.615
 WAVE3P (4,2)=339.005
 WAVE3P (5,2)=339.395
 WAVE3P (6,2)=339.775
 WAVE3P (7,2)=340.155
 WAVE3P (8,2)=340.535
 WAVE3P (9,2)=340.915
 WAVE3P (10,2)=341.294
 WAVE3P (11,2)=341.664
 WAVE3P (12,2)=342.044
 WAVE3P (13,2)=342.424
 WAVE3P (14,2)=342.794
 WAVE3P (15,2)=343.174
 WAVE3P (16,2)=343.554
 WAVE3P (17,2)=343.934
 WAVE3P (18,2)=344.324
 WAVE3P (20,2)=345.103
 WAVE3P (21,2)=345.503
 WAVE3P (22,2)=345.913
 WAVE3P (23,2)=346.323
 WAVE3P (24,2)=346.743
 WAVE3P (25,2)=347.173
 WAVE3P (26,2)=347.633
 WAVE3P (27,2)=348.093
 WAVE3P (28,2)=348.582

C

WAVE3Z (4,2)=336.866
 WAVE3Z (5,2)=336.906
 WAVE3Z (6,2)=336.946
 WAVE3Z (7,2)=336.986
 WAVE3Z (8,2)=337.026
 WAVE3Z (9,2)=337.066
 WAVE3Z (10,2)=337.116

WAVE3Z (11,2)=337.166
WAVE3Z (12,2)=337.226
WAVE3Z (13,2)=337.276
WAVE3Z (14,2)=337.356
WAVE3Z (15,2)=337.426
WAVE3Z (16,2)=337.515
WAVE3Z (17,2)=337.605
WAVE3Z (18,2)=337.705
WAVE3Z (19,2)=337.815
WAVE3Z (20,2)=337.945
WAVE3Z (21,2)=338.085
WAVE3Z (22,2)=338.235
WAVE3Z (23,2)=338.405
WAVE3Z (24,2)=338.595
WAVE3Z (25,2)=338.785
WAVE3Z (26,2)=339.005
WAVE3Z (27,2)=339.215
WAVE3Z (28,2)=339.445

C

WAVE3R (2,2)=335.736
WAVE3R (3,2)=335.416
WAVE3R (4,2)=335.106
WAVE3R (5,2)=334.796
WAVE3R (6,2)=334.486
WAVE3R (7,2)=334.186
WAVE3R (8,2)=333.887
WAVE3R (9,2)=333.587
WAVE3R (10,2)=333.307
WAVE3R (11,2)=333.027
WAVE3R (12,2)=332.767
WAVE3R (13,2)=332.507
WAVE3R (14,2)=332.267
WAVE3R (15,2)=332.037
WAVE3R (16,2)=331.817
WAVE3R (17,2)=331.627
WAVE3R (18,2)=331.437
WAVE3R (19,2)=331.277
WAVE3R (20,2)=331.137
WAVE3R (21,2)=331.007
WAVE3R (22,2)=330.907
WAVE3R (23,2)=330.827
WAVE3R (24,2)=330.777
WAVE3R (25,2)=330.757
WAVE3R (26,2)=330.817
WAVE3R (27,2)=330.887
WAVE3R (28,2)=331.007
WAVE3R (29,2)=331.177

C

WAVE2P (3,2)=338.335
WAVE2P (4,2)=338.715
WAVE2P (5,2)=339.095
WAVE2P (6,2)=339.465
WAVE2P (7,2)=339.845
WAVE2P (8,2)=340.215
WAVE2P (9,2)=340.585
WAVE2P (10,2)=340.955
WAVE2P (11,2)=341.334
WAVE2P (12,2)=341.704

WAVE2P (13,2)=342.074
WAVE2P (14,2)=342.444
WAVE2P (15,2)=342.824
WAVE2P (16,2)=343.194
WAVE2P (17,2)=343.574
WAVE2P (18,2)=343.954
WAVE2P (19,2)=344.334
WAVE2P (20,2)=344.723
WAVE2P (21,2)=345.113
WAVE2P (22,2)=345.513
WAVE2P (23,2)=345.913
WAVE2P (24,2)=346.323
WAVE2P (25,2)=346.743
WAVE2P (26,2)=347.173
WAVE2P (27,2)=347.633
WAVE2P (28,2)=348.093
WAVE2P (29,2)=348.582

C

WAVE2Z (2,2)=336.886
WAVE2Z (3,2)=336.926
WAVE2Z (4,2)=336.956
WAVE2Z (5,2)=336.986
WAVE2Z (6,2)=337.006
WAVE2Z (7,2)=337.036
WAVE2Z (8,2)=337.066
WAVE2Z (9,2)=337.096
WAVE2Z (10,2)=337.136
WAVE2Z (11,2)=337.176
WAVE2Z (12,2)=337.226
WAVE2Z (13,2)=337.276
WAVE2Z (14,2)=337.336
WAVE2Z (15,2)=337.406
WAVE2Z (16,2)=337.476
WAVE2Z (17,2)=337.555
WAVE2Z (18,2)=337.655
WAVE2Z (19,2)=337.745
WAVE2Z (20,2)=337.865
WAVE2Z (21,2)=337.985
WAVE2Z (22,2)=338.115
WAVE2Z (23,2)=338.275
WAVE2Z (24,2)=338.445
WAVE2Z (25,2)=338.625

C

WAVE2R (3,2)=335.846
WAVE2R (4,2)=335.516
WAVE2R (5,2)=335.196
WAVE2R (6,2)=334.876
WAVE2R (7,2)=334.556
WAVE2R (8,2)=334.236
WAVE2R (9,2)=333.936
WAVE2R (10,2)=333.637
WAVE2R (11,2)=333.347
WAVE2R (12,2)=333.057
WAVE2R (13,2)=332.797
WAVE2R (14,2)=332.537
WAVE2R (15,2)=332.287
WAVE2R (16,2)=332.057
WAVE2R (17,2)=331.837

WAVE2R(18,2)=331.637
WAVE2R(19,2)=331.457
WAVE2R(20,2)=331.287
WAVE2R(21,2)=331.137
WAVE2R(22,2)=331.017
WAVE2R(23,2)=330.907
WAVE2R(24,2)=330.827
WAVE2R(25,2)=330.777
WAVE2R(26,2)=330.757
WAVE2R(27,2)=330.817
WAVE2R(28,2)=330.887
WAVE2R(29,2)=331.007
WAVE2R(30,2)=331.177

C

WAVE1P(3,2)=338.185
WAVE1P(4,2)=338.525
WAVE1P(5,2)=338.865
WAVE1P(6,2)=339.215
WAVE1P(7,2)=339.565
WAVE1P(8,2)=339.925
WAVE1P(9,2)=340.285
WAVE1P(10,2)=340.645
WAVE1P(11,2)=341.005
WAVE1P(12,2)=341.364
WAVE1P(13,2)=341.734
WAVE1P(14,2)=342.104
WAVE1P(15,2)=342.474
WAVE1P(16,2)=342.844
WAVE1P(17,2)=343.214
WAVE1P(18,2)=343.584
WAVE1P(19,2)=343.964
WAVE1P(20,2)=344.334
WAVE1P(21,2)=344.723
WAVE1P(22,2)=345.113
WAVE1P(23,2)=345.513
WAVE1P(24,2)=345.913
WAVE1P(25,2)=346.323
WAVE1P(26,2)=346.743
WAVE1P(27,2)=347.173
WAVE1P(28,2)=347.623
WAVE1P(29,2)=348.083
WAVE1P(30,2)=348.572

C

WAVE1Z(12,2)=337.206
WAVE1Z(13,2)=337.246
WAVE1Z(14,2)=337.296
WAVE1Z(15,2)=337.356
WAVE1Z(16,2)=337.416
WAVE1Z(17,2)=337.486
WAVE1Z(18,2)=337.565
WAVE1Z(19,2)=337.655
WAVE1Z(20,2)=337.745
WAVE1Z(21,2)=337.865
WAVE1Z(22,2)=337.985
WAVE1Z(23,2)=338.115
WAVE1Z(24,2)=338.265
WAVE1Z(25,2)=338.435
WAVE1Z(26,2)=338.615

```

C      WAVE1Z(27,2)=338.805

      WAVE1R(5,2)=335.656
      WAVE1R(6,2)=335.306
      WAVE1R(7,2)=334.966
      WAVE1R(8,2)=334.626
      WAVE1R(9,2)=334.306
      WAVE1R(10,2)=333.986
      WAVE1R(11,2)=333.677
      WAVE1R(12,2)=333.387
      WAVE1R(13,2)=333.097
      WAVE1R(14,2)=332.827
      WAVE1R(15,2)=332.557
      WAVE1R(16,2)=332.307
      WAVE1R(17,2)=332.077
      WAVE1R(18,2)=331.857
      WAVE1R(19,2)=331.647
      WAVE1R(20,2)=331.467
      WAVE1R(21,2)=331.297
      WAVE1R(22,2)=331.137
      WAVE1R(23,2)=331.017
      WAVE1R(24,2)=330.907
      WAVE1R(25,2)=330.827
      WAVE1R(26,2)=330.777
      WAVE1R(27,2)=330.757
      WAVE1R(28,2)=330.807
      WAVE1R(29,2)=330.877
      WAVE1R(30,2)=330.997
      WAVE1R(31,2)=331.157

C
2700  WRITE (9,2700)
      FORMAT (/, 'LINE CALCULATIONS COMPLETE - SCANNING UNDERWAY',/)
      CLOSE (UNIT=23)

C
C      NOW START SCANNING OVER LINES
C
      DO 3000 I=1, NDATA
3000  WSCAN(I)=0.000
      WSCAN(0)=WINIT
      DO 5000 K=1, NDATA
      DO 3100 I2=1, NDATA
3100  EINCR(I2)=0.000
      DO 3200 I3=1, NDATA
3200  ENET(I3)=0.000
      M=K-1
      WSCAN(K)=WSCAN(M)+0.0175

C
C      SCAN OVER THREE VIBRATIONAL LEVELS
C
      DO 4300 NV1=1, 3

C
C      NOW SCAN OVER 3 R BRANCH LINES
C
      DO 4000 J1=3, 35
      WDELTA=WSCAN(K)-WAVE1R(J1, NV1)
      DELTA=ABS(WDELTA)
      IF (DELTA.GT.RES) GO TO 3900
      FRAC=(RES-DELTA)/RES

```

```

GO TO 3950
3900  FRAC=0.000
3950  EINCR(J1)=FRAC*E11(J1,NV1)*SJR(J1)
      ENET(K)=ENET(K)+EINCR(J1)
4000  CONTINUE
      DO 4100 J1=3,35
      WDELTA=WSCAN(K)-WAVE2R(J1,NV1)
      DELTA=ABS(WDELTA)
      IF(DELTA.GT.RES) GO TO 4025
      FRAC=(RES-DELTA)/RES
      GO TO 4050
4025  FRAC=0.000
4050  EINCR(J1)=FRAC*E12(J1,NV1)*SJR(J1)
      ENET(K)=ENET(K)+EINCR(J1)
      ESUM(K)=ENET(K)
4100  CONTINUE
      DO 4200 J1=3,35
      WDELTA=WSCAN(K)-WAVE3R(J1,NV1)
      DELTA=ABS(WDELTA)
      IF(DELTA.GT.RES) GO TO 4125
      FRAC=(RES-DELTA)/RES
      GO TO 4150
4125  FRAC=0.000
4150  EINCR(J1)=FRAC*E13(J1,NV1)*SJR(J1)
      ENET(K)=ENET(K)+EINCR(J1)
      ESUM(K)=ENET(K)
4200  CONTINUE
C
C      NOW SCAN OVER 3 P BRANCH LINES
C
      DO 4215 J1=3,35
      WDELTA=WSCAN(K)-WAVE1P(J1,NV1)
      DELTA=ABS(WDELTA)
      IF(DELTA.GT.RES) GO TO 4205
      FRAC=(RES-DELTA)/RES
      GO TO 4210
4205  FRAC=0.000
4210  EINCR(J1)=FRAC*E11(J1,NV1)*SJP(J1)
      ENET(K)=ENET(K)+EINCR(J1)
4215  CONTINUE
      DO 4230 J1=3,35
      WDELTA=WSCAN(K)-WAVE2P(J1,NV1)
      DELTA=ABS(WDELTA)
      IF(DELTA.GT.RES) GO TO 4220
      FRAC=(RES-DELTA)/RES
      GO TO 4225
4220  FRAC=0.000
4225  EINCR(J1)=FRAC*E12(J1,NV1)*SJP(J1)
      ENET(K)=ENET(K)+EINCR(J1)
      ESUM(K)=ENET(K)
4230  CONTINUE
      DO 4245 J1=3,35
      WDELTA=WSCAN(K)-WAVE3P(J1,NV1)
      DELTA=ABS(WDELTA)
      IF(DELTA.GT.RES) GO TO 4235
      FRAC=(RES-DELTA)/RES
      GO TO 4240
4235  FRAC=0.000

```

```

4240  EINCR(J1)=FRAC*E13(J1,NV1)*SJP(J1)
      ENET(K)=ENET(K)+EINCR(J1)
      ESUM(K)=ENET(K)
4245  CONTINUE
C
C      NOW SCAN OVER 3 Q BRANCH LINES
C
      DO 4260 J1=3,35
      WDELTA=WSCAN(K)-WAVE1Z(J1,NV1)
      DELTA=ABS(WDELTA)
      IF(DELTA.GT.RES) GO TO 4250
      FRAC=(RES-DELTA)/RES
      GO TO 4255
4250  FRAC=0.000
4255  EINCR(J1)=FRAC*E11(J1,NV1)*SJZ(J1)
      ENET(K)=ENET(K)+EINCR(J1)
4260  CONTINUE
      DO 4275 J1=3,35
      WDELTA=WSCAN(K)-WAVE2Z(J1,NV1)
      DELTA=ABS(WDELTA)
      IF(DELTA.GT.RES) GO TO 4265
      FRAC=(RES-DELTA)/RES
      GO TO 4270
4265  FRAC=0.000
4270  EINCR(J1)=FRAC*E12(J1,NV1)*SJZ(J1)
      ENET(K)=ENET(K)+EINCR(J1)
      ESUM(K)=ENET(K)
4275  CONTINUE
      DO 4290 J1=3,35
      WDELTA=WSCAN(K)-WAVE3Z(J1,NV1)
      DELTA=ABS(WDELTA)
      IF(DELTA.GT.RES) GO TO 4280
      FRAC=(RES-DELTA)/RES
      GO TO 4285
4280  FRAC=0.000
4285  EINCR(J1)=FRAC*E13(J1,NV1)*SJZ(J1)
      ENET(K)=ENET(K)+EINCR(J1)
      ESUM(K)=ENET(K)
4290  CONTINUE
4300  CONTINUE
C
C      NOW WRITE DATA TO FILE IF DESIRED
C
C      WRITE(23,4950) WSCAN(K),CHAR(9),ENET(K)
C      4950  FORMAT (F8.3,A1,F8.2)
C      WRITE (9,4975) K
C      4975  FORMAT (I4)
C
      IF (K.EQ.175) GO TO 4900
      IF (K.EQ.350) GO TO 4900
      IF (K.EQ.525) GO TO 4900
      IF (K.EQ.700) GO TO 4900
      IF (K.EQ.1000) GO TO 4900
      IF (K.EQ.1250) GO TO 4900
      IF (K.EQ.1500) GO TO 4900
      GO TO 5000
4900  WRITE (9,4950) K,NDATA
4950  FORMAT (I4,' / ',I4,' POINTS')

```

```

4951 GO TO 5000
5000 CONTINUE
      WRITE (9,5100)
5100 FORMAT (/, 'SCANNING COMPLETE - POST-PROCESSING UNDERWAY')
      OPEN(UNIT=23, FILE='DATA', FORM='FORMATTED', STATUS='NEW')

C
C   NOW CHANGE DATA TO FAST FORMAT
C
      COLUMNS=2
      WRITE(23)COLUMNS
      CALL FASTSAVE('Wavelength, nm ',NDATA,WSCAN)
      CALL FASTSAVE('NH intensity ',NDATA,ESUM)
      CALL CRICKET('DATA')
8200 CLOSE (UNIT=23)
8300 END
C
C   REAL FASTSAVE SUBROUTINE
C
      SUBROUTINE FASTSAVE(TITLE, NUM, L )
      CHARACTER*15 TITLE
      INTEGER*2 NUM
      REAL L( NUM )
      CHARACTER*32 BUFFER

      INTEGER*2 COUNT
      CHARACTER*16 TITLEP

C
C   determine the output data size in bytes
C
100   COUNT = NUM * 11
C
C   change the column title to a pascal string
      TITLEP = char(len(trim(TITLE))//TITLE
      WRITE( 23 )TITLEP
      WRITE( 23 )COUNT
C
      DO 300 I=1, NUM, 1
C   write integer data to string buffer so ascii character
      WRITE( BUFFER, 200 )L( I )
200   FORMAT( F10.3 )
      WRITE( 23 )trim( BUFFER )//char( 13 )
300   CONTINUE
C
      RETURN
      END

C
C   This subroutine changes the File whose name is passed
C   to the type and creator of a Cricket Graph Fast Format
C   file.
C
      SUBROUTINE CRICKET( NAME )
C
      character*(*) NAME
      INTEGER*4 toolbx
      CHARACTER*256 FILENAME
      INTEGER PTR

```



```

PARAMETER (PTR=Z'C0000000')

C
include XP 20:FORTTRAN:INCLUDE FILES:file.inc
include XP 20:FORTTRAN:INCLUDE FILES:params.inc
C
change the file name to a PASCAL string
FILENAME = char(len(TRIM( NAME)))/TRIM(NAME )
C
set the toolbox parameters to call PBGETFILEINFO
ionameptr = toolbox(PTR, FILENAME )
iocompletion = 0
iofdirindex = -1
iocompletion = 0
iohrefnum = 0
iofversnum = 0
C
toolbox routine to get file info
CALL toolbox(PBGETFILEINFO, toolbox(PTR, params))
C
Cricket Graph Fast Format type and Creator
fdtype = 'STWK'
fdcreator = 'CGRF'
C
toolbox routine to set file info
CALL toolbox(PBSETFILEINFO, toolbox(PTR, params))
C
RETURN
END

```

APPENDIX C. LISTING OF HEAT OF EXPLOSION (Hex) PROGRAM

This program uses Fortran 2.2 for the Macintosh as did the programs in Appendices A and B. The program is discussed in Section 3.3.

```

PROGRAM HEXCALC
REAL NC(5),NH(5),NO(5),NN(5),HEATF(5),MSFRAC(5)
REAL MLFRAC(5),MOLES(5),XMW(5)
REAL MC,MH,MO,MN,MCNET,MHNET,MONET,MNNET
REAL HPROD,HREACT,MWREAC
REAL HEX,DELTA E,MOLSUM,DELTA H,DELTA N
REAL MCO2,MCO,MH2O,MH2,MN2,MO2
CHARACTER*5 TITLE(5)
INTEGER MM,DD,YY
OPEN(UNIT=23,FILE='XP 20:FORTTRAN:HEXIN',
1   FORM='FORMATTED',STATUS='OLD')
READ (23,800) NCOM
800  FORMAT (I1)
WRITE (9,805) NCOM
805  FORMAT (I1)
DO 902 I=1,NCOM
READ (23,825) TITLE(I),NC(I),NH(I),NO(I),NN(I),
1   HEATF(I),MSFRAC(I)
825  FORMAT (A5,4F9.3,F10.3,F5.3)
WRITE (9,900) TITLE(I),NC(I),NH(I),NO(I),NN(I),
1   HEATF(I),MSFRAC(I)
900  FORMAT (A5,/, 'C',F9.3,/, 'H',F9.3,/,
1   'O',F9.3,/, 'N',F9.3,/, 'HEATF',F10.3,/, 'MSFRAC=',F5.3)
902  CONTINUE
CLOSE (UNIT=23)
OPEN (UNIT=23,
1   FILE='XP 20:FORTTRAN:HEXOUT',STATUS='NEW')
CALL DATE(MM,DD,YY)
WRITE (23,903) MM,DD,YY
903  FORMAT (//,9X,'HEX CALCULATION FOR ',I2,'/',I2,'/',I2)
DO 905 I=1,NCOM
WRITE (23,904) TITLE(I),NC(I),NH(I),NO(I),NN(I),
1   HEATF(I),MSFRAC(I)
904  FORMAT (A5,/,F9.3,/,F9.3,/,F9.3,/,F9.3,/,F10.3,/,F5.3)
MOLES(I)=0.00
905  CONTINUE
MCNET=0.00
MHNET=0.00
MONET=0.00
MNNET=0.00
DO 920 I=1,NCOM
XMW(I)=NC(I)*12.01115+NH(I)*1.00797+NO(I)*15.9994+NN(I)*14.0067
WRITE (23,915) XMW(I)
915  FORMAT (F9.3)
MOLES(I)=MSFRAC(I)/XMW(I)
920  CONTINUE
MOLSUM=MOLES(1)+MOLES(2)+MOLES(3)+MOLES(4)+MOLES(5)
DO 930 I=1,NCOM
MLFRAC(I)=MOLES(I)/MOLSUM
MC=MLFRAC(I)*NC(I)
MCNET=MCNET+MC
WRITE (23,925) I,XMW(I)
925  FORMAT (I1,/, 'XMW=',F9.3)

```

```

      MH=MLFRAC(I)*NH(I)
      MHNET=MHNET+MH
      MO=MLFRAC(I)*NO(I)
      MONET=MONET+MO
      MN=MLFRAC(I)*NN(I)
      MNNET=MNNET+MN
930  CONTINUE
      WRITE (23,935) MCNET,MHNET,MONET,MNNET
935  FORMAT ('MCNET=',F9.5,/, 'MHNET=',F9.5,/,
1      'MONET=',F9.5,/, 'MNNET=',F9.5)
C
C      NOW CALCULATE DELTA H (RXN)
C
      DO 940 I=1, NCOM
      HREACT=HREACT+MLFRAC(I)*HEATF(I)
940  CONTINUE
C
C      STOICHIOMETRY
C
      TEST1=2*MCNET+0.5*MHNET
      TEST2=MCNET+0.5*MHNET
C
      IF (MONET.GE.TEST1) GO TO 950
      IF (MONET.GE.TEST2) GO TO 960
      GO TO 970
C
C      OXYGEN RICH: O2 in products, no CO, H2 ( $no \geq 2nc + nh/2$ )
C
950  MCO2=MCNET
      MH2O=0.5*MHNET
      MN2=0.5*MNNET
      MO2=(MONET-2*MCNET-0.5*MHNET)/2
      MH2=0.00
      MCO=0.00
      GO TO 990
C
C      INTERMEDIATE: CO, CO2 found, no H2 ( $nc + nh/2 \leq no \leq 2nc + nh/2$ )
C
960  MCO2=MONET-0.5*MHNET-MCNET
      MN2=0.5*MNNET
      MCO=2*MCNET+0.5*MHNET-MONET
      MH2O=0.5*MHNET
      MH2=0.00
      MO2=0.00
      GO TO 990
C
C      FUEL RICH: CO, H2O, AND H2 FOUND, NO CO2 ( $nc \leq no \leq nc + nh/2$ )
C
970  MCO=MCNET
      MH2O=MONET-MCNET
      MH2=(MHNET-2*(MONET-MCNET))/2
      MN2=0.5*MNNET
      MCO2=0.00
      MO2=0.00
C
990  WRITE (23,1000) MCO2,MCO,MH2O,MH2,MN2,MO2
1000 FORMAT ('MCO2=',F9.5,/, 'MCO=',F9.5,/,
1      'MH2O=',F9.5,/, 'MH2=',F9.5,/, 'MN2=',F9.5,/, 'MO2=',F9.5)

```

```

HPROD=MCO2*(-1*94.050)+MCO*(-1*26.420)+MH2O*(-1*68.320)
DELTAH=HPROD-HREACT
DELTAN=MNNET/2+MONET/2-MHNET/4
DELTAE=DELTAH-DELTAN*1.987*298/1000
MWREAC=1/MOLSUM
HEX=-1*DELTAE*MOLSUM
WRITE (23,1050) HEX,MWREAC
1050 FORMAT ('HEX=',F9.4,' KCAL/GM',/, 'MWREAC=',F9.3,' GM/MOL')
WRITE (23,1060) DELTAH, DELTAN, DELTAE
1060 FORMAT ('DELTAH=',F7.1,' KCAL/MOLE',/, 'DELTAN=',
1 F7.1,/, 'DELTAE=',F7.1)
WRITE (9,1070) HEX,MWREAC
1070 FORMAT ('HEX=',F9.4,' KCAL/GM',/, 'MWREAC=',F9.3,' GM/MOL')
WRITE (9,1075)
1075 FORMAT ('STOICHIOMETRY:')
DO 1100 I=1,NCOM
WRITE (9,1080) MLFRAC(I),TITLE(I)
1080 FORMAT (F7.5,' ',A5,' + ')
1100 CONTINUE
WRITE (9,1110) MCO2,MCO,MH2O,MH2,MN2,MO2
1110 FORMAT ('--> ',F7.3,' CO2 + ',F7.3,' CO + ',F7.3,
1 ' H2O + ',F7.3,' H2 + ',F7.3,' N2 + ',F7.3,' O2')
WRITE (23,1120)
1120 FORMAT ('STOICHIOMETRY:')
DO 1140 I=1,NCOM
WRITE (23,1130) MLFRAC(I),TITLE(I)
1130 FORMAT (F7.5,' ',A5,' + ')
1140 CONTINUE
WRITE (23,1150) MCO2,MCO,MH2O,MH2,MN2,MO2
1150 FORMAT ('--> ',F7.3,' CO2 + ',F7.3,' CO + ',F7.3,
1 ' H2O + ',F7.3,' H2 + ',F7.3,' N2 + ',F7.3,' O2')
CLOSE (UNIT=23)
WRITE (9,1160)
1160 FORMAT (/, '** PRESS RETURN TO RESUME FINDER **')
PAUSE
1200 END

```

Input file ("HEXIN" in program):

aaaaacccccccchhhhhhhhhoooooooooonnnnnnnnnbbbbbbbbbbwww

where, a=5 letter ingredient ID (A5), c=carbon subscript in stoichiometric formulation (1 for methane, 4 for HMX, etc.) (F9.3), h=hydrogen subscript (F9.3), o=oxygen subscript (F9.3), n=nitrogen subscript (F9.3), b=heat of formation in kcal/mol (F10.3), w=weight fraction of ingredient in propellant\ (F5.3). The first line is the number of components in the propellant (5 max in this program, easily changed). Thus, a typical file might be:

```

3
NCB 6.000    7.260    10.480    2.74    -161.960    0.435
NG  3.000    5.000    9.000    3.000    -90.75000    0.202
HMX 4.000    8.000    8.000    8.000    17.930000    0.363
2NDPA12.000 10.000    2.000    2.000    17.00000    0.025

```

DEP	12.000	14.000	4.000	0.000	-180.00000	0.040
PGA	4.580	7.500	2.340	0.000	-118.30000	0.10
IMETN	5.000	9.000	9.000	3.000	-105.90000	0.17
NCC	6.000	7.365	10.290	2.64	-164.789	1.000
NCA	6.000	7.550	9.900	2.45	-169.067	1.000
NCD	6.000	7.680	9.645	2.32	-172.146	1.000

Note that only the first three ingredient lines are read so unused ingredients can be "stored" instead of being retyped each time.

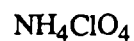
APPENDIX D. PROPELLANT INGREDIENTS

Ingredient

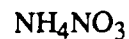
Structure

Oxidizers:

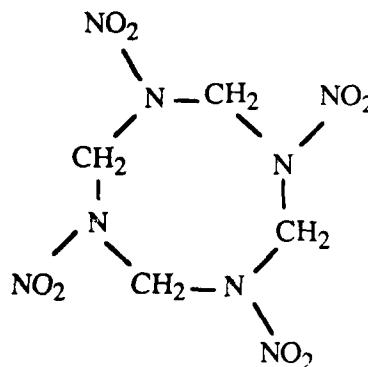
Ammonium perchlorate (AP)



Ammonium nitrate (AN)



HMX (cyclotetramethylene tetranitramine, octogen, etc.)

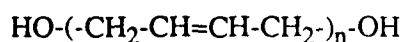


RDX (cyclotrimethylene trinitramine, hexogen, etc.)

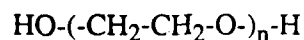
6 member ring analog of HMX

Polymers: (n varies depending upon polymerization conditions)

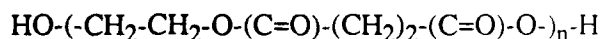
Hydroxy-terminated polybutadiene (HTPB)



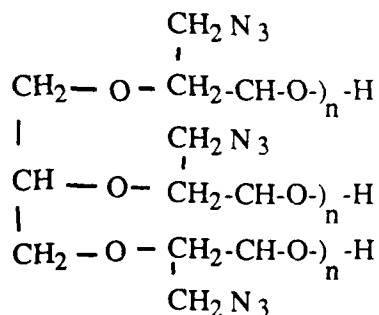
Polyethylene glycol (PEG)



Polydiethylene glycol adipate (PGA)

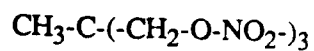


Glycidyl azide polymer (GAP)

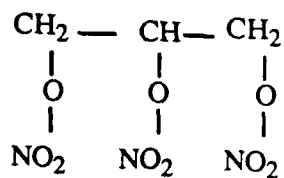


Plasticizers:

Trimethylol ethane trinitrate (TMETN)

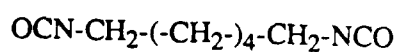


Nitroglycerin (NG)

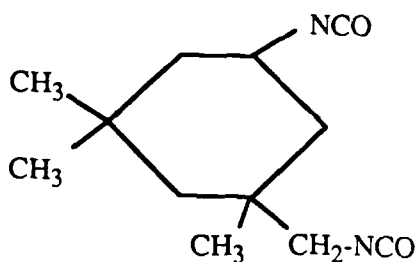


Curatives:

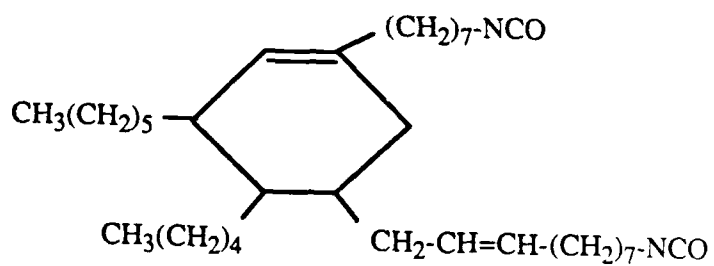
Hexamethylene diisocyanate (HDI)



Isophorone diisocyanate (IPDI)



Dimer acid diisocyanate (DDI)



APPENDIX E. FLAME EMISSION SUMMARY

Flame	Emitting species	Comments
H ₂ /O ₂	OH, O ₂ , blue cont.	
H ₂ /N ₂ O	OH, NH, NO, NH ₂	
H ₂ /NO	OH, NO [†] , O ₂	
H ₂ /NO ₂	OH [†] , NO+O	
CO/O ₂	CO+O, O ₂ [†] , CO ₂	
C/O ₂	C ₂ , CO+O,	
CO/NO _x	CO+O, NO+O, O ₂ , CO ₂	
HC/O ₂	OH, CH, C ₂ , HCO [†]	
CH ₃ OH/O ₂	OH, C ₂ ^{††} , CH ₂ O, CH [†]	
CH ₂ O/O ₂	OH, CO+O	
CH ₂ O ₂ /O ₂	OH, CO+O	
CH ₄ /NO	OH, CH, NH, CN, C ₂ ^{††} , NO, NH ₂ ^{††}	
HC/NO	OH, CH, NH, CN, C ₂ , NO	no NH ₂
HC/NO ₂	OH [†] , CH, NH, CN, C ₂ , NO (2nd)	NO+O (1st)
CH ₄ /ClO ₂	OH, CH, C ₂ , CH ₂ O	
CH ₄ /HClO ₄ (1st)	OH [†] , CH [†]	
CH ₄ /HClO ₄ (2nd)	OH, CH, CN [†]	no ClO
H ₂ /Cl ₂ , CH ₃ Cl/O ₂	OH, ClO	
Fuel N (org.)/O ₂	OH, CH, NH, CN, NO	
C ₂ N ₂ /air (diffusion)	C ₂	
C ₂ N ₂ /air	CN, C ₂ [†]	
C ₂ N ₂ /O ₂	CN, C ₂ , NO	
CH ₃ OH/N ₂ O	OH, CH, NH, CN, NH ₂	no CH ₂ O
CH ₄ /N ₂ O	OH, CH, NH, CN, C ₂ [†] , NO, NH ₂	
HC/N ₂ O	OH, CH, NH, CN, C ₂ , NO, NH ₂	
CH ₂ O/N ₂ O	OH, CH ^{††} , NH, CN, NO?, NH ₂	
CH ₂ O ₂ /N ₂ O	OH, CO+O, NO+O	
C ₂ H ₂ /N ₂ O	OH, CH, NH, CN, C ₂ , NH ₂	
C ₇ H ₁₆ /N ₂ O	OH, CH, NH, CN, C ₂ , NH ₂	
(CH ₃) ₂ CO/N ₂ O	OH, CH, CN	
C ₂ H ₅ OH/N ₂ O	OH, CH, NH, CN, C ₂ [†] , NH ₂	
NH ₃ /NO	OH [†] , NH, NO [†] ?	
NH ₃ /O ₂	OH [†] , NH, NO [†] ?, NO+O, NH ₂	

- Notes: (1). all flames premixed except as noted
(2). [†] = weak, ^{††} = very weak
(3). 1st and 2nd refer to 1st and 2nd reaction zones in flames with multiple zones
(4). Data from References 104, 145 primarily
(5). HC=hydrocarbon (general category)